



Provided by the author(s) and University of Galway in accordance with publisher policies. Please cite the published version when available.

Title	An experimental and computational investigation of the mechanics of degradation in polymer bioresorbable scaffolds
Author(s)	Fiuza, Constantino
Publication Date	2023-10-03
Publisher	NUI Galway
Item record	<a href="http://hdl.handle.net/10379/17934">http://hdl.handle.net/10379/17934</a>

Downloaded 2024-04-29T01:59:36Z

Some rights reserved. For more information, please see the item record link above.



**AN EXPERIMENTAL AND COMPUTATIONAL  
INVESTIGATION OF THE MECHANICS OF DEGRADATION  
IN POLYMER BIORESORBABLE SCAFFOLDS**

**Constantino Fiuza B.E.**



**OLLSCOIL NA GAILLIMHÉ**  

---

**UNIVERSITY OF GALWAY**

A thesis submitted to the University of Galway as fulfilment of the requirements for the Degree of  
Doctor of Philosophy

**2022**

Discipline of Biomedical Engineering,  
College of Science and Engineering,  
University of Galway

Supervisor of Research:

Dr. Ted Vaughan

Co-Supervisors of Research:

Dr. William Ronan

Dr. Katarzyna Polak-Kraśna

# Abstract

Drug-eluting stents (DES) have established themselves as the gold-standard in treating arterial blockages, with over 1.3 million stent procedures carried out across Europe in coronary vessels alone. However, these permanent metallic devices remain in the body well beyond the timeframe that their structural role has been completed, which can cause long-term complications, such as strut failure, late-stage thrombosis and restenosis. Polymer bioresorbable scaffolds (BRS) showed great potential as the next generation of coronary stents, whereby they would support the vessel during the healing period and subsequently being resorbed into the surrounding tissue once their functional role was complete. However, the development of polymer BRS have encountered a number of setbacks in recent years that has led to the withdrawal of several commercial devices from the market due to inferior long-term performance compared to DES. While the underlying reasons for this poor performance are complicated, some of the primary contributing factors is thought to be the mechanical changes that take place during the degradation process, which remain poorly understood strut thickness and vessel sizing.

The objective of this thesis is to investigate the physical and mechanical degradation behaviour of polymer BRS through a combined experimental and computational approach. Detailed experimental bench-top studies using an accelerated degradation protocol were carried out to evaluate the long-term physical and mechanical performance of two polymer BRS. In parallel, a phenomenological degradation framework was developed and implemented within the Abaqus finite element code and the model parameters were calibrated to fully predict the radial response of one of these devices over the course of degradation. Experiments were carried out to validate the calibrated model by implanting the polymer BRS within a silicone vessel and subjecting it the accelerated degradation protocol and comparing the long-term degradation performance to the computational prediction. The developed computational framework was used to conduct a detailed investigation of the individual roles of scaffolds geometry/design and material properties on both the short-and long-term performance of polymer BRS. Finally, the computational degradation framework was integrated into an in silico clinical trial platform for the development of coronary stents and used to predict the long-term performance of several BRS in a range of clinical scenarios.

It was found that both polymer BRS were highly effective in maintaining their radial stiffness and strength during short-and medium-term degradation, but underwent a ductile to brittle transition in later stages of degradation. This brittle behaviour coincided with distinct increases in relative crystallinity of the polymer and highlighted a possible reason for polymer BRS poor long-term performance in clinical settings. The computational degradation framework was able to successfully capture the short-term deployment behaviour and the long-term degradation response under radial loading, including all aspects of elastic, yield and post-yield behaviour throughout all time-points. However, in an effort to validate the degradation model, the polymer BRS showed distinct creep behaviour in the early stages of the degradation response, where the diameter of the BRS was greatly reduced when implanted in a silicone vessel and under constant load from a parallel plate test. This was not captured by the computational model and suggests that a further understanding of the creep performance of these devices is required, both experimentally and computationally to enable future BRS development. It was found that optimising the geometry of the polymer BRS generally improved only the short-term deployment performance, with design changes only providing modest benefits to long-term degradation behaviour. This indicates that material development is the primary route that can be targeted to enhance the degradation performance of BRS. The work in this thesis enhances the current understanding of the mechanics of degradation in polymer BRS and provides a benchmark for the future development in this area.

# List of Publications

## Journal Articles

The following publications have arisen from the work presented in this thesis:

- **Fiuza C**, Polak-Krasna K, Antonini L, Petrini L, Carroll O, Ronan W, Vaughan TJ. An Experimental Investigation into the Physical, Thermal and Mechanical Degradation of a Polymeric Bioresorbable Scaffold. *Journal of the Mechanical Behaviour of Biomedical Materials*, 125 (2022), pp. 1-9

The following manuscripts are either in submission, or in preparation for submission for peer-review.

- **Fiuza C**, Poletti G, Antonini L, Pennati G, Polak-Krasna K, Ronan W, Vaughan TJ. Predicting the Short and Long-Term Performance of a Polymer Bioresorbable Stent, (*in submission*).
- **Fiuza C**, McKenna C, Ronan W, Vaughan TJ. A Computational Investigation into the Effect of Stent Geometry and Material Properties on the Long-Term Degradation Performance of Polymer Bioresorbable Stents, (*in preparation*).
- **Fiuza C**, Ronan W, Vaughan TJ. Understanding the Long-term Degradation Performance of Polymer Bioresorbable Stents – A Review, (*in preparation*).

## International Conference Proceedings

- **Fiuza, C**, Polak-Krasna K, Ronan, W, Vaughan, TJ. An Experimental Investigation of the Degradation Behaviour of a Bioresorbable Polymer Vascular Scaffold. 26<sup>th</sup> European Society of Biomechanics, July 2021, Milan, Italy.
- **Fiuza, C**, Polak-Krasna K, Antonini L, Poletti G, Pennati G, Ronan, W, Vaughan, TJ. A Phenomenological Degradation Model to predict the Long-term Performance of a Polymeric Bioresorbable Scaffold. 11<sup>th</sup> European Solid Mechanics Conference, July 2022, Galway, Ireland.
- **Fiuza, C**, Polak-Krasna K, Antonini L, Poletti G, Pennati G, Ronan, W, Vaughan, TJ. A Phenomenological Degradation Model to predict the Long-term Performance of a Polymeric Scaffold. 27<sup>th</sup> European Society of Biomechanics, June 2022, Porto, Portugal.

## Acknowledgements

First, I would like to express my sincere thanks and gratitude to my supervisor Dr. Ted Vaughan, for his support, guidance and encouragement throughout my studies. I am truly grateful for your expertise, mentoring and a constant reminder to keep the bigger picture in mind.

I would also like to thank my co-supervisors Dr. Katarzyna Polak-Kraśna for all your guidance, suggestions and helping me to find my feet in the beginning and to Dr. William Ronan for sharing your knowledge on computational modelling.

Next, I wish to acknowledge my funding sources, the European Union Horizon 2020, as well as the Irish Centre for High-End Computing (ICHEC) for the provision of essential computational facilities and support. Thanks to Dave, Maja and all the technical staff at University of Galway for their willingness to answer questions and generously giving their time and assistance with experimental work. Thanks also to colleagues in Politecnico di Milano; Luca and Gianluca for insightful discussions on modelling and experiments.

Thank you to all my friends and colleagues at NUI Galway (or University of Galway now!), for the lunchtime chats, baked goods and conferences. It has been a pleasure to work with each of you. Special thanks to Ali and Eoghan for all the lunch-time chats and discussions.

To my family and Ciara without whose encouragement and support I would not have gotten to where I am, thank you.

## Declaration of Originality

I declare that the work presented in this thesis is my own.

Constantino Fiuza

# Table of Contents

<b>Abstract</b> .....	<b>i</b>
<b>List of Publications</b> .....	<b>ii</b>
<b>Acknowledgements</b> .....	<b>iii</b>
<b>Declaration of Originality</b> .....	<b>iv</b>
<b>Table of Contents</b> .....	<b>v</b>
<b>Introduction</b> .....	<b>1</b>
1.1. Coronary Artery Stenting and Associated Complications .....	<b>2</b>
1.2. Overview of Coronary Stents.....	<b>4</b>
1.2.1. Bare Metal Stents (BMS) .....	<b>4</b>
1.2.2. Drug Eluting Stents (DES) .....	<b>5</b>
1.2.3. Bioresorbable Scaffolds (BRS) .....	<b>6</b>
1.3. Biomechanics and Computational Modelling of Coronary Stents.....	<b>9</b>
1.3.1. Stent Mechanics .....	<b>9</b>
1.3.2. Computational Methods used in Stent Development .....	<b>11</b>
1.4. Thesis Objectives .....	<b>12</b>
1.5. Thesis Structure.....	<b>13</b>
1.6. References .....	<b>15</b>
<b>Literature Review</b> .....	<b>19</b>
2.1. Biodegradable Polymers .....	<b>19</b>
2.2. Mechanical Properties of Biodegradable Polymers .....	<b>21</b>
2.2.1. General Mechanical Properties of Polymers used in BRS Applications.....	<b>21</b>
2.2.2. Influence of Environmental Factors on Mechanical Properties .....	<b>23</b>
2.2.3. Tailoring the Mechanical Response of Polymers used in BRS Applications .....	<b>25</b>
2.2.4. Degradation Mechanisms and Effects on Mechanical Performance of Polymers ..	<b>28</b>
2.3. Experimental Testing of BRS .....	<b>33</b>
2.3.1. BRS Devices.....	<b>33</b>
2.3.2. Standardised Testing of BRS – Short-Term Performance .....	<b>34</b>
2.3.3. Bench testing of BRS – Short-Term Performance .....	<b>38</b>
2.3.4. In Vitro Degradation Characterisation of BRS .....	<b>42</b>
2.4. Overview of Computational Modelling of Coronary BRS .....	<b>47</b>

2.4.1. Short-Term Modelling of BRS.....	48
2.4.2. Long-term Modelling of BRS .....	55
2.5. Conclusions.....	65
2.6. References .....	67
<b>Theory .....</b>	<b>76</b>
3.1 Continuum Mechanics .....	76
3.1.1 Notation.....	76
3.1.2 Deformation and Motion .....	77
3.1.3 Strain Measures .....	77
3.1.4 Stress Measures .....	80
3.2 Material Constitutive Behaviours .....	81
3.2.1 Elasto-Plasticity and Johnson-Cook Plasticity .....	81
3.2.2 Isotropic Hyperelasticity .....	83
3.2.3 Ductile Damage.....	85
3.3 Finite Element Method.....	86
3.3.1 Implicit Finite Element Method .....	86
3.3.2 Explicit Finite Element Method .....	88
3.4 Finite Element Method Implementation .....	90
3.5 References .....	92
<b>An Experimental Investigation into the Physical, Thermal and Mechanical Degradation of Two Polymeric Bioresorbable Scaffolds.....</b>	<b>93</b>
4.1. Introduction.....	93
4.2. Methods.....	95
4.2.1 In Vitro Accelerated Degradation .....	95
4.2.2 Gravimetric Analysis.....	97
4.2.3 Thermal Properties .....	97
4.2.4 Molecular Weight Properties.....	98
4.2.5 Mechanical Characterisation – Radial Compression Testing.....	98
4.2.6 Mechanical Characterisation – Nanoindentation Testing .....	100
4.3 Results.....	102
4.3.1 Gravimetric Results .....	102
4.3.2 Thermal Analysis .....	103
4.3.3 Molecular Weight.....	105
4.3.4 Mechanical Characterisation – Radial Compression Results.....	106



4.3.5 Mechanical Characterisation – Nanoindentation Results.....	111
4.4 Discussion .....	113
4.5 Conclusion .....	116
4.6 References .....	118
<b>Development, Implementation and Validation of a Phenomenological Degradation Model for a Polymeric Bioresorbable Scaffold .....</b>	<b>123</b>
5.1. Introduction.....	123
5.2. Methods.....	126
5.2.1 Model Geometry.....	126
5.2.2 Material and Degradation Framework Description.....	127
5.2.3 Model Verification – Single Element Test.....	129
5.2.4 Crimping and Calibration of Initial Time Point .....	130
5.2.5 Degradation Framework Calibration.....	131
5.2.6 Experimental Validation – Silicone Vessel Degradation and Parallel Plate Test .	133
5.2.7 Computational Models of Mock Vessel Degradation and Parallel Plate Testing .	135
5.3. Results .....	137
5.3.1. Degradation Framework Implementation .....	137
5.3.2. Degradation Framework Calibration Results .....	138
5.3.3. Degradation Framework Validation Results .....	142
5.4. Discussion .....	145
5.5. Conclusions .....	149
5.7. References .....	150
<b>A Computational Investigation into the Effect of Scaffold Geometry and Degradation Parameters on the Long-Term Degradation Performance .....</b>	<b>154</b>
6.1. Introduction.....	154
6.2. Methods.....	157
6.2.1. Study Design .....	157
6.2.2. Model Geometries .....	158
6.2.3. Constitutive Material Models.....	161
6.2.4. Simulation Work-Flow .....	164
6.2.5. Post Processing.....	165
6.3. Results .....	166
6.3.1. Effect of Degradation Parameters on Scaffold Performance .....	166
6.3.2. Effect of Geometric Parameters on Short and Long-Term Performance .....	168

6.3.3. Comparison of Absorb and Non-Commercial Scaffolds .....	175
6.4. Discussion .....	178
6.5. Conclusions .....	182
6.7. References .....	183
<b>Concluding Remarks and Future Perspectives .....</b>	<b>186</b>
7.1 Summary of Key Contributions .....	186
7.2 Future Recommendations .....	190
7.3 References .....	193
<b>Demonstration of an In-Silico Platform for the Design and Development of Vascular Scaffolds – Degradation Module.....</b>	<b>194</b>
8.1. Introduction .....	194
8.2. Methods.....	196
8.2.1. InSilc Platform .....	196
8.2.2. InSilc Degradation Module – General Overview .....	197
8.2.3. InSilc Scenarios – Simulation Setup and Clinical Outputs .....	199
8.3. Results .....	204
8.3.1. Scenario 1 – Comparison of Patient Anatomies.....	204
8.3.2. Scenario 2 – Comparison of Stent Designs .....	206
8.3.3. Scenario 3 – Comparison of Different Stents.....	207
8.4. Discussion .....	208
8.5. Conclusions .....	211
8.6. References .....	213

# Chapter 1

## Introduction

---

The introduction of endovascular stenting has revolutionised the treatment of coronary artery disease, when compared with the prior standard of open-heart surgery and coronary bypass. Since the introduction of the first market approved stent in 1987 (Palmaz *et al.*, 1985; Schatz *et al.*, 1991), several generations of coronary stents have been developed to further improve patient outcomes and treat the unfortunate associated treatment complications of coronary artery disease. The latest generation of coronary stents in development include bioresorbable metal and polymer stents. These stents are intended to be completely resorbed into the patient's body once vessel healing is complete to avoid the late-stage complications associated with the current generation of coronary stents (Canan and Lee, 2010; Ong and Jang, 2015). However, the development of bioresorbable scaffolds (BRS) has suffered significant setbacks in recent years. Several companies have pioneered the development of polymer-based BRS, with significant clinical data already generated. Unfortunately, this first-generation of BRS has essentially failed, with 2-year follow up data from Abbott's ABSORB III device demonstrating increased risk of late-stage adverse events (Byrne *et al.*, 2018). This resulted in the European Society for Cardiology making a formal recommendation that current BRS should not be preferred to conventional drug-eluting stents for percutaneous coronary intervention in clinical practice. There have been devastating consequences to the wider industry, with other major manufacturers removing their devices from the market ('Reva Revives', 2022), halting development of polymer-based bioresorbable devices (Densford 2017) and even filing for bankruptcy protection ('Reva Revives', 2022). While the underlying reasons for poor clinical

performance of polymer-based bioresorbables are complicated, the primary contributing factors are the relatively low strength and stiffness that has necessitated relatively thick stent struts (Ang *et al.*, 2017) and slow degradation behaviour (Suuronen *et al.*, 1998) that results in adverse late-stage events. Recent developments in BRS have seen sub 100  $\mu\text{m}$  thick struts to mitigate these previous clinical weaknesses. The work undertaken in this thesis adopts both experimental and computational techniques to investigate the biomechanical and degradation behaviour of laser-cut polymer BRS.

## **1.1. Coronary Artery Stenting and Associated Complications**

Atherosclerosis is the build-up of calcified plaque within blood vessels, which begins to occlude the blood vessel and reduces the oxygen supply to the target area. This occlusion, if found to occur in the heart, may cause ischemic heart disease (IHD), which is characterised by a reduction in blood supply to the heart muscle and may lead to cardiac infarction. IHD can cause chest pain or angina and, in severe cases, death. Cardiovascular diseases are responsible for 20% of deaths in the US in people aged less than 70 years (Tsao *et al.*, 2022) and affect 1.72% of the world population (Khan *et al.*, 2020). The heart muscle is served by two coronary arteries; the left and right as shown in Figure 1.1(a), which bring oxygenated blood to the heart. These arteries can be found at the base of the aorta above the aortic valve. As time passes, the diameter of these coronary lumen may be reduced due to the build-up of plaque within the artery walls. Plaque formation begins with endothelial dysfunction, which leads to the formation of fatty streaks. The deposited material within the artery walls is a plaque that can be made from fibrous tissue, foam cells and cholesterol that has permeated through the artery walls (Bentzon *et al.*, 2014). Figure 1.1(c) shows an example of a plaque that may develop.

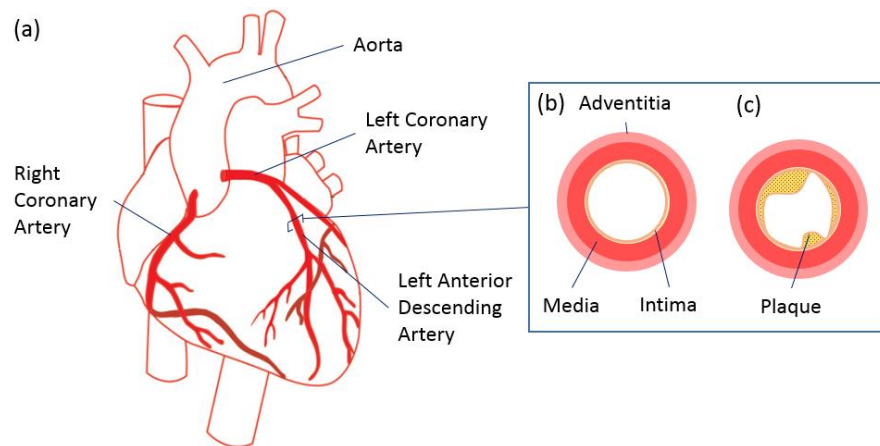


Figure 1.1. Schematic showing (a) the coronary arteries in relation to the heart muscle, (b) layer structure of a healthy coronary blood vessel and (c) build-up of a plaque within the vessel lumen causing an occlusion.

Perforation of the plaque could release the contents into the blood stream causing emboli to form in the blood. These emboli may continue throughout the vascular system where they can cause blockages in smaller vessels. The calcification of the plaque also changes the elasticity of the vessel, which can lead to a pressure increase within the lumen. The plaque may remain intact and continue to increase in size until it totally occludes the vessel. These occlusions are typically treated through a percutaneous coronary intervention (PCI) where a balloon is expanded to open the restriction. This is followed by the deployment of either a balloon-expandable or self-expanding stent. The occluded region is accessed through an incision in the groin to the femoral artery or the radial artery in the arm where a guidewire is navigated to the occlusion with the assistance of computed tomography (CT) or x-ray. The expansion of the stent restores the patency of the vessel and allows the vessel to remodel. Stents are only required to provide mechanical support to the surrounding vessel walls while the vessel is remodelling (Onuma and Serruys, 2011). After this, the stent is no longer required and it becomes embedded into the vessel wall for the duration of the patient's lifespan. Despite the advancements in stent design, a number of late-stage complications are associated with stent implantation. These include thrombosis (Ong and Jang, 2015), in-stent restenosis (Moussa *et al.*, 2020), strut fracture (Kan *et al.*, 2016), failure to return the original vessel vasomotion

(Onuma and Serruys, 2011) or a permanent narrowing of the section of vessel when a stent is implanted in younger patients (Ang *et al.*, 2017).

## **1.2. Overview of Coronary Stents**

Since their introduction in 1987, there have been a number of generations of coronary stent devices. The following section gives a brief overview of each generation of coronary stent, their particular complications and the various developments in each generation.

### **1.2.1. Bare Metal Stents (BMS)**

The first stents were introduced to overcome the shortcomings of the initial PCI treatments, which consisted of dilating the stenosed region through balloon angioplasty. However, this method resulted in a high incidence of restenosis or re-blocking of the vessel. This restenosis was due to the largely elastic vessel returning or recoiling to its original configuration or re-occlusion of the vessel due to new cell growth caused by damage to the vessel wall during balloon inflation. Re-occluding of the artery can lead to severe complications that could require an emergency coronary bypass graft. The introduction of bare metal stents (BMS) significantly reduced the incidence of vessel recoil or collapse, leading to an overall reduction in rates of acute restenosis (de Feyter *et al.*, 1994), when compared to balloon angioplasty alone. Despite the success of using BMS in restoring blood flow through the vessel, it was found that BMS implantation caused damage to the endothelium of the intima, resulting in the proliferation of endothelial cells leading to restenosis and further occlusion of the vessel. This was found to occur in 5-42% of PCI patients within 6 months of treatment (Serruys *et al.*, 1988). Deployment of the stents may also lead to stent thrombosis, which is the activation of platelets in the vicinity of the exposed metal stent surface and the formation of a blood clot (Ong and Jang, 2015). Typically, the treatment for restenosis, known as target region revascularisation is a repeat procedure to reopen the vessel. These effects have led to the development and innovation for the next generation of coronary stents.

### 1.2.2. Drug Eluting Stents (DES)

To address the complication of restenosis in BMS implantation, drug eluting stents (DES) were developed whereby devices were coated in an anti-proliferative drugs to reduce the neointimal hyperplasia caused by the stent implantation. It was found that the use of DES greatly reduced the rate of restenosis in patients that underwent stenting procedures (Moses *et al.*, 2003). The first generation of DESs had the paclitaxel or sirolimus drug embedded in a biodegradable polymer coating that would intentionally degrade to locally release the drugs into the surrounding tissue. This first generation of DES was quickly replaced due to biocompatibility issues with the drug impregnated polymer coating (Garg, *et al.*, 2013). The current DES are still coated with this family of anti-proliferative drugs to reduce neo-intimal hyperplasia, however new coating materials have been introduced to overcome the initial complications. The materials used in DES manufacture also evolved, with stiffer materials such as platinum-chromium and cobalt-chromium being used. This allowed for the manufacture of thinner stent struts. Figure 1.2 provides a summary of commercially available stents and how there has been a trend for gradual thinning of strut dimensions over time. Several of the most recent DES designs that have been released to market have sub-100  $\mu\text{m}$  strut thicknesses, with the Biotronic Osiro ('Biotronik Osiro', Berlin, Germany, 2022) having the thinnest struts of only 60  $\mu\text{m}$ .

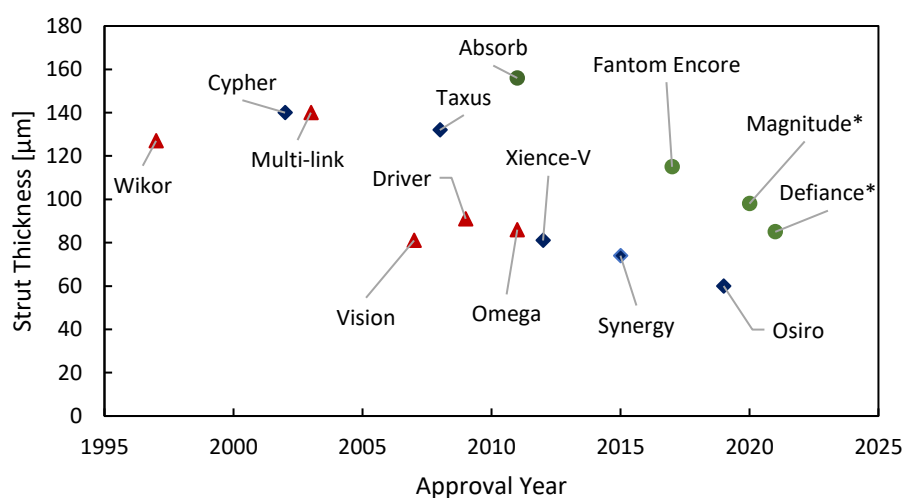


Figure 1.2. Schematic plotting the downward trend in stent strut thickness of a few selected market approved balloon expanded BMS, DES and BRS over time. Note that \* denotes waiting for approval.

Despite the improved patient outcomes with DES, a number of late-stage complications persisted (Ong and Jang, 2015; Kan *et al.*, 2016), such as late-stage restenosis, catastrophic strut fracture, thrombosis and the associated complications of permanent structures placed in the vessels of younger patients and failure to return the original vessel vasomotion. Ultimately, despite DES ability to treat the vessel blockage, these devices still remain within the patient long after their useful function has been performed.

### **1.2.3. Bioresorbable Scaffolds (BRS)**

Bioresorbable scaffolds (BRS) are intended to avoid the late-stage complications associated with DES and BMS by completely resorbing into the patient's body through passive processes. Bioresorbtion being the total elimination of the compound from the body through dissolution, assimilation and excretion (Byrne *et al* 2014). The materials for these scaffolds consist of metals that are already available in trace amounts in the body, such as magnesium, iron, zinc and their various alloys and biodegradable polymers, such as poly-lactic acid (PLLA) and poly-glycolic acid (PLGA), which are eliminated from the body through metabolic processes. The degradation of these polymers progresses through a number of stages including hydration, depolymerization and hydrolysis. The polymer chains are broken down further, which are metabolized by phagocytes into soluble monomers. These monomers are further metabolized, these then enter the Krebs cycle and eventually are converted into carbon dioxide and water (Gleadall *et al.*, 2014). In developing polymer BRS, a major challenge has been that the polymer materials used in cardiovascular applications have lower mechanical properties compared to the existing metallic materials used for DES.



Table 1.1. Comparison of conventional constitutive permanent stent materials versus those used in both polymer and metal bioresorbable applications.

Material Name	Elastic Modulus (GPa)	Yield Strength (MPa)	Strain to Failure (%)	Degradation Time	Ref.
316 SS	200	264	40-45	-	(Lee <i>et al.</i> , 2011; Conway <i>et al.</i> , 2012)
Platinum Chrome	203	480	44.8	-	(O'Brien <i>et al.</i> , 2010)
WE43 (Magnesium Alloy)	40-50	220-330	2-20	1.35 mm/y	(McMahon <i>et al.</i> , 2018)
Iron	207	200	40	0.19 mm/y	(McMahon <i>et al.</i> , 2018) (McMahon <i>et al.</i> , 2018)
PLLA	1-7	60	2-300	1-5 years	(Pan, Zhu and Inoue, 2007)
PCL	0.25-0.44	12-30	80-800	2-3 years	(Bartnikowski <i>et al.</i> , 2019)

Poly (L-lactide) (PLLA) is by far the most commonly used bioresorbable material for BRS devices, with Absorb (Abbott Vascular, Santa Clara, CA, USA), DeSolve (Elixir Medical, Sunnyvale, CA, USA), Amaranth (Amaranth Medical Inc., CA, USA), Acute BRS (Orbus Neich, Fort Lauderdale, FL, USA) and the Igaki-Tamai scaffold (Kyoto Medical Planning Co, Ltd, Kyoto, Japan) all made from this polylactide-based polymer. Due to their lower stiffness, polymer BRS have less radial strength when compared with conventional BMS and DES, requiring thicker struts to provide a similar level of support, which potentially reduces the conformability and increases the crossing-profile of the device. The higher strut thickness also increases the time for endothelialisation of the struts. Figure 1.3 summarises the differences in strut thickness between metallic BMS and DES when compared with the original and current strut thickness of BRS. Original polymer BRS strut thicknesses are closer to those BMS that were initially developed, with Figure 1.2 showing that they can be more than twice the thickness as the thinnest DES currently available. However newer BRS that are in development show great improvement in strut thickness.

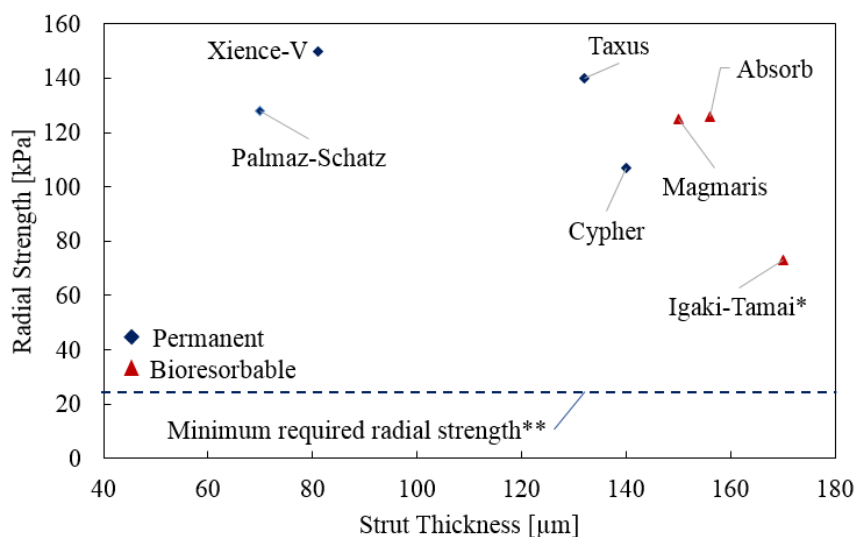


Figure 1.3. Radial strength versus strut thickness from a selection of permanent BMS/DES and bioresorbable BRS. \*Computational derived radial strength value from (Qiu, Song and Zhao, 2018). \*\*Value for minimum required radial strength obtained from (Agrawal *et al.*, 1992).

Some of the earliest polymer BRS to be developed included the Kyoto Medical Igaki-Tamai and Abbott Absorb BRS. The Igaki-Tamai PLLA BRS was the first BRS to be implanted in humans. It had a unique heated deployment approach, whereby heated contrast agent at 70 °C in the delivery balloon was used to initiate the initial self-expansion via shape memory through heating the polymer above its glass transition temperature. Final expansion occurred 20-30 minutes later at 37 °C. However, due to the unusual heated expansion process, and lack of a drug coating, it was not widely adopted (Nishio *et al.*, 2012). The Abbott Absorb was the first FDA approved polymer BRS and underwent several major clinical trials. Initial trials, ABSORB (Patrick W. Serruys *et al.* 2009), showed the device to be safe and non-inferior to DES at one year follow-up. However, more recent long-term follow up of the ABSORB III trial has shown increased rates of thrombosis when compared with conventional stents (Byrne *et al.* 2018; Ellis 2020). The inferior performance was attributed to poor understanding of the late-stage performance of the PLLA scaffold and the high strut thickness. Following this, Abbott Vascular voluntarily removed the Absorb from the market in 2017. Despite being removed from the market, and negative consequences for other manufacturers, several new polymer BRS are still under development, such as the DESolve NX by Elixir Medical. The

target functional properties of BRS presents a difficult balancing act between (i) providing enough vessel support in the first number of months and (ii) minimising subsequent absorption time to reduce the possibility of late-stage events. The complex degradation relationship of the coupled physical and mechanical properties is highlighted by the initial favourable short-term performance of the polymer BRS, but long-term performance that remains to be fully understood. **Despite the number of polymer BRS that have been under development, there is little information on the long-term degradation behaviour of these scaffolds. The late-stage underperformance of the polymer scaffolds coupled with the high strut thickness thus far can be attributed to poor understanding of the long-term degradation behaviour.**

### **1.3. Biomechanics and Computational Modelling of Coronary Stents**

#### **1.3.1. Stent Mechanics**

Stent designs typically make use of a sinusoidal-like pattern consisting of struts and hinges. All balloon-expandable stents use the idea of a plastic hinge, an example of which can be seen in Figure 1.4. For the stent and delivery system to be navigated to the treatment site, the stent is required to have a small outer diameter such that its crossing profile allows it to be navigated through narrowed sections of the vessel. Once the delivery system reaches the restricted area of the vessel, the balloon is inflated increasing the outer diameter of the stent such that it makes contact with the vessel walls. The change in diameter is facilitated by the hinge-like geometries in the stent profile. The opening of the stent results in plastic deformation in the hinge regions, which prevents the stent returning to its crimped diameter, as shown in Figure 1.4. Stent material properties and design requires a careful balance such that the device can undergo large deformation during deployment and maintain the vessel diameter even when the deployed scaffold relaxes following balloon inflation.

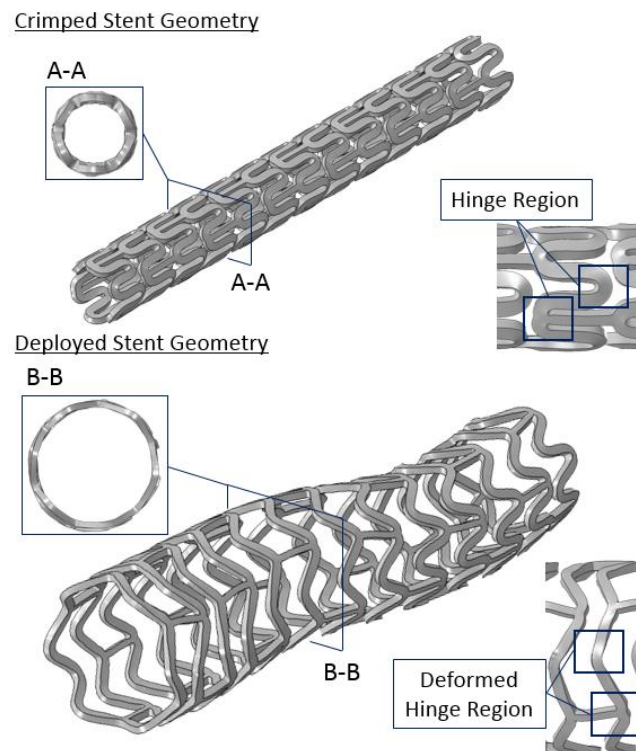


Figure 1.4. Schematic showing the expansion of the stent is facilitated by the plastic deformation of the hinge regions within the geometry.

Stents can be designed in several configurations, open-, closed-cell or hybrid. Closed-cell stents typically possess more connections between each circumferential ring compared with open-cell designs. Fewer of these connections facilitates a more flexible design, allowing for greater conformability to tortuous vessels and allows for easier navigability to the site of the occlusion (Migliavacca *et al.*, 2004). Greater conformability also reduces the chance of malapposition, where the stent strut does not maintain contact with the vessel wall. Malapposed struts can interrupt the blood flow within the vessel and cause thrombi to form (Ong and Jang, 2015). Stent geometry and strut dimensions have been shown to greatly affect the short-term stent performance (Migliavacca *et al.* 2002; Ormiston *et al.* 2015; Bressloff, Ragkousis, and Curzen 2016). In general, thicker stent struts result in a higher radial stiffness, where the increase in radial strength must be balanced with the strain experienced within the stent strut to avoid premature failure. **However, despite the known impact of geometry and strut dimensions, these design facets have not been explored for polymer BRS in terms of the long-term degradation performance.**

### 1.3.2. Computational Methods used in Stent Development

Computational modelling can be used to simulate a BRS and its environment and can be used to predict the real-life behaviour of the system. Due to the complexity of these systems, the finite element method (FEM) is employed as the numerical modelling method and is indeed a required component by regulatory bodies when proving the safety and efficacy of a design. This method has a number of advantages when used in the stent design process, as it can reduce the over-reliance of experimental bench testing and the need for trial-and-error prototyping. It can also provide insight into scenarios that are difficult or unfeasible to replicate in a laboratory setting. However, the vast majority of studies on polymer BRS have focussed on developing models to capture the short-term behaviour of polymer devices. These computational models of the short-term mechanical performance of BRS are reasonably well-established and generally consider mechanical performance in the absence of degradation (Schiavone, Qiu, and Zhao 2017; Bobel *et al.* 2015; Hoddy *et al.* 2021). However, unlike their metallic counterparts, the deployment behaviour of polymeric bioresorbable devices are highly sensitive to rate-dependent aspects of the procedure (e.g. inflation rate, inflation protocol), which presents certain complications. Significant efforts have been made to understand the role of non-linear or time-dependent behaviour on device performance through the implementation of visco-elastic and visco-plastic (Schiavone, Qiu, and Zhao 2017; Bobel *et al.* 2015; Hoddy *et al.* 2022) constitutive material models that capture rate-dependent short-term behaviour in the absence of degradation. Others have sought to understand the role of anisotropy induced during manufacturing on the short-term response (Hoddy *et al.* 2021). However, the prediction of the long-term degradation performance of BRS presents further challenges, as degradation kinetics are influenced by many factors including loading rate, loading history, temperature and environmental conditions (Simamora and Chern, 2006). There remains a distinct lack of understanding how microstructural alterations that take place in polymers during degradation

are responsible for deterioration in mechanical properties. As such, predicting the long-term degradation performance of polymer based BRS devices has generally relied on phenomenological approaches to describe the degradation of the mechanical properties. These methods generally use a continuum damage mechanics framework to introduce phenomenological degradation variables that operate on the constitutive material parameters to predict material degradation (Nuutinen *et al.*, 2003; Naseem *et al.*, 2017). However, these approaches generally rely on substantial amounts of calibration (Venkatraman *et al.*, 2003) and have rarely been validated beyond a limited set of circumstances. These approaches are further limited as models developed to date are not compatible with short-term time-dependent constitutive models, which are required to accurately predict behaviour during the deployment phase. **For the continued development of polymer BRS, robust and consistent computational models are required to fully capture the mechanical effects of degradation and enable predictions of the long-term performance of polymer BRS.**

#### **1.4. Thesis Objectives**

The global aim of this thesis is to investigate the effects of degradation of on the mechanical performance of polymer BRS using a combined experimental and computational approach. This work will facilitate a better understanding of the long-term performance of these devices and contribute towards the design and development of the next generation of polymer BRS.

The specific objectives of this research are as follows:

- (i) To experimentally characterise the long-term physical, thermal and mechanical degradation behaviour of several polymer BRS devices through an accelerated degradation protocol.
- (ii) To develop and implement a rate-dependent computational degradation framework that can predict both the short-term (e.g. deployment) and long-term performance of several polymer BRS devices.

- (iii) To use the computational degradation framework to investigate the roles of both material and geometry in determining the long-term degradation performance of polymer BRS.
- (iv) To predict the long-term behaviour of polymer BRS in several patient-specific scenarios through an integrated *in silico* clinical trial platform demonstration.

## 1.5. Thesis Structure

The outline of this thesis is as follows:

**Chapter 2** outlines the existing literature relevant to polymer degradation and current polymer BRS devices and development. This chapter describes the polymer degradation process, environmental factors affecting polymer BRS and current standards associated with experimental scaffold characterisation. It also provides a review of various experimental and computational techniques as well as previously developed computational degradation models that have been employed to evaluate scaffold performance.

**Chapter 3** presents an overview of the fundamental theory of continuum mechanics, particularly in context with the finite element method and the associated constitutive material models used in this thesis.

**Chapter 4** presents an experimental investigation into the thermal, physical and mechanical effects of degradation on two polymer BRS (REVA Medical Fantom Encore and a non-commercial PLLA BRS) using an accelerated degradation protocol. A number of experimental techniques are used to characterise the degradation performance of the two polymer BRS.

**Chapter 5** presents a flexible computational degradation framework that is developed and implemented to capture the various changes in mechanical properties during degradation. This model is then applied and calibrated with one of the scaffolds (non-commercial polymer BRS)

to capture the degradation behaviour characterised in Chapter 4. The calibrated model is then used to predict the long-term performance of that scaffold in a mock blood vessel.

**Chapter 6** uses the developed computational degradation framework to study the effect of degrading individual mechanical parameters and its effect on the mechanical performance of polymer BRS. Also investigated is the extent to which simple geometrical changes to the geometry of the scaffold can alter the long-term degradation performance. Both of these investigations are performed on freely expanded and vessel expanded cases. A final case is also investigated comparing two different scaffolds in the same vessel using the material and degradation performance as shown in the literature and in Chapter 4.

The primary conclusions of this thesis are summarised and recommendations for future work are discussed in **Chapter 7**.

**Appendix Chapter** demonstrates the implementation of the computational degradation framework and its integration within an in-silico clinical trial platform to give clinically relevant long-term performance data. This in silico chapter acting as a demonstration of the degradation module for the InSilc project A number of scenarios are considered such as the same BRS used to treat different vessel geometries or the effects of design changes to deployment within the same vessel geometries.



## 1.6. References

- Agrawal, C. M., K. F. Haas, D. A. Leopold, and H. G. Clark. 1992. "Evaluation of Poly(L-Lactic Acid) as a Material for Intravascular Polymeric Stents." *Biomaterials* 13 (3): 176–82. [https://doi.org/10.1016/0142-9612\(92\)90068-Y](https://doi.org/10.1016/0142-9612(92)90068-Y).
- Ang, Hui Ying, Ying Ying Huang, Soo Teik Lim, Philip Wong, Michael Joner, and Nicolas Foin. 2017. "Mechanical Behavior of Polymer-Based vs. Metallic-Based Bioresorbable Stents." *Journal of Thoracic Disease* 9 (Suppl 9): S923–34. <https://doi.org/10.21037/jtd.2017.06.30>.
- Bartnikowski, Michal, Tim R. Dargaville, Sašo Ivanovski, and Dietmar W. Hutmacher. 2019. "Degradation Mechanisms of Polycaprolactone in the Context of Chemistry, Geometry and Environment." *Progress in Polymer Science* 96: 1–20. <https://doi.org/10.1016/j.progpolymsci.2019.05.004>.
- Bentzon, Jacob Fog, Fumiya Otsuka, Renu Virmani, and Erling Falk. 2014. "Mechanisms of Plaque Formation and Rupture." *Circulation Research* 114 (12): 1852–66. <https://doi.org/10.1161/CIRCRESAHA.114.302721>.
- "Biotronik Orsiro." 2022. *Biotronik.Com*. <https://www.biotronik.com/en-gb/products/coronary/orsiro>.
- Bobel, A. C., S. Petisco, J. R. Sarasua, W. Wang, and P. E. McHugh. 2015. "Computational Bench Testing to Evaluate the Short-Term Mechanical Performance of a Polymeric Stent." *Cardiovascular Engineering and Technology* 6 (4): 519–32. <https://doi.org/10.1007/s13239-015-0235-9>.
- Bressloff, Neil W., Giorgos Ragkousis, and Nick Curzen. 2016. "Design Optimisation of Coronary Artery Stent Systems." *Annals of Biomedical Engineering* 44 (2): 357–67. <https://doi.org/10.1007/s10439-015-1373-9>.
- Byrne, Robert A, Giulio G Stefanini, Davide Capodanno, Yoshinobu Onuma, Andreas Baumbach, Javier Escaned, Michael Haude, Stefan James, Michael Joner, and Peter Ju. 2018. "Report of an ESC-EAPCI Task Force on the Evaluation and Use of Bioresorbable Scaffolds for Percutaneous Coronary Intervention : Executive Summary," no. July 2014: 1591–1601. <https://doi.org/10.4244/EIJ20170912-01>.
- Canan, Timothy, and Michael S. Lee. 2010. "Drug-Eluting Stent Fracture: Incidence, Contributing Factors, and Clinical Implications." *Catheterization and Cardiovascular Interventions* 75 (2): 237–45. <https://doi.org/10.1002/ccd.22212>.
- Conway, C., F. Sharif, J. P. McGarry, and P. E. McHugh. 2012. "A Computational Test-Bed to Assess Coronary Stent Implantation Mechanics Using a Population-Specific Approach." *Cardiovascular Engineering and Technology* 3 (4): 374–87. <https://doi.org/10.1007/s13239-012-0104-8>.
- Densford, Fink. 2017. "Boston Scientific to End Renuvia Bioresorbable Coronary Stent Program." *Massdevice.Com*. <https://www.massdevice.com/boston-scientific-end-renuvia-bioresorbable-coronary-stent-program/>.
- Ellis, Stephen G. 2020. "A Clinical Evaluation of Absorb<sup>TM</sup> BVS, the Everolimus Eluting Bioresorbable Vascular Scaffold in the Treatment of Subjects With de Novo Native Coronary Artery Lesions." National Library of Medicine (USA). 2020. <https://clinicaltrials.gov/ct2/show/study/NCT01751906>.
- Feyter, Pim J. de, Peter P.T. de Jaegere, and Patrick W. Serruys. 1994. "Incidence, Predictors, and Management of Acute Coronary Occlusion after Coronary Angioplasty." *American Heart Journal* 127 (3): 643–51. [https://doi.org/10.1016/0002-8703\(94\)90675-0](https://doi.org/10.1016/0002-8703(94)90675-0).
- Garg, Scot, Christos Bourantas, and Patrick W Serruys. 2013. "New Concepts in the Design of Drug-Eluting Coronary Stents." *Nature Reviews Cardiology* 10 (5): 248–60. <https://doi.org/10.1038/nrcardio.2013.13>.

- Gleadall, Andrew, Jingzhe Pan, Marc Anton Krufft, and Minna Kellomäki. 2014. "Degradation Mechanisms of Bioresorbable Polyesters. Part 1. Effects of Random Scission, End Scission and Autocatalysis." *Acta Biomaterialia* 10 (5): 2223–32. <https://doi.org/10.1016/j.actbio.2013.12.039>.
- Hoddy, Ben, Naveed Ahmed, Kadem Al-lamee, Nial Bullett, and Neil W. Bressloff. 2022. "Exploring a Parallel Rheological Framework to Capture the Mechanical Behaviour of a Thin-Strut Polymeric Bioresorbable Coronary Scaffold." *Journal of the Mechanical Behavior of Biomedical Materials* 130 (December 2021): 105154. <https://doi.org/10.1016/j.jmbbm.2022.105154>.
- Hoddy, Ben, Naveed Ahmed, Kadem Al-Lamee, Nial Bullett, Nick Curzen, and Neil W. Bressloff. 2021. "Investigating the Material Modelling of a Polymeric Bioresorbable Scaffold via In-Silico and in-Vitro Testing." *Journal of the Mechanical Behavior of Biomedical Materials* 120 (February): 104557. <https://doi.org/10.1016/j.jmbbm.2021.104557>.
- Kan, Jing, Zhen Ge, Jun Jie Zhang, Zhi Zhong Liu, Nai Liang Tian, Fei Ye, Sui Ji Li, et al. 2016. "Incidence and Clinical Outcomes of Stent Fractures on the Basis of 6,555 Patients and 16,482 Drug-Eluting Stents From 4 Centers." *JACC: Cardiovascular Interventions* 9 (11): 1115–23. <https://doi.org/10.1016/j.jcin.2016.02.025>.
- Khan, Moien AB, Muhammad Jawad Hashim, Halla Mustafa, May Yousif Baniyas, Shaikha Khalid Buti Mohamad Al Suwaidi, Rana AlKatheeri, Fatmah Mohamed Khalfan Alblooshi, et al. 2020. "Global Epidemiology of Ischemic Heart Disease: Results from the Global Burden of Disease Study." *Cureus* 12 (7). <https://doi.org/10.7759/cureus.9349>.
- Lee, Woei Shyan, Tao Hsing Chen, Chi Feng Lin, and Wen Zhen Luo. 2011. "Dynamic Mechanical Response of Biomedical 316L Stainless Steel as Function of Strain Rate and Temperature." *Bioinorganic Chemistry and Applications* 2011. <https://doi.org/10.1155/2011/173782>.
- McMahon, Sean, Nicky Bertollo, Eoin D.O' Cearbhaill, Jochen Salber, Luca Pierucci, Patrick Duffy, Thomas Dürig, Vivian Bi, and Wenxin Wang. 2018. "Bio-Resorbable Polymer Stents: A Review of Material Progress and Prospects." *Progress in Polymer Science* 83: 79–96. <https://doi.org/10.1016/j.progpolymsci.2018.05.002>.
- Migliavacca, Francesco, Lorenza Petrini, Maurizio Colombo, Ferdinando Auricchio, and Riccardo Pietrabissa. 2002. "Mechanical Behavior of Coronary Stents Investigated through the Finite Element Method." *Journal of Biomechanics* 35 (6): 803–11. [https://doi.org/10.1016/S0021-9290\(02\)00033-7](https://doi.org/10.1016/S0021-9290(02)00033-7).
- Migliavacca, Francesco, Lorenza Petrini, Paolo Massarotti, Silvia Schievano, Ferdinando Auricchio, and Gabriele Dubini. 2004. "Stainless and Shape Memory Alloy Coronary Stents: A Computational Study on the Interaction with the Vascular Wall." *Biomechanics and Modeling in Mechanobiology* 2 (4): 205–17. <https://doi.org/10.1007/S10237-004-0039-6>.
- Moses, Jeffrey W., Martin B Leon, Jeffrey J. Popma, Peter J. Fitzgerald, David R. Holmes, Charles O'Shaughnessy, Tonald P. Caputo, et al. 2003. "Sirolimus-Eluting Stents versus Standard Stents in Patients with Stenosis in a Native Coronary Artery." *The New England Journal of Medicine* 349 (14): 1315–23.
- Moussa, Issam D., Divyanshu Mohanane, Jorge Saucedo, Gregg W. Stone, Robert W. Yeh, Kevin F. Kennedy, Ron Waksman, Paul Teirstein, Jeffrey W. Moses, and Chuck Simonton. 2020. "Trends and Outcomes of Restenosis After Coronary Stent Implantation in the United States." *Journal of the American College of Cardiology* 76 (13): 1521–31. <https://doi.org/10.1016/j.jacc.2020.08.002>.
- Naseem, Raasti, Ligu Zhao, Yang Liu, and Vadim V. Silberschmidt. 2017. "Experimental and Computational Studies of Poly-L-Lactic Acid for Cardiovascular Applications: Recent Progress." *Mechanics of Advanced Materials and Modern Processes* 3 (1). <https://doi.org/10.1186/s40759-017-0028-y>.
- Nishio, Soji, Kunihiko Kosuga, Keiji Igaki, Masaharu Okada, Eisho Kyo, Takafumi Tsuji, Eiji Takeuchi, et al. 2012. "Long-Term (>10 Years) Clinical Outcomes of First-in-Human Biodegradable

Poly-L-Lactic Acid Coronary Stents: Igaki-Tamai Stents.” *Circulation* 125 (19): 2343–52. <https://doi.org/10.1161/CIRCULATIONAHA.110.000901>.

Nuutinen, Juha Pekka, Claude Clerc, Raija Reinikainen, and Pertti Törmälä. 2003. “Mechanical Properties and in Vitro Degradation of Bioabsorbable Self-Expanding Braided Stents.” *Journal of Biomaterials Science, Polymer Edition* 14 (3): 255–66. <https://doi.org/10.1163/156856203763572707>.

O’Brien, Barry J., Jon S. Stinson, Steve R. Larsen, Michael J. Eppihimer, and William M. Carroll. 2010. “A Platinum-Chromium Steel for Cardiovascular Stents.” *Biomaterials* 31 (14): 3755–61. <https://doi.org/10.1016/j.biomaterials.2010.01.146>.

Ong, Daniel S., and Ik Kyung Jang. 2015. “Causes, Assessment, and Treatment of Stent Thrombosis-Intravascular Imaging Insights.” *Nature Reviews Cardiology* 12 (6): 325–36. <https://doi.org/10.1038/nrcardio.2015.32>.

Onuma, Yosinobu, and Patrick W. Serruys. 2011. “Bioresorbable Scaffold: The Advent of a New Era in Percutaneous Coronary and Peripheral Revascularization?” *Circulation* 123 (7): 779–97. <https://doi.org/10.1161/CIRCULATIONAHA.110.971606>.

Ormiston, John A., Bruce Webber, Ben Ubod, Olivier Darremont, and Mark W.I. Webster. 2015. “An Independent Bench Comparison of Two Bioresorbable Drug-Eluting Coronary Scaffolds (Absorb and DESolve) with a Durable Metallic Drug-Eluting Stent (ML8/Xpedition).” *EuroIntervention* 11 (1): 60–67. [https://doi.org/10.4244/EIJY15M02\\_03](https://doi.org/10.4244/EIJY15M02_03).

Palmaz, J. C., R. R. Sibbitt, S. R. Reuter, F. O. Tio, and W. J. Rice. 1985. “Expandable Intraluminal Graft: A Preliminary Study.” *Radiology* 156 (1): 73–77. <https://doi.org/10.1148/radiology.156.1.3159043>.

Pan, Pengju, Bo Zhu, and Yoshio Inoue. 2007. “Enthalpy Relaxation and Embrittlement of Poly(L-Lactide) during Physical Aging.” *Macromolecules* 40 (26): 9664–71. <https://doi.org/10.1021/ma071777c>.

Qiu, T. Y., M. Song, and L. G. Zhao. 2018. “A Computational Study of Crimping and Expansion of Bioresorbable Polymeric Stents.” *Mechanics of Time-Dependent Materials* 22 (2): 273–90. <https://doi.org/10.1007/s11043-017-9371-y>.

“Reva Revives.” 2022. *Evaluated.Com*. <https://www.evaluate.com/vantage/articles/news/deals-snippets/reva-revives>.

Schatz, Richard A., Donald S. Baim, Martin Leon, Stephen G. Ellis, Sheldon Goldberg, John W. Hirshfeld, Michael W. Cleman, et al. 1991. “Clinical Experience with the Palmaz-Schatz Coronary Stent: Initial Results of a Multicenter Study.” *Circulation* 83 (1): 148–61. <https://doi.org/10.1161/01.CIR.83.1.148>.

Schiavone, Alessandro, Tian-Yang Qiu, and Li-Guo Zhao. 2017. “Crimping and Deployment of Metallic and Polymeric Stents -- Finite Element Modelling.” *Vessel Plus* 1 (1): 12–21. <https://doi.org/10.20517/2574-1209.2016.03>.

Serruys, P. W., H. E. Luijten, K. J. Beatt, R. Geuskens, P. J. De Feyter, M. Van Den Brand, J. H.C. Reiber, H. J. Ten Katen, G. A. Van Es, and P. G. Hugenholtz. 1988. “Incidence of Restenosis after Successful Coronary Angioplasty: A Time-Related Phenomenon. A Quantitative Angiographic Study in 342 Consecutive Patients at 1, 2, 3, and 4 Months.” *Circulation* 77 (2): 361–71. <https://doi.org/10.1161/01.CIR.77.2.361>.

Serruys, Patrick W., John A. Ormiston, Yoshinobu Onuma, Evelyn Regar, Nieves Gonzalo, Hector M. Garcia-Garcia, Koen Nieman, et al. 2009. “A Bioabsorbable Everolimus-Eluting Coronary Stent System (ABSORB): 2-Year Outcomes and Results from Multiple Imaging Methods.” *The Lancet* 373 (9667): 897–910. [https://doi.org/10.1016/S0140-6736\(09\)60325-1](https://doi.org/10.1016/S0140-6736(09)60325-1).

Simamora, Pahala, and Wendy Chern. 2006. “Poly-L-Lactic Acid: An Overview.” *Journal of Drugs in*

*Dermatology* : *JDD* 5 (5): 436—440. <http://europepmc.org/abstract/MED/16703779>.

Suuronen, Riitta, Timo Pohjonen, Jarkko Hietanen, and Christian Lindqvist. 1998. “A 5-Year in Vitro and in Vivo Study of the Biodegradation of Polylactide Plates.” *Journal of Oral and Maxillofacial Surgery* 56 (5): 604–14. [https://doi.org/10.1016/S0278-2391\(98\)90461-X](https://doi.org/10.1016/S0278-2391(98)90461-X).

Tsao, Connie W., Aaron W. Aday, Zaid I. Almarzooq, Alvaro Alonso, Andrea Z. Beaton, Marcio S. Bittencourt, Amelia K. Boehme, et al. 2022. *Heart Disease and Stroke Statistics-2022 Update: A Report From the American Heart Association. Circulation.* Vol. 145. <https://doi.org/10.1161/CIR.0000000000001052>.

Venkatraman, Subbu, Tan Lay Poh, Tjong Vinalia, Koon Hou Mak, and Freddy Boey. 2003. “Collapse Pressures of Biodegradable Stents.” *Biomaterials* 24 (12): 2105–11. [https://doi.org/10.1016/S0142-9612\(02\)00640-3](https://doi.org/10.1016/S0142-9612(02)00640-3).

# Chapter 2

## Literature Review

---

### 2.1. Biodegradable Polymers

Polymers are macromolecules that comprise of interconnected monomer units. The constitutive properties of polymers are dictated through the arrangement of these monomers, which can be grouped in to (i) unorganised amorphous regions or (ii) organised crystalline regions. A polymer that comprises of both amorphous and crystalline regions is described as semi-crystalline, which is represented schematically in Figure 2.5. Apart from the relative proportion of these regions, the length of polymer chains throughout the structure contributes to the physical properties of the polymer. Longer polymer chains result in entanglements and decrease the chain mobility, which in turn increase the mechanical properties and make the polymer more stable at higher temperatures. Shorter chains result in polymers with lower mechanical properties and are usually soft rubber like solids or viscous liquids.

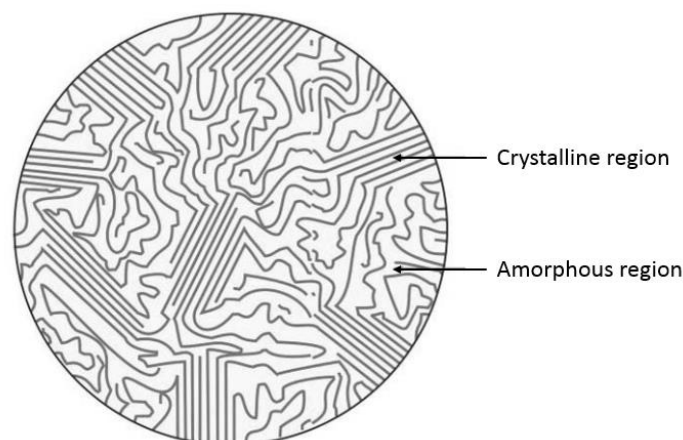


Figure 2.5. Diagram showing the arrangement of amorphous and crystalline regions within a polymer. Adapted from (Callister Jr and Rethwisch, 2020).

Polymers have been used in a wide variety of biomedical applications such as biodegradable sutures (Lee, Singla and Lee, 2001), tissue engineering scaffolds (Song *et al.*, 2018), dental and orthopaedic applications (Leenslag *et al.*, 1987), drug delivery devices/coatings (Farah, Anderson and Langer, 2016) and bioresorbable vascular scaffolds (McMahon *et al.*, 2018). The ability to tailor the mechanical and degradation properties by controlling molecular variables such as the crystallinity, molecular weight and degree of crosslinking (Liu, Zhang and Wang, 2014) make polymers a highly favourable material, and their use in several biomedical fields highlights this. Biodegradable polymers are typically categorised as either natural or synthetic (Song *et al.*, 2018). Some examples of natural polymers include collagen, silk and chitin and these have primarily been used in biodegradable sutures and tissue engineering scaffolds (Lee, Singla and Lee, 2001). Issues associated with natural polymers include the presence of biological material, which can elicit an immune response and cause the failure of the scaffold or the ability to transport microbes and viruses (Schmidt and Baier, 2000; Lee, Singla and Lee, 2001), and the relative difficulty in controlling both mechanical properties and degradation rates. On the other hand, synthetic polymers offer higher relative strength and stiffness, as well as the ability to tailor mechanical properties, which make them an attractive choice for cardiovascular applications. Currently, there is ongoing interest in using polymers for temporary scaffolding in cardiovascular applications. Synthetic polymers used for vascular scaffold applications include polymers such as poly lactic acid (PLA), poly-L-lactic acid (PLLA), poly-L-glycolic acid (PLGA) and polycaprolactone (PCL). The use of a temporary or biodegradable scaffold potentially provides several advantages over a permanent device as they could avoid certain late-stage complications associated with permanent stents. This is particularly beneficial in younger patients, where the use of a permanent device can limit vessel growth, reduce vasomotion (Welch, Nugent and Veeram Reddy, 2019) and should a revision procedure be required avoid any interference with subsequently implanted devices.

## 2.2. Mechanical Properties of Biodegradable Polymers

### 2.2.1. General Mechanical Properties of Polymers used in BRS Applications

Polymers such as PLA, PLLA, PLGA and PCL have been used in bioresorbable scaffold (BRS) applications and are semi-crystalline in nature. As such, the mechanical response and overall performance of these polymers depends on the ratio of amorphous and crystalline phase within the bulk material. Amorphous polymers are characterised by lower strength and greater ductility than more crystalline polymers. Thus, depending on the degree of crystallinity within the polymer, the mechanical properties can vary greatly, with reported values for elastic modulus varying between 1-7GPa (Garlotta, 2001; McMahon *et al.*, 2018) and failure strain varying between 2-300% for PLLA (Pan, Zhu and Inoue, 2007; Farah, Anderson and Langer, 2016). The mechanical behaviour of semi-crystalline polymers demonstrate both plastic and non-linear viscoelastic responses. Figure 2.6 shows the typical tensile response under a number of conditions for a semi-crystalline polymer, whereby an initial linear response is observed at small strains until a defined point of yielding and typically increasing stresses past the point of yielding. The microstructural responses that take place under a tensile load within the polymer can be summarised by an initial linear increase in stress caused by elastic loading of polymer chains within both amorphous and crystalline regions, which causes an untangling of the polymer chains. Yielding in semi-crystalline polymers is a complex process and is dependent on the underlying microstructure. During the early stages of deformation, the crystals become permanently distorted. Further deformation causes the crystalline microstructure to break down and a new fibrillar structure forms (Peterlin, 1971). A defined point of yielding and increased plasticity without an increase in stress then follows. Hardening behaviour, an increase in the stress-strain response after yielding, is caused by large scale orientation of the polymer chain molecules and crystals which align in the direction of loading.

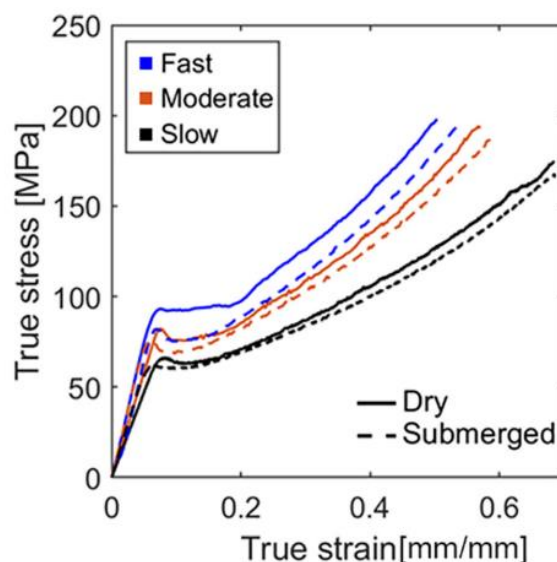


Figure 2.6. True stress-strain tensile response of PLLA under dry and submerged conditions with different applied loading rates (Adapted from (P. Wang et al., 2018)).

The ratio of crystalline to amorphous regions within a polymer plays a critical role in determining its mechanical properties. A number of authors (Perego, *et al.*, 1996) have shown that the mechanical properties of polymers generally increase with an increase in crystallinity at the expense of ductility. Tsuji *et al* (1995) demonstrated that higher crystallinity resulted in increases in the elastic modulus and tensile strength, coupled with a decrease in the elongation at failure. Even small changes in the crystallinity, as little as 5%, were responsible for increasing the elastic modulus from 173 MPa to 200 MPa. Lizundia *et al* (2013) also showed an increase in the glass transition temperature was associated with increased crystallinity, allowing the PLLA to retain its mechanical properties under higher temperatures. Semi-crystalline polymers also exhibit viscous behaviour, such as creep and stress relaxation under continuous loading. Bobel *et al* (2016) investigated the tensile behaviour of solvent-cast PLLA by subjecting PLLA samples to varying strain rates, cyclic loading and stress relaxation and creep tests. It was found that increased strain rates resulted in a higher yield stress. Cyclic loading showed material softening, leading to decreased resistance to further deformation. Upon continuous loading, the PLLA samples demonstrated a stress relaxation response, with stress in the samples gradually reducing. Kimble *et al* (2015) subjected injection moulded



PLLA dog-bones to creep testing by hanging a 10N load at 37°C. They showed that PLLA exhibits a creep response with a creep of 2% strain measure from a 10N load after 16 hours with the creep rate decreasing slightly after approximately 8 hours. Creep evaluation for polymers used in scaffold applications is of vital performance due to the nature of loading on a deployed scaffold. The scaffold must be able to resist the constant compressive loading applied by the surrounding blood vessel to maintain vessel patency.

### **2.2.2. Influence of Environmental Factors on Mechanical Properties**

Polymer BRS can be exposed to multiple environmental factors that can alter the mechanical properties during their development including temperature and hydration. Figure 2.7 demonstrates the extent to which the mechanical properties of PLA can change when subjected to different conditions. Moetaxedian *et al* (2020) subjected PLA dog-bones to a range of testing conditions consisting of dry vs hydrated and ambient (20°C) and elevated temperatures (37°C). Tensile testing at elevated temperatures reduced the ultimate tensile strength and increased the strain-to-failure. Samples tested under elevated temperatures showed a more ductile response under a tensile load when compared to the other dry and hydrated samples tested at ambient temperature, with samples being loaded up to 40% strain prior to failure. A similar response was also seen by Grasso *et al* (2018). Tests performed at 60°C are within the range of the glass transition temperature for PLA. Polymers tested near or above the glass transition temperature typically become more elastic and ductile. Bobel *et al* (2016) also demonstrated that elevated temperatures result in greater strain recovery coupled with the decrease in mechanical properties. The samples tested at elevated temperatures (42°C) did not have a distinct yield point compared with samples tested at lower temperatures. Elevated temperatures provide the polymer chains with greater mobility thus resulting in a reduction in the mechanical properties of the polymer overall.

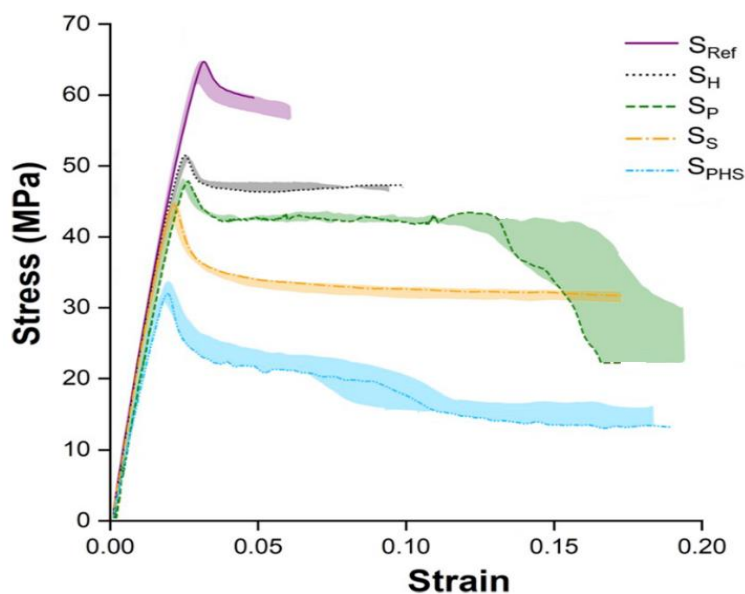


Figure 2.7. Stress-strain curves of testing conditions of PLA dog-bones under different loading conditions;  $S_{REF}$ : dry, ambient temperature,  $S_P$ : dry, elevated temperature,  $S_H$ : hydrated, ambient temperature,  $S_S$ : dry, submerged,  $S_{PHS}$ : hydrated, submerged and elevated temperature (Adapted from (Moetazedian et al., 2020)). One representative curve is shown within the shaded region.

Polymers used in BRS applications also perform differently when under dry and hydrated conditions. When exposed to water, the water is absorbed by the polymer, with Yew *et al* (2005) demonstrating that the rate of water absorption plateaued after approximately 4 days of immersion for PLA with a total increase in mass of approximately 1% by weight. Moetazedian *et al* (2020) demonstrated that the adsorption of water led to a lower yield strength and a larger strain-to-failure when compared with the dry PLLA sample, Figure 2.7. This response is exacerbated when exposed to water and elevated temperatures. Bartkowiak-Jowska *et al* (2013) showed that within 24 hours of hydration, the mechanical response had changed completely for PDGLA. It was also noted that all specimens of PLLA, PGLA and PDGLA demonstrated an almost 100-fold increase in strain-to-failure compared with dry specimens. Thermal analysis found that hydrated samples also had a lower glass transition temperature. Similar findings have been observed in (Yew *et al.*, 2005; P. Wang *et al.*, 2018; Oosterbeek *et al.*, 2019; Moetazedian *et al.*, 2020), with the hydration of PLA resulting in a decrease in elastic modulus and yield strength and an increase in strain to failure. These effects have been found across both amorphous PLLA and PLLA of varying crystallinities (Renouf-Glauser *et al.*, 2005).

Sterilization processes may also impact the performance of the constitutive polymers. Grabow *et al* (2005) subjected PLLA to a number of standard sterilization techniques including ethylene oxide (EtO),  $\beta$  and  $\gamma$  irradiation and H<sub>2</sub>O<sub>2</sub>-plasma before investigating its effect on mechanical and physical properties. They found that irradiation sterilization techniques to greatly reduced the molecular weight with an 85% reduction reported (by 85%). Irradiated samples also exhibited lower elastic modulus, tensile strength and elongation at break, while an increase in crystallinity was observed.

### **2.2.3. Tailoring the Mechanical Response of Polymers used in BRS Applications**

Changes in the crystallinity and molecular weight can change the mechanical response of polymers. These characteristics can be used to control the mechanical response of the polymer. A summary of some techniques used to tailor the mechanical response is covered in this section.

Heat treatments can be used to control the crystallinity of the polymer by annealing at elevated temperatures, usually above the glass transition temperature (~55 °C for PLLA). The cooling rate may also be controlled to allow for crystal growth. Tábi *et al* (2010) subjected PLA sheets to annealing temperatures of 80°C and 120°C for varying amounts of time. They found samples maintained at 80°C for 10 minutes and 60 minutes resulted in crystallinities of 3.3% and 21% respectively. The change in crystallinity was clearly seen from the DSC thermographs, as shown in Figure 2.8. Initially, when the polymer had a higher amorphous content, there was a clear cold-crystallisation peak visible at 90°C on the thermograph. This peak was absent in samples with longer annealing times, with the larger melting peak observed indicating an increase in crystallinity. Other studies (Tsuji *et al.*, 2006; Lim *et al.*, 2008; Lizundia *et al.*, 2013; Dillon *et al.*, 2019) have also noted annealing as an effective means of increasing the crystallinity with rapid cooling resulting in a highly amorphous polymer, due to insufficient time for crystal growth. On the other hand, longer cooling times allowing for polymer crystals to grow from the nucleation sites.

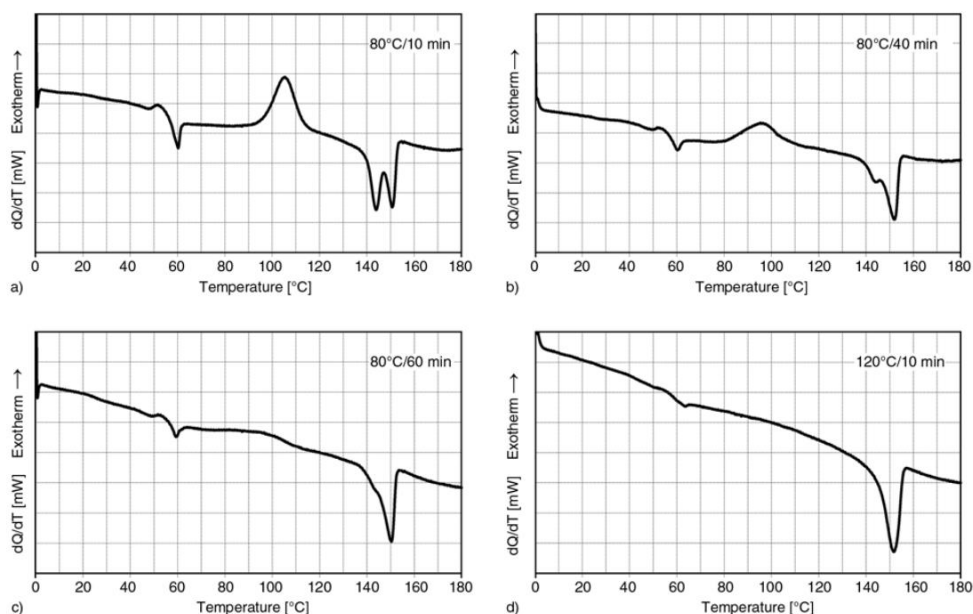


Figure 2.8. DSC curves of annealed PLA at 80°C for (a) 10, (b) 40, (c) 60 minutes and (d) 120°C for 10 minutes. Reduction in glass transition peak coupled with increasing melting peak typically denoted an increase in crystallinity (adapted from (Tábi et al., 2010)).

Molecular weight has a large role in determining the strength and make-up of a polymer. For example, a very low molecular weight results in polymers being a viscous liquid if the glass transition temperature is below the ambient temperature (Nunes *et al.*, 1982). With higher molecular weight, the number of molecular bonds increase resulting in a higher strength polymer. For BRS applications, high molecular weight polymers are generally used. Xie *et al* (2016) prepared PLLA and PEG membranes of varying molecular weights and subjected them to thermal analysis and degradation at phosphate buffered saline (PBS) at different temperatures. They showed that higher molecular weight samples possessed a higher glass transition temperature. Higher glass transition temperature would allow the polymer to be used in higher temperature applications without softening. Perego *et al* (1996) synthesised PLLA of varying molecular weights and subjected them to tensile testing. They demonstrated that increasing the molecular weight did result in slightly increased mechanical properties including elastic modulus, yield strength and flexural strength, with the greatest change observed being a higher strain to failure. Figure 2.9 demonstrate the effects of crystallinity and molecular weight on the mechanical performance.

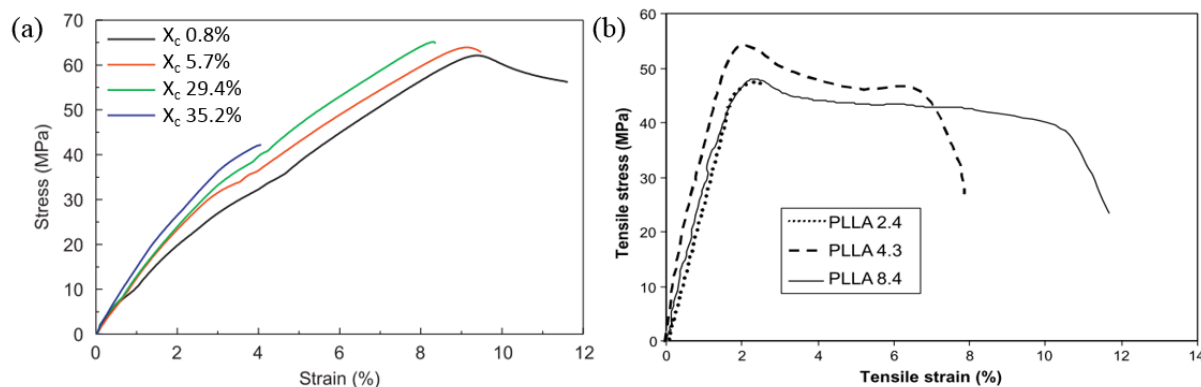


Figure 2.9. (a) Stress-strain plot demonstrating the effects of increasing crystallinity, where increasing crystallinity results in more brittle failure (adapted from (Lizundia, et al, 2013)). (b) Stress-strain plot demonstrating the effect on molecular weight on stress-strain response, where increasing molecular weight results in a transition from brittle to more ductile failure (adapted from (Venkatraman et al., 2003)).

The manufacturing methods to produce the constitutive material for scaffold applications can also influence the final mechanical properties. Some common techniques used in the manufacture of biomedical polymer implants include compression, injection, blow and extrusion moulding with additive manufacturing processes also becoming popular. Reinoso *et al* (2021) investigated the difference between injection- and compression-moulding a Poly (L-lactide-co-D,L-lactide)/Poly(L-lactide-co- $\epsilon$ -caprolactone) blend. Compression moulded samples had lower elastic moduli and yield stress compared with injection-moulded samples. However, the compression-moulded samples were more ductile with a strain-to-failure of 503% compared with 145%. Thermal analysis showed the injection-moulded samples had a higher crystallinity. These differences highlight the impact of manufacturing process despite similar preparation in melting and cooling. Dillon *et al* (2019) produced PLLA tubing by extrusion and stretch blow moulding technique. The latter technique involved heating the PLLA tubes above its glass transition temperature and circumferentially expanding at a strain rate of  $12 \text{ s}^{-1}$ . The expansion process resulted in an increase of 65% of the elastic modulus, 45% increase in the maximum tensile stress and an 18-fold increase the strain at maximum load when compared to extruded PLLA. Thermal analysis showed a higher crystallinity in the expanded samples. The expanded samples were also shown not to have a glass transition peak on the DSC thermograms, which is usually indicative of a highly crystalline polymer.

#### 2.2.4. Degradation Mechanisms and Effects on Mechanical Performance of Polymers

The primary mechanism of degradation for aliphatic polyesters such as PLLA is bulk degradation via hydrolysis. Experiments evaluating degradation mechanisms for PLLA have shown that water is the primary instigator for degradation, with more complex degradation solutions that mimic human bodily fluids not contributing or altering the mechanism of degradation (Mainil-Varlet, 1997; Suuronen *et al.*, 1998; Luo *et al.*, 2014). *In vitro* degradation studies are typically performed by immersing the polymer into phosphate buffered saline (PBS). However, a number of *in vitro* degradation studies have been performed in other solutions such as an enzymatic solution (Cai *et al.*, 1996) and distilled water (Deroiné *et al.*, 2014). It has also been shown that degradation *in vivo* follows similar mechanisms to the degradation process as those noted *in vitro* (Mainil-Varlet, Curtis and Gogolewski, 1997). The degradation process can be broken down into two stages. First, the penetration of water from the surrounding environment into the bulk polymer where it breaks the ester bonds of the amorphous phase. The initial degradation can be characterised by a sharp reduction in the molecular weight as the length of the polymer chains are reduced. Second, the mass of the polymer decreases as the polymer chains, which are gradually reduced in length, become soluble and diffuse out of the polymer (Gleadall *et al.*, 2014). This causes a plateau in the number average molecular weight caused by a balance of low molecular weight oligomers being lost through diffusion and higher molecular weight polymer chains being degraded. Owing to the biased degradation of the amorphous phase of polymers, the relative crystallinity has been found to increase over time as the quantity of amorphous phase of the polymer is reduced. Experiments have also shown that the degradation of polymers can be affected by the crystallinity, molecular weight, physical age and chain orientation (Tsuji, Mizuno and Ikada, 2000; Saha and Tsuji, 2006).

*In Vitro Degradation Testing of Polymers - Real time studies*

To represent the physiological environment, *in vitro* degradation studies have generally been carried out by immersing polymer specimens in an aqueous solution, such as PBS, over time periods that range from several weeks to years. Many studies recreate the physiological environment by carrying out testing at 37°C. Degradation has been shown to have several effects on the mechanical performance of polymers, with the elastic modulus, strain-to-failure and yield stress all found to be impacted by degradation, Table 2.2.

Table 2.2. *In Vitro* degradation studies performed on biomedical polymers showing the degradation conditions and the mechanical properties affected by the degradation.

Materials	Degradation Condition	Material Property Degraded			Reference
		Elastic Modulus	Yield Strength	Strain to Failure	
PLLA, PGLA, PDGLA	Dog-bone samples degraded in distilled water at 37°C for a period of 24, 7 and 1 months for PLLA, PGLA and PDGLA respectively.	✓	✓		(Bartkowiak-Jowska <i>et al.</i> , 2013)
PLLA	Pin samples degraded in PBS at 38°C for a period of 24 weeks	✓		✓	(Duek, <i>et al.</i> , 1999)
PLLA	Dog-bone samples degraded in PBS at 37°C for a period of 65 weeks. Comparison samples implanted in rats for 44 weeks.	✓	✓	✓	(Weir <i>et al.</i> , 2004)
PLLA	Dog-bone samples subjected to accelerated degradation in PBS at 50°C and 70°C for a period of 115 and 23 days respectively for the 50°C and 70°C samples	✓	✓	✓	(Weir <i>et al.</i> , 2004)
PLLA	Film samples degraded in PBS at 37°C for a period of 36 months	✓	✓	✓	(Tsuji, 2000)
PLLA	Film samples degraded in PBS at 37°C for a period of 36 months	✓	✓	✓	(Tsuji and Ikada, 2000)
Polyglyconate B	Dumbbell samples degraded in PBS at 37°C for a period of 31 days		✓	✓	(Farrar and Gillson, 2002)
PLLA/PBS	Dog-bone samples degraded in PBS at 37°C for a period of 24 weeks	✓	✓		(Kimble and Bhattacharyya, 2015)
PLLA	Dog-bone samples subjected to accelerated degradation in PBS at 50°C for a period of 112 days		✓	✓	(Katarzyna <i>et al.</i> , 2021)

Bartkowiak-Jowska *et al* (2013) investigated the effect of degradation on PLLA samples, which consisted of dog-bone specimens that were immersed in distilled water at 37°C for a period of

24 months. Mechanical testing showed an increase in the elastic modulus from months 7 to 17, while a decreasing trend was observed for the tensile strength and the failure strain from month 10. The unaffected creep properties of the PLLA samples were attributed to the increase in crystallinity that takes place throughout the degradation process.

Duek *et al* (1999) subjected PLLA pins of different starting crystallinities (10% and 50%) to immersion in PBS at physiological temperatures for 24 weeks. PLLA with a lower starting crystallinity was found to be more mechanically stable than the samples with higher starting crystallinity. This was seen in the lower rate in the reduction in bending strength, elastic modulus and strain-to-failure. Tsuji *et al* (2000) investigated the effect of varying crystallinity and on degradation on PLLA films immersed in PBS 37°C for 36 months. Degradation of the films reduced the molecular weight across all samples at a similar rate and an increase in polymer dispersity. No mass loss was noted until month 12, after which samples with higher starting crystallinities had higher mass loss than those samples with lower starting crystallinities. All samples showed an increase in crystallinity over the course of the study. Mechanical evaluation showed a faster reduction in elastic modulus, elongation at break and tensile strength in samples with higher starting crystallinity, see Figure 2.10 below. The higher rate of degradation in samples with higher starting crystallinity was attributed to the crystals disturbing the chain arrangement of the amorphous region allowing for faster hydrolysis. Another possible reason for the increased rate of degradation is the crystals in samples with higher starting crystallinity have exposed polymer end groups, which are more hydrophilic and facilitate the ingress water to start hydrolysis.



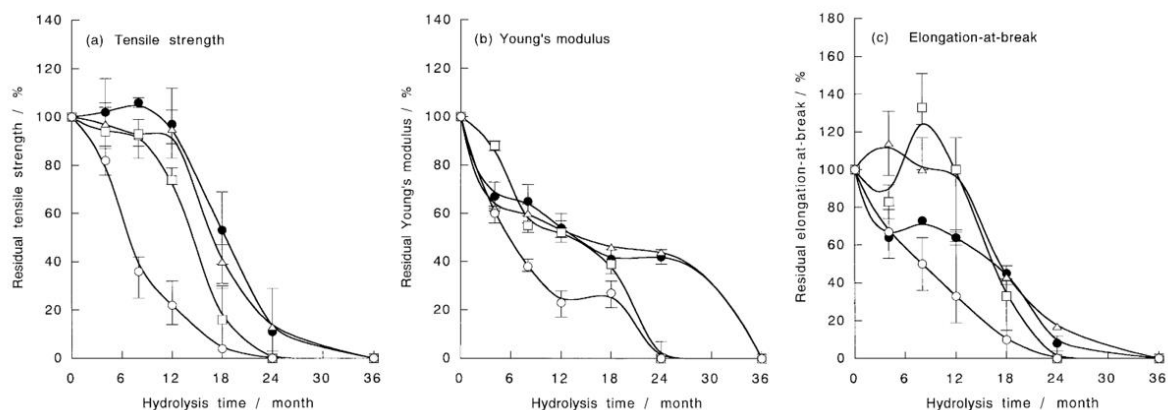


Figure 2.10. Evolution in (a) residual tensile strength, (b) Young's modulus and (c) Elongation-at-break for PLLA films of varied initial crystallinity versus degradation time. (●) PLLA100; (△) PLLA120; (□) PLLA140; and (○) PLLA160. Adapted from (Tsuji and Ikada, 2000).

Saha and Tsuji (2006) demonstrated the effect of varying molecular weight on the degradation process of PLLA. Amorphous PLLA films were degraded in PBS at 37°C for 60 weeks. The starting molecular weight had less of an effect on the degradation rate than the starting crystallinity for the initial period of the study (Weeks 0-32). These initial effects of starting crystallinity/molecular weight did not play a role in determining the rate of degradation in the second period of the study (Weeks 32-60) due to the accumulation of oligomers and the increase in crystallinity caused by the degradation. Interestingly, the samples with zero starting crystallinity remained completely amorphous with no increase in crystallinity over the course of the study, while the samples with some starting crystallinity (1.6%) experienced an increase in crystallinity (10.2%). This was attributed to the starting crystallized areas acting as nucleation points for further crystallization during the degradation. The different starting molecular weight had no effect on the evolution in mechanical properties with the elongation to break, elastic modulus and tensile strength reduced similarly.

### In Vitro Degradation Testing of Polymers - Accelerated Degradation

The degradation rate of polymers is highly dependent on the environmental temperature, with elevated temperatures shown to increase the rate of degradation (Weir *et al.*, 2004). Many studies have used this to conduct thermally-accelerated degradation studies. The effect of

temperature on degradation kinetics can be described by Arrhenius relationship, which is described by Equation ( 2-1 ), and relates the process back to the service temperature,

$$k = Ae^{\frac{-Ea}{RT}} \quad (2-1)$$

$$\ln k = -\left(\frac{Ea}{R}\right)\left(\frac{1}{T}\right) + \ln A \quad (2-2)$$

where  $k$  is the rate constant,  $A$  is a constant,  $Ea$  is the activation energy,  $R$  is the universal gas constant and  $T$  is the temperature. For an ideal system, a linear relationship should exist between the  $\ln k$  versus  $1/T$ . Weir *et al* (2004) showed that the mechanisms of degradation remain the same at elevated temperatures provided the glass transition temperature of the polymer was not exceeded. Samples of PLLA were immersed in PBS at 37°C, 50°C and 70°C. It was found that changes in mass and thermal properties caused by the degradation were not affected by the elevated temperatures. It was found that the relationship between the tensile strength and the molecular weight remain largely unchanged between the samples degraded at different temperatures, highlighting that elevated temperature can be appropriately used to accelerate the degradation process. This is advantageous owing to the long-time scales involved in degradation of polymers used in BRS applications, which is typically greater than two years for PLLA (McMahon *et al.*, 2018).

### *In-vivo Degradation Comparison*

While *in vitro* experiments aim to replicate physiological conditions, several aspects of the *in vivo* environment may also affect the degradation process. Many *in vitro* experiments are performed with the degradation sample immersed freely within an aqueous solution. Weir *et al* (2004) compared the degradation of PLLA pins degraded in PBS at 37°C with *in vivo* samples implanted in rats. The *in vitro* samples were immersed for a total of 65 weeks while the *in vivo* samples remained implanted for 44 weeks. Molecular weight analysis of the two sample groups showed a similar rate of molecular weight loss over the 44-week period.

Thermal analysis showed an increase in crystallinity in both groups also. While the degradation mechanism is suggested to remain similar for both sample groups, with similar evolutions in both mechanical and physical properties, the *in vivo* samples did show evidence of fibrous encapsulation, with little inflammatory response noted. This low inflammatory response was attributed to the slow rate of degradation and thus slow change of the local pH as the polymer degraded.

## **2.3. Experimental Testing of BRS**

### **2.3.1. BRS Devices**

The development of BRS devices has suffered significant setbacks over the past number of years, with 2-year follow up data from the ABSORB III trial on the Abbott Absorb demonstrating increased risk of late-stage adverse events (Ellis, 2020). A European Society of Cardiology (ESC) taskforce (Byrne *et al.* 2018) set up to evaluate clinical outcomes of approved BRS devices found evidence of excess very late stent thrombosis with the Abbott Absorb in comparison with conventional DES. The hypothesized factors for the lesser performance include alteration of laminar flow as a consequence of high strut thickness and loss in backbone integrity, leading to prolapse of part of the scaffold into the lumen of the vessel, thrombogenicity of degradation products and/or extracellular matrix replacing voids within the scaffold and finally inflammation caused by degradation of the scaffold. Each of these hypotheses relating to the long-term performance of a BRS and highlights the need to alter test protocols and characterise all stages of the BRS life cycle.

### 2.3.2. Standardised Testing of BRS – Short-Term Performance

Throughout development, BRS must undergo a series of bench-top, animal testing and human trials to demonstrate their safety and efficacy before being approved. A number of guidance documents exist recommending an extensive list of the bench-top tests and minimum requirements for vascular stents, with several of these tests summarised in Table 2.3 below. These include the FDA guidance document on “Non-Clinical Tests and Recommended Labelling for Intravascular Stents and Associated Delivery Systems” (FDA, 2010), the International Organisation for Standardisation (ISO) document entitled “Cardiovascular Implants - Endovascular Devices - Part 2: Vascular Stents” (ISO 25539-2) and the American Society for Testing and Materials (ASTM) guidance on Standard Guide for Testing Absorbable Stents (ASTM F3036-21). Specific guidelines that describe *in vitro* testing of BRS (e.g. ASTM F3036-13, ISO 17137) and associated materials (ASTM F1635, ISO 13781) are also now available. For design evaluation of BRS, both ASTM F3036-13 and ISO 17137 require the use of suitable *in vitro* models for the anticipated degradation mechanism that should reflect the implant composition and interaction with the surrounding environment. ISO 13781 outlines that implant performance should be characterized *in vitro* at multiple time points that encompass the timeframe for implantation (“Procedural Stage”), active degradation (“Intermediate Stage”), and the expected final *in vivo* histological disappearance of the bioresorbable implant or component (“Advanced Stage”), with these phases represented schematically in Figure 2.11.

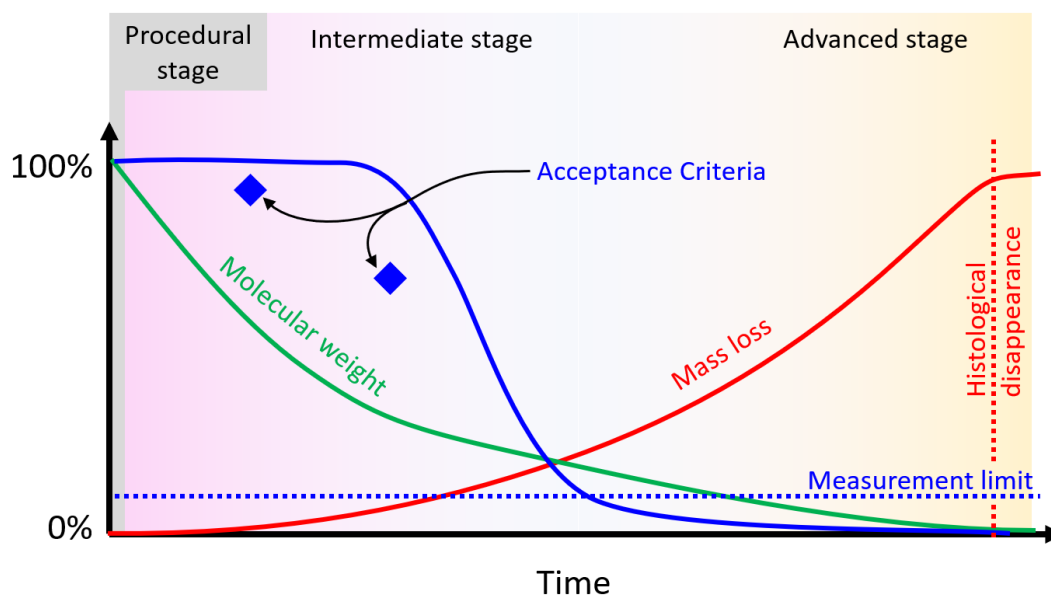


Figure 2.11. Evolving relationship between physical properties and mechanical support provided by a BRS during various stages in the degradation (adapted from ISO/TS 17137:2019)

For bioresorbable implants, ISO 13781 outlines that post-deployment performance must specifically ensure that the initial functional design performance is not affected by any excessive shrinkage/swelling, premature degradation and/or release of degradation/corrosion product(s) that could lead to unwanted defects or unintended loss in mechanical function in the short-term. Beyond the procedural stage, the intermediate stage of degradation spans the end of the procedure to where the measured mechanical attribute of the implant being tested is no longer detectable, which is schematically represented in Figure 2.11. From ISO 13781, the primary focus in the intermediate stage is that the decline in “mechanical attributes” of the BRS occurs with acceptable measurement limits that are described at multiple relevant time points during degradation. *In vitro* characterisation protocols should, as much as possible, simulate *in vivo* degradation, typically using a physiologically-relevant aqueous solution that maintains the appropriate pH and thermal conditions. Depending on the intended *in vivo* environment, *in vitro* characterisation should consider physiological loading conditions from vessels (such as pulsatile axial, torsional, bending tests) to determine if the expected loading has a significant impact on the degradation profile. Mechanical and/or performance properties need to be evaluated at time intervals in accordance with the requirements of the product specific relevant

standards. Such *in vitro* fatigue testing needs to be of sufficient duration to characterize the anticipated functional life of the implant, which may vary depending on the design attribute being evaluated.

Together, the tests recommended in these standards appear comprehensive, enabling detailed device characterisation across the entire lifetime of the device. However, while these standards provide a broad testing framework, there is substantial room for interpretation within these protocols. There is a clear focus on the mechanical performance of the device, suggesting that the underlying mechanisms that could be determined through physio-chemical characterisation are secondary. The standards provide limited guidance on evaluating the thermal or molecular changes that occur to polymers when degraded. Furthermore, while acceptance criteria for the short-term performance of the device during implantation (e.g. procedural stage) are well-established, the longer-term acceptance criteria for mechanical performance are not well-defined. Such information would depend on the intended use of the device and the scaffold manufacturer's interpretation of these acceptance criteria. Crucially, it is difficult to say precisely how these are interpreted as this information is commercially sensitive, with very limited information in the public domain.

Table 2.3. List of some of the various mechanical and bench tests to be performed on vascular stents for the process of demonstrating safety and efficacy.

Test	Test description	FDA Guidance	ISO 25539-2	ASTM F3036-21
Dimensional Verification	Determine the deployed stent dimensions including outer diameter(s), wall thickness (es), and all other appropriate dimensions, for verification to design specifications.	✓	✓	✓
Percent surface area	Report the percent surface area of the stent for both the smallest and largest nominal expanded diameters for each stent design.	✓		
Foreshortening	Decrease in length of the stent between the catheter-loaded condition and the deployed diameters	✓	✓	✓
Recoil	Measured change in diameter of your stent between post-balloon expansion and after balloon deflation	✓	✓	✓
Stent Integrity	Visual examination to detect any evidence of cracks, scratches, permanent set and coating delamination	✓		
Radial Stiffness and Strength in-vitro	Radial stiffness, i.e., the change in stent diameter as a function of uniformly applied external radial pressure; and radial strength, i.e., the pressure at which your stent experiences irrecoverable deformation.	✓	✓	✓
Three-point Bending in-vitro	Three-point bend testing to assess the bending stiffness, strength and flexibility	✓		✓
Kink resistance	Determine the minimum radius that the endovascular prosthesis can accommodate without kinking.		✓	
Mechanical Properties of constitutive material	Tensile testing on constitutive material to determine ultimate tensile strength (UTS), yield strength (YS), elongation	✓		
Simulated Use	Testing to demonstrate that the delivery catheter can safely and reliably deliver the stent to the intended location and that the stent is not adversely affected by the delivery catheter, both during deployment and withdrawal	✓	✓	✓
Accelerated Durability Testing	perform long-term durability testing that models the physiological loads and boundary conditions that your stent is likely to experience under its intended use	✓	✓	
Particulate Evaluation	Measure the total number of particulates and size of the particulates generated during the simulated delivery and deployment	✓		✓
MRI Safety and Compatibility	Investigate issues affecting safety and compatibility of your stent in the MRI environment	✓	✓	
Radiopacity	Evaluate visibility of stent in real-time and plane film x-ray during delivery, deployment and after implantation	✓	✓	
Biocompatibility	Determine the biocompatibility of all patient-contacting materials present in your device.	✓	✓	
Degraded Three-point Bending in-vitro	Three-point bend testing to assess the bending stiffness, strength and flexibility on degraded samples			✓

### 2.3.3. Bench testing of BRS – Short-Term Performance

These bench tests outlined in Table 2.3 describe the various test requirements to demonstrate functional performance of the device *in vitro*. Of most importance, radial testing is used to measure the outward force of the stent to ensure it can withstand the loading imparted upon it by the vessel, pulsation from blood flow and musculoskeletal movement. Radial testing can be performed using several methods including parallel plates (Bonin *et al.*, 2018), v-clamps (Maleckis *et al.*, 2017), hydraulic/pneumatic crushing (Barkholt *et al.*, 2020) and segmented head/iris closure (McKenna and Vaughan, 2020). Methods such as the segmented head and hydraulic crushing that completely radially encompass the stent typically provide most accurate measurement. Figure 2.12 shows the typical radial force-diameter loading curve for a balloon-expandable stent under a segmented head apparatus. The initial linear loading portion of the curve is taken as the radial stiffness. The curve then plateaus as the stent undergoes plastic deformation during crimping. In the absence of damage, unloading will take place parallel to initial loading line, while some recoil occurs this type of loading shown in Figure 2.12 leads to permanent deformation of the BRS upon removal of the load. Radial strength is defined by ASTM-F3067 as the offset parallel to the unloading line (ASTM International, Corro- and Test-, 2005) or an arbitrary offset parallel to the loading line (Qiu *et al.*, 2018; Qiu *et al.*, 2019). Despite this ASTM standard definition, there are several examples in the literature where radial strength has been defined differently, for example where cross-sectional area was reduced by 25% (Ormiston *et al.*, 2015).



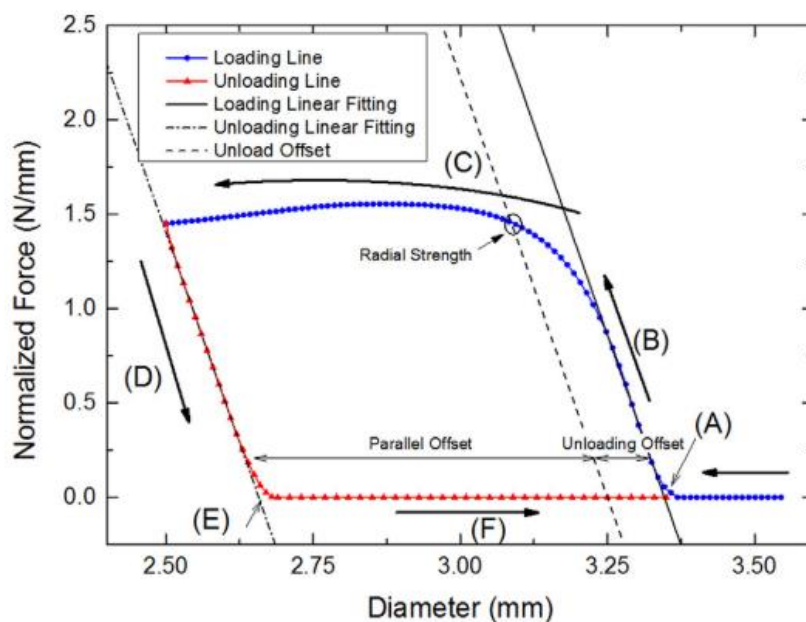


Figure 2.12. Typical radial force vs diameter curve for a balloon expanded BRS with radial strength determined from an offset line parallel to the unloading curve. Radial stiffness is determined from the slope of the initial linear region (Wang *et al.*, 2017).

Axial tests are typically performed by applying an axial compressive or tensile load to one end of the stent while the other end is fixed. Axial testing is used to evaluate the tensile/compressive loads and to investigate stent deformation such as buckling and reduction of cross-sectional area. Bending tests can be performed using several techniques including three-point bend tests (Wang *et al.*, 2017) and a free bend test by fixing one end and applying a load to the other to measure bending stiffness or stent flexibility (Schmidt *et al.*, 2009), as shown in Figure 2.13. This is an important metric given the tortuous nature of the blood vessels of the human anatomy. Bending tests allow for the characterisation of a stent's flexibility and tests can be performed on the deployed and un-deployed configurations. These tests can indicate the performance and interaction within a blood vessel, whether it conforms with, or stiffens the surrounding vessel or the ease in which the deployment system may be navigated to the site of injury.

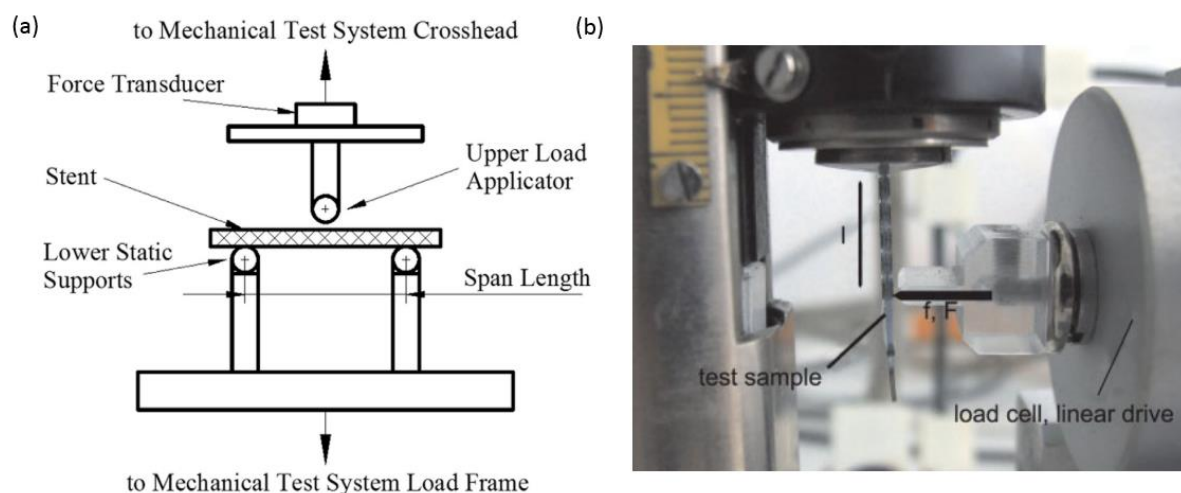


Figure 2.13. Experimental test set-ups for bending tests, showing (a) three-point bend test and (b) free bending fixture. Adapted from (Wang et al., 2017) and (Schmidt et al., 2009) respectively.

Other common experimental bench tests for BRS include inflation pressure versus diameter, measuring recoil and deployment flexibility testing. This is due to the tests accessibility and not having to rely on specialised equipment other than an axial testing machine. Table 2.4 below summarises several published studies that have conducted in-house bench top tests on polymer BRS. From this, it is clear that published experimental data on polymer BRS is limited, with many of the studies focussing on the Abbott Absorb scaffold, or an in-house BRS design, with only limited examples of other commercial BRS.

Table 2.4. In-vitro experimental studies assessing the initial mechanical performance of polymer BRS devices.

Scaffold Tested	Mechanical Tests Performed	Physical Tests Performed	Temp.	Testing Media	Loading Conditions	Ref.
Absorb, Desolve, Desolve Cx	Longitudinal strength, radial strength, recoil, post-dilation and fracture	Not performed	37°C	SBF Bath	Static	(Barkholt <i>et al.</i> , 2020)
Reva Fantom	Free expansion, longitudinal tensile	Not performed	37°C	Water bath	Static	(Antonini, <i>et al.</i> , 2021)
Absorb, DESolve	Free expansion, recoil, radial strength, flexibility/bending stiffness	Not performed	37°C	Water/saline bath	Static	(Schmidt <i>et al.</i> , 2016)
Absorb, DESolve	Free expansion, recoil, radial strength, post-dilation and fracture	Not performed	37°C	Water bath	Static	(Ormiston <i>et al.</i> , 2015)
Novel BRS	Recoil, collapse pressure	Molecular weight, thermal analysis	37°C	Air	Static	(Grabow, <i>et al.</i> , 2007)
Novel BRS	Annealing treatment, free expansion, collapse pressure,	Thermal analysis	Room temp. (20°C)	Air	Static	(Welch <i>et al.</i> , 2009)
Novel PLLA BRS	Fatigue loading, scaffold placed in silicone vessels and subjected to a flow rate of 40-50ml/min	Not performed	37°C	PBS	Dynamic	(Wang <i>et al.</i> , 2020)
Novel PLLA BRS	Crimping, free expansion, 3-point bending, radial strength / stiffness, collapse pressure	Not performed	37°C	Not Disclosed	Static	(Wang <i>et al.</i> , 2017)

Schmidt et al (2016) subjected two polymer (Abbott Absorb and Elixir DESolve) and a magnesium (Biotronik Magmaris) BRS to a suite of mechanical testing, including expansion within a rigid and compliant mock vessel, recoil, radial strength and flexibility testing. It was found that the polymer BRS had higher rates of acute recoil and 1-hour post implantation recoil than the magnesium BRS. Magmaris and Absorb BRS had similar crush resistance, with values of 197 kPa and 172 kPa, respectively. Ormiston et al (2015) performed a number of bench tests on the Abbott Absorb and DESolve BRS, comparing the deployment characteristics against a commercial DES (Xcience Xpedition). All scaffolds had a nominal diameter of 3mm and recoil, radial strength, crossing profile, deployment post dilation and side branch dilation were

investigated. The DES had the lowest crossing profile of the scaffolds examined, with a strut thickness of 89  $\mu\text{m}$  compared with the polymer BRS 157-150  $\mu\text{m}$  for the Absorb and DESolve respectively, resulting in the polymer scaffold being more difficult to deliver than the DES. The radial strength was assessed by applying a uniform pressure on the outside of the scaffold until the cross-sectional area was reduced by 25%. The DES required a pressure of 1.6atm to reduce the cross-sectional area compared with 1.3 atm and 1.1 atm for the Absorb and DESolve respectively. Post dilation of the scaffold was performed to measure the diameter the scaffold could be expanded to before strut fracture. The Absorb fractured at a diameter of 3.8 mm, the DESolve fractured at a diameter of 5 mm while the Xcience DES did not fracture during this test. These bench studies have shown that polymer BRS could still have functional performance similar to DES, although this was facilitated by thicker struts. While these investigations have provided key insight into the mechanical performance of polymer BRS, it is evident from Table 2.4 that evaluation of physiochemical properties are lacking. The degree of crystallinity, molecular weight and thermal properties are known to effect the mechanical response of the polymer, and subsequent degradation kinetics, but there are limited examples of these properties being reported in such studies. Bench testing should be performed in conditions as close as possible as those experienced *in vivo*, while testing conditions are less critical for metal DES the ambient temperature and humidity can have drastic effects on the mechanical performance of a polymer BRS. These details are of vital importance as discussed earlier in (Section 2.2) as these can influence the initial and lifetime performance of a polymer BRS.

#### **2.3.4. In Vitro Degradation Characterisation of BRS**

While the guidance documents presented in Section 2.3.2, summarise a standards-based approach to device characterisation, with particular interest in the mechanical characterisation of the implantation performance, there is substantial variation in the published literature when conducting *in vitro* degradation tests for polymer based BRS. Table 2.5 provides an overview

of relevant *in vitro* degradation studies of polymer BRS. Across these studies, processing techniques and/or the type of specimen being evaluated have varied significantly and include 3D printed scaffolds (Chausse *et al.*, 2021), braided wire scaffolds (Nuutinen *et al.*, 2003) and final laser-cut scaffold designs (Luo *et al.*, 2014; Naseem *et al.*, 2019). These studies use similar approaches to degradation testing as those summarised in Section 2.2.4. To represent the physiological environment, *in vitro* degradation studies have generally been carried out by immersing specimens such as full devices in PBS, at 37°C over time periods ranging from several weeks (Nuutinen *et al.*, 2003) to years (Qiu *et al.*, 2018). In most studies, degradation of the scaffolds was evaluated with immersion in a static degradation media, with only a handful of studies examining the effect of fluid flow on the scaffold being investigated (Luo *et al.*, 2014).

Table 2.5. In-Vitro degradation studies on novel and commercial polymer BRS devices. Table first appeared in (Shine, 2020) it has been modified to include both PLLA and other polymer BRS tests with additional entries added.

Sample Type	Degradation conditions	Loading Conditions	Property Characterisation	Reference to standards	Ref.
Braided PLLA scaffolds	Degradation at 37°C (six fibres and 4 stents tested) for 104 weeks. Samples were gamma sterilised prior to degradation.	Static	Molecular weight, mechanical properties, mass loss, crystallinity	-	(Nuutinen <i>et al.</i> , 2003)
PLLA and PLLA helical scaffolds	PLLA tensile specimens degraded in a saline environment at 37°C for 3 months. Stents immersed in similar conditions for 5 weeks	Static	Tensile properties, glass transition temperature, molecular weight, collapse pressure.	No	(Venkatraman <i>et al.</i> , 2003)
PLLA fibres and coiled PLLA stents	Fibres degraded in PBS at 37°C for 6 weeks. PLLA stents were investigated for 20 weeks in the same conditions.	Static	Mass loss, tensile properties, radial compression strengths (stents)	-	(Zilberman <i>et al.</i> , 2005)
PLLA/P4HB slotted tube scaffolds	Stents degraded in Sørensen's buffer solution at 37°C for up to 48 weeks.	Static	Molecular weight, stent collapse pressure	No	(Grabow, <i>et al.</i> , 2007)
PLLA slotted tube scaffolds	Stents degraded in Sørensen's buffer solution at 37°C for up to 24 weeks.	Static	Molecular weight, stent collapse pressure	-	(Grabow, <i>et al.</i> , 2007)
PLLA prototype scaffolds	Degradation in a customised in-vitro system. Stents immersed for 6 months and examined under applied pressure and fluid flow.	Dynamic, fluid flow	Molecular weight, radial strength, thermal properties	-	(Luo <i>et al.</i> , 2014)
PLLA scaffold sub-units	Degradation of samples under fatigue and static conditions. Degradation carried out at 42°C for 100 days in both cases.	Cyclic	Tensile properties, molecular weight, crystallinity	-	(Dreher, <i>et al.</i> , 2016)
PLLA scaffold and sheets	Degradation in PBS under static conditions at 37°C for 110 days.	Static	Molecular weight, crystallinity	-	(P. J. Wang <i>et al.</i> , 2018)
PLLA scaffold supplied by Abbott Vascular	Stents incubated in glass vials containing PBS at 37°C for 24 months	Static	Radial force testing,	-	(Qiu <i>et al.</i> , 2018)
PLLA scaffold supplied by Abbott Vascular	Stent sections containing 3–4 rings were produced using a sharp blade in a sterile environment and incubated in glass vials containing PBS at 37°C for 24 months	Static	Molecular weight, crystallinity, elastic response (nano-indentation)	-	(Naseem <i>et al.</i> , 2019)
PLLA scaffold supplied by Abbott Vascular	Real time degradation with time points at 0, 9 and 18 months.	Static	Surface morphology,	-	(Ramachandran <i>et al.</i> , 2018)

PLLA prototype scaffold	In vitro degradation in PBS at 37°C for 3 months	Static	Molecular weight, collapse pressure, crystallinity, water uptake.	-	(Tan <i>et al.</i> , 2005)
PCL Prototype scaffold	In vitro degradation in PBS at 37°C for 8 weeks	Dynamic, fluid flow	Dry and wet mass, surface morphology	-	(Guerra and Ciurana, 2017)
3D printed PLLA/PLCL novel scaffold	In vitro degradation in PBS at 37°C for 3 months	Static	Crystallinity, radial strength, thrombogenicity, cytotoxicity, radiopacity	-	(Chausse <i>et al.</i> , 2021)
Braided PLLA scaffold	Degradation performed under physiological flow conditions for 32 weeks	Dynamic, fluid flow	Crystallinity, molecular weight, tensile properties,	-	(Khalaj Amnieh <i>et al.</i> , 2021)
Braided PDO scaffold	In vitro degradation in PBS at 37°C for 10-16 weeks	Static	Crystallinity, radial strength, mass loss, bending strength, surface morphology	No	(Wang and Zhang, 2016)
Novel PLA/Mg scaffold	In vitro degradation in Hanks solution at 37°C for 30 days, stents immersed for 7 days	Static	Crystallinity, thermal properties, parallel plate crush, surface morphology	No	(Hasanpur <i>et al.</i> , 2021)
Novel PLA Blend scaffold	In vitro degradation in distilled water and Ringer's solution at 37°C for 6 weeks	Static	Radial force, pH, surface morphology, protein adhesion	No	(Bartkowiak-Jowska <i>et al.</i> , 2011)

A range of characterisation techniques have been used across these studies, which generally capture changes in chemical, thermal properties and/or mechanical properties. Unsurprisingly, studies have reported a wide variation in mechanical performance across PLLA-based materials (Tsuji and Ikada, 2000; Gleadall *et al.*, 2014; Katarzyna *et al.*, 2021) and PLLA-based devices (Luo *et al.*, 2014; Qiu *et al.*, 2018) undergoing degradation. It is notable that differences are not only observed in the timescale(s) at which load-bearing capacity is reduced, but also fundamental differences are observed in how mechanical properties (e.g. stiffness, strength, ductility) are impaired during degradation. For example, an *in vitro* study on PLLA tubes reported substantial reductions in both tensile strength and tensile failure strain, but little reduction in either elastic modulus or yield stress following immersion (Naseem *et al.*, 2020). Others have determined that degradation resulted in reduced yield stress of PLLA over time, with little reduction in elastic modulus or failure strain (Qiu *et al.*, 2018). In contrast, other studies performed on the bulk polymer have demonstrated that elastic modulus, tensile strength and strain-to-failure all deteriorate during immersion (Tsuji and Ikada, 2000). While these differences are driven by variations in either the polymer composition or processing parameters, there is a surprisingly limited understanding of the physical basis for these temporal changes in mechanical behaviour during degradation. It is also worth noting that the majority of our understanding of bioresorbable polymer degradation behaviour has been derived from static conditions, with only limited studies evaluating the role of dynamic fluid flow and/or cyclic loading conditions on degradation performance. Degradation in a dynamic environment allows for the degradation products to be removed from the area immediately surrounding the scaffold and causes an increase in the rate of degradation by increasing the diffusion gradient between the inside of the polymer scaffold and the surrounding environment. Dreher *et al* (2016) have demonstrated a clear a role for cyclic loading conditions on measured mechanical properties and molecular weight during degradation with cyclically loaded samples



experiencing increased stiffness and molecular weight loss when compared to the static control. Guerra *et al* (2017) have shown the influence of flow on PCL scaffold sub-units, with samples exposed to fluid flow experiencing an increase in mass compared with the static control, with the increase in mass attributed to a faster absorption of water in the samples exposed to fluid flow. Therefore, many of the reported results from *in vitro* studies may not fully represent the physiological environment, which further adds to the challenges in predicting degradation of implanted BRS *in vivo*.

## 2.4. Overview of Computational Modelling of Coronary BRS

While benchtop testing is a necessary and important component in the development of BRS, it can require large amounts of device prototyping. Computational modelling is a powerful tool that can be used to simulate the complex material behaviour and *in vivo* loading conditions of coronary BRS. Typically, computational methods for evaluating scaffold mechanics are performed using the finite element method. Indeed, it is a required component in the development of coronary stents and forms part of the regulatory submission process (FDA, 2010). Computational modelling can provide a host of additional information such as failure mechanisms, the stress state within scaffold struts, scaffold -vessel interactions and it reduces the time in evaluating the long-term behaviour such as degradation and fatigue of BRS.

In recent years, there has been a growing number of studies and projects advocating for the adoption of *in silico* clinical trials, whereby computational methods are used to predict outcomes of device interventions (Viceconti *et al.*, 2019). These platforms have a number of advantages over conventional clinical trials in terms of reduced cost and time needed to complete a trial. A repository of *in silico* or virtual patients can be gathered and in the case of BRS the ‘patients’ can consist of the relevant blood vessels which are scanned and reconstructed for use computationally. Patients for the trials could then be selected using the desired vessel geometry or history. However, a number of issues still remain before the

adoption of *in silico* trials as part of the device approval process. First, is developing a platform that sufficiently captures the complexity of the trial one is trying to perform. In terms of vascular stents, a platform must be capable of capturing the initial deployment processes as well as late-stage performance, biological and fluid interactions. Second, is the issue of credibility of *in silico* models. While computational modelling has been used for some time to predict mechanical performance of stents, more advanced modelling is required to capture biological aspects (e.g. neo-intimal growth) and degradation responses and require in-depth validation before being adopted by regulatory agencies.

#### **2.4.1. Short-Term Modelling of BRS**

Computational finite element models of the short-term mechanical performance of bioresorbable scaffold are reasonably well-established and generally consider mechanical performance of devices in the absence of degradation. Table 2.6 provides a general summary of computational studies that have investigated the short-term performance of polymer BRS. Where the short-term is defined as the crimping, deployment and recoil of the BRS. Many have simulated *in vitro* bench testing protocols (e.g. radial force, bending behaviour, crush resistance) to predict functional device properties and predicted the implantation performance of polymer BRS. The computational bench testing of novel vascular devices is also a requirement during the approval process with the FDA issuing guidance documents on the computational assessment of scaffold (which were covered in Section 2.3.2)

Table 2.6. A summary of computational polymer BRS studies showing the material models used, the method of calibrating the material model for the short-term performance of BRS and the short-term loading conditions examined.

Material	Material Model	BRS Modelled	Source of Material Parameters	Strain Rate (mm/min)	Test Materials	Conditions Examined	Expansion Method	Vessel Deployment	Simulation Solver	Ref.
PLLA	Hyperelastic	Novel BRS	Uniaxial tensile testing	1, 2, 4	PLLA Fibres	Pressure applied to external surface	Not given	No	Abaqus	(Soares, <i>et al.</i> , 2010)
PLLA	Elastic-plastic	Novel BRS	Tensile testing	Not Given	Not Given	Radial compression, fatigue	Rigid Cylinder	Simplified vessel	Abaqus Explicit	(Luo <i>et al.</i> , 2014)
PLLA	Viscoelastic	Multilink, Absorb, Igaki–Tamai	Uniaxial tensile testing	5	PLLA Sheet	Radial compression, flexibility, axial crush	Displaced inner surface	No	Abaqus Standard	(Bobel <i>et al.</i> , 2015)
PLLA	Anisotropic elastic-plastic	Absorb (modified), Novel BRS	Uniaxial tensile testing in circumferential and longitudinal directions	5.08	PLLA Tubes	Pressure applied to external surface	Displaced inner surface	No	Abaqus Standard	(Pauck and Reddy, 2015)
PLLA	Hyperelastic visco-plastic	Absorb	Uniaxial tensile testing	1, 10, 100	PLLA Tubes	Pressure/diameter curves	Balloon	No	Abaqus Standard	(Debusschere, <i>et al.</i> , 2015)
PLLA	Elastic-Plastic	Absorb	Circumferential data from Pauck & Reddy (2015)	5.08	--	Pressure/diameter curves, dog-boning, crimping, vessel stress	Balloon	Simplified vessel, wt. plaque	Abaqus	(Schiaivone, <i>et al.</i> , 2016)
PLLA	Elastic-plastic	Absorb	Uniaxial tensile testing	1	PLLA Tubes	Crimping, deployment, flexibility, radial compression	Rigid Cylinder	No	Abaqus Standard	(Wang, <i>et al.</i> , 2017)
PLLA	Elastic-plastic	Elixir, Xience	Circumferential data from Pauck & Reddy (2015)	5.08	--	Pressure/diameter curves, dog-boning, crimping, vessel stress	Balloon	Simplified vessel, wt. plaque	Abaqus Explicit	(Schiaivone, Qiu, <i>et al.</i> , 2017)
PLLA	Elastic visco-plastic	Renuvia	Uniaxial tensile testing	0.001, 0.01, 0.1	PLLA Tubes	Axial expansion, parallel plate crush	Rigid Cylinder	Simplified vessel, single layer	Abaqus Standard/Explicit	(P. Wang, <i>et al.</i> , 2018)

PLLA	Elastic visco-plastic	Absorb	Not Given	Not Given	Not Given	Chronic outward force	Not Given	No	Abaqus Explicit	(Dong, Wang, et al., 2018)
PLLA	Elastic-plastic	Absorb, Elixir, Igaki-Tamai, Fantom	Circumferential data from Pauck & Reddy (2015)	5.08	--	Recoil, radial compression, crimping, deployment, pressure/diameter curves	Balloon	No	Abaqus Explicit	(Qiu, Song, et al., 2018)
PLLA	PRF Model	Absorb	Uniaxial Tensile Testing Bobel et al (2016)	1.0, 2.5, 5	PLLA Dog-bones	Deployment, deployment rate, recoil, fracture	Rigid cylinder	No	Abaqus Explicit	Bobel and McHugh. 2018)
PLLA	Elastic-viscoplastic	Renuvia	Uniaxial Tensile Testing Wang et al (2018)	Not Given	PLLA Tubes	Crimping, deployment, recoil, multimodal loading (axial compression, bending, torsion)	Balloon	Simplified vessel, single layer	Abaqus Standard	(Wang et al., 2020)
Tyrocore	PRF Model (single visco-elastic branch parallel to an elastic-plastic branch)	Fantom Encore	Tensile testing of BRS scaffolds (axial direction)	1.5, 6	BRS Scaffolds	Axial tension, radial compression, pressure/diameter curves	Balloon	No	Abaqus Explicit	(Antonini, Berti, et al., 2021)
PLLA	Hyperelastic plastic	Absorb	Uniaxial Tensile Testing Hayman et al (2014)	1	PLLA Fibres	Chronic outward force	Not Given	Simplified vessel	Abaqus Standard	(Shine, 2021)
PLLA	Elastic visco-plastic	Absorb	Uniaxial Tensile Testing	0.005, 0.05	PLLA Dog-bones	Different crimping protocols, force/diameter curves	Balloon	No	Abaqus Explicit	(Antonini, Poletti et al., 2021)
PLLA	Anisotropic elastic-plastic	ArterioSorb	Uniaxial tensile testing in circumferential and	1	PLLA Dog-bones	Crimping, deployment, recoil, radial compression	Balloon	No	Abaqus Explicit	(Hoddy et al., 2021)

longitudinal directions										
PLLA	Elastic visco-plastic	Novel BRS	Uniaxial tensile testing performed at different temperatures	0.001, 0.01, 0.1	PLLA Dog-bones	Pressure/diameter curves, dog-boning, foreshortening	Balloon	No	PAK	(Filipovic <i>et al.</i> , 2021)
PLLA	Elastic visco-plastic	Absorb, Modified Absorb, Novel BRS	Uniaxial tensile data from Filipovic et al (2021)	0.001, 0.01, 0.1	PLLA Dog-bones	Radial compression, flexibility, deployment, crimping,	Balloon	No	PAK	(Milosevic <i>et al.</i> , 2021)
PLLA	PRF Model	ArterioSorb	Uniaxial tensile testing in circumferential and longitudinal directions	1	PLLA Dog-bones	Crimping, deployment, recoil, radial compression	Balloon	No	Abaqus Explicit	(Hoddy <i>et al.</i> , 2022)
PLLA/PCL	Elastic-plastic	Novel BRS	PLLA data from Circumferential data from Pauck & Reddy (2015) PCL data from	5.08	--	Crimping, deployment, recoil, foreshortening,	Balloon	Simplified vessel, single layer wt. plaque	FE Bio	(Donik <i>et al.</i> , 2022)

A range of constitutive material models have been used to predict the short-term response of BRS during crimping and deployment. Several authors (Schiavone, Qiu and Zhao, 2017; Qiu, Song and Zhao, 2018) have used circumferential tensile data from Pauck and Reddy (2015) as an input for an elastic-plastic material model to compare the performance of different BRS. Schiavone *et al* (2017) compared the pressure-diameter inflation curves along with elastic recoil, dog-boning, crimping force and radial strength of each BRS device. They showed that residual stresses within the BRS affected the recoil and rate of expansion. It has also been shown that the geometry of the BRS has a large effect of the overall mechanical properties of the whole device (Qiu, Song and Zhao, 2018). Short-term modelling of BRS has also included deployment within a blood vessel. It has been shown that owing to the lower elastic modulus of the polymer BRS in comparison with conventional DES, they impart less stress on the plaque and vessel (Schiavone *et al.*, 2016; Schiavone, Qiu and Zhao, 2017; Qiu, Zhao and Song, 2019). Lower imparted stress is seen as favourable as scaffolds which induce higher stresses on their surrounding environment provoke a more aggressive biological response in the artery wall and more neo-intimal growth (Timmins *et al.*, 2011).

Pauck and Reddy (2015) developed an anisotropic elastic-plastic model calibrated using PLLA tubes. Tensile tests were performed on dog-bones cut from the tubes in the circumferential and longitudinal directions. Three BRS geometries were simulated, with the elastic recoil after deployment and radial strength compared. Their analysis showed that, while the geometry of a scaffold can alter the radial performance, the strut thickness, width and material stiffness are the primary factors in radial strength. Bobel *et al* (2015) focussed on evaluating several BRS by simulating radial compression, flexibility and longitudinal resistance using a non-linear viscoelastic material model calibrated from uniaxial tensile tests on dog-bones. Figure 2.14 shows the geometries considered and the benchtop tests they were subjected to. The simulated

benchtop tests demonstrated the importance of scaffold geometry in adding mechanical performance to PLLA.

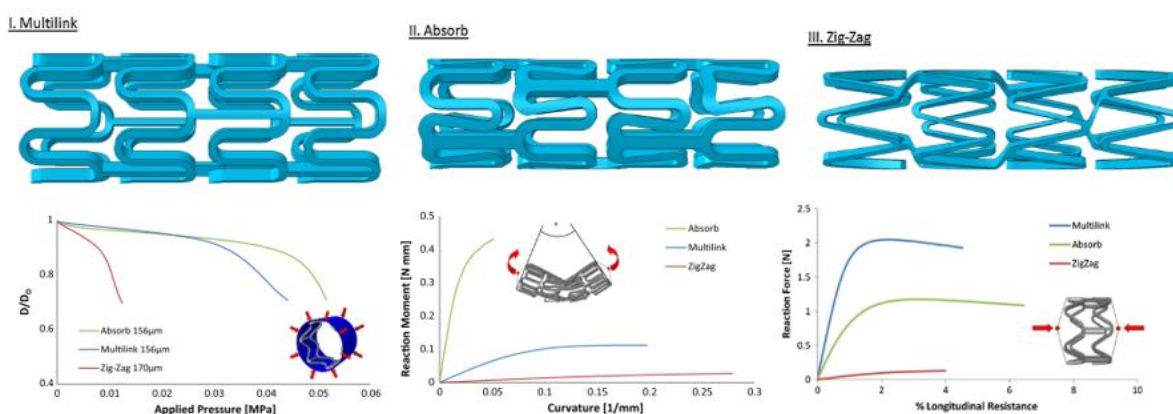


Figure 2.14. Several BRS designs subjected to simulated bench top tests, radial compression, flexibility and longitudinal resistance (Adapted from (Bobel et al., 2015)).

Unlike their metallic counterparts, the deployment behaviour of polymeric bioresorbable devices are more sensitive to rate-dependent aspects of the procedure (e.g. inflation rate) and significant efforts have been made to understand the role of non-linear and time-dependent behaviour on device performance. Studies have implemented hyperelastic (Li *et al.*, 2017), visco-plastic (Debusschere *et al.*, 2015; Antonini, Poletti, *et al.*, 2021) and/or visco-elastic (Bobel *et al.*, 2015; Antonini, Berti, *et al.*, 2021, Hoddy *et al.*, 2022) constitutive material models that capture short-term behaviour in the absence of degradation (summarised in Table 2.6). Debusschere *et al* (2015) demonstrated the effect that balloon expansion techniques can have on the stress state within a polymer BRS. The PLLA material was modelled using a hyperelastic visco-plastic material constitutive law. It was shown that a step-wise dilation method reduces the internal stresses within the BRS in comparison with the single inflation step typically employed for DES deployments, as shown in Figure 2.15. This reduction in stress within the scaffold struts can be attributed to the stress relaxation effect seen in polymers. This method differs to the established protocol for deploying balloon expanded DES in use clinically which is typically performed under a single step, as metals typically do not exhibit viscous or strain rate behaviour. Beyond the device itself, differences to the clinical procedure have also

been suggested for BRS compared to DES, with Schiavone *et al* (2016) suggesting that additional post balloon dilation be performed to achieve the desired vessel diameter in BRS devices.

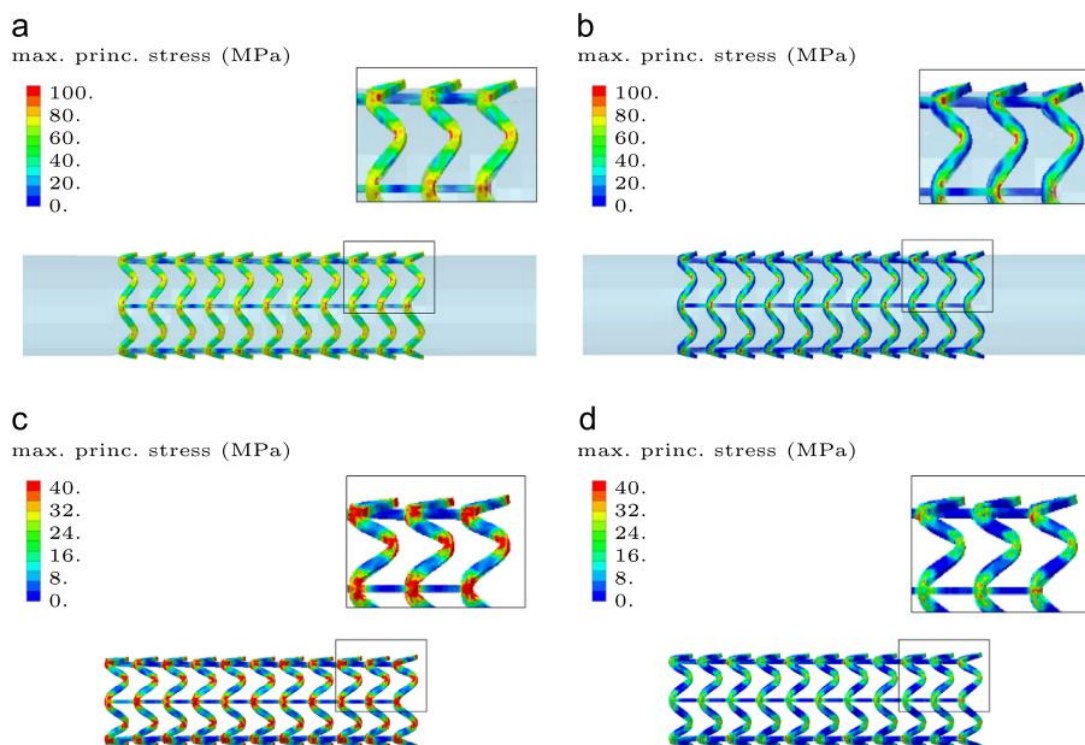


Figure 2.15. Finite element contour plots showing the maximum principal stress of direct inflation at the end of deployment (a), and recoil (c) compared against the step wise deployment at the end of deployment (b), and recoil (d). Adapted from (Debusschere *et al.*, 2015).

Another difference between DES and BRS is the temperature dependence associated with BRS materials, where the material exhibits different mechanical responses under different temperatures. This temperature dependence can affect the stress-strain response of the crimping or deployment process. During manufacture, crimping of polymer BRS is typically carried out at elevated temperatures, which changes the mechanical response of the polymer. Antonini *et al* (2021) demonstrated that this altered mechanical response must be taken into account to accurately predict the crimped configuration in BRS devices. It was found that higher temperature (52°C) crimping leads to lower forces, with their simulations predicting that crimping at elevated temperatures results in lower elastic recoil of the scaffold and a small external diameter achieved after crimping. The state of hydration for the polymer is also of



importance. The ingress of water into the backbone polymer can also affect the mechanical properties as found by Wang *et al* (2018). They showed that when hydrated under uniaxial tensile testing, the polymer exhibits lower yield stresses, more deformability and a more compliant behaviour to the dry condition.

#### **2.4.2. Long-term Modelling of BRS**

Degradation has a number of consequences on the long-term performance of a BRS, affecting the physical, chemical and mechanical properties of the polymer. The prediction of long-term BRS performance can be influenced by the deployment history, loading rate, local environment and temperature conditions. While computational studies are a required part of analysing the mechanical performance of a BRS, currently there is no guidance from regulatory bodies on the use of computational modelling to predict the long-term degradation behaviour. The prediction of the long-term degradation behaviour in computational modelling of polymer BRS can be subdivided into two categories; physically based and phenomenologically based models.

##### *Physical Modelling*

Physically-based degradation models account for the physical processes involved in degradation (summarised in Section 2.2.4) and typically use first order kinetic equations to capture degradation kinetics. These include the diffusion of water molecules and monomers, the scission of ester bonds and changes in crystallinity. Table 2.7 shows a selection of physically-based degradation models and the method used to capture physio-chemical degradation process. Shine *et al* (2021) presented a physio-chemical model that accounts for the scission of ester bonds due to hydrolysis and thus reduction in molecular weight and increase in relative crystallinity over time. This physio-chemical model was coupled to a damage model that used the values of molecular weight and crystallinity to evaluate the mechanical response at time  $t$ . This degradation approach was applied to a PLLA BRS in

conjunction with a hyperelastic-plastic material model and is used to model scaffold -vessel interaction over time. The model predicted a loss in lumen diameter and a reduction in the force applied to the vessel over a simulated two-year period. This work also accounted for tissue coverage following deployment, with partial and full coverage of tissue to represent the effect of neo-intimal remodelling on degradation behaviour. Ferdous *et al* (2013) examined the evolution of molecular weight and crystallinity on a two-dimensional scaffold strut exposed to blood flow and two configurations; fully embedded within the artery wall and partially embedded with a surface exposed. The degradation model was used to predict the sensitivity of the mechanical performance to changes in physical properties, such as molecular weight, dispersity, initial crystallinity, rate of crystallinity change and lactide doping (computational addition of lactic acid chains). It was shown that higher crystallinity resulted in slower degradation, and that lactide doping could be used to tune the degradation response. While some of these physical models capture the evolution in physical properties, many do not capture their corresponding effect on the mechanical properties. A more detailed review on physically based models is available in (Boland *et al.*, 2016).

Table 2.7. Summary of physio-chemical degradation models that have been used to simulate the degradation behaviour of BRS (original table from (Shine, 2020) adapted and additional entries added).

BRS Device	Model Description	Key Equations	Parameters	Model Outputs and Comparator for Validation	Ref.
Abbott Absorb, Scaffold strut	First order degradation model developed based on transient diffusion-reaction equations for each polymer species S (1-5). Each species was described as a function of the hydrolysis K, autocatalysis effects Ka and its stoichiometric coefficient n1-5. Lactic acid concentrations C0s examined using diffusion-based model.	$S_1 \rightarrow n_2 S_2 \rightarrow n_3 S_3 \rightarrow n_4 S_4 \rightarrow n_5 S_5$ $\frac{\delta C_x^S}{\delta t} = f(K, K_a, C_{1-5} n_{1-5})$ $\frac{\delta C_0^S}{\delta t} = \nabla \cdot (D_0^S \nabla C_0^S) + 2 \sum_{m=1}^n K C_m^S K_a$	$C_0^S$ – conc. of soluble species $D_0^S$ – diffusion coeff. of soluble species n – number of ester bonds K – hydrolytic degradation rate $C_m^S$ - insoluble species conc. with the number of ester bonds between n and i+1	Outputs: Molecular weight, lactide concentrations, mass, Comparator:	(Shazly, et al., 2012, Ferdous, et al., 2013)
Scaffold strut	Simultaneous model of the biodegradation and drug release for a PLLA based stent coating. Presented four equations in terms of transport of the polymer (CP shown on right), water molecules, oligomers and lactic acids.	$\frac{\delta C_P}{\delta t} = \frac{\delta}{\delta x} \left( D_P \frac{\delta C_P}{\delta x} \right) - k_{pW} C_P C_W (1 + \alpha C_L)$	$C_P, C_W, C_L$ – conc. of PLA, water and lactic acid D – diffusivity of the respective molecules $\alpha$ - account for the autocatalytic effect caused by generation of lactic acid on PLA deg.	Outputs: Water uptake, concentration of drug, lactic acid and PLA Comparator: Degradation in-vitro study of PLA stent coating, GPC and mass loss recorded	(Prabhu, et al., 2006)
PLLA Plate	Degradation controlled using set of simplified reaction-diffusion equations to control the interaction of hydrolysis and monomer diffusion.	$\frac{d\bar{C}_m}{d\bar{t}} = \bar{k}_1 \bar{C}_e + \bar{C}_e \bar{C}_m^n + \bar{D}_0 \operatorname{div}_{\bar{x}_i} \left\{ 1 + \alpha [1 - (\bar{C}_m + \bar{C}_e)] \operatorname{grad}_{\bar{x}_i}(\bar{C}_m) \right\}$ $\frac{d\bar{C}_e}{d\bar{t}} = -(\bar{k}_1 \bar{C}_e + \bar{C}_e \bar{C}_m^n)$	$C_p$ - conc. of monomer $C_p$ - conc. of ester bonds. D – phenomenological diff. coefficient N – dissociation of acid end gaps $k_1/k_2$ – reaction rate constants	Outputs: Molecular weight, ester bond concentration Comparator: In-vitro degradation of plates, films and beads. Molecular weight and mass loss recorded	(Wang, et al., 2008)

Abbott Absorb	First-order kinetic equations model the changes in mole concentrations of ester bonds, monomers produced through hydrolysis and diffusion of monomers through the material.	$\rho c_c \frac{\delta C_m}{\delta t} = \rho c_c H + \nabla \cdot \{ \rho c_c C_m \}$	<p><math>\rho</math> – density  <math>c_c</math> – specific energy  <math>C_m</math> – conc. of monomers at a given temp.  <math>H</math> – external heat source, diff. flux of monomers</p>	<p>Outputs: Changes in molecular weight</p> <p>Comparator: Degradation of PLA plates and films</p>	(Shine, et al., 2017)
Abbott Absorb	Changes in the molecular weight and crystallinity are controlled by first-order kinetic equations. These equations are coupled to damage variables to represent the extent of physio-chemical degradation.	$d_{M_w} = 1 - \bar{M}_w = 1 - \frac{C_e}{C_{e0}}$ $d_{M_n} = 1 - \bar{M}_n = 1 - \frac{M_n}{M_{n0}}$ $d_{X_c} = \left( 1 - \left( \frac{M_n}{M_{n0}} \right) \left( \frac{X_c}{X_{c0}} \right) \right)$	<p><math>C_e</math> - conc. ester bonds  <math>M_w</math> – weight avg. molecular weight.  <math>M_n</math> – number avg. molecular weight  <math>X_c</math> – deg. Of crystallinity</p>	<p>Outputs: Changes in number and weight average molecular weight and crystallinity</p> <p>Comparator:</p>	(Shine, et al., 2021)

### Phenomenological Modelling

Phenomenological models have been more widely used to predict the mechanical changes that take place over the course of degradation of BRS. Table 2.8 summarises phenomenological models that have been used to predict degradation of polymeric BRS devices in the literature. While there are key differences in model implementation across these studies, their general principles assume that degradation results in a reduction in one or more material properties. These techniques are generally based on the continuum damage approach where a damage variable or multiple variables are defined to degrade the chosen material parameters over time and control the severity of degradation.

Soares *et al.* (2010) developed a model for the long-term behaviour of PLLA-based biodegradable scaffold by assuming isotropic Neo-Hookean behaviour, where a reduction in the number of cross-linked segments led to a reduction in mechanical properties in the material. Here, the phenomenological scalar degradation variable,  $d(t)$ , was introduced to represent the degree of degradation of a material particle at a time  $t$ . A value of  $d = 0$  represented the virgin undamaged material, while a value of  $d = 1$  represented the material at a state of complete degradation. The model assumed a linear relationship between degradation and material properties, such that the Neo-Hookean material properties  $\lambda$  and  $\mu$  were linear functions of the damage variable and  $\lambda_0$  and  $\mu_0$ , which are the virgin state material constants, as summarised in Table 2.8. It was also assumed that degradation itself was a function of the deformation. The model was implemented in the Abaqus finite element code through a User defined Field (USDFLD) subroutine and was used to predict degradation and recoil of several different scaffold types over time due to constant pressurisation. While this model can capture a wide range of deteriorating mechanical behaviour during the degradation in the elastic response, the model does not consider any plastic behaviour of the PLLA, and therefore prediction of permanent deformation processes that would play a prominent role during the deployment

phase is not possible. Qiu *et al.* (2018) presented a model for the long-term behaviour of the Abbot Absorb BRS, where it was assumed that the PLLA material behaved as an elastic-plastic material that exhibits linear hardening. The model was implemented in the Abaqus finite element code and assumed that degradation was responsible for alteration in the yield stress of the material, such that  $\sigma^Y = \sigma_0^Y(1 - d)$  where  $\sigma^Y$  is the yield stress,  $\sigma_0^Y$  is the original yield stress and  $d$  is the damage. The model was calibrated to the radial response of the Absorb BRS and it was demonstrated that it captured the changes in scaffold radial stiffness and strength over time, see Figure 2.16. By simulating device expansion, the degradation model was also used to predict the scaffold -artery interaction over the time period of degradation. However, it is notable that the model does not consider any alteration in either elastic response, hardening performance or ductility of the material.

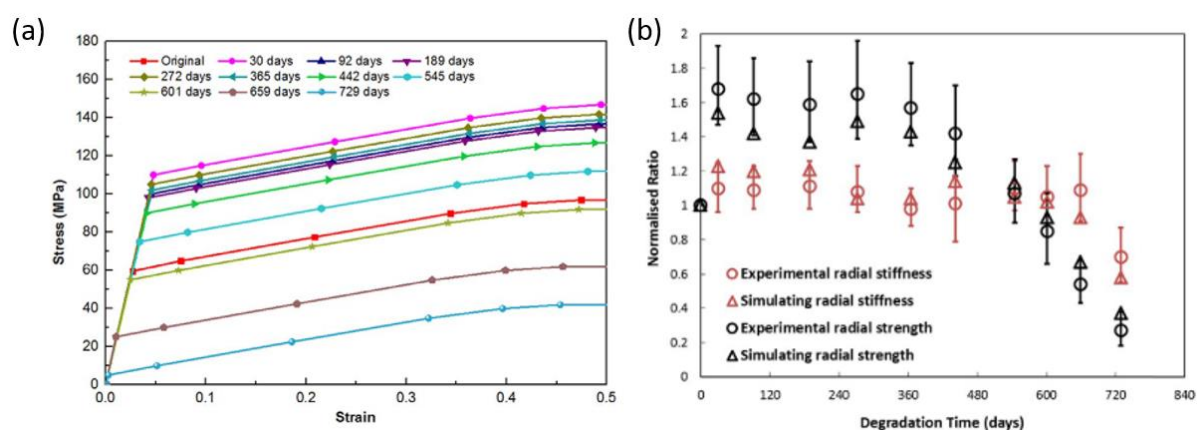


Figure 2.16. (a) Constructed PLLA stress-strain curves for Absorb scaffold at different degradation time points and (b) Experimental and computational evolution in radial strength and stiffness of the Abbott Absorb, computational matched values obtained from changing the yield stress.

Luo *et al.* (2014) presented an elastic-plastic material model that was degraded through a scalar damage variable, which was described as a function of the fracture elongation ratio before and after degradation. It was used to predict the combined elastic, plastic and fracture behaviour over time. Calibration of the parameters, which are identified in Table 2.8, was performed through tensile testing of dog-bone samples that had undergone a pre-stretch prior to degradation testing. The model was used to predict the radial performance of the BRS and compare the performance against an in-vitro and in-vivo study. Several other studies used this

degradation model (Dong, *et al.*, 2018; Lin *et al.*, 2020) with Lin *et al.* (2020) applying the model to the Abbott Absorb GT1. This version of the degradation model also predicted mass loss. Muliana *et al.* (2012) considers a quasi-linear viscoelastic (QLV) model that accounts for hydrolysis and the magnitude of strains within the material. They assume that the rate of degradation increased with strain and water concentration. It was also assumed that the polymer softens with degradation and the rate of relaxation increased. The model was calibrated against uniaxial tensile testing performed by Soares *et al.* (2008). The model was used to predict the vessel-scaffold interaction with the scaffold being a polymer cylinder. The water concentration was highest at the inner surface of the cylinder and diffuses through the thickness of the cylinder as the degradation progresses. This model also does not consider changes in the ductility of the polymer. The degradation frameworks presented above highlight that a standardised model form for degradation is not yet available. It is notable that, apart from differences in the underlying constitutive description of the virgin material, the underlying assumption(s) of how degradation actually affects material behaviour across these models is vastly different. Computational studies have assumed that degradation only deteriorates elastic response, while others assume that degradation affects only the yield (Qiu *et al.*, 2018), hardening (Vieira *et al.*, 2011) or elongation properties (Luo *et al.*, 2014), with other models have assumed deterioration of combinations of these parameters. While studies provide a certain amount of reasoning for their model form, generally attributing it to the observed experimental behaviour, the physical basis for these differences in model implementation is generally not clear. It would appear that several models happen to be effective in reducing the load-bearing capacity of the device. While this might re-create the observed response of the device under certain loading conditions, the justification of the model form is generally not provided and this may limit their applications in circumstances beyond those for which these models were calibrated.

Table 2.8. Summary of phenomenological degradation models used in the literature to predict the long-term performance of polymeric BRS devices.

BRS Device	Model Description	Model Parameters	Model Inputs	Model Outputs and Comparator for Validation	Refs.
High molecular weight PLLA	<p><b>Neo-Hookean Model</b> where scalar variable <math>d</math>, which represents the degree of degradation on an isotropic hyperelastic solid.</p> $\lambda = \lambda_0(1 - d)$ $\mu = \mu_0(1 - d)$ <p>Phenomenological reasoning, expecting that greater deformation leads to greater degradation</p> $\dot{d} = (1 - d)k(\mathbf{F})$	$\mu$ – shear modulus $d$ – deg. of degradation $k(\mathbf{F})$ – deformation gradient	<p><b>No of model parameters:</b> for Neo-Hookean law derived from time-zero experiments on PLLA filaments. Degradation model defined by one parameter.</p> <p><b>Model input parameters:</b> Not derived from experimental data. Linear degradation process (normalised to time) assumed.</p>	<p><b>Model Outputs:</b> Model used to predictions the recoil behaviour of polymer scaffolds over time.</p> <p><b>Model Comparator:</b> Model outputs are not compared against any experimental data.</p>	(Soares, Moore and Rajagopal, 2008)
PLLA Scaffold	<p>Quasi-linear viscoelastic model;</p> $E(d, t) = E_\infty(1 - \lambda_i d) + \sum_{n=1}^N E_n(1 - \lambda_n d)e^{-\frac{t}{\tau_{Rn}}}$ <p>Rate of degradation increases with an increase in the magnitude of strains and concentration of water, expressed as;</p> $\frac{\delta d}{\delta t} = \frac{1}{\tau_D}(1 - d)f(\varepsilon)g(c)$	$E$ – material /relaxation moduli $\tau_{Rn}$ – relaxation time $\lambda$ – degradation coeff. $\tau_D$ – degradation time $f(\varepsilon) = J_2 - 2^{\text{nd}}$ invariant of dev. strain $g(c) = e^{\beta c} - \beta$ - mat. constant, $c$ - conc. of water	<p><b>No of model parameters:</b> Extensive number of model parameters describing QLV framework. Degradation captured by scalar damage variable; whose function is described by time constant.</p> <p><b>Model input parameters:</b> Not derived from experimental testing.</p>	<p><b>Model Outputs:</b> Model used to predict degradation of viscoelastic polymeric scaffold implanted in an artery. Wet and dry conditions examiner.</p> <p><b>Model Comparator:</b> Model outputs are not compared against any experimental data.</p>	(Muliana and Rajagopal, 2012)
High molecular weight PLLA	<p>A scalar damage variable that is a function of the fracture elongation ratio of the material before and after degradation. Relative degree of deterioration for each was considered by a power function</p> $d(\varepsilon, t) = a(b + c + \varepsilon^n) \times t^m$ <p>Interpolated deformation dependence for 0%, 20% and 40% pre-stretched states.</p>	$d$ – fracture elongation ratio/deg. of degradation $\varepsilon$ – strain $t$ – time $a, b, c, n, m$ – mat. constants	<p><b>No of model parameters:</b> Degradation model described by five material constants, which collective describe the “degree of degradation”.</p> <p><b>Model input parameters:</b> Model inputs derived from uniaxial tensile testing carried out on laser-cut dog-bone specimens with various level of pre-stretch. Samples immersed in PBS over 30 days.</p>	<p><b>Model Outputs:</b> Degradation trends in different locations</p> <p><b>Model Comparator:</b> Predicted radial response of device compared to experimental re-crimping of the device following 10 days, 20 days and 30 days of degradation.</p>	(Luo <i>et al.</i> , 2014)



Absorb PLLA	<p>Elastic-plastic model where a scalar function is used to describe alteration in material yield strength during degradation, according to:</p> $\sigma^Y(t) = \sigma_0^Y(1 - d)$ <p>Implementation of model also allows for strengthening in early phase of degradation.</p>	<p><math>\sigma^Y</math> – yield stress  <math>d</math> – damage parameter</p>	<p><b>No of model parameters:</b>  Degradation model defined by <b>one parameter</b> that alters the material yield strength.</p> <p><b>Model input parameters:</b> Parameters were calibrated based on the experimentally measured radial force response of ABSORB devices following two years degradation testing</p>	<p><b>Model Outputs:</b> Model used to predict device performance in implanted artery during degradation.</p> <p><b>Model Comparator:</b> Model predictions are not compared to other experimental data.</p>	(Qiu <i>et al.</i> , 2018)
High molecular weight PLLA	<p>Same implementation as Luo <i>et al.</i>, whereby fracture elongation ratio of the material before and after degradation. Relative degree of deterioration for each was considered by a power function.</p> $d(\varepsilon, t) = a(b + c + \varepsilon^n) \times t^m$	<p><math>d</math> – fracture elongation ratio/deg. of degradation  <math>\varepsilon</math> – strain  <math>t</math> – time  <math>a, b, c, n, m</math> – mat. constants</p>	<p><b>No of model parameters:</b>  Degradation model described by five material constants, which collective describe the “degree of degradation”.</p> <p><b>Model input parameters:</b> Parameters from Luo <i>et al.</i> used to define degradation behaviour.</p>	<p><b>Model Outputs:</b></p> <p><b>Model Comparator:</b> Model predictions are not compared to other experimental data.</p>	(Lin <i>et al.</i> , 2020)
PLA-PCL fibres	<p>Hyperelastic material model where the damage due to hydrolysis is related to the molecular weight.</p> $\sigma = \sigma_\infty - \frac{B}{M_{n0} e^{-u_m t}}, d_h = 1 - \frac{\sigma}{\sigma_0}$	<p><math>\sigma</math> – fracture strength  <math>\sigma_\infty</math> - fracture strength at infinite molecular weight  <math>B</math> – mat. constant  <math>M_n</math> – number avg. molecular weight  <math>u_m</math> – rate of hydrolysis  <math>d_h</math> – damage due to hydrolysis</p>	<p><b>No. of model parameters:</b>  Degradation model defined by molecular weight loss.</p> <p><b>Model Input parameters:</b> Parameters were calibrated based on experimentally measured uniaxial tensile tests</p>	<p><b>Model Outputs:</b> Model used to predict evolution in uniaxial tensile response.</p> <p><b>Model Comparator:</b> Model predictions are not compared to other experimental data.</p>	(Vieira <i>et al.</i> , 2011)
PLA film	<p>Quasi-linear viscoelastic model to describe the mechanical behaviours evolution of biodegradable polymers during hydrolytic degradation. Damage due to hydrolysis is governed by:</p> $d_h = 1 - \left(1 - K \left(\frac{M_{n0}}{M_n} - 1\right)\right)^n$	<p><math>d_h</math> – damage due to hydrolysis  <math>K</math> – degradation kinetic parameter  <math>M_n</math> – number avg. molecular weight</p>	<p><b>No. of model parameters:</b>  Degradation model defined by molecular weight loss.</p> <p><b>Model Input parameters:</b> Parameters were calibrated based on experimentally measured uniaxial tensile tests performed to 2%, 4% and 6% strain at a rate of 500mm/min</p>	<p><b>Model Outputs:</b> Model used to predict evolution in uniaxial tensile response.</p> <p><b>Model Comparator:</b> Model predictions are not compared to other experimental data.</p>	(Breche <i>et al.</i> , 2016)

PLLA scaffold	<p>To explore the time-dependent mechanical behaviour of the PLA stents, a QLV model was used in which the mechanical load, fluid diffusion and degradation are in direct relation so that increasing the degradation rate is corresponded to increasing of strain rate and diffusion</p> $d^t = d^{t-\Delta t} + \frac{\Delta t}{\tau_D} (1 - d^t) f(\bar{\varepsilon}^t) g(c^t)$	<p>E – material /relaxation moduli  <math>\tau_{Rn}</math> – relaxation time  <math>\lambda</math> – degradation coeff.  <math>\tau_D</math> – degradation time  <math>f(\varepsilon) = J_2 - 2^{\text{nd}}</math> invariant of dev. strain  <math>g(c) = e^{\beta c} - \beta</math> - mat. constant, c - conc. of water</p>	<p><b>No. of model parameters:</b>  Degradation model defined</p> <p><b>Model Input:</b> Parameters were calibrated based on PLA fibres degraded under flow and subjected to uniaxial tensile testing.</p>	<p><b>Model Outputs:</b> Model used to predict recoil for several polymer BRS and localised degree of degradation.</p> <p><b>Model Comparator:</b> Model predictions are not compared to other experimental data.</p>	(Amnieh <i>et al.</i> , 2021)
PLLA scaffold unit	<p>Same implementation as Luo <i>et al</i>, whereby fracture elongation ratio of the material before and after degradation. Relative degree of deterioration for each was considered by a power function.</p> $d(\varepsilon, t) = a(b + c + \varepsilon^n) \times t^m$	<p>d – fracture elongation ratio/deg. of degradation  <math>\varepsilon</math> – strain  t – time  a, b, c, n, m – mat. constants</p>	<p><b>No of model parameters:</b>  Degradation model described by five material constants, which collective describe the “degree of degradation”.</p> <p><b>Model input:</b> Parameters from Luo <i>et al.</i> used to define degradation behaviour</p>	<p><b>Model Outputs:</b> Degradation trends in different locations</p> <p><b>Model Comparator:</b> Model predictions are not compared to other experimental data.</p>	(Dong, Wang and Gu, 2018)

## 2.5. Conclusions

Biodegradable polymers, in particular PLLA, have emerged as the most popular choice for BRS applications. This was due to its excellent biocompatibility and the potential to tailor the mechanical properties through processing techniques. However, the development of polymer-based BRS has suffered significant setbacks over the past number of years and this first-generation of bioresorbable scaffold has essentially failed, with 2-year follow up data from Abbott's ABSORB III device demonstrating increased risk of late-stage adverse events (Ellis, 2020) From a review of the literature, relevant to polymer BRS and device characterisation a number of critical areas of focus to fully understand the issues that have arisen.

- While there have been significant efforts to characterise the performance of polymer BRS, there has been a clear focus on the mechanical performance of the devices. Even the ISO and ASTM standards that set out the requirements of testing, place lesser importance on the underlying mechanisms of degradation that can be determined from physio-chemical. There is a need for more comprehensive experimental characterisation approaches for BRS devices to provide insight into the mechanical, thermal and molecular properties of BRS as degradation progresses.
- Unlike their metallic counterparts, the deployment behaviour of polymeric BRS are highly sensitive to rate-dependent aspects of the procedure. This presents certain complications in the development of computational approaches to predict the short-term deployment and long-term degradation performance of polymer BRS. While various models have been developed to address such aspects, these activities have generally been separate to one another. There is a distinct need to develop a consistent computational framework that can capture both short- and long-term performance of polymer BRS.

- In predicting degradation performance, the experimental literature summarised has demonstrated that behaviour is wide-ranging and highly sensitive to factors such as processing techniques, environmental conditions and/or loading regime. Furthermore, the computational modelling approaches that were summarised highlight that a standardised model form for degradation is not yet available. While certain models to date have been effective in re-creating the observed responses, very few of these models have undergone robust validation, which limits their applicability. There is a distinct need to use robust model comparators to act as an independent evaluation of the model credibility.

By addressing these key aspects, a better understanding of aspects of both short- and long-term performance of polymer-based BRS will be possible, which may provide opportunity to optimise designs and overcome issues that have led to device failures in the past.

## 2.6. References

- Amnieh, Sasan Khalaj, Mohammad Mashayekhi, Ehsan Shahnooshi, Mehdi Tavafoghi, and Peiman Mosaddegh. 2021. “Biodegradable Performance of PLA Stents Affected by Geometrical Parameters : The Risk of Fracture and Fragment Separation.” *Journal of Biomechanics* 122: 110489. <https://doi.org/10.1016/j.jbiomech.2021.110489>.
- Antonini, Luca, Francesca Berti, Benedetta Isella, Dipok Hossain, Lorenzo Mandelli, Giancarlo Pennati, and Lorenza Petrini. 2021. “From the Real Device to the Digital Twin: A Coupled Experimental-Numerical Strategy to Investigate a Novel Bioresorbable Vascular Scaffold.” *Plos One* 16 (6): e0252788. <https://doi.org/10.1371/journal.pone.0252788>.
- Antonini, Luca, Gianluca Poletti, Lorenzo Mandelli, Gabriele Dubini, Giancarlo Pennati, and Lorenza Petrini. 2021. “Comprehensive Computational Analysis of the Crimping Procedure of PLLA BVS : Effects of Material Viscous-Plastic and Temperature Dependent Behavior.” *Journal of the Mechanical Behavior of Biomedical Materials* 123 (April): 104713. <https://doi.org/10.1016/j.jmbbm.2021.104713>.
- ASTM International, Evaluating Corro-, and Corrosion Test-. 2005. “G 46-94 Standard Guide for Examination and Evaluation of Pitting Corrosion” 12 (June 1973): 1–8. <https://doi.org/10.1520/G0046-94R13.2>.
- Barkholt, Trine, Bruce Webber, Niels R. Holm, and John A. Ormiston. 2020. “Mechanical Properties of the Drug-Eluting Bioresorbable Magnesium Scaffold Compared with Polymeric Scaffolds and a Permanent Metallic Drug-Eluting Stent.” *Catheterization and Cardiovascular Interventions* 96 (7): E674–82. <https://doi.org/10.1002/ccd.28545>.
- Bartkowiak-Jowska, Magdalena, Romuald Będziński, Anna Kozłowska, Jarosław Filipiak, and Celina Pezowicz. 2013. “Mechanical, Rheological, Fatigue, and Degradation Behavior of PLLA, PGLA and PDGLA as Materials for Vascular Implants.” *Meccanica* 48 (3): 721–31. <https://doi.org/10.1007/s11012-012-9626-2>.
- Bartkowiak-Jowska, Magdalena, Romuald Bedziński, Barbara Szaraniec, and Jan Chlopek. 2011. “Mechanical, Biological, and Microstructural Properties of Biodegradable Models of Polymeric Stents Made of PLLA and Alginate Fibers.” *Acta of Bioengineering and Biomechanics* 13 (4): 21–28.
- Bobel, A. C., S. Petisco, J. R. Sarasua, W. Wang, and P. E. McHugh. 2015. “Computational Bench Testing to Evaluate the Short-Term Mechanical Performance of a Polymeric Stent.” *Cardiovascular Engineering and Technology* 6 (4): 519–32. <https://doi.org/10.1007/s13239-015-0235-9>.
- Bobel, Anna C., Stefan Lohfeld, Reyhaneh Neghabat Shirazi, and Peter E. McHugh. 2016. “Experimental Mechanical Testing of Poly (L-Lactide) (PLLA) to Facilitate Pre-Degradation Characteristics for Application in Cardiovascular Stenting.” *Polymer Testing* 54: 150–58. <https://doi.org/10.1016/j.polymertesting.2016.07.011>.
- Boland, Enda L., Rosa Shine, Nicola Kelly, Caoimhe A. Sweeney, and Peter E. McHugh. 2016. “A Review of Material Degradation Modelling for the Analysis and Design of Bioabsorbable Stents.” *Annals of Biomedical Engineering* 44 (2): 341–56. <https://doi.org/10.1007/s10439-015-1413-5>.
- Bonin, Mickael, Patrice Guerin, Jean Marc Olive, Fabienne Jordana, and François Huchet. 2018. “Standardized Bench Test Evaluation of Coronary Stents: Biomechanical Characteristics.” *Catheterization and Cardiovascular Interventions* 92 (7): E465–70. <https://doi.org/10.1002/ccd.27912>.
- Breche, Q., G. Chagnon, G. Machado, B. Nottelet, X. Garric, E. Girard, and D. Favier. 2016. “A Non-Linear Viscoelastic Model to Describe the Mechanical Behavior’s Evolution of Biodegradable Polymers during Hydrolytic Degradation.” *Polymer Degradation and Stability* 131: 145–56. <https://doi.org/10.1016/j.polymdegradstab.2016.07.014>.

- Byrne, Robert A, Giulio G Stefanini, Davide Capodanno, Yoshinobu Onuma, Andreas Baumbach, Javier Escaned, Michael Haude, Stefan James, Michael Joner, and Peter Ju. 2018. "Report of an ESC-EAPCI Task Force on the Evaluation and Use of Bioresorbable Scaffolds for Percutaneous Coronary Intervention: Executive Summary." *European Heart Journal* 39 (July): 1591–1601. <https://doi.org/10.4244/EIJ20170912-01>.
- Cai, Hua, Vipul Dave, Richard A. Gross, and Stephen P. McCarthy. 1996. "Effects of Physical Aging, Crystallinity, and Orientation on the Enzymatic Degradation of Poly(Lactic Acid)." *Journal of Polymer Science, Part B: Polymer Physics* 34 (16): 2701–8. [https://doi.org/10.1002/\(SICI\)1099-0488\(19961130\)34:16<2701::AID-POLB2>3.0.CO;2-S](https://doi.org/10.1002/(SICI)1099-0488(19961130)34:16<2701::AID-POLB2>3.0.CO;2-S).
- Callister Jr, William D, and David G Rethwisch. 2020. *Fundamentals of Materials Science and Engineering: An Integrated Approach*. John Wiley & Sons.
- Chausse, Victor, Romain Schieber, Yago Raymond, Brian Ségry, Ramon Sabaté, Kumaran Kolandaivelu, Maria Pau Ginebra, and Marta Pegueroles. 2021. "Solvent-Cast Direct-Writing as a Fabrication Strategy for Radiopaque Stents." *Additive Manufacturing* 48 (PB): 102392. <https://doi.org/10.1016/j.addma.2021.102392>.
- Debusschere, Nic, Patrick Segers, Peter Dubruel, Benedict Verhegghe, and Matthieu De Beule. 2015. "A Finite Element Strategy to Investigate the Free Expansion Behaviour of a Biodegradable Polymeric Stent." *Journal of Biomechanics* 48 (10): 2012–18. <https://doi.org/10.1016/j.jbiomech.2015.03.024>.
- Deroiné, Morgan, Antoine Le Duigou, Yves Marie Corre, Pierre Yves Le Gac, Peter Davies, Guy César, and Stéphane Bruzaud. 2014. "Accelerated Ageing of Polylactide in Aqueous Environments: Comparative Study between Distilled Water and Seawater." *Polymer Degradation and Stability* 108: 319–29. <https://doi.org/10.1016/j.polymdegradstab.2014.01.020>.
- Dillon, Brian, Patrick Doran, Evert Fuenmayor, Andrew V. Healy, Noel M. Gately, Ian Major, and John G. Lyons. 2019. "Influence of Annealing and Biaxial Expansion on the Properties of Poly(L-Lactic Acid) Medical Tubing." *Polymers* 11 (7). <https://doi.org/10.3390/polym11071172>.
- Dong, Pengfei, Longzhen Wang, and Linxia Gu. 2018. "Degradation Modeling Of Bioabsorbable Polymer Stent." *IMECE2018*.
- Donik, B. Nečemer, S. Glodež, and J. Kramberger. 2022. "Finite Element Analysis of the Mechanical Performance of a Two-Layer Polymer Composite Stent Structure." *Engineering Failure Analysis* 137 (December 2021). <https://doi.org/10.1016/j.engfailanal.2022.106267>.
- Dreher, Maureen L., Srinidhi Nagaraja, and Benjamin Batchelor. 2016. "Effects of Fatigue on the Chemical and Mechanical Degradation of Model Stent Sub-Units." *Journal of the Mechanical Behavior of Biomedical Materials* 59: 139–45. <https://doi.org/10.1016/j.jmbbm.2015.12.020>.
- Duek, E. A.R., C. A.C. Zavaglia, and W. D. Belangero. 1999. "In Vitro Study of Poly(Lactic Acid) Pin Degradation." *Polymer* 40 (23): 6465–73. [https://doi.org/10.1016/S0032-3861\(98\)00846-5](https://doi.org/10.1016/S0032-3861(98)00846-5).
- Ellis, Stephen G. 2020. "A Clinical Evaluation of Absorb<sup>TM</sup> BVS, the Everolimus Eluting Bioresorbable Vascular Scaffold in the Treatment of Subjects With de Novo Native Coronary Artery Lesions." National Library of Medicine (USA). 2020. <https://clinicaltrials.gov/ct2/show/study/NCT01751906>.
- Farah, Shady, Daniel G. Anderson, and Robert Langer. 2016. "Physical and Mechanical Properties of PLA, and Their Functions in Widespread Applications — A Comprehensive Review." *Advanced Drug Delivery Reviews* 107: 367–92. <https://doi.org/10.1016/j.addr.2016.06.012>.
- Farrar, D F, and R K Gillson. 2002. "Hydrolytic Degradation of Polyglyconate B: The Relationship between Degradation Time, Strength and Molecular Weight." *Biomaterials* 23: 3905–12.
- FDA. 2010. "Guidance Document for Industry and FDA Staff Non-Clinical Engineering Tests and Recommended Labeling for Intravascular Stents and Associated Delivery Systems and Human Services Food and Drug Administration Center for Devices and Radiological Health Interv." *US Department of*

*Health and Human Services; Food and Drug Administration, Centre for Devices and Radiological Health*, 18–20.  
<http://www.fda.gov/MedicalDevices/DeviceRegulationandGuidance/GuidanceDocuments/ucm0>.

Ferdous, Jahid, Vijaya B Kolachalama, and Tarek Shazly. 2013. “Impact of Polymer Structure and Composition on Fully Resorbable Endovascular Scaffold Performance.” *Acta Biomaterialia* 9 (4): 6052–61. <https://doi.org/10.1016/j.actbio.2012.12.011>.

Filipovic, Nenad, Dalibor Nikolic, Velibor Isailovic, Miljan Milosevic, Vladimir Geroski, Georgia Karanasiou, Martin Fawdry, Aiden Flanagan, Dimitrios Fotiadis, and Milos Kojic. 2021. “In Vitro and in Silico Testing of Partially and Fully Bioresorbable Vascular Scaffold.” *Journal of Biomechanics* 115: 110158. <https://doi.org/10.1016/j.jbiomech.2020.110158>.

Garlotta, Donald. 2001. “A Literature Review of Poly ( Lactic Acid ).” *Journal of Polymers and the Environment* 9 (2): 63–84.

Gleadall, Andrew, Jingzhe Pan, Marc Anton Krufft, and Minna Kellomäki. 2014. “Degradation Mechanisms of Bioresorbable Polyesters. Part 1. Effects of Random Scission, End Scission and Autocatalysis.” *Acta Biomaterialia* 10 (5): 2223–32. <https://doi.org/10.1016/j.actbio.2013.12.039>.

Grabow, Niels, Carsten M. Bünger, Christine Schultze, Kathleen Schmohl, David P. Martin, Simon F. Williams, Katrin Sternberg, and Klaus Peter Schmitz. 2007. “A Biodegradable Slotted Tube Stent Based on Poly(L-Lactide) and Poly(4-Hydroxybutyrate) for Rapid Balloon-Expansion.” *Annals of Biomedical Engineering* 35 (12): 2031–38. <https://doi.org/10.1007/s10439-007-9376-9>.

Grabow, Niels, Carsten M. Bünger, Katrin Steinberg, Steffen Mews, Kathleen Schmohl, and Klaus Peter Schmitz. 2007. “Mechanical Properties of a Biodegradable Balloon-Expandable Stent from Poly(L-Lactide) for Peripheral Vascular Applications.” *Journal of Medical Devices, Transactions of the ASME* 1 (1): 84–88. <https://doi.org/10.1115/1.2355683>.

Grasso, Marzio, Lyes Azzouz, Paula Ruiz-Hincapie, Mauro Zarrelli, and Guogang Ren. 2018. “Effect of Temperature on the Mechanical Properties of 3D-Printed PLA Tensile Specimens.” *Rapid Prototyping Journal* 24 (8): 1337–46. <https://doi.org/10.1108/RPJ-04-2017-0055>.

Guerra, Antonio Jesús, and Joaquim Ciurana. 2017. “Effect of Fibre Laser Process on In-Vitro Degradation Rate of a Polycaprolactone Stent a Novel Degradation Study Method.” *Polymer Degradation and Stability* 142: 42–49. <https://doi.org/10.1016/j.polymdegradstab.2017.05.028>.

Hasanpur, Ehsan, Akbar Ghazavizadeh, Alireza Sadeghi, and Mohamed Haboussi. 2021. “In Vitro Corrosion Study of PLA/Mg Composites for Cardiovascular Stent Applications.” *Journal of the Mechanical Behavior of Biomedical Materials* 124 (August): 104768. <https://doi.org/10.1016/j.jmbbm.2021.104768>.

Hoddy, Ben, Naveed Ahmed, Kadem Al-lamee, Nial Bullett, and Neil W. Bressloff. 2022. “Exploring a Parallel Rheological Framework to Capture the Mechanical Behaviour of a Thin-Strut Polymeric Bioresorbable Coronary Scaffold.” *Journal of the Mechanical Behavior of Biomedical Materials* 130 (December 2021): 105154. <https://doi.org/10.1016/j.jmbbm.2022.105154>.

Hoddy, Ben, Naveed Ahmed, Kadem Al-Lamee, Nial Bullett, Nick Curzen, and Neil W. Bressloff. 2021. “Investigating the Material Modelling of a Polymeric Bioresorbable Scaffold via In-Silico and in-Vitro Testing.” *Journal of the Mechanical Behavior of Biomedical Materials* 120 (February): 104557. <https://doi.org/10.1016/j.jmbbm.2021.104557>.

Katarzyna, Polak-Krasna, Ali Reza Abaei, Reyhaneh Neghabat Shirazi, Eoin Parle, Oliver Carroll, William Ronan, and Ted J Vaughan. 2021. “Physical and Mechanical Degradation Behaviour of Semi-Crystalline PLLA for Bioresorbable Stent Applications.” *Journal of the Mechanical Behaviour of Biomedical Materials*, 135938. <https://doi.org/10.1016/j.jmbbm.2021.104409>.

Kereiakes, Dean J., Stephen G. Ellis, Christopher Metzger, Ronald P. Caputo, David G. Rizik, Paul S.

Teirstein, Marc R. Litt, et al. 2017. “3-Year Clinical Outcomes With Everolimus-Eluting Bioresorbable Coronary Scaffolds: The ABSORB III Trial.” *Journal of the American College of Cardiology* 70 (23): 2852–62. <https://doi.org/10.1016/j.jacc.2017.10.010>.

Khalaj Amnieh, Sasan, Peiman Mosaddegh, Mohammad Mashayekhi, and Mahshid Kharaziha. 2021. “Biodegradation Evaluation of Poly (Lactic Acid) for Stent Application: Role of Mechanical Tension and Temperature.” *Journal of Applied Polymer Science* 138 (19). <https://doi.org/10.1002/app.50389>.

Kimble, Lloyd Dylan, and Debes Bhattacharyya. 2015. “In Vitro Degradation Effects on Strength, Stiffness, and Creep of PLLA/PBS: A Potential Stent Material.” *International Journal of Polymeric Materials and Polymeric Biomaterials* 64 (6): 299–310. <https://doi.org/10.1080/00914037.2014.945203>.

Lee, Chi H., Anuj Singla, and Yugyung Lee. 2001. “Biomedical Applications of Collagen.” *International Journal of Pharmaceutics* 221 (1–2): 1–22. [https://doi.org/10.1016/S0378-5173\(01\)00691-3](https://doi.org/10.1016/S0378-5173(01)00691-3).

Leenslag, Jan W, Albert J Pennings, Ruud R M Bos, Fred R Rozema, and Geert Boering. 1987. “Resorbable Materials of Poly(l-Lactide). VI. Plates and Screws for Internal Fracture Fixation.” *Biomaterials*. 8 (1): 70–73.

Li, Ying, Zhaowei Chu, Xiaoming Li, Xili Ding, Meng Guo, Haoran Zhao, Jie Yao, Lizhen Wang, Qiang Cai, and Yubo Fan. 2017. “The Effect of Mechanical Loads on the Degradation of Aliphatic Biodegradable Polyesters.” *Regenerative Biomaterials* 4 (3): 179–90. <https://doi.org/10.1093/rb/rbx009>.

Lim, L. T., R. Auras, and M. Rubino. 2008. “Processing Technologies for Poly(Lactic Acid).” *Progress in Polymer Science (Oxford)* 33 (8): 820–52. <https://doi.org/10.1016/j.progpolymsci.2008.05.004>.

Lin, Shengmao, Pengfei Dong, Changchun Zhou, Luis Augusto P. Dallan, Vladislav N. Zimin, Gabriel T.R. Pereira, Juhwan Lee, et al. 2020. “Degradation Modeling of Poly-L-Lactide Acid (PLLA) Bioresorbable Vascular Scaffold within a Coronary Artery.” *Nanotechnology Reviews* 9 (1): 1217–26. <https://doi.org/10.1515/ntrev-2020-0093>.

Liu, Guoming, Xiuqin Zhang, and Dujin Wang. 2014. “Tailoring Crystallization: Towards High-Performance Poly (Lactic Acid).” *Advanced Materials* 26 (40): 6905–11. <https://doi.org/10.1002/adma.201305413>.

Lizundia, Erlantz, Susana Petisco, and Jose Ramon Sarasua. 2013. “Phase-Structure and Mechanical Properties of Isothermally Melt-and Cold-Crystallized Poly (L-Lactide).” *Journal of the Mechanical Behavior of Biomedical Materials* 17: 242–51. <https://doi.org/10.1016/j.jmbbm.2012.09.006>.

Luo, Qiyi, Xiangkun Liu, Zhonghua Li, Chubo Huang, Wen Zhang, Juan Meng, Zhaohua Chang, and Zezhao Hua. 2014. “Degradation Model of Bioabsorbable Cardiovascular Stents.” *PLoS ONE* 9 (11): 1–9. <https://doi.org/10.1371/journal.pone.0110278>.

Mainil-Varlet, Pierre, Raymond Curtis, and Sylwester Gogolewski. 1997. “Effect of in Vivo and in Vitro Degradation on Molecular and Mechanical Properties of Various Low-Molecular-Weight Polylactides.” *Journal of Biomedical Materials Research* 36 (3): 360–80. [https://doi.org/10.1002/\(SICI\)1097-4636\(19970905\)36:3<360::AID-JBM11>3.0.CO;2-I](https://doi.org/10.1002/(SICI)1097-4636(19970905)36:3<360::AID-JBM11>3.0.CO;2-I).

Maleckis, Kaspars, Paul Deegan, William Poulson, Cole Sievers, Anastasia Desyatova, Jason MacTaggart, and Alexey Kamenskiy. 2017. “Comparison of Femoropopliteal Artery Stents under Axial and Radial Compression, Axial Tension, Bending, and Torsion Deformations.” *Journal of the Mechanical Behavior of Biomedical Materials* 75 (March): 160–68. <https://doi.org/10.1016/j.jmbbm.2017.07.017>.

McKenna, Ciara G., and Ted J. Vaughan. 2020. “An Experimental Evaluation of the Mechanics of Bare and Polymer-Covered Self-Expanding Wire Braided Stents.” *Journal of the Mechanical Behavior of*



- Biomedical Materials* 103 (October 2019): 103549. <https://doi.org/10.1016/j.jmbbm.2019.103549>.
- McMahon, Sean, Nicky Bertollo, Eoin D.O' Cearbhaill, Jochen Salber, Luca Pierucci, Patrick Duffy, Thomas Dürig, Vivian Bi, and Wenxin Wang. 2018. "Bio-Resorbable Polymer Stents: A Review of Material Progress and Prospects." *Progress in Polymer Science* 83: 79–96. <https://doi.org/10.1016/j.progpolymsci.2018.05.002>.
- Milosevic, Miljan, Milos Anic, Dalibor Nikolic, Vladimir Geroski, Bogdan Milicevic, Milos Kojic, and Nenad Filipovic. 2021. "Application of in Silico Platform for the Development and Optimization of Fully Bioresorbable Vascular Scaffold Designs." *Frontiers in Medical Technology* 3 (October): 1–13. <https://doi.org/10.3389/fmedt.2021.724062>.
- Moetazedian, Amirpasha, Andrew Gleadall, Xiaoxiao Han, and Vadim V. Silberschmidt. 2020. "Effect of Environment on Mechanical Properties of 3D Printed Polylactide for Biomedical Applications." *Journal of the Mechanical Behavior of Biomedical Materials* 102 (August 2019): 103510. <https://doi.org/10.1016/j.jmbbm.2019.103510>.
- Muliana, Anastasia, and K R Rajagopal. 2012. "Modeling the Response of Nonlinear Viscoelastic Biodegradable Polymeric Stents." *International Journal of Solids and Structures* 49 (7–8): 989–1000. <https://doi.org/10.1016/j.ijsolstr.2011.12.007>.
- Naseem, Raasti, Ligu Zhao, Senthil K. Eswaran, and Helen Willcock. 2020. "Characterization of Biodegradable Poly(L-Lactide) Tube over Accelerated Degradation." *Polymer Engineering and Science* 60 (7): 1430–36. <https://doi.org/10.1002/pen.25390>.
- Naseem, Raasti, Ligu Zhao, Vadim Silberschmidt, Yang Liu, Ollie Scaife, Helen Willcock, Senthil Eswaran, and Syed Hossainy. 2019. "Mechanical and Chemical Characterisation of Bioresorbable Polymeric Stent over Two-Year in Vitro Degradation." *Journal of Biomaterials Applications* 34 (1): 61–73. <https://doi.org/10.1177/0885328219839591>.
- Nunes, Ronald W., John R. Martin, and Julian F. Johnson. 1982. "Mechanical Properties of Polymers: The Influence of Molecular Weight and Molecular Weight Distribution." *Polymer Engineering and Science* 22 (4): 205–28. <https://doi.org/10.1080/15321797208068169>.
- Nuutinen, Juha Pekka, Claude Clerc, Raija Reinikainen, and Pertti Törmälä. 2003. "Mechanical Properties and in Vitro Degradation of Bioabsorbable Self-Expanding Braided Stents." *Journal of Biomaterials Science, Polymer Edition* 14 (3): 255–66. <https://doi.org/10.1163/156856203763572707>.
- Oosterbeek, Reece N., Kyung Ah Kwon, Patrick Duffy, Sean McMahon, Xiang C. Zhang, Serena M. Best, and Ruth E. Cameron. 2019. "Tuning Structural Relaxations, Mechanical Properties, and Degradation Timescale of PLLA during Hydrolytic Degradation by Blending with PLCL-PEG." *Polymer Degradation and Stability* 170: 109015. <https://doi.org/10.1016/j.polymdegradstab.2019.109015>.
- Ormiston, John A., Bruce Webber, Ben Ubod, Olivier Darremont, and Mark W.I. Webster. 2015. "An Independent Bench Comparison of Two Bioresorbable Drug-Eluting Coronary Scaffolds (Absorb and DESolve) with a Durable Metallic Drug-Eluting Stent (ML8/Xpedition)." *EuroIntervention* 11 (1): 60–67. [https://doi.org/10.4244/EIJY15M02\\_03](https://doi.org/10.4244/EIJY15M02_03).
- Pan, Pengju, Bo Zhu, and Yoshio Inoue. 2007. "Enthalpy Relaxation and Embrittlement of Poly(L-Lactide) during Physical Aging." *Macromolecules* 40 (26): 9664–71. <https://doi.org/10.1021/ma071777c>.
- Pauck, R. G., and B. D. Reddy. 2015. "Computational Analysis of the Radial Mechanical Performance of PLLA Coronary Artery Stents." *Medical Engineering and Physics* 37 (1): 7–12. <https://doi.org/10.1016/j.medengphy.2014.09.014>.
- Perego, Gabriele, Gian Domenico Cella, and Catia Bastioli. 1996. "Effect of Molecular Weight and Crystallinity on Poly(Lactic Acid) Mechanical Properties." *Journal of Applied Polymer Science* 59 (1):

37–43. [https://doi.org/10.1002/\(sici\)1097-4628\(19960103\)59:1<37::aid-app6>3.0.co;2-n](https://doi.org/10.1002/(sici)1097-4628(19960103)59:1<37::aid-app6>3.0.co;2-n).

Peterlin, A. 1971. “Molecular Model of Drawing Polyethylene and Polypropylene.” *Journal of Materials Science* 6 (6): 490–508. <https://doi.org/10.1007/BF00550305>.

Prabhu, Santosh, and Hossainy Syed. 2006. “Modeling of Degradation and Drug Release from a Biodegradable Stent Coating.” *Journal of Biomedical Materials Research Part A* 79 (4): 963–73. <https://doi.org/10.1002/jbm.a.31053>.

Qiu, T., R. He, C. Abunassar, S. Hossainy, and L. G. Zhao. 2018. “Effect of Two-Year Degradation on Mechanical Interaction between a Bioresorbable Scaffold and Blood Vessel.” *Journal of the Mechanical Behavior of Biomedical Materials* 78 (November 2017): 254–65. <https://doi.org/10.1016/j.jmbbm.2017.11.031>.

Qiu, T. Y., M. Song, and L. G. Zhao. 2018. “A Computational Study of Crimping and Expansion of Bioresorbable Polymeric Stents.” *Mechanics of Time-Dependent Materials* 22 (2): 273–90. <https://doi.org/10.1007/s11043-017-9371-y>.

Qiu, T. Y., L. G. Zhao, and M. Song. 2019. “A Computational Study of Mechanical Performance of Bioresorbable Polymeric Stents with Design Variations.” *Cardiovascular Engineering and Technology* 10 (1): 46–60. <https://doi.org/10.1007/s13239-018-00397-9>.

Ramachandran, Karthik, Tiziana Di Luccio, Artemis Ailianou, Mary Beth Kossuth, James P. Oberhauser, and Julia A. Kornfield. 2018. “Crimping-Induced Structural Gradients Explain the Lasting Strength of Poly L-Lactide Bioresorbable Vascular Scaffolds during Hydrolysis.” *Proceedings of the National Academy of Sciences of the United States of America* 115 (41): 10239–44. <https://doi.org/10.1073/pnas.1807347115>.

Reinoso, Mariana Rodriguez, Marco Civera, Vito Burgio, Annalisa Chiappone, Oliver Grimaldo Ruiz, Alessandra D’anna, Carmela Riccio, et al. 2021. “Effects of the Manufacturing Methods on the Mechanical Properties of a Medical-Grade Copolymer Poly(L-Lactide-Co-d,l-Lactide) and Poly(l-Lactide-Co-ε-Caprolactone) Blend.” *Materials* 14 (21). <https://doi.org/10.3390/ma14216381>.

Renouf-Glauser, Annette C., John Rose, David F. Farrar, and Ruth Elizabeth Cameron. 2005. “The Effect of Crystallinity on the Deformation Mechanism and Bulk Mechanical Properties of PLLA.” *Biomaterials* 26 (29): 5771–82. <https://doi.org/10.1016/j.biomaterials.2005.03.002>.

Saha, Swapan Kumar, and Hideto Tsuji. 2006. “Effects of Molecular Weight and Small Amounts of D-Lactide Units on Hydrolytic Degradation of Poly(l-Lactic Acid)S.” *Polymer Degradation and Stability* 91 (8): 1665–73. <https://doi.org/10.1016/j.polyimdegradstab.2005.12.009>.

Schiavone, A, C Abunassar, S Hossainy, and L G Zhao. 2016. “Computational Analysis of Mechanical Stress – Strain Interaction of a Bioresorbable Scaffold with Blood Vessel.” *Journal of Biomechanics* 49 (13): 2677–83. <https://doi.org/10.1016/j.jbiomech.2016.05.035>.

Schiavone, Alessandro, Tian-Yang Qiu, and Li-Guo Zhao. 2017. “Crimping and Deployment of Metallic and Polymeric Stents -- Finite Element Modelling.” *Vessel Plus* 1 (1): 12–21. <https://doi.org/10.20517/2574-1209.2016.03>.

Schmidt, Christine E., and Jennie M. Baier. 2000. “Acellular Vascular Tissues: Natural Biomaterials for Tissue Repair and Tissue Engineering.” *Biomaterials* 21 (22): 2215–31. [https://doi.org/10.1016/S0142-9612\(00\)00148-4](https://doi.org/10.1016/S0142-9612(00)00148-4).

Schmidt, Wolfram, Peter Behrens, Christoph Brandt-Wunderlich, Stefan Siewert, Niels Grabow, and Klaus Peter Schmitz. 2016. “In Vitro Performance Investigation of Bioresorbable Scaffolds – Standard Tests for Vascular Stents and Beyond.” *Cardiovascular Revascularization Medicine* 17 (6): 375–83. <https://doi.org/10.1016/j.carrev.2016.05.001>.

Schmidt, Wolfram, P. Lanzer, P. Behrens, L. D.T. Topoleski, and K. P. Schmitz. 2009. “A Comparison of the Mechanical Performance Characteristics of Seven Drug-Eluting Stent Systems.” *Catheterization*

and *Cardiovascular Interventions* 73 (3): 350–60. <https://doi.org/10.1002/ccd.21832>.

Shazly, Tarek, Vijaya B. Kilachalama, Jahid Ferdous, James P. Oberhauser, Syed Hossainy, and Elazer R. Edelman. 2012. “Assessment of Material By-Product Fate from Bioresorbable Vascular Scaffolds.” *Annals of Biomedical Engineering* 40 (4): 955–65. <https://doi.org/10.1007/s10439-011-0445-8>. Assessment.

Shine, Connor J, Peter E Mchugh, and William Ronan. 2021. “Impact of Degradation and Material Crystallinity on the Mechanical Performance of a Bioresorbable Polymeric Stent.” *J Elast.* <https://doi.org/10.1007/s10659-021-09835-7>.

Shine, Conor. 2020. “Computational Modelling of the Degradation of Poly L Lactide for a Bioresorbable Polymeric Stent.”

Shine, Rosa, Reyhaneh Neghabat Shirazi, William Ronan, Caoimhe A. Sweeney, Nicola Kelly, Yury A. Rochev, and Peter E. McHugh. 2017. “Modeling of Biodegradable Polyesters With Applications to Coronary Stents.” *Journal of Medical Devices* 11 (2): 021007. <https://doi.org/10.1115/1.4035723>.

Soares, João S., James E. Moore, and Kumbakonam R. Rajagopal. 2008. “Constitutive Framework for Biodegradable Polymers with Applications to Biodegradable Stents.” *ASAIO*, 295–301. <https://doi.org/10.1097/MAT.0b013e31816ba55a>.

———. 2010. “Modeling of Deformation-Accelerated Breakdown of Polylactic Acid Biodegradable Stents.” *Journal of Medical Devices, Transactions of the ASME* 4 (4). <https://doi.org/10.1115/1.4002759>.

Song, Richard, Maxwell Murphy, Chenshuang Li, Kang Ting, Chia Soo, and Zhong Zheng. 2018. “Current Development of Biodegradable Polymeric Materials for Biomedical Applications.” *Drug Design, Development and Therapy* 12: 3117–45. <https://doi.org/10.2147/DDDT.S165440>.

Suuronen, Riitta, Timo Pohjonen, Jarkko Hietanen, and Christian Lindqvist. 1998. “A 5-Year in Vitro and in Vivo Study of the Biodegradation of Polylactide Plates.” *Journal of Oral and Maxillofacial Surgery* 56 (5): 604–14. [https://doi.org/10.1016/S0278-2391\(98\)90461-X](https://doi.org/10.1016/S0278-2391(98)90461-X).

Tábi, T., I. E. Sajó, F. Szabó, A. S. Luyt, and J. G. Kovács. 2010. “Crystalline Structure of Annealed Polylactic Acid and Its Relation to Processing.” *Express Polymer Letters* 4 (10): 659–68. <https://doi.org/10.3144/expresspolymlett.2010.80>.

Tan, L.P., Subu S. Vebkatraman, J.F.D. Joso, and Freddy Y.C. Boey. 2005. “Collapse Pressures of Bilayered Biodegradable Stents.” *Journal of Biomedical Materials Research. Part B, Applied Biomaterials* 83 (2): 340–44. <https://doi.org/10.1002/jbmb>.

Timmins, Lucas H, Matthew W Miller, Fred J Clubb Jr, and James E Moore Jr. 2011. “Increased Artery Wall Stress Post-Stenting Leads to Greater Intimal Thickening.” *Laboratory Investigation* 91 (November 2010): 955–67. <https://doi.org/10.1038/labinvest.2011.57>.

Tsuji, Hideto, and Yoshito Ikada. 1995. “Properties and Morphologies of Poly(l-Lactide): 1. Annealing Condition Effects on Properties and Morphologies of Poly(l-Lactide).” *Polymer* 36 (14): 2709–16. [https://doi.org/10.1016/0032-3861\(95\)93647-5](https://doi.org/10.1016/0032-3861(95)93647-5).

Tsuji, Hideto, and Yoshito Ikada. 2000. “Properties and Morphology of Poly(L-Lactide) 4. Effects of Structural Parameters on Long-Term Hydrolysis of Poly(L-Lactide) in Phosphate-Buffered Solution.” *Polymer Degradation and Stability* 67 (1): 179–89. [https://doi.org/10.1016/S0141-3910\(99\)00111-1](https://doi.org/10.1016/S0141-3910(99)00111-1).

Tsuji, Hideto, Akira Mizuno, and Yoshito Ikada. 2000. “Properties and Morphology of Poly(L-Lactide). III. Effects of Initial Crystallinity on Long-Term In Vitro Hydrolysis of High Molecular Weight Poly(L-Lactide) Film in Phosphate-Buffered Solution.” *Journal of Applied Polymer Science* 77 (7): 1452–64. [https://doi.org/10.1002/1097-4628\(20000815\)77:7<1452::AID-APP7>3.0.CO;2-S](https://doi.org/10.1002/1097-4628(20000815)77:7<1452::AID-APP7>3.0.CO;2-S).

Tsuji, Hideto, Rumiko Okino, Hiroyuki Daimon, and Koichi Fujie. 2006. “Water Vapor Permeability

of Poly(Lactide)s: Effects of Molecular Characteristics and Crystallinity.” *Journal of Applied Polymer Science* 99 (5): 2245–52. <https://doi.org/10.1002/app.22698>.

Venkatraman, Subbu, Tan Lay Poh, Tjong Vinalia, Koon Hou Mak, and Freddy Boey. 2003. “Collapse Pressures of Biodegradable Stents.” *Biomaterials* 24 (12): 2105–11. [https://doi.org/10.1016/S0142-9612\(02\)00640-3](https://doi.org/10.1016/S0142-9612(02)00640-3).

Viceconti, Marco, Miguel A. Juárez, Cristina Curreli, Marzio Pennisi, Giulia Russo, and Francesco Pappalardo. 2019. “Credibility of in Silico Trial Technologies - A Theoretical Framing.” *IEEE Journal of Biomedical and Health Informatics* 24 (1): 4–13.

Vieira, A. C., J. C. Vieira, J. M. Ferra, F. D. Magalhães, R. M. Guedes, and A. T. Marques. 2011. “Mechanical Study of PLA-PCL Fibers during in Vitro Degradation.” *Journal of the Mechanical Behavior of Biomedical Materials* 4 (3): 451–60. <https://doi.org/10.1016/j.jmbbm.2010.12.006>.

Wang, Cong Er, and Pei Hua Zhang. 2016. “In Vitro Degradation Behaviours of PDO Monofilament and Its Intravascular Stents with Braided Structure.” *Autex Research Journal* 16 (2): 80–89. <https://doi.org/10.1515/aut-2015-0031>.

Wang, Pei-jiang, Francesca Berti, Luca Antonini, Farhad Rikhtegar Nezami, Lorenza Petrini, Francesco Migliavacca, and Elazer R. Edelman. 2020. “Multimodal Loading Environment Predicts Bioresorbable Vascular Scaffolds’ Durability.” *Annals of Biomedical Engineering*.

Wang, Pei-jiang, Farhad Rikhtegar, Maysam B Gorji, Francesca Berti, Lorenza Petrini, Tomasz Wierzbicki, Francesco Migliavacca, and Elazer R Edelman. 2018. “Effect of Working Environment and Procedural Strategies on Mechanical Performance of Bioresorbable Vascular Scaffolds.” *Acta Biomaterialia* 82: 34–43. <https://doi.org/10.1016/j.actbio.2018.10.020>.

Wang, Pei Jiang, Nicola Ferralis, Claire Conway, Jeffrey C. Grossman, and Elazer R. Edelman. 2018. “Strain-Induced Accelerated Asymmetric Spatial Degradation of Polymeric Vascular Scaffolds.” *Proceedings of the National Academy of Sciences of the United States of America* 115 (11): 2640–45. <https://doi.org/10.1073/pnas.1716420115>.

Wang, Qian, Gang Fang, Yinghong Zhao, Guohui Wang, and Tao Cai. 2017. “Computational and Experimental Investigation into Mechanical Performances of Poly-L-Lactide Acid (PLLA) Coronary Stents.” *Journal of the Mechanical Behavior of Biomedical Materials* 65: 415–27. <https://doi.org/10.1016/j.jmbbm.2016.08.033>.

Wang, Ying, Jingzhe Pan, Xiaoxiao Han, Csaba Sinka, and Lifeng Ding. 2008. “A Phenomenological Model for the Degradation of Biodegradable Polymers.” *Biomaterials* 29: 3393–3401. <https://doi.org/10.1016/j.biomaterials.2008.04.042>.

Weir, N. A., F. J. Buchanan, J. F. Orr, and G. R. Dickson. 2004. “Degradation of Poly-L-Lactide. Part 1: In Vitro and in Vivo Physiological Temperature Degradation.” *Proceedings of the Institution of Mechanical Engineers, Part H: Journal of Engineering in Medicine* 218 (5): 307–19. <https://doi.org/10.1243/0954411041932782>.

Weir, N A, F J Buchanan, J F Orr, D F Farrar, and G R Dickson. 2004. “Degradation of Poly-L-Lactide. Part 2: Increased Temperature Accelerated Degradation.” *Proceedings of the Institution of Mechanical Engineers, Part H: Journal of Engineering in Medicine* 218 (5): 321–30. <https://doi.org/10.1243/0954411041932809>.

Welch, Tré R., Robert C. Eberhart, and Cheng Jen Chuong. 2009. “The Influence of Thermal Treatment on the Mechanical Characteristics of a PLLA Coiled Stent.” *Journal of Biomedical Materials Research - Part B Applied Biomaterials* 90 B (1): 302–11. <https://doi.org/10.1002/jbm.b.31286>.

Welch, Tre R., Alan W. Nugent, and Surendranath R. Veeram Reddy. 2019. “Biodegradable Stents for Congenital Heart Disease.” *Interventional Cardiology Clinics* 8 (1): 81–94. <https://doi.org/10.1016/j.iccl.2018.08.009>.

---

Xie, Yu Ying, Jong Soon Park, and Soon Kook Kang. 2016. "Studies on the Effect of Molecular Weight on Biodegradable Polymer Membrane." *International Journal of Bio-Science and Bio-Technology* 8 (3): 315–22. <https://doi.org/10.14257/ijbsbt.2016.8.3.32>.

Yew, G. H., A. M. Mohd Yusof, Z. A. Mohd Ishak, and U. S. Ishiaku. 2005. "Water Absorption and Enzymatic Degradation of Poly(Lactic Acid)/Rice Starch Composites." *Polymer Degradation and Stability* 90 (3): 488–500. <https://doi.org/10.1016/j.polymdegradstab.2005.04.006>.

Zilberman, Meital, Kevin D. Nelson, and Robert C. Eberhart. 2005. "Mechanical Properties and in Vitro Degradation of Bioresorbable Fibers and Expandable Fiber-Based Stents." *Journal of Biomedical Materials Research - Part B Applied Biomaterials* 74 (2): 792–99. <https://doi.org/10.1002/jbm.b.30319>.

# Chapter 3

## Theory

---

This chapter provides a theoretical background for the simulations and constitutive material models used in this thesis. The theoretical framework, deformation kinematics and governing equations for these problems are introduced in Section 3.1. The relevant material constitutive models and background are covered in Section 3.2. The finite element method implemented through the commercially available Abaqus CAE (DS Simulia, RI, USA) code is introduced in Section 3.3.

### 3.1 Continuum Mechanics

#### 3.1.1 Notation

Throughout this chapter, capital letters are used to denote tensors and matrices, while lower case letters denote vectors. Bold typeface denotes tensors, vectors and matrices, while components are denoted in italics. The outline of continuum mechanics is given in the context of a Cartesian coordinate system, resulting in the following set of basis vectors:  $e_1 = (1, 0, 0)$ ,  $e_2 = (0, 1, 0)$  and  $e_3 = (0, 0, 1)$ . Index notation is often used to simplify vector equations where summations are implied through a repeated index. An example of this is the dot product between two vectors ( $\mathbf{u}$ ,  $\mathbf{v}$ ) in three dimensional space, given by,

$$\mathbf{uv} = u_i v_i = \sum_{i=1}^3 u_i v_i = u_1 v_1 + u_2 v_2 + u_3 v_3 \quad (3-1)$$

In the case of a  $3 \times 3$  tensor, the location of each component is given by two subscripts,  $i$  and  $j$ , which indicate its position within the tensor. Component  $A_{ij}$  is the value located in the  $i^{\text{th}}$  row and  $j^{\text{th}}$  column of the second order tensor  $A$ .

### 3.1.2 Deformation and Motion

Figure 3.17 below shows the schematic of an arbitrary undeformed continuum body in space occupying the reference configuration ( $B_R$ ), at time  $t_0$  undergoing a kinematic deformation ( $\chi$ ) to the deformed or current configuration ( $B_C$ ) at time  $t_t$ . An infinitesimal ‘fibre’ is described by  $d\mathbf{X}$  in the reference configuration and by  $d\mathbf{x}$  in the current configuration. The motion from  $B_R$  to  $B_C$  is described by the deformation gradient tensor  $\mathbf{F}$ , where,

$$\mathbf{F} = \frac{\partial \mathbf{x}}{\partial \mathbf{X}} \text{ or } F_{ij} = \frac{\partial x_i}{\partial X_j} \quad (3-2)$$

The determinant of the deformation gradient is the Jacobian ( $J$ ), which denotes the ratio of volume change from the reference/undeformed to the current/deformed configurations.

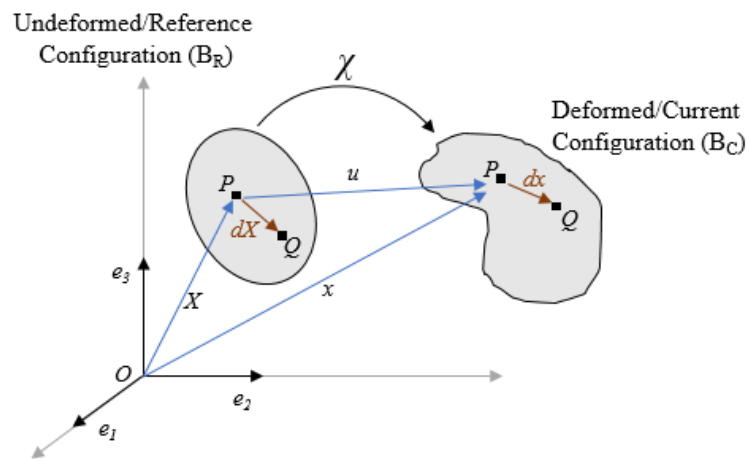


Figure 3.17. Motion of a continuum body from an undeformed configuration to a deformed configuration.

### 3.1.3 Strain Measures

The deformation gradient tensor  $\mathbf{F}$  is a fundamental measure where large material deformation is encountered, from which a number of strain measures can be determined. The Green-Lagrange strain  $\mathbf{E}$  depicts strain with respect to the reference configuration and is defined as,

$$\mathbf{E} = \frac{1}{2}(\mathbf{F}^T \mathbf{F} - \mathbf{I}) \text{ or } E_{ij} = \frac{1}{2} \left( \frac{\partial u_i}{\partial X_j} + \frac{\partial u_j}{\partial X_i} + \frac{\partial u_k}{\partial X_i} \frac{\partial u_k}{\partial X_j} \right) \quad (3-3)$$

where  $\mathbf{F}^T$  is the transpose of tensor  $\mathbf{F}$  and  $\mathbf{I}$  is the identity tensor where  $\mathbf{F}\mathbf{I} = \mathbf{F}$ . The infinitesimal or small strain can be found from  $\mathbf{E}$  by assuming the product of the infinitesimal or small strain is negligible  $\left( \frac{\partial u_k}{\partial X_i} \frac{\partial u_k}{\partial X_j} \approx 0 \right)$ . The infinitesimal strain  $\varepsilon_{ij}$  can be given by,

$$\varepsilon_{ij} = \frac{1}{2} \left( \frac{\partial u_i}{\partial X_j} + \frac{\partial u_j}{\partial X_i} \right) \quad (3-4)$$

The Eulerian strain tensor  $\mathbf{e}$  depicts strain with respect to the current/deformed configuration and is given as,

$$\mathbf{e} = \frac{1}{2}(\mathbf{I} - \mathbf{F}^{-T} \mathbf{F}^{-1}) \quad (3-5)$$

The left and right Cauchy-Green deformation tensors denoted by  $\mathbf{B}$  and  $\mathbf{C}$  respectively are useful measures of stretch ( $\lambda$ ) and are defined as,

$$\mathbf{B} = \mathbf{F}\mathbf{F}^T \text{ and } \mathbf{C} = \mathbf{F}^T \mathbf{F} \quad (3-6)$$

For strain energy density functions it is useful to define the following strain tensor invariants, where  $\lambda_i$  is the stretch in the principal directions and the three principal strain invariants are calculated from the Cauchy-Green strain tensors as follows,

$$\begin{aligned} I_1 &= \text{tr}(\mathbf{C}) = \lambda_1^2 + \lambda_2^2 + \lambda_3^2 \\ I_2 &= \frac{1}{2}[\mathbf{I}^2 - \text{tr}(\mathbf{C}^2)] = \lambda_1^2 \lambda_2^2 + \lambda_1^2 \lambda_3^2 + \lambda_2^2 \lambda_3^2 \\ I_3 &= \det(\mathbf{C}) = \mathbf{J}^2 = \lambda_1^2 \lambda_2^2 \lambda_3^2 \end{aligned} \quad (3-7)$$

The deformation gradient tensor  $\mathbf{F}$  can be decomposed using the polar decomposition theorem into the orthogonal rotation tensor  $\mathbf{R}$  and the right and left stretch tensors denoted by  $\mathbf{U}$  and  $\mathbf{V}$  respectively, this relationship is given by,

$$\mathbf{F} = \mathbf{R}\mathbf{U} = \mathbf{V}\mathbf{R} \quad (3-8)$$

where  $(\mathbf{F}=\mathbf{R}\mathbf{U})$  represents a rigid rotation followed by a stretch and the opposite for  $(\mathbf{F}=\mathbf{V}\mathbf{R})$ .

These can related to the left and right Cauchy deformation tensors by,



$$\mathbf{B} = \mathbf{V}^2 \text{ and } \mathbf{C} = \mathbf{U}^2 \quad (3-9)$$

The eigenvalues of  $\mathbf{U}$  give the principal stretches ( $\lambda_i=1, 2, 3$ ). The logarithmic strain or true strain can be determined from  $\mathbf{V}$ ,

$$\boldsymbol{\varepsilon} = \ln \mathbf{V} \quad (3-10)$$

The velocity  $\mathbf{v}$  of point  $P$  in Figure 3.17 above can be described as the rate of change in position  $\mathbf{x}$  as a function of time  $t$ ,

$$\mathbf{v} = \frac{d\mathbf{x}}{dt} \quad (3-11)$$

The difference in velocity between the two points can be given as,

$$d\mathbf{v} = \frac{d\mathbf{v}}{d\mathbf{x}} d\mathbf{x} = \mathbf{L}d\mathbf{x} \quad (3-12)$$

where  $\mathbf{L}$  is the velocity gradient tensor. The velocity gradient and deformation gradient are related as follows,

$$d\mathbf{v} = \mathbf{L}d\mathbf{x} = \mathbf{L}\mathbf{F}d\mathbf{X} \quad (3-13)$$

$$d\mathbf{v} = \frac{\partial}{\partial t}(\mathbf{F}d\mathbf{X}) = \dot{\mathbf{F}}d\mathbf{X} \quad (3-14)$$

The velocity gradient tensor can be decomposed into a symmetric stretching or rate of deformation tensor  $\mathbf{D}$  and an asymmetric spin tensor  $\mathbf{W}$  given by,

$$\mathbf{D} = \frac{1}{2}(\mathbf{L} + \mathbf{L}^T) \quad (3-15)$$

$$\mathbf{W} = \frac{1}{2}(\mathbf{L} - \mathbf{L}^T) \quad (3-16)$$

The rate of deformation tensor  $\mathbf{D}$  represents the rate of true strain ( $\mathbf{D} = \dot{\boldsymbol{\varepsilon}}$ ). Under the conditions that the principal reference axes remain fixed with respect to the material coordinates, the logarithmic strain  $\boldsymbol{\varepsilon}$  described in the Abaqus Theory Manual (DS SIMULIA, RI, USA) can be given by the following expression,

$$\boldsymbol{\varepsilon}(t) = \int_0^t \mathbf{D} dt \quad (3-17)$$

### 3.1.4 Stress Measures

The Cauchy (true) stress  $\boldsymbol{\sigma}$  is a measure of the force acting on an infinitesimal area  $dS$  within the vicinity of material point  $P$  of the current/deformed configuration. The traction  $\mathbf{t}$  is the force per unit area acting on the surface  $dS$  described by its unit normal  $\mathbf{n}$ . The Cauchy stress is given by,

$$\mathbf{t} = \boldsymbol{\sigma} \mathbf{n} \quad (3-18)$$

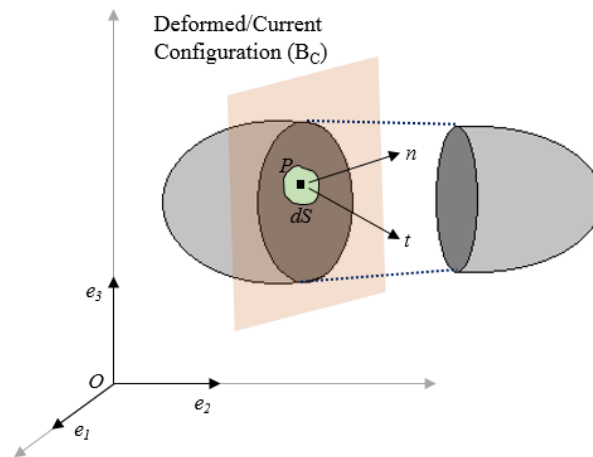


Figure 3.18. Schematic showing a slice taken through the current configuration showing a traction  $\mathbf{t}$  acting on an infinitesimal surface  $dS$  with surface normal  $\mathbf{n}$  on the deformed configuration.

The Cauchy stress can be decomposed into two subsets; the deviatoric stress  $\mathbf{S}$  which is related to the change in shape of the body, given by,

$$\boldsymbol{\sigma} = \mathbf{S} - p\mathbf{I} \quad (3-19)$$

and the hydrostatic stress  $p$  which is related to the change in volume of the body, given by,

$$p = \frac{1}{3} \text{tr}(\boldsymbol{\sigma}) \quad (3-20)$$

where  $\text{tr}(\boldsymbol{\sigma}) = \sigma_{ii}$ . The von Mises equivalent stress  $\sigma_e$  which is useful in the analysis of elastic-plastic materials is given by,

$$\sigma_e = \sqrt{\frac{3}{2} S_{ij} S_{ij}} \quad (3-21)$$

The Kirchhoff stress tensor  $\boldsymbol{\tau}$  expresses the stress relative to the reference configuration and is given by,

$$\boldsymbol{\tau} = J\boldsymbol{\sigma} \quad (3-22)$$

where  $J$  is the Jacobian ( $\det \mathbf{F}$ ), which denotes the ratio of volume change from the reference/undeformed to the current/deformed configurations. Where incompressible materials are considered, the Cauchy stress equals the Kirchhoff stress. The first Piola-Kirchhoff stress tensor  $\mathbf{P}$  represents the force per unit area in the reference/undeformed configuration. It is a non-symmetric tensor given by,

$$\mathbf{P} = J\boldsymbol{\sigma}\mathbf{F}^{-T} \quad (3-23)$$

while the nominal stress  $\tilde{\boldsymbol{\sigma}}$  can be related to the Cauchy stress through,

$$\tilde{\boldsymbol{\sigma}} = J\mathbf{F}^{-1}\boldsymbol{\sigma} = \mathbf{P}^T \quad (3-24)$$

Results from finite element simulations in this thesis are presented in terms of von Mises stress  $\sigma_e$  and Cauchy stress  $\boldsymbol{\sigma}$ .

## 3.2 Material Constitutive Behaviours

### 3.2.1 Elasto-Plasticity and Johnson-Cook Plasticity

The material behaviour of the scaffold materials investigated in the computational chapters of this thesis are assumed to be homogeneous, isotropic, elastic-plastic and in particular cases rate-dependant. The constitutive equation consists of a recoverable elastic deformation and a permanent plastic deformation. This can be written as,

$$\mathbf{F} = \mathbf{F}^e \mathbf{F}^p \quad (3-25)$$

where  $\mathbf{F}$  is the deformation gradient,  $\mathbf{F}^e$  is the elastic component and  $\mathbf{F}^p$  is the plastic component. The multiplicative decomposition of the deformation gradient can be approximated in terms of an additive decomposition of the mechanical strain rates for small elastic strains (< 5%) (Dunne, 2005),

$$\dot{\boldsymbol{\epsilon}} = \dot{\boldsymbol{\epsilon}}^e + \dot{\boldsymbol{\epsilon}}^p \quad (3-256)$$

where  $\dot{\boldsymbol{\epsilon}}$  is the total strain rate and  $e$  and  $p$  denote the elastic and plastic components respectively. Integrating with respect to time given the total strain tensor  $\boldsymbol{\epsilon}$ ,

$$\boldsymbol{\varepsilon} = \boldsymbol{\varepsilon}^e + \boldsymbol{\varepsilon}^p \quad (3-27)$$

The elastic component of the material deformation for an isotropic material can be related to stress through the material bulk modulus  $K$  and the shear modulus  $G$ ,

$$K = \frac{E}{3(1 - 2\nu)} \quad (3-28)$$

$$G = \frac{E}{2(1 + \nu)} \quad (3-29)$$

where  $E$  is the elastic modulus and  $\nu$  is the Poisson's Ratio. The elastic strain is composed of volumetric and deviatoric components. These are related to the deviatoric stress  $\boldsymbol{S}$  and hydrostatic pressure  $p$  as follows,

$$\boldsymbol{\varepsilon}_{vol}^e = tr(\boldsymbol{\varepsilon}^e) = -\frac{p}{K} \quad (3-30)$$

The deviatoric stress  $\boldsymbol{S}$  and deviatoric elastic strain  $\boldsymbol{e}^e$  are defined as,

$$\boldsymbol{e}^e = \boldsymbol{\varepsilon}^e - \frac{1}{3}\boldsymbol{\varepsilon}_{vol}^e \boldsymbol{I} \quad (3-31)$$

$$\boldsymbol{S} = 2G\boldsymbol{e}^e \quad (3-32)$$

The von Mises yield criterion is used to determine the point at which the materials used in this thesis yield or transition from elastic to plastic deformation. It is defined by the following,

$$f = \sigma_e - \sigma_y = \sqrt{\frac{3}{2}S_{ij}S_{ij}} - \sigma_y \quad (3-33)$$

where  $f$  is the yield function, such that  $f=0$  is the yield criterion,  $\sigma_e$  is the von Mises equivalent stress and  $\sigma_y$  is the yield stress.

The Johnson-Cook plasticity model is a version of von Mises plasticity with analytical forms of the hardening law and rate-dependency. It also has the option of temperature dependency. This material model is used as the constitutive material model for PLLA in Chapter 5. It consists of three terms, the first defining the yield stress, the second defining the strain rate

dependence and the third term defining temperature dependence. The yield stress and rate-dependent hardening is defined as,

$$\sigma_y = [A + B(\bar{\epsilon}_p)^n] \left[ 1 + C \ln \left( \frac{\bar{\epsilon}_p}{\dot{\epsilon}_0} \right) \right] [1 - \hat{\theta}^m] \quad (3-34)$$

where  $\bar{\epsilon}_p$  is the equivalent plastic strain and  $A$ ,  $B$ ,  $n$ ,  $C$ ,  $\dot{\epsilon}_0$  and  $m$  are material parameters measured at or below the transition temperature,  $\hat{\theta}_{transition}$ .  $\hat{\theta}$  is a non-dimensional temperature defined as,

$$\hat{\theta} = \begin{cases} 0 & \text{for } \theta < \theta_{transition} \\ (\theta - \theta_{transition}) / (\theta_{melt} - \theta_{transition}) & \text{for } \theta_{transition} \leq \theta \leq \theta_{melt} \\ 1 & \text{for } \theta > \theta_{melt} \end{cases} \quad (3-35)$$

In the context of this thesis, the temperature-dependence of the Johnson-Cook material model can be used to soften the material response. This is used in the development of the degradation framework, outlined in Chapter 5. A varying temperature field can then be used to control the strength of the material and evolve the material response as seen from the material degradation.

### 3.2.2 Isotropic Hyperelasticity

Hyperelastic materials are materials that exhibit highly non-linear elastic behaviour and undergo large deformations in which the stress-strain relationship is defined through a strain energy density function. Hyperelastic constitutive laws are widely used to describe the behaviour of soft biological tissue such as the arterial vessels (Migliavacca *et al.*, 2004; Gervaso *et al.*, 2008; Gijssen *et al.*, 2008; Schiavone, Qiu and Zhao, 2017). The first Piola-Kirchoff stress  $\mathbf{P}$  can be related to strain energy density function through,

$$\mathbf{P} = \frac{\delta \Psi(\mathbf{F})}{\delta \mathbf{F}} \quad (3-36)$$

where  $\Psi$  is the strain energy density function and  $\mathbf{F}$  is the deformation gradient. The true stress (Cauchy) can be expressed as follows,

$$\boldsymbol{\sigma} = \frac{1}{J} \mathbf{F} \mathbf{P}^T \quad (3-37)$$

Several hyperelastic constitutive models are used in this thesis to represent the non-linear response of arterial tissue and polymer-based inflation balloons. Arterial tissue is a highly complex biological tissue that shows highly non-linear stress-strain behaviour. Much work has been performed to evaluate the mechanical behaviour of arterial tissue (Holzapfel *et al.*, 2005) and develop constitutive mechanical laws (Holzapfel, Stadler and Schulze-Bauer, 2002; Gasser, Ogden and Holzapfel, 2006). The polynomial strain energy density hyperelastic model is a phenomenological model and is used to model arterial behaviour as is expressed as follows,

$$\Psi = \sum_{i+j=1}^N C_{ij} (\bar{I}_1 - 3)^i (\bar{I}_2 - 3)^j + \sum_{i=1}^N \frac{1}{D_i} (J - 1)^{2i} \quad (3-38)$$

where  $N$  is the number of polynomial terms used in the series,  $C_{ij}$  and  $D_i$  are experimentally determined temperature dependant material parameters. A sixth-order reduced form of this model is used in this thesis to model the isotropic arterial tissue mechanical response. This reduced model is given as,

$$\Psi = \sum_{i=1}^N C_{i0} (\bar{I}_1 - 3)^i + \sum_{i=1}^N \frac{1}{D_i} (J - 1)^{2i} \quad (3-39)$$

where  $C_{i0}$  and  $D_i$  are experimentally determined temperature dependant material parameters, with values determined from (Holzapfel *et al.*, 2005) and  $N=6$ . Another hyperelastic model used in this thesis is Ogden form of the strain energy density function, defined as,

$$\Psi = \sum_{i=1}^N \frac{2\mu_i}{\alpha_i^2} (\bar{\lambda}_1^{\alpha_i} \bar{\lambda}_2^{\alpha_i} \bar{\lambda}_3^{\alpha_i} - 3) + \sum_{i=1}^N \frac{1}{D_i} (J - 1)^{2i} \quad (3-40)$$

where  $\lambda_i$  are the deviatoric principal stretches,  $\mu_i$ ,  $\alpha_i$  and  $D_i$  are experimentally determined material parameters.

### 3.2.3 Ductile Damage

Part of the degradation model developed in Chapter 4 makes use of the ductile damage model available in Abaqus CAE. This is a phenomenological model that has been developed to predict the onset of damage due to nucleation, growth and coalescence of voids. Damage is initiated through a user specified equivalent plastic strain  $\bar{\epsilon}_D^p$ , which is a function of stress triaxiality and the strain rate,

$$\bar{\epsilon}_D^p(\eta, \dot{\epsilon}^p) \quad (3-41)$$

where  $\eta = -p/\sigma_e$  is the stress triaxiality or the ratio between the Hydrostatic pressure  $p$  and von Mises stress  $\sigma_e$  and  $\dot{\epsilon}^p$  is the equivalent plastic strain rate. Damage is initiated when the following criterion is met,

$$\omega_D = \int \frac{d\bar{\epsilon}^p}{\bar{\epsilon}_D^p(\eta, \dot{\epsilon}^p)} = 1 \quad (3-42)$$

where  $\omega_D$  is a state variable that increases monotonically with plastic deformation. Once the damage initiation criterion has been achieved, the damage evolution is controlled through the effective plastic displacement and is given by,

$$\dot{u}^p = L \dot{\bar{\epsilon}}^p \quad (3-43)$$

where  $L$  is the characteristic element length and  $\dot{\bar{\epsilon}}^p$  is the effective plastic strain rate. The evolution in the damage variable is governed by,

$$\varphi = \frac{\dot{u}^p}{\bar{u}_f^p} \quad (3-44)$$

where  $\dot{u}^p$  is the current element displacement and  $\bar{u}_f^p$  is the final user defined displacement at element failure. When  $\varphi = 1$  within an element, the element is considered to have failed and stress in that element is reduced to 0.

### 3.3 Finite Element Method

The finite element method is a popular approach to numerically solve structural analysis problems in which a solid body is subdivided into a discrete number of volumes or areas (elements) for the three-dimensional and two-dimensional cases respectively, with each of these elements connected at the endpoints (nodes). The computational simulations performed in this thesis makes use of the finite element method to numerically solve continuum mechanics problems. Abaqus Implicit and Explicit (DS Simulia, RI, USA) are commercially-available finite element solvers. They are used to solve the problems presented in this thesis. The following sections give an overview of the fundamental theory of the implicit and explicit finite element approaches.

#### 3.3.1 Implicit Finite Element Method

In Abaqus/Standard, non-linear systems are solved using the implicit solver. The governing equations are calculated for each element in the finite element mesh and are assembled to form a system of algebraic equations to describe the meshed body. By applying mechanical loads and boundary conditions to this system of equations, the stress and strain can be calculated for each element in the meshed body. A fundamental equation of this method is the principle of virtual work, given by,

$$\int_V \delta \boldsymbol{\varepsilon}^T \boldsymbol{\sigma} dV = \int_S \delta \mathbf{u}^T \mathbf{t} dS \quad (3-45)$$

where  $V$  is the reference volume bounded by the surface  $S$  and  $\boldsymbol{\sigma}$  and  $\mathbf{t}$  are the stress and traction vectors respectively, while  $\delta \boldsymbol{\varepsilon}$  and  $\delta \mathbf{u}$  are the virtual strain and virtual displacement vectors respectively. The following interpolation holds true for each element “ $e$ ” in the finite element mesh,

$$\delta \boldsymbol{\varepsilon} = \mathbf{B}_e \delta \mathbf{u}_e \quad (3-46)$$



$$\delta \mathbf{u} = \mathbf{N}_e \delta \mathbf{u}_e \quad (3-47)$$

where  $\mathbf{B}_e$  are the shape function gradients,  $\mathbf{N}_e$  are the element shape functions and  $\delta \mathbf{u}_e$  is the vector of virtual nodal displacements for the element. Substituting these terms into Equation 3.45 and rearranging, the finite element approximation can be summed over all the elements in the mesh as follows,

$$\sum_e \int_{V_e} \delta \mathbf{u}_e^T \mathbf{B}_e^T \boldsymbol{\sigma}(u_e) dV = \sum_e \int_{V_e} \delta \mathbf{u}_e^T \mathbf{N}_e^T \mathbf{t} dS \quad (3-268)$$

A global expression is obtained by removing the arbitrary virtual quantities and assembling the element quantities into global quantities. This global expression is given as,

$$\int_V \mathbf{B}^T \boldsymbol{\sigma}(\mathbf{u}) dV = \int_V \mathbf{N}^T \mathbf{t} dS \quad (3-49)$$

where  $\mathbf{B}$  is the global shape function gradient,  $\mathbf{N}$  is the global shape function matrix and  $\mathbf{u}$  is the global nodal displacement vector of the mesh. It is possible to rearrange this expression further to obtain a global force balance,  $\mathbf{G}(\mathbf{u})$  and is given as follows,

$$\mathbf{G}(\mathbf{u}) = \int_V \mathbf{B}^T \boldsymbol{\sigma}(\mathbf{u}) dV - \int_V \mathbf{N}^T \mathbf{t} dS = 0 \quad (3-50)$$

A range of implicit solvers are available in Abaqus/Standard. A form of the Newton-Raphson method is used to solve this global system of equations where the state of the analysis is updated using incremental steps in time, where the time is updated from time  $t$  to time  $t + \Delta t$ . Following an initial guess for the global nodal displacements  $\mathbf{u}_i^{t+\Delta t}$  in a particular increment, the Newton-Raphson scheme iterates until a stable equilibrium is achieved between the internal forces and externally applied loads. An estimation of the roots of Equation ( 3-50 ) is made, such that for the  $i^{th}$  iteration,

$$\delta \mathbf{u}_{i+1} = \mathbf{u}_{i+1}^{t+\Delta t} - \mathbf{u}_i^{t+\Delta t} = - \left[ \frac{\delta \mathbf{G}(\mathbf{u}_i^{t+\Delta t})}{\delta \mathbf{u}} \right]^{-1} \mathbf{G}(\mathbf{u}_i^{t+\Delta t}) \quad (3-51)$$

where  $t$  is the time at the start of the increment,  $\Delta t$  is the time increment used and  $i$  is the iteration number. The current estimate of nodal displacements at the end of the time increment  $\mathbf{u}_i^{t+\Delta t}$  is updated to an improved estimate  $\mathbf{u}_{i+1}^{t+\Delta t}$  at the end of the iteration. This process is repeated until a converged solution for  $\mathbf{u}_i^{t+\Delta t}$  is found. The partial derivative on the right of Equation ( 3-51 ) is the Jacobian matrix or global stiffness matrix  $\mathbf{K}$  and may be expressed as,

$$\mathbf{K}(\mathbf{u}_{i+1}^{t+\Delta t}) = \frac{\delta \mathbf{G}(\mathbf{u}_i^{t+\Delta t})}{\delta \mathbf{u}} \quad (3-52)$$

$$\mathbf{K}(\mathbf{u}_{i+1}^{t+\Delta t}) \delta \mathbf{u}_{i+1} = \delta \mathbf{G}(\mathbf{u}_i^{t+\Delta t}) \quad (3-53)$$

Equation ( 3-53 ) must be solved for each iteration, and for each iteration  $\mathbf{K}$  must be inverted. While this is a computationally expensive operation, it ensures a relatively large time increment can be used while maintaining accuracy of the solution (Smith, 2016). Complications can arise with the implicit solution if simulating high contact/sliding or large deformations. An alternative to the implicit method outlined above is the use of the Abaqus Explicit solver described in the following section.

### 3.3.2 Explicit Finite Element Method

The Abaqus/Explicit solution scheme was originally developed for dynamic simulations but is also useful in simulations with large amounts of contact and large deformations. Accelerations and velocities are assumed to be constant at a particular point at time  $t$ , this is then used to solve for the next point in time  $t + \Delta t$ . The following are the Central Difference method equations,

$$\mathbf{u}^{i+1} = \mathbf{u}^i + \Delta t^{i+1} \dot{\mathbf{u}}^{i+\frac{1}{2}} \quad (3-54)$$

$$\dot{\mathbf{u}}^{i+\frac{1}{2}} = \dot{\mathbf{u}}^{i-\frac{1}{2}} + \frac{\Delta t^{i+1} + \Delta t^i}{2} \ddot{\mathbf{u}}^i \quad (3-55)$$

where  $\mathbf{u}$  is the nodal displacement,  $\dot{\mathbf{u}}$  and  $\ddot{\mathbf{u}}$  are the velocity and accelerations respectively,  $i$  is the increment number with  $i + \frac{1}{2}$  and  $i - \frac{1}{2}$  being the value a half increment before and after the  $i^{\text{th}}$  increment. It should be noted that for explicit solving methods  $i$  refers to the increment

number as opposed to  $i$  referring to the number of iterations in implicit solvers. The accelerations are computed at the start of each increment by,

$$\ddot{\mathbf{u}}^i = \mathbf{M}^{-1}(\mathbf{F}^i - \mathbf{I}^i) \quad (3-56)$$

where  $\mathbf{M}$  is the lumped mass matrix,  $\mathbf{F}$  is the vector of externally applied forces and  $\mathbf{I}$  is the vector of internal forces. These quantities are given by:

$$\mathbf{M} = \int_V \rho \mathbf{N} dV \quad (3-57)$$

$$\mathbf{F}^i = \int_S \mathbf{N}^T \mathbf{t}^i dS + \int_V \mathbf{N}^T \mathbf{P}^i dV \quad (3-58)$$

$$\mathbf{I}^i = \int_V \mathbf{B}^T \boldsymbol{\sigma}^i dV \quad (3-59)$$

where  $\rho$  is the material density and  $\mathbf{P}$  is the vector of nodal forces. All the other quantities have already been defined, as shown in Equations (3-46) and (3-47). Rearranging Equation (3-56) in terms of the lumped mass matrix gives  $\mathbf{M}\ddot{\mathbf{u}} = \mathbf{F} - \mathbf{I}$ , which is a comparable expression to that shown in the implicit analysis (see Equation (3-53)). As the lumped mass matrix is diagonalised, it is easier to invert compared to the global stiffness matrix  $\mathbf{K}$  making each increment more computationally inexpensive.

A large number of small time increments are required to ensure accuracy for the explicit finite element solver, where the size of each increment is given by,

$$\Delta t \leq \frac{2}{\omega_{max}} \quad (3-60)$$

where  $\omega_{max}$  is the maximum element eigenvalue. A practical method of implementing the inequality shown above is,

$$\Delta t = \min\left(\frac{L^e}{c^d}\right) \quad (3-61)$$

where  $L^e$  is the characteristic element length and  $c^d$  is the dilatational wave speed, given by,

$$c^d = \sqrt{\frac{\lambda + 2\mu}{\rho}} \quad (3-62)$$

where  $\lambda$  and  $\mu$  are the Lamé constants and  $\rho$  is the material density. The importance of a good finite element mesh with a regular element size can be seen in Equation ( 3-61 ) above where the minimum time stability limit is dependent on the element length, a regular mesh is required so that a single small element does not reduce the time increment of the whole model.

A number of methods can be used to artificially reduce the computational runtime of an explicit simulation, including; reducing the time over which the deformation is applied and increasing the density of the material in the model (known as mass scaling). An important factor when performing quasi-static analysis using explicit solvers is that the inertial forces do not affect the mechanical response and provide unrealistic dynamic results. It has been shown that by keeping the ratio of internal energy to kinetic energy below 5% the dynamic effects are negligible (Choi *et al.*, 2002). This criterion is employed to ensure analysis in this thesis remain quasi-static. For further reading and information on the finite element method, the reader is referred to (Smith, 2016).

### 3.4 Finite Element Method Implementation

Simulations in this thesis are implemented using the Abaqus/Explicit finite element code (Dassault Systèmes Simulia Corp., Providence, RI, USA) linked with Intel® Parallel Studio XE 2016 for user-defined subroutine execution. Notably, the Explicit solution process is accelerated by selecting a suitable mass-scaling parameter, which in turn governs the minimum time increment. For each of the explicit simulations performed in this thesis the parameters were carefully chosen to avoid dynamic effects by ensuring that the proportion of kinetic energy to the kinetic energy in a model is less than 5%. Simulations are solved using high-performance parallel computing resources, typically on two 20-core 2.4 GHz Intel Xeon Gold

6148 processors (Irish Centre for High-End Computing, ICHEC). The time increment for each simulation is outlined individually in each chapter.

### 3.5 References

- Choi, H. H., S. M. Hwang, Y. H. Kang, J. Kim, and B. S. Kang. 2002. "Comparison of Implicit and Explicit Finite-Element Methods for the Hydroforming Process of an Automobile Lower Arm." *International Journal of Advanced Manufacturing Technology* 20 (6): 407–13. <https://doi.org/10.1007/s001700200170>.
- Dunne, Fionn. 2005. *Introduction to Computational Plasticity*. Oxford ; New York: Oxford University Press.
- Gasser, T. Christian, Ray W. Ogden, and Gerhard A. Holzapfel. 2006. "Hyperelastic Modelling of Arterial Layers with Distributed Collagen Fibre Orientations." *Journal of the Royal Society Interface* 3 (6): 15–35. <https://doi.org/10.1098/rsif.2005.0073>.
- Gervaso, Francesca, Claudio Capelli, Lorenza Petrini, Simone Lattanzio, Luca Di Virgilio, and Francesco Migliavacca. 2008. "On the Effects of Different Strategies in Modelling Balloon-Expandable Stenting by Means of Finite Element Method." *Journal of Biomechanics* 41 (6): 1206–12. <https://doi.org/10.1016/j.jbiomech.2008.01.027>.
- Gijsen, Frank J.H., Francesco Migliavacca, Silvia Schievano, Laura Socci, Lorenza Petrini, Attila Thury, Jolanda J. Wentzel, Anton F.W. van der Steen, Patrick W.S. Serruys, and Gabriele Dubini. 2008. "Simulation of Stent Deployment in a Realistic Human Coronary Artery." *BioMedical Engineering Online* 7: 1–11. <https://doi.org/10.1186/1475-925X-7-23>.
- Holzapfel, Gerhard A., Gerhard Sommer, Christian T. Gasser, and Peter Regitnig. 2005. "Determination of Layer-Specific Mechanical Properties of Human Coronary Arteries with Nonatherosclerotic Intimal Thickening and Related Constitutive Modeling." *American Journal of Physiology-Heart and Circulatory Physiology* 289 (5): H2048–58. <https://doi.org/10.1152/ajpheart.00934.2004>.
- Holzapfel, Gerhard A., Michael Stadler, and Christian A. J. Schulze-Bauer. 2002. "A Layer-Specific Three-Dimensional Model for the Simulation of Balloon Angioplasty Using Magnetic Resonance Imaging and Mechanical Testing." *Annals of Biomedical Engineering* 30 (6): 753–67. <https://doi.org/10.1114/1.1492812>.
- Migliavacca, Francesco, Lorenza Petrini, Paolo Massarotti, Silvia Schievano, Ferdinando Auricchio, and Gabriele Dubini. 2004. "Stainless and Shape Memory Alloy Coronary Stents: A Computational Study on the Interaction with the Vascular Wall." *Biomechanics and Modeling in Mechanobiology* 2 (4): 205–17. <https://doi.org/10.1007/S10237-004-0039-6>.
- Schiavone, Alessandro, Tian-Yang Qiu, and Li-Guo Zhao. 2017. "Crimping and Deployment of Metallic and Polymeric Stents -- Finite Element Modelling." *Vessel Plus* 1 (1): 12–21. <https://doi.org/10.20517/2574-1209.2016.03>.
- Smith, Michael. 2016. *ABAQUS/Standard User's Manual, Version 2016*. United States: Dassault Systèmes Simulia Corp.

# Chapter 4

## An Experimental Investigation into the Physical, Thermal and Mechanical Degradation of Two Polymeric Bioresorbable Scaffolds

---

### 4.1. Introduction

Despite their success in reducing the shortcomings of bare metal stents and their widespread use, drug-eluting stents (DES) suffer from a number of late-stage complications such as in-stent restenosis, thrombosis and strut failure (Garg, Bourantas and Serruys, 2013; Räber *et al.*, 2015; Kan *et al.*, 2016; Kufner *et al.*, 2019; Moussa *et al.*, 2020; Singh *et al.*, 2020). These permanent structures may also limit vasomotion, lumen and vessel growth and lead to complications when additional surgical interventions are required (Serruys *et al.*, 2009). Bioresorbable scaffolds (BRS) can potentially avoid these late-stage complications by using the physiological and passive processes of the patient to completely degrade once they have completed their scaffolding function. BRS are typically made of biodegradable metals such as magnesium, iron, zinc and their alloys, or polymers such as poly-L-lactic acid (PLLA) and poly(lactic-co-glycolic acid) (PLGA). While short-term clinical data has demonstrated the safety and efficacy of BRS devices across several device platforms, including Abbot ABSORB (Gonzalo, Gonzalo and Macaya, 2012; Kraak *et al.*, 2015) and Reva Medical Fantom (Abizaid *et al.*, 2017; Chevalier *et al.*, 2019), three-year follow up data from the ABSORB III trial (Kereiakes *et al.*, 2017) showed increased incidences of stent thrombosis and myocardial infarction during follow up when compared to DES, with other trials showing similar negative

long-term outcomes (Cassese *et al.*, 2016; Lipinski *et al.*, 2016; Serruys *et al.*, 2016). While it has been suggested that late stent fracture or discontinuity may have been the cause of late-stage thrombosis (Stone and Granada, 2015; Patel *et al.*, 2017; Sorrentino *et al.*, 2017), there is generally a lack of long-term experimental data describing the physical and mechanical degradation of BRS devices coupled with thick scaffold struts.

Polymeric BRS are typically made from semi-crystalline polymers, which consist of crystalline and amorphous regions. The relative volume fractions of these regions contribute to the mechanical properties of the bulk polymer, where higher percentage crystallinity polymers are typically characterised as stronger, but less ductile, than polymers with a higher amorphous content (Liu *et al.*, 2014). The degradation of semi-crystalline polymers generally takes place through bulk degradation by the process hydrolysis (von Burkersroda *et al.*, 2002; Song and Atrens, 2003; Cheng *et al.*, 2013). Water from the surrounding environment is absorbed and breaks the ester bonds of the amorphous phase, with scission of the long polymer chains leading to a reduction in molecular weight, which in turn affects mechanical and thermal properties. A number of studies have been performed on PLLA (Duek, Zavaglia and Belangero, 1999; Tsuji and Ikada, 2000; Tsuji, Mizuno and Ikada, 2000; Weir *et al.*, 2004; Lyu *et al.*, 2007; Naseem *et al.*, 2020; Katarzyna *et al.*, 2021) that characterise the effect degradation on the mechanical and physical properties. While degradation generally results in a reduction in molecular weight early in the degradation process, thermal analysis has found that this can coincide with increases in relative crystallinity for PLLA (Tsuji and Ikada, 2000; Tsuji, Mizuno and Ikada, 2000; Weir *et al.*, 2004), which presents a complex evolving relationship when mechanical performance is considered. It has been found that degradation of PLLA-based polymers can affect the mechanical performance to varying degrees. However, the understanding of the relationship between physical properties and mechanical performance of BRS remains limited (Luo *et al.*, 2014; Wang *et al.*, 2017; Qiu *et al.*, 2018; Naseem *et al.*, 2019). Existing



experimental BRS studies focused on characterising mechanical performance such as radial strength and nanoindentation response (Luo *et al.*, 2014; Shirazi *et al.*, 2014; Wang *et al.*, 2017; Qiu *et al.*, 2018; Naseem *et al.*, 2019) or physical performance such as thermal and molecular behaviour (Otsuka *et al.*, 2014; Naseem *et al.*, 2019). However, the vast majority of these studies have been carried out on either Abbot Absorb (Qiu *et al.*, 2018; Ramachandran *et al.*, 2018; Naseem *et al.*, 2019, 2020) or other non-commercial devices (Nuutinen *et al.*, 2003; Zilberman, Nelson and Eberhart, 2005; Wang *et al.*, 2018; Naseem *et al.*, 2019), limiting information on the performance of other polymer BRS devices.

In this study, a systematic evaluation of the physical, thermal and mechanical performance of the Reva Medical Fantom Encore BRS (Reva Medical, San Diego, CA, USA) and another non-commercial BRS undergoing thermally-accelerated degradation was carried out. These scaffolds were chosen as they were acquired through the InSilc project through which this work was funded. The Fantom Encore is made of a proprietary polymer called Tyrocore, a copolymer of short chain PLA and tyrosine analogue, while the non-commercial BRS was made from medical grade PLLA. The Fantom Encore and non-commercial BRS were immersed in phosphate-buffered saline (PBS) at 50°C for 112 and 181 days, respectively. Physical and thermal properties were determined by measuring mass loss, molecular weight, thermal properties and degree of crystallinity at consecutive time points. Mechanical testing of the BRS was carried out through radial force testing, whereby radial strength and stiffness was determined, while local properties were measured through nano-indentation testing.

## **4.2. Methods**

### **4.2.1 In Vitro Accelerated Degradation**

The BRS samples used in this study were removed from their respective packaging and freely expanded as per their instructions for use (IFU), with the Fantom Encore inflated with a manual

pump by InSilc collaborators and the non-commercial BRS inflated by the manufacturer with a computer-controlled pump. Table 4.1 below shows the expansion protocol for both BRS.

Table 4.1. Free expansion protocol used to freely expand the Fantom Encore and Non-Commercial BRS

BRS	Expansion Pressure (atm)	Inflation Time (s)	Hold Period (s)
Fantom Encore	7	10	30
Non-Commercial BRS	10	24	30

The freely expanded geometries of the Fantom Encore and non-commercial BRS used in this study are shown in Figure 4.(a). The Fantom Encore BRS consists of 6 repeating units per circumference connected to the subsequent ring with 3 struts and 10 rings across the length of the BRS. The non-commercial BRS consists of 9 repeating units per circumference with two platinum markers and 9 connecting struts for the end rings. While the inner rings are connected with 3 struts per ring.

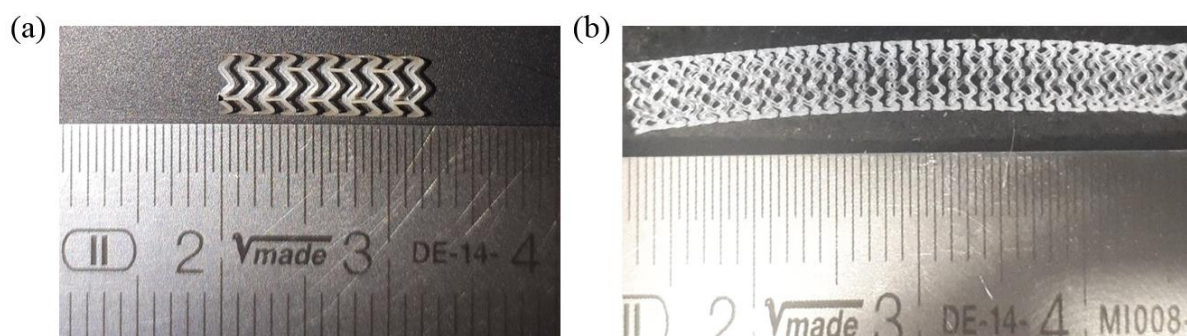


Figure 4.1. (a) Reva Medical Fantom Encore BRS, length 12mm diameter 3mm. (b) Non-commercial BRS, length 32mm diameter 3mm.

In total, 24 Fantom Encore BRS and 36 non-commercial BRS were deployed. For the Fantom Encore, 2 samples were tested at each time point for use in mechanical testing with a further 2 samples reserved for nanoindentation. For the non-commercial BRS, 3 samples were tested at each time point with 2 samples also reserved for nanoindentation. Both BRS were subjected to an *in vitro* thermally accelerated degradation study in which samples were immersed for a period of 112 and 181 days for the Fantom Encore and non-commercial BRS respectively at 50°C in phosphate-buffered saline solution (PBS) (Thermo Fisher Scientific, Hamton, NH, USA) where the solution pH was monitored each week to remain within  $7.4 \pm 0.2$  according to

ISO 13781 (ISO, 2010). It has been shown previously for PLLA that immersion at 50°C equates to a four-fold increase in the degradation time when compared to degradation performed at 37°C through the Arrhenius relationship (Wise, Gillen and Clough, 1995).

$$k = Ae^{-Ea/RT} \quad (4-1)$$

where  $k$  is a rate constant;  $A$  is a constant;  $Ea$  is the activation energy,  $R$  is the universal gas constant, and  $T$  is the temperature. Based on constants used in a previous study, where *in vitro* accelerated degradation protocols were validated, degradation processes in PLLA experience a four-fold increase at 50°C compared to physiological temperatures of 37°C (Weir *et al.*, 2004). A range of tests to evaluate the evolution in material and mechanical properties were performed throughout the accelerated study (Fantom Encore: Days 0, 7, 21, 35, 49, 57, 63, 70, 77, 91, 112, Non-commercial BRS: Days 0, 7, 21, 35, 49, 54, 65, 70, 77, 112, 146, 160, 181).

#### 4.2.2 Gravimetric Analysis

Mass of the BRS were recorded before immersion and at each time point to assess mass change caused by hydration and degradation. Wet mass was measured after removing the scaffold from the solution and drying with a paper towel to remove surface moisture. Dry mass was measured after drying at 50°C overnight. Change in the dry mass was assessed over the course of the study.

#### 4.2.3 Thermal Properties

Thermal behaviour of the BRS was measured using Differential Scanning Calorimetry (DSC), which was performed using a Netzsch DSC 214 Polyma (NETZSCH - Gerätebau GmbH, Germany). Samples consisted of 2 mg of BRS material that was placed in pierced aluminium pans. Four samples were tested at each time point. All measurements began at room temperature (20°C) and heated to 200°C at a rate of 10°C/minute with measurements obtained under a nitrogen atmosphere. Glass transition temperature ( $T_g$ ), melting temperature ( $T_m$ ) and

enthalpy of fusion ( $\Delta H_{melt}$ )/crystallinity ( $X_c$ ) were determined from the resulting thermograms. To determine the crystallinity of the PLLA in the non-commercial BRS the  $\Delta H_{melt}$  for a 100% crystalline sample was used, reported to be 93 J/g (Fischer, Sterzel and Wegner, 1973). It should be noted that while a 100% crystalline reference sample is not available for the Fantom Encore, the changes in the crystallinity of these samples could still be discerned by noting changes in the  $\Delta H_{melt}$ .

#### 4.2.4 Molecular Weight Properties

The number average ( $M_n$ ), weight average ( $M_w$ ) molecular weight and polydispersity ( $M_w/M_n$ ) of the samples were determined using Gel Permeation Chromatography (GPC) on a 3-detector Malvern system PANalytical Viscotek TDMax (Spectris, Egham, UK). The GPC system was calibrated with narrow molecular weight distributed polystyrene standards, and results expressed as polystyrene equivalent molecular weight at each time point. At each time point, the samples were dissolved in 1g Tetrahydrofuran (THF) and a 100  $\mu$ l sample was eluted with a flow rate of 1ml/min at 35°C. Calculations were performed using the refractive index detector.

#### 4.2.5 Mechanical Characterisation – Radial Compression Testing

The evolution in mechanical properties of the BRS was evaluated throughout the degradation period. To determine the radial response of the BRS at each time point, samples were radially compressed using an 8-plate crimping head (RCM-H60, MPT Europe), connected to a Zwick uniaxial test machine with a 100N load cell (Zwick Roell, GmbH, Germany), as shown in Figure 4.(a). The plates were heated to 37°C and the BRS placed between the crimping plates for 5 minutes prior to testing to come up to temperature. The test protocol for both BRS is shown in Table 4.2 below.

*Table 4.2. Radial compression protocol for the Fantom Encore and non-commercial BRS.*

<b>BRS</b>	<b>Start Diameter (mm)</b>	<b>Final Diameter (mm)</b>	<b>Hold Period (s)</b>
Fantom Encore	3.5	2.0	25

Non-commercial BRS	3.2	2.4	25
-----------------------	-----	-----	----

Crimping and un-crimping of BRS was carried out a displacement rate of 0.52mm/s. Friction between the crimping plates was measured by running the test without a sample present and the loading profile was subtracted from the subsequent force curves (McKenna and Vaughan, 2020). Day 0 samples were soaked in PBS at 37°C for 1 hour with excess PBS removed prior to testing. All other samples were removed from the media with excess PBS removed before radial testing and tested immediately.

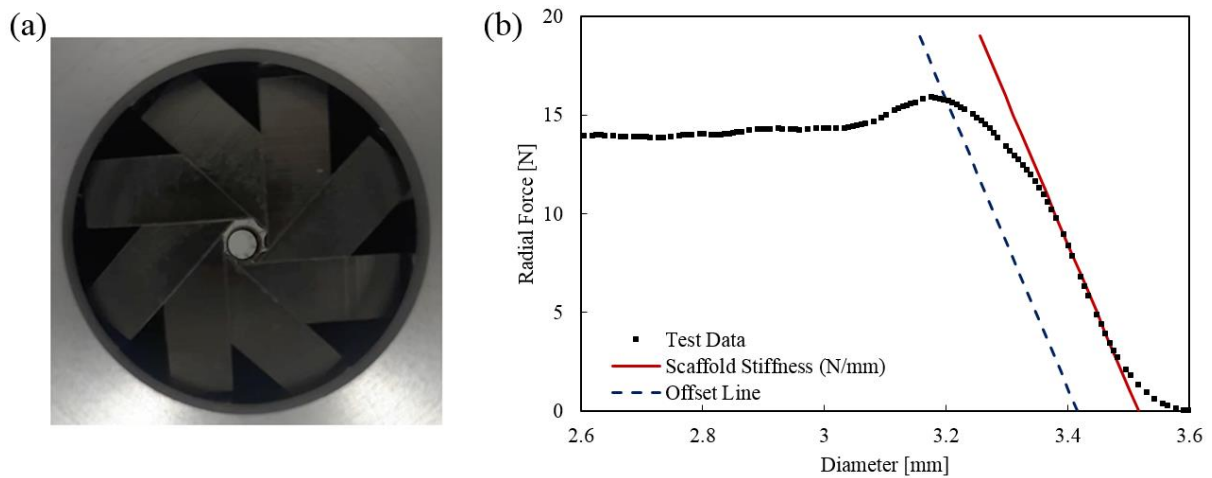


Figure 4.2. (a) Schematic drawing of radial compression testing. (b) Radial force-diameter curve obtained from radial compression testing showing the stiffness and offset line used to assess radial strength.

The output from this test is force at the load cell ( $F_L$ ) and crosshead position ( $C_H$ ). The crosshead position is converted to crimping head diameter ( $D$ ) using Equation ( 4-2 ) below and parameters obtained from calibration.

$$D = \frac{C_H - O_F}{S} \quad (4-2)$$

where  $O_F$  is the offset from the calibration curve and  $S$  is the slope of the calibration curve which are parameters determined during the radial crimp head calibration. The radial force was then calculated using Equation ( 4-3 ), which was derived from a balance of moments of the crimping plates, such that:

$$F_R = \frac{F_L \times 135 \times A}{\sqrt{27^2 - \left(\frac{D}{2}\right)^2}} \quad (4-3)$$

where  $A$  is a factor given by the manufacturer that corresponds to the effect of a lever mechanism within the radial tester. The initial loading peak and radial stiffness were calculated from the radial force curves, as shown in Figure 4.(b), with radial strength determined with a line parallel to the radial stiffness and offset by 0.1mm as per Qiu *et al* (2018). The work-to-fracture was also measured, which consisted of the area beneath the loading portion of the force-diameter curves, starting at the point the crimping plates made contact with the scaffold and finishing at 75% of the original diameter (or fracture, if it occurred before this). The results of each radial test were averaged and normalised by the BRS length. For comparison the radial strength, stiffness and work-to-fracture were also normalised against the initial timepoint and plotted against the immersion time.

#### 4.2.6 Mechanical Characterisation – Nanoindentation Testing

Nanoindentation testing was performed using a Keysight Nano Indenter G200 (Keysight Technologies, Santa Rosa, USA) with a Berkovich tip. Samples consisted of scaffold rings mounted in 25mm diameter clear epoxy cylinders and sectioned once cured to ensure both surfaces were parallel, as shown in Figure 4.3(b). Samples were hand ground to expose the BRS surface and then were semi-automatically ground and polished using progressively finer diamond suspension solutions to a final suspension size of 1 $\mu$ m to obtain a smooth surface finish for nanoindentation. Indents were performed through displacement-controlled loading to an indentation depth of 2,000 nm, holding the indenter at peak displacement for 30 s and unloading to 90% of the peak load, and holding for a further 100 s to calibrate for drift. The Oliver and Pharr (1992) method was used to determine the modulus and hardness. Hardness ( $H$ ) is defined as the load on the indenter tip over the projected contact area.

$$H = \frac{P}{A_c} \quad (4-4)$$

where  $P$  is the load and  $A_c$  is the projected contact area. Both elastic and plastic deformation are experienced simultaneously when loading the sample, which is why the unloading curve is

used for calculating the elastic properties, whereby only the elastic portion is recovered during unloading. The contact stiffness is defined as the initial slope of the unloading curve. This can be related to the reduced elastic modulus of the contact.

$$S = \frac{dP}{dh} = \frac{2E_r\sqrt{A_c}}{\sqrt{\pi}} \quad (4-5)$$

Where  $S$  is the slope of the unloading curve or ‘contact stiffness’ at maximum depth,  $P$  is the applied load and  $E_r$  is the reduced modulus of the contact. The contact area ( $A_c$ ) was determined using the area function for the indenter tip geometry used. This function expresses the projected contact area as a function of the contact depth ( $h_c$ ).

A series of 7-14 indents were performed in total for each sample. Sites for indentation were selected using an optical microscope. It was recorded whether the site selected for indentation was a hinge, defined by the circled regions in Figure 4.3(a), or a connecting strut. As the hinge regions were subjected to more mechanical deformation during crimp and deployment than the connecting struts, a comparison was made to determine if this resulted in differences on the elastic modulus and hardness at a localised level. Statistical analysis (t-Tests) was used to compare the day 0 sample against the other time points and to investigate the hinge and strut regions for variations in mechanical properties. T-tests were performed at a 95% confidence level.

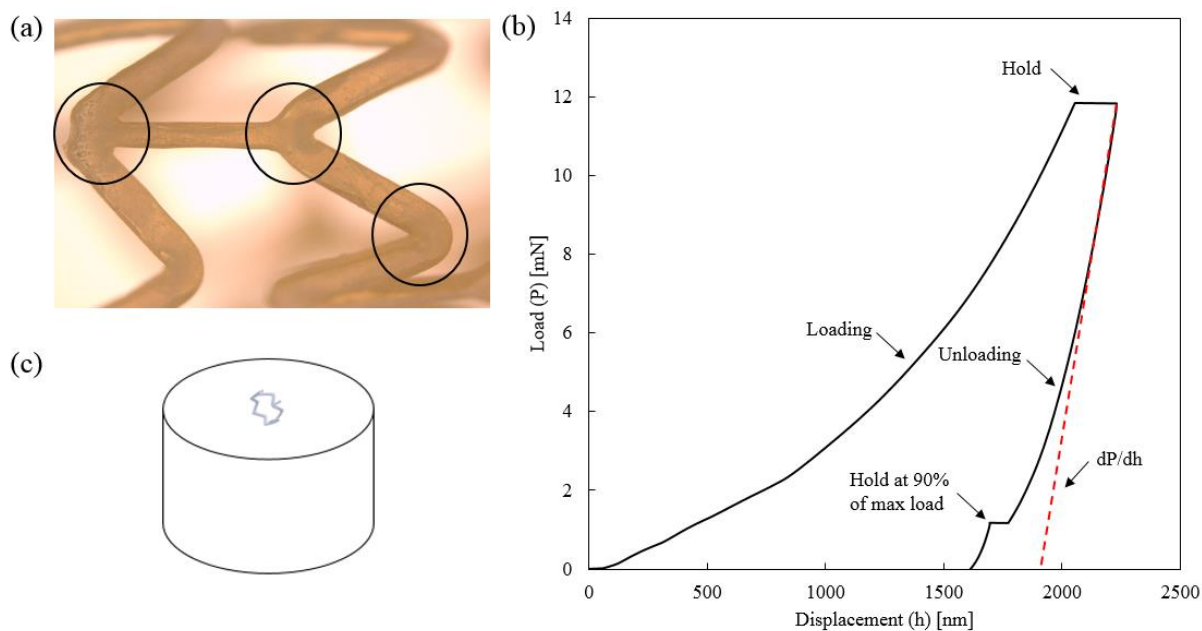


Figure 4.3. (a) Circled areas showing hinge regions on the Fantom Encore and interconnecting strut regions. (b) Orientation of the scaffold rings within the epoxy cylinder. (c) Typical loading curve for a nanoindentation test showing the slope of the unloading curve and the hold at max displacement and 90% max load.

## 4.3 Results

### 4.3.1 Gravimetric Results

Figure 4.4 shows that there was minimal mass change over the course of the study, with only slight mass losses at the final time points for the Fantom BRS, which suggests that the constitutive material of both BRS were only in the hydrolysis phase of degradation until these later time points. The Fantom Encore shows an increased uptake of water from day 77 with a larger difference shown between the wet and dry mass.

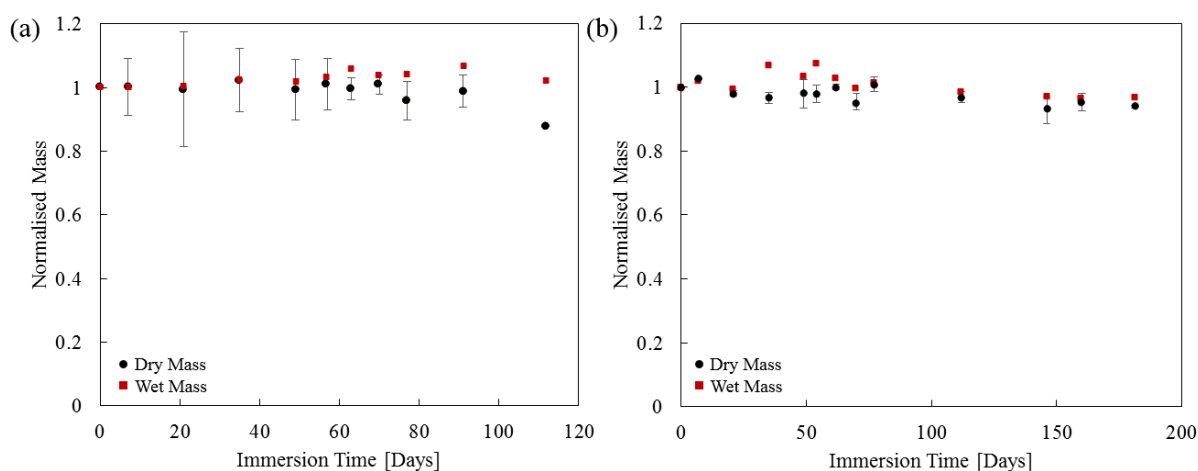


Figure 4.4. Normalised wet and dry mass change of the (a) Fantom Encore BRS over the 112 day degradation period and (b) non-commercial BRS over the 181 day degradation period.



### 4.3.2 Thermal Analysis

#### 4.3.2.1 Fantom Encore BRS

DSC analysis showed the  $T_m$  for Tyrocore to be approximately 150°C at day 0. Figure 4.5(a) shows the profile of the DSC curves for days 0, 7, 35, 77, and 112. Interestingly, no glass transition peak was seen during the thermal analysis at the initial time point. This is typically associated with semi-crystalline polymers indicating that this polymer likely had a high crystallinity. It was also noted that several time points had a decreasing slope throughout the test. The averaged results from the DSC analysis for  $\Delta H_{melt}$  and  $T_m$  are shown in Figure 4.5(b) and (c), respectively. An increasing trend in the  $\Delta H_{melt}$  is evident over the course of degradation indicating an increase in the energy required to melt the polymer, the maximum  $\Delta H_{melt}$  measured at day 70 was approximately 40% higher than day 0 which can be related to an increase in the relative crystallinity of the polymer.

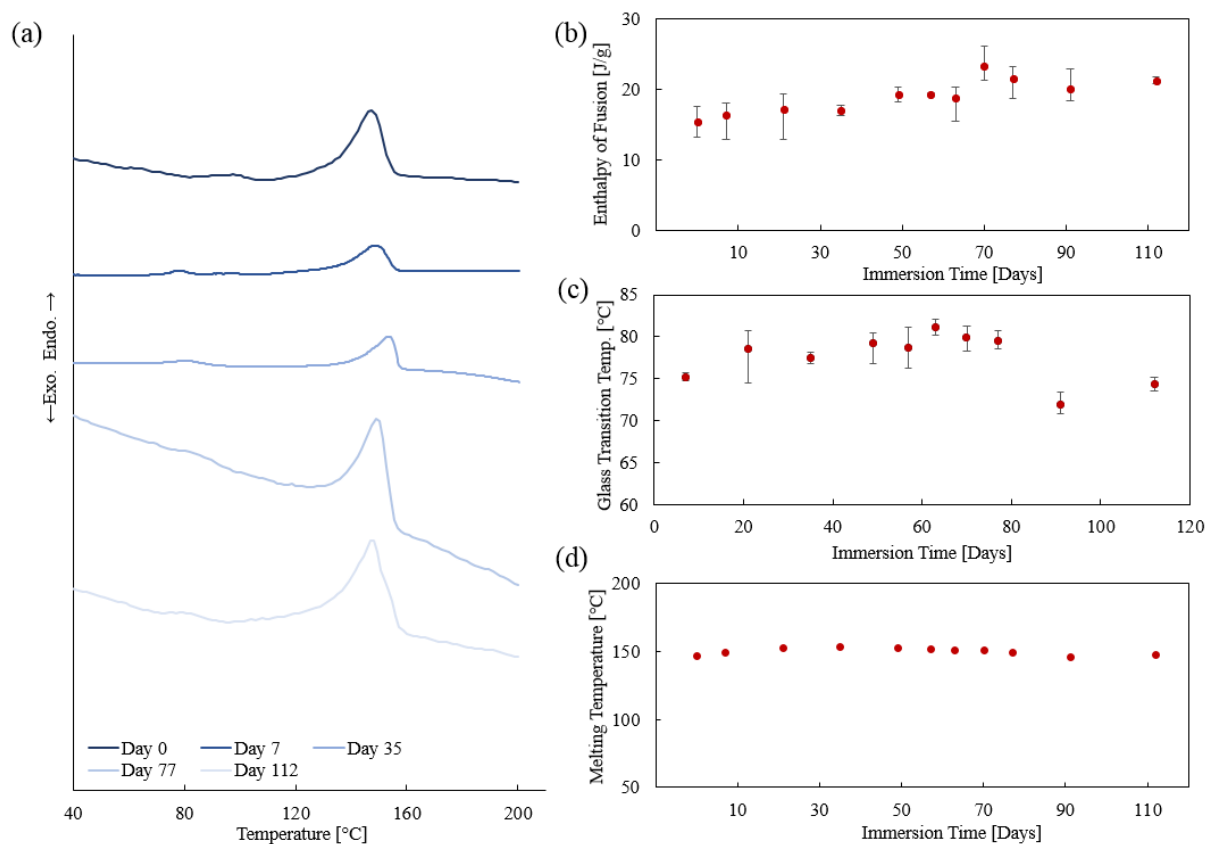


Figure 4.5. (a) Heat flow curves from day 0, 7, 35, 77 and 112 showing endothermic peaks during heating to 200°C. (b)  $\Delta H_{melt}$  for Tyrocore throughout the degradation period showing error of 1 S.D. (c)  $T_g$  for Tyrocore, day 0 found no  $T_g$ . (d)  $T_m$  for Tyrocore throughout the degradation period. Note, no error bars for melting temperature due to small variation ( $\pm 0.5^{\circ}\text{C}$ )

### 4.3.2.2 Non-Commercial BRS

DSC analysis showed the  $T_m$  for the non-commercial BRS PLLA to be approximately 175°C at day 0. Figure 4.6 below shows the DSC curves for days 0, 7, 49, 77, 146 and 181. These PLLA samples lack a cold crystallisation exothermic peak indicating the PLLA used in this BRS is of a highly crystalline nature. Measuring the relative crystallinity of the polymer throughout the degradation period shows an increase in crystallinity to day 146, whereby a decrease was then observed. The  $T_g$  was observed to increase from the initial time point, after which no change was observed until the final time points where no  $T_g$  was observed. There was no change in  $T_m$  of the PLLA until the final time points, where it decreased.

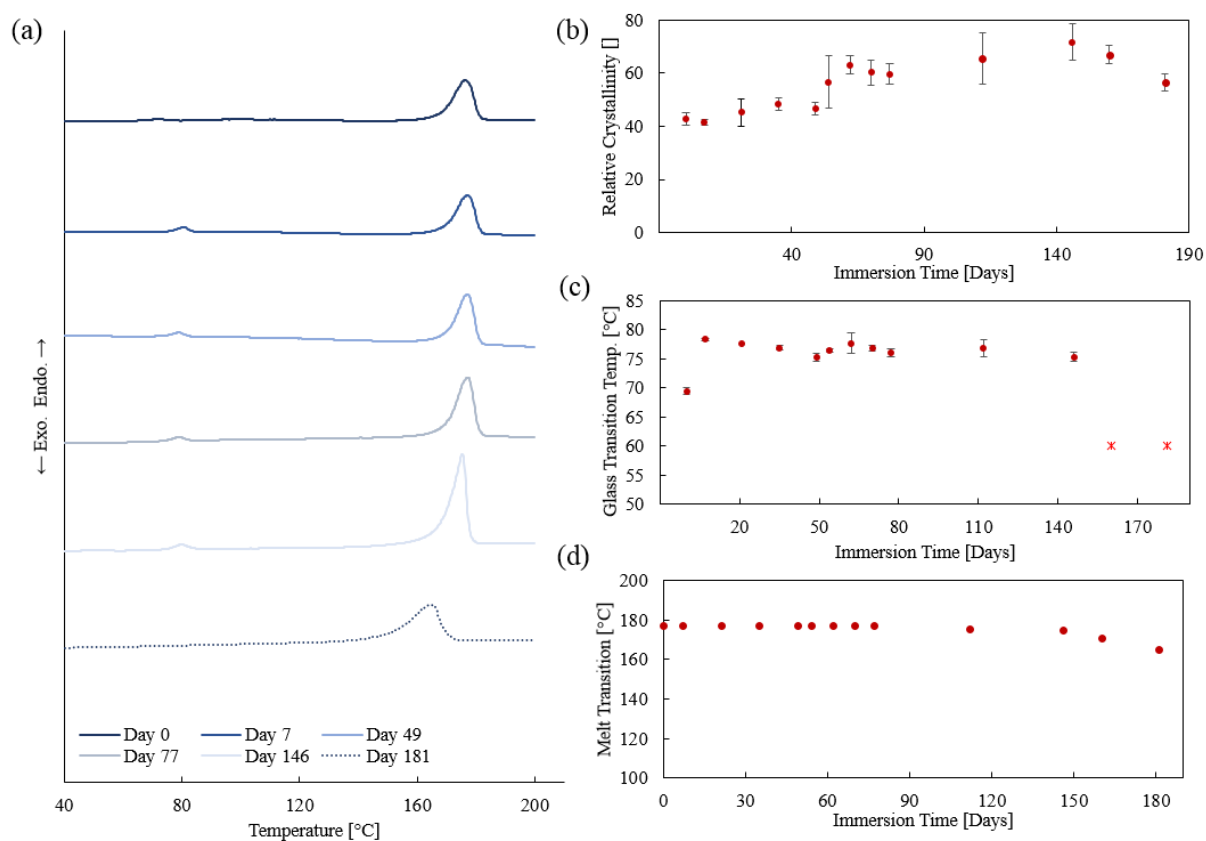


Figure 4.6. (a) Heat flow curves from day 0, 7, 49, 77, 146 and 181 showing endothermic peaks during heating to 200°C. (b) Change in crystallinity for PLLA throughout the degradation period showing error of 1 S.D. (c)  $T_g$  for Tyrocore, day 0 found no  $T_g$ . (d)  $T_m$  for Tyrocore throughout the degradation period. Note, no error bars for melting temperature due to small variation ( $\pm 0.5^\circ\text{C}$ )

### 4.3.3 Molecular Weight

#### 4.3.3.1 Fantom Encore BRS

The change in  $M_n$  and  $M_w$  over the course of the degradation period is shown in Figure 4.7 for the Fantom Encore. It shows an initial rapid decrease in both  $M_w$  and  $M_n$  from days 0 to 35 before the decrease levelled out. Dispersity ( $M_w/M_n$ ) increases during the degradation process, as shown in Table 4.3 below.

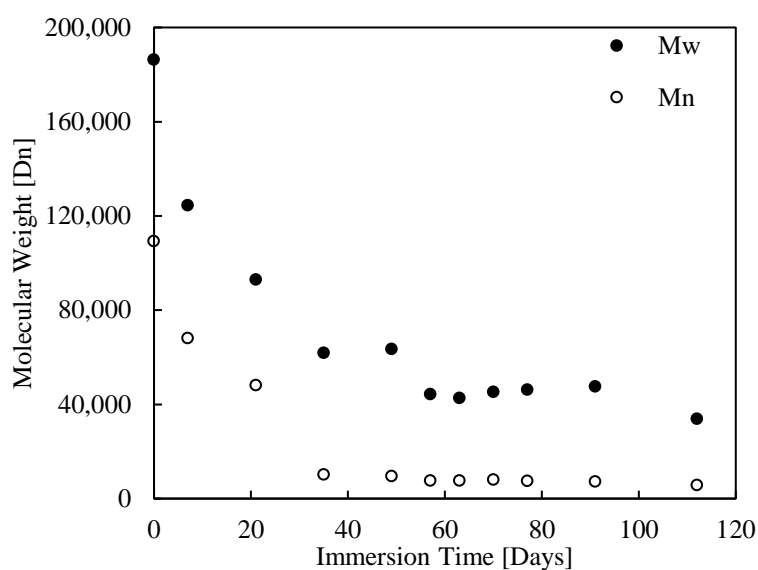


Figure 4.7.  $M_n$  and  $M_w$  molecular weight of Tyrocore over the 112 day degradation period.

Table 4.3. Dispersity,  $M_w$  and  $M_n$  molecular weight of the Tyrocore material.

Day	0	7	21	35	49	57	63	70	77	91	112
$M_w/M_n$	1.70	1.83	1.93	6.09	6.68	5.88	5.58	5.71	6.19	6.58	5.97
$M_w$	186,291	124,436	92,916	61,764	63,490	44,342	42,693	45,262	46,142	47,522	33,860
$M_n$	109,293	68,045	48,076	10,149	9,507	7,542	7,646	7,933	7,460	7,218	5,667

#### 4.3.3.2 Non-Commercial BRS

The change in  $M_n$  and  $M_w$  of the non-commercial BRS over the course of the degradation period is shown in Figure 4.8 below. It shows an initial rapid decrease in molecular weight.

Dispersity is shown in Table 4.4.

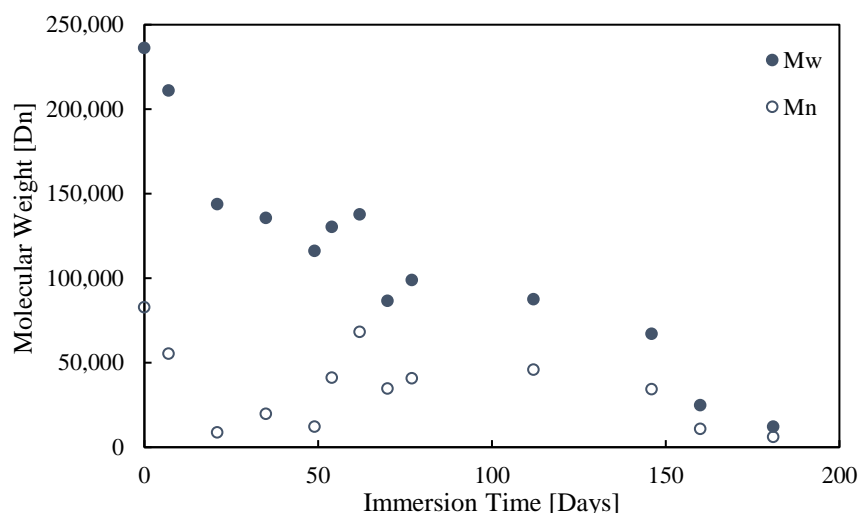


Figure 4.8.  $M_n$  and  $M_w$  of PLLA over the 181 day degradation period.

Table 4.4. Dispersity of the non-commercial BRS PLLA material.

Day	0	7	21	35	49	54	62
Dispersity	2.85	3.82	16.85	6.90	9.53	3.16	2.02
$M_w$	236,148	210,978	143,840	135,638	116,156	130,241	137,788
$M_n$	82875	55267	8,715	19,680	12,183	41,168	68,110
Day	70	77	112	146	160	181	
Dispersity	2.5	2.43	1.9	1.96	2.3	1.97	
$M_w$	86,661	98,960	87,441	67,045	24,820	12,047	
$M_n$	34,618	40,710	45,925	34,236	10,774	6,127	

### 4.3.4 Mechanical Characterisation – Radial Compression Results

#### 4.3.4.1 Fantom Encore BRS

The averaged radial force response for the Fantom Encore BRS of each time point is shown in Figure 4.9(a-e). Here, the radial force on the y-axis has been normalised to the overall length of the scaffold (N/mm). The radial response at day 0 showed a linear increase and plateau region upon loading, a relaxation period during the hold and unloading with permanent deformation of the BRS. It was found that the BRS increased in radial strength by almost 50% from days 0 – 21. Beyond this time point, the peak strength gradually reduced and the plateau region became more limited (see Figure 4.9(c-e)). By day 49, a substantial loss in the plateau region was evident (see Figure 4.9(c)), where a sharp decrease in the plateau region was seen, with subsequent time points lacking a plateau region entirely. An artefact of the friction deduction is shown before the loading region in Figures 4.9(b, c, e).

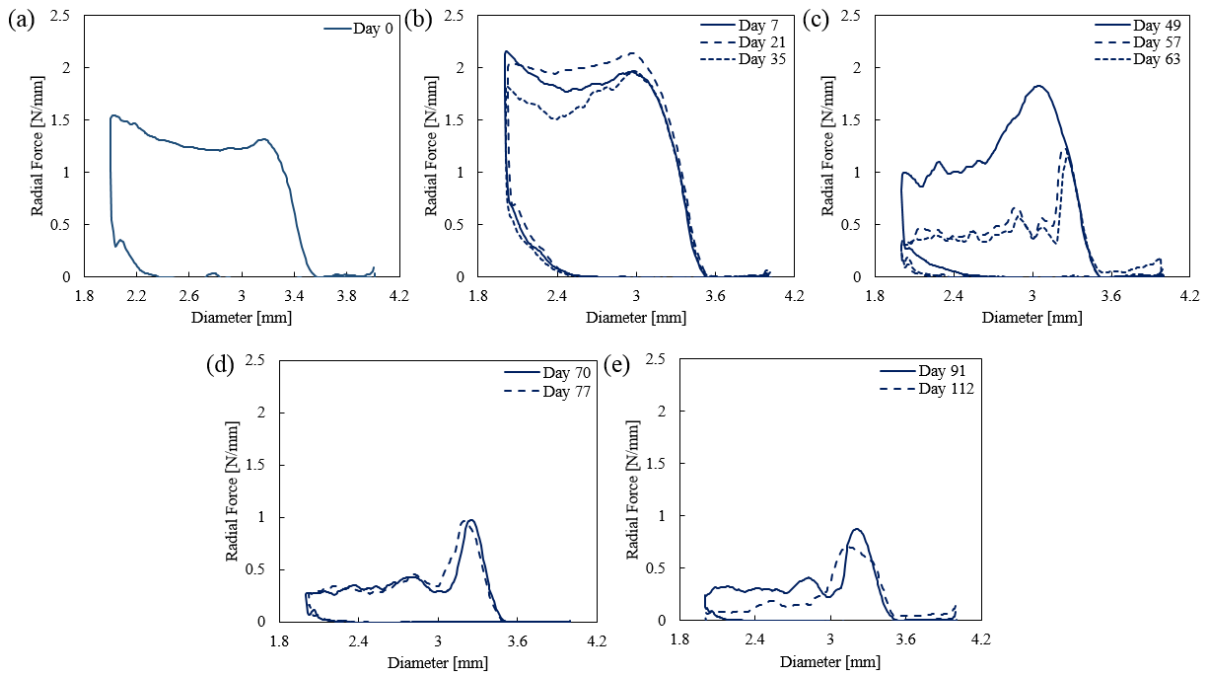


Figure 4.9(a-e). Normalised and averaged radial force-diameter curves obtained from radial compression testing for each time point.

Figure 4.10 shows the normalised radial strengths, stiffness and work-to-fracture. Following the initial increase, the radial strength decreased after day 21, with a sudden decrease in radial strength seen between day 49 and 57. The radial stiffness increased after day 0 corresponding with the increase in the radial strength. No major change was seen in radial stiffness to day 63, where the stiffness only gradually decreased. The decrease in ductility was clearly evident after day 49, with a sudden rapid loss in the work-to-fracture. The sudden decrease corresponded with fracture of the BRS on day 49.

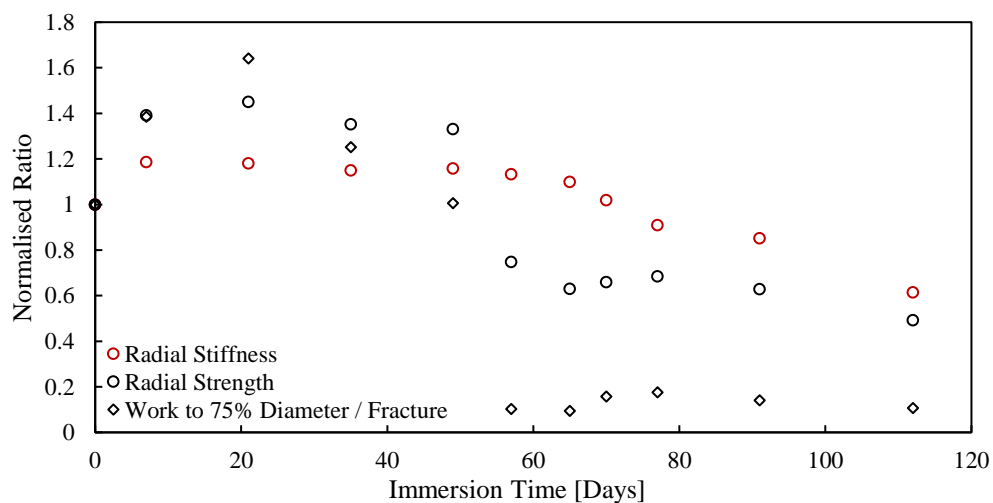


Figure 4.10. Evolution of the measured radial strength, stiffness and work to 75% of the original diameter/fracture of the Phantom Encore BRS over the degradation period with max. and min. values.

Images taken after radial testing show the decrease in ductility and the increasing brittleness of the BRS, with days 0-35 undergoing permanent plastic deformation, this is evident when compared against Figure 4.11. While fracture was more readily observed in later time points (after day 49), as shown in Figure 4.11. In these devices, the initial site of fracture tended to be at the base of connecting struts (see day 49 in Figure 4.11). As the degradation continued, fracture was found to occur in both the base of the connecting struts and the plastic hinges.

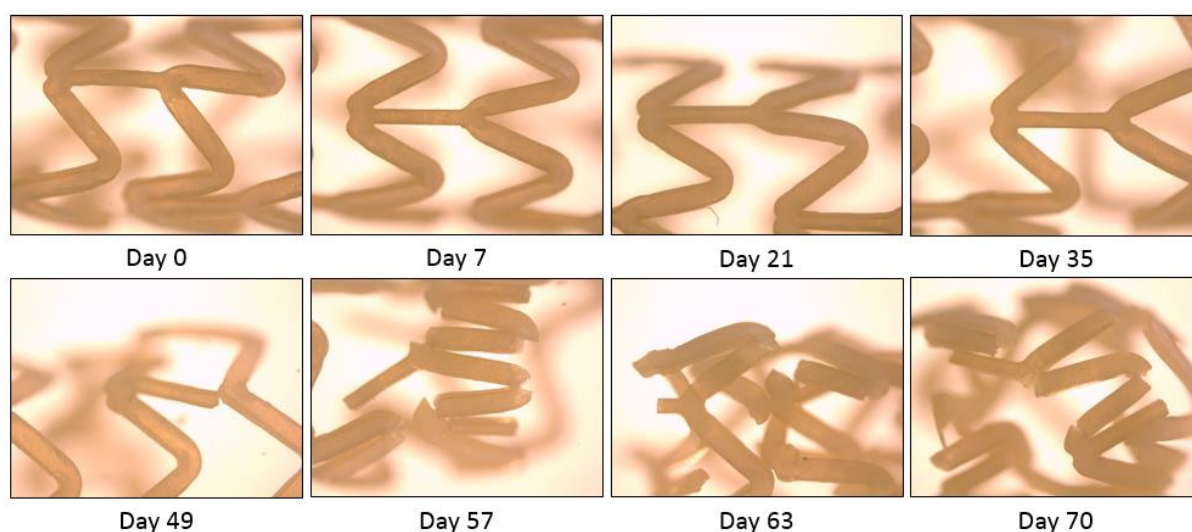


Figure 4.11. Images of *Fantom Encore* after radial testing. Scaffold fracture is clear from day 49 onwards. As degradation progresses the BRS lose their ability to crimp uniformly, with radially tested samples becoming more deformed after testing.

#### 4.3.4.2 Non-Commercial BRS

The averaged radial force response of each time point is shown in Figure 4.12(a-e) for the non-commercial BRS. Again, the radial force on the y-axis has been normalised to the overall length of the scaffold (N/mm). The radial response at day 0 shows a linear increase and plateau region upon loading, a relaxation period during the hold and unloading with permanent deformation similar with the *Fantom Encore*. Degradation clearly affects this plateau region with Figure 4.12(d) showing a dramatic decrease in ductility. The loss of the plateau region is evident from after day 77, Figure 4.12(d-e) where a sharp decrease in the plateau region is seen, with subsequent time points lacking a plateau region entirely.

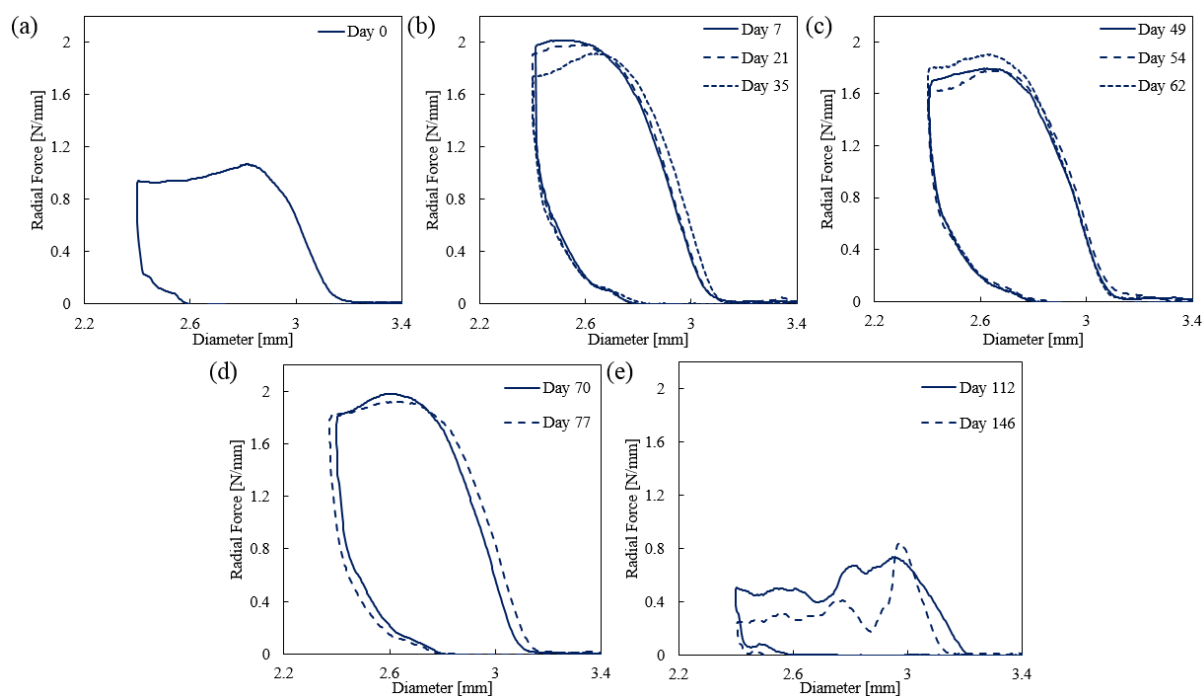


Figure 4.12 (a-e). Normalised and averaged radial force-diameter curves obtained from radial compression testing for each time point.

It was found that the radial strength almost doubles between days 0 and 7. Figure 4.13 shows the normalised radial strengths, stiffness and work to fracture over the period of degradation. A reduction in radial strength occurred after day 77, with a dramatic decrease in radial strength between by day 112. The radial stiffness increased after day 0 corresponding with the increase in the radial strength. No major change was seen in radial stiffness to day 146, after which the BRS were too brittle to test. The decrease in ductility is clearly evident at day 112, with a sudden rapid loss in the work-to-fracture of the devices. Note that there was a slight increase in work-to-fracture for days 35, 70 and 77, which was caused by these samples having a slightly higher starting diameter than the other time points.

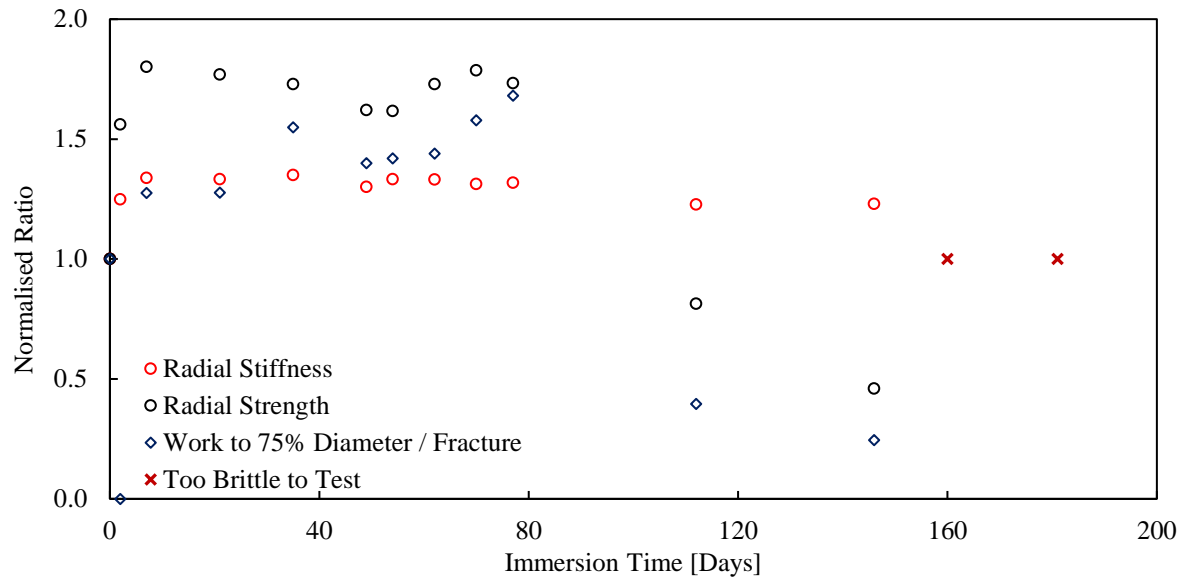


Figure 4.13. Evolution of the measured radial strength and stiffness of the Non-commercial BRS over the degradation timeframe.

Images taken of the non-commercial BRS after radial testing of the various time-points are shown in Figure 4.14. It shows a transition to brittle failure over the course of degradation. This is evident from the deformation from the radial crush visible at day 0 and the fracture and lack of deformation in the later time-points. For later time points (e.g. days 146 and 181), the struts become less clear with artefacts noted at the hinge regions of the BRS.

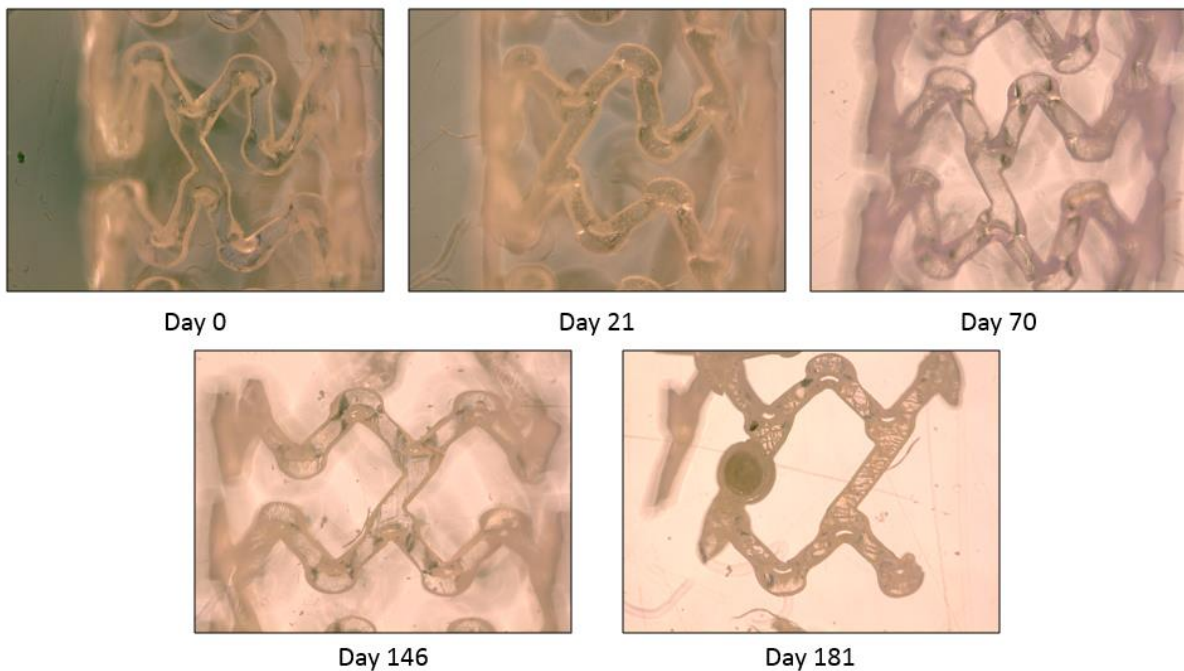


Figure 4.14. Images of non-commercial BRS after radial testing. Scaffold fracture is clear from day 146 onwards. As degradation progresses the scaffolds lose their ability to crimp uniformly, with radially tested samples becoming more deformed after testing. Note the fractures and cracks within the material of the struts.



### 4.3.5 Mechanical Characterisation – Nanoindentation Results

#### 4.3.5.1 Fantom Encore BRS

Figure 4.15(a-d) show the measured reduced elastic modulus and hardness for each time point from nanoindentation testing in the hinge (Figure 4.15(a, c)) and strut regions (Figure 4.15(b, d)), represented in terms of mean  $\pm$  S.D. A large variability in the elastic modulus and hardness was observed for both regions. Indents between the hinge and strut regions show slightly less variance in elastic modulus in hinge regions compared with the struts from days 0-49.

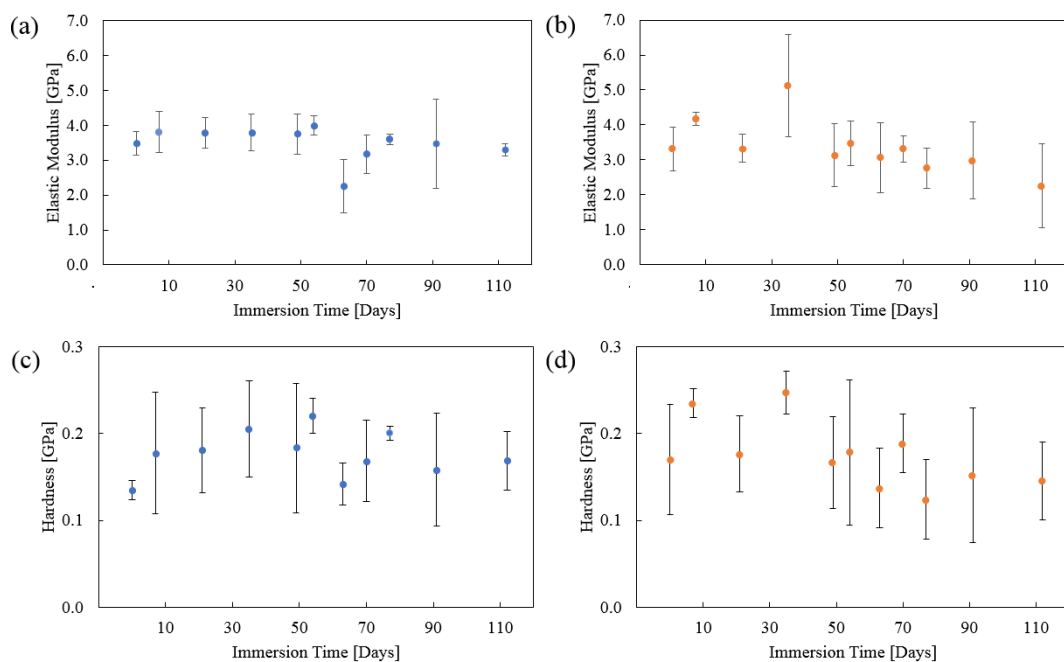


Figure 4.15. Average values of the hinge (a, c) and strut (b, d) regions for Reduced Elastic Modulus and Hardness for each time point tested (average of 7-14 indents per time point) with  $\pm 1$  S.D.

Statistical analysis was performed on the data (t-Tests) with the results shown in Table 4.5. The analysis compared the measured elastic modulus and hardness of all the indents for each time point against those of day 0 to discern any change over the course of the degradation and also compared the hinge versus strut regions for each time point. The majority of the time points showed no significant difference in elastic modulus or hardness either overall or strut versus hinge, with the exception of two time points (days 7 and 35) for the overall comparison that were found to have a significant difference in elastic modulus compared with the day 0 time point.

Table 4.5. Statistical analysis of the nanoindentation performed on the Phantom Encore scaffold (Note that \* denotes a significant difference).

Day	Elastic Modulus (GPa)		Hardness (GPa)	
	P-value (Overall value against day 0)	P-value (Strut vs. hinge regions)	P-value (Overall values against day 0)	P-value (Strut vs. hinge regions)
0	--	0.5916	--	0.1889
7	0.00626*	0.4598	0.0148*	0.3734
21	0.3136	0.0858	0.2232	0.5517
35	0.014*	0.0714	0.0318*	0.4543
49	0.8565	0.2493	0.4082	0.6964
54	0.2561	0.2940	0.1129	0.3100
63	0.00528*	0.9573	0.1084	0.8039
70	0.5311	0.6423	0.2314	0.4645
77	0.3344	0.0763	0.9487	0.0678
91	0.5458	0.5502	0.9684	0.9010
112	0.1328	0.3497	0.8791	0.5503

\* shows results of statistical significant with a 95% confidence level

#### 4.3.5.2 Non-Commercial BRS

Figure 4.16(a-d) shows the measured reduced elastic modulus and hardness for each time point from nanoindentation testing in the hinge (Figure 4.16(a, c)) and strut regions (Figure 4.16(b, d)), represented in terms of mean  $\pm$  S.D. A large variability in the elastic modulus and hardness was observed for both regions.

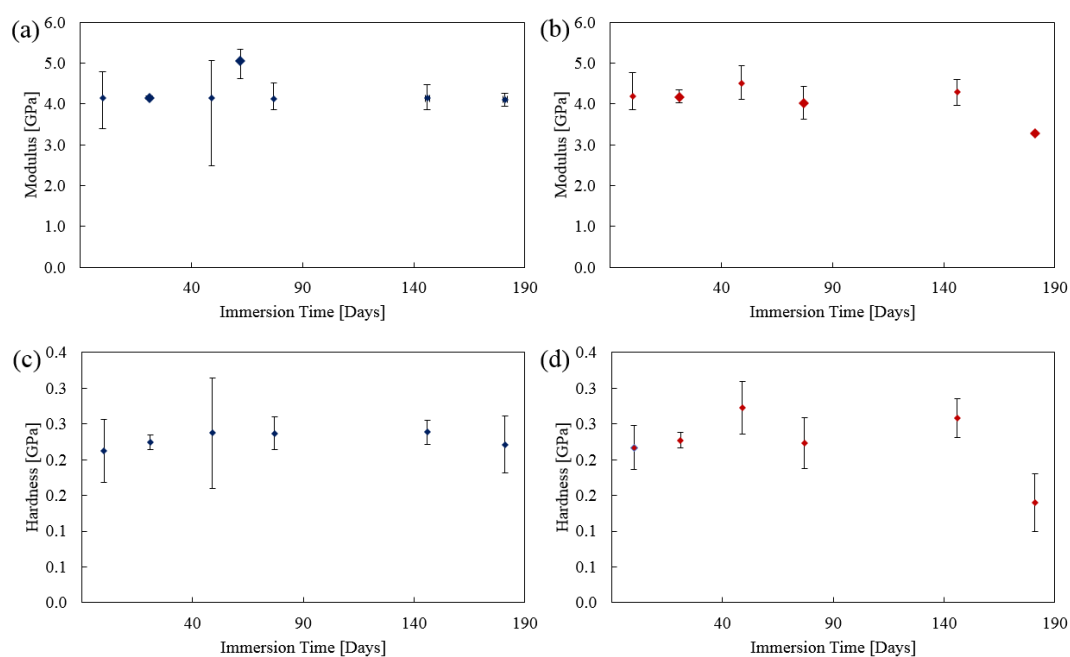


Figure 4.16. Average values of the hinge (a, c) and strut (b, d) regions for Reduced Elastic Modulus and Hardness for each time point tested (average of 5-10 indents per time point) with  $\pm 1$  S.D.

Results from the statistical analysis is shown in Table 4.6 below. As with the Fantom Encore the measured elastic modulus and hardness of all the indents for each time point were compared against those of day 0 to discern any change over the course of the degradation and also compared the hinge versus strut regions for each time point. No significant difference was found between the various time points over the course of the degradation.

*Table 4.6. Statistical analysis of the nano-indentations performed on the non-commercial BRS.*

Day	Elastic Modulus (GPa)		Hardness (GPa)	
	P-Value (Overall value against day 0)	P-value (strut vs. hinge regions)	P-Value (Overall value against day 0)	P-value (strut vs. hinge regions)
0	--	0.90212	--	0.8766
21	0.939125274	0.82457	0.425	0.7464
49	0.661025536	0.48232	0.165	0.47991
77	0.564856944	0.52909	0.364	0.54917
146	0.840997452	0.39107	0.061	0.26776
181	0.349460117	--	0.613	--

#### 4.4 Discussion

In this chapter, a comprehensive evaluation of the mechanical and physical behaviour of two polymeric BRS undergoing a thermally accelerated degradation was presented. The mechanical and physical changes seen over the study can be broken into several stages. The initial stage (Days 0-21), the BRS showed an increase in radial strength and stiffness, with a rapid loss in molecular weight. This stage also showed a slight increase in  $T_m$ . The second stage (Days 35-54 for Fantom Encore and Days 35-77 for non-commercial BRS) saw the increased mechanical strength maintained despite a continued loss in molecular weight, however a reduction in the failure strain was noted on Day 49 for the Fantom Encore, fracture occurred during radial testing. In the final stages (Day 63-112 Fantom Encore and Day 112-146 non-commercial BRS), the load-bearing capacity of both BRS showed continued reduction, with lower radial stiffness and strength, and drastic decreases in the work-to-fracture in both BRS in the final time points. This was particularly evident in the non-commercial BRS which was too brittle to undergo radial testing on days 160 and 181. Throughout each phase, there was an

increase in the relative crystallinity (as observed in the enthalpy changes), with limited mass loss in the scaffolds until the final time point and only minor changes in glass transition and melt temperatures. Limited changes were observed in nano-mechanical properties, with local elastic moduli and hardness values remaining largely similar throughout degradation.

Mechanical testing of both BRS showed an increase in radial strength and stiffness within the first 7 days of immersion. Increased strength was maintained well into the degradation process, despite considerable reductions in molecular weight. Under thermally-accelerated conditions, (Weir *et al.*, 2004), it is expected that the experimental timeframe represents a four-fold increase from physiological conditions, which indicates that the load-bearing capacity of the scaffold would be fully maintained for approximately 8 months at 37°C for the Fantom Encore and 15 months for the non-commercial BRS. In both cases, this timeframe is longer than the typical vessel healing period which is typically 3-6 months (Kastrati *et al.*, 2000). This phenomena of increased strength for a polymer scaffold within the initial stages of degradation has also been observed in real time degradation study of the Abbott Absorb (Qiu *et al.*, 2018), where the increase in strength was attributed to a recrystallization process following hydration of the polymer (Göpferich, 1996). After 49 days of immersion, while radial strength and stiffness were largely maintained, the scaffolds became notably more brittle and fracture of the Fantom Encore BRS occurred shortly after the peak load was reached. This was also particularly evident with the non-commercial BRS in which the final time points could not be mechanically tested. The reduced ductility coincided with increased  $\Delta H_{melt}$ , measured through DSC, which would suggest an increase in relative crystallinity. The polymer's crystalline phase is generally responsible for strength and stiffness (Liu *et al.*, 2014; Dillon *et al.*, 2019), with more amorphous polymers lending ductility to the material as, under loading, the tangled polymer chains untangle, providing a gradual energy dissipation mechanism through plastic deformation. Other studies (Naseem *et al.*, 2019, 2020; Katarzyna *et al.*, 2021) on PLLA-based

materials have also observed increased brittleness that coincides with increases in relative crystallinity. Given that the *in vitro* conditions represented a four-fold acceleration of physiological conditions, these suggest that the BRS samples could exhibit substantially brittle behaviour after approximately one year of implantation. For example, by the final time point, overall fracture of the Fantom Encore BRS samples occurred after a reduction of only 0.2mm of the crimp diameter. By that time, the overall work-to-fracture has reduced by 90% its initial value (e.g. post-deployment). The increasingly brittle behaviour of these devices could pose substantial risk *in vivo* once implanted, as the likelihood of fracture increases (Wang *et al.*, 2018). Stent fracture has been attributed to thrombosis, embolization and ischemic events (Canan and Lee, 2010). A review of clinical trial data from approved BRS by the European Society of Cardiology (Byrne *et al.*, 2018) hypothesised that one of the reasons for excess very late thrombosis seen in human trials could be attributed to an alteration in the laminar flow. The loss in the polymer integrity could be attributed to an increase in brittleness due to re-crystallisation of the polymer.

The degradation of physical properties of the Fantom Encore and non-commercial BRS showed similar behaviour to other PLLA-based materials (Duek *et al.*, 1999; Beslikas *et al.*, 2011; Katarzyna *et al.*, 2021) and BRS devices (Otsuka *et al.*, 2014). The molecular weight substantially reduced to approximately 50% of its original value after only 21 days of immersion. The molecular weight loss is caused by preferential chain scission of the amorphous phase of a polymer due to hydrolysis, with degradation in this phase resulting in an increase in relative crystallinity, similar to other degradation studies (Elsawy *et al.*, 2017). Typically for polymers, loss of molecular weight ( $M_n$ ) results in a reduction in strength (Duek *et al.*, 1999; Renouf-Glauser *et al.*, 2005; Bartkowiak-Jowska *et al.*, 2013), however this was not the case, with the Fantom Encore BRS maintaining radial strength and stiffness similar to other BRS devices (e.g. Abbott Absorb (Qiu *et al.*, 2018; Naseem *et al.*, 2019)). This behaviour

may also be attributed to a lower rate of degradation occurring at the scaffold hinges due to structural changes incurred in the polymer during the deployment and crimping processes (Ramachandran *et al.*, 2018). Nano-indentation testing found no significant difference between the mechanical responses in these two regions. However, a large variation in the elastic modulus was found across the scaffold rings, making it difficult to discern changes throughout the degradation period. This was also seen by Naseem *et al.* (2019) and was attributed to the semi-crystalline nature of the polymer. It was interesting to note that, in general, less variance in the elastic modulus was found in the hinge region compared with the struts.

The first limitation of this study is the use of elevated temperature to accelerate the degradation process compared with degradation at physiological temperatures. This thermally-accelerated protocol established by Weir *et al.* (2004), demonstrated that the mechanism of degradation remains the same once the temperature remains below the  $T_g$  of the polymer. The thermal analysis of the Fantom Encore scaffold polymer found the glass transition of the Tyrocore material to be between 75-80°C, which was higher than the temperature conditions used in this study (e.g. 50°C). Second, the Fantom Encore which consists of the proprietary polymer Tyrocore, and is compared against the current literature of PLLA-based scaffolds. Many of the degradation responses seen with Tyrocore are consistent with other studies performed on other semi-crystalline polymers used for scaffolding applications and also the non-commercial BRS also tested. This includes changes in the mechanical properties (Hayman *et al.*, 2014; Luo *et al.*, 2014; Qiu *et al.*, 2018), rapid loss of molecular weight while maintaining mechanical strength (Otsuka *et al.*, 2014; Yuan *et al.*, 2015), a decrease in the ductility of the material (Duek, *et al.*, 1999) and increases in crystallinity (Bobel *et al.*, 2016).

## 4.5 Conclusion

In this chapter, a systematic evaluation of the mechanical and physical properties of the Reva Medical Fantom Encore and a non-commercial BRS subjected to an accelerated degradation

protocol was presented. From Day 0 to Day 21, the Fantom Encore BRS showed increased radial strength and stiffness, despite a substantial reduction in molecular weight. Between Days 35-54, radial stiffness and strength of the Fantom Encore BRS were maintained despite a continued loss in molecular weight. In the final phase (Day 63-112), the load-bearing capacity of the Fantom Encore BRS reduced, but most notably, the devices exhibit drastic losses in ductility, with their overall work-to-fracture being reduced to <10% their initial value. A similar trend was shown for the non-commercial BRS, with an immediate increase in radial strength and stiffness (Day 0 to 7). The non-commercial BRS also experienced a decrease in molecular weight and increase in crystallinity over the course of the degradation period. The radial strength was maintained despite the decrease in molecular weight to Day 77 before fracture of the BRS occurred. In the case of the non-commercial BRS the final time-points could not be mechanically tested due to the BRS becoming too brittle. Considering the accelerated timeframe of this in vitro study, these results indicate that these BRS could see substantial risk of fracture in a clinical setting in the second year following implantation.

## 4.6 References

- Abizaid, Alexandre, Didier Carrié, Norbert Frey, Matthias Lutz, Joachim Weber-Albers, Darius Dudek, Bernard Chevalier, et al. 2017. “6-Month Clinical and Angiographic Outcomes of a Novel Radiopaque Sirolimus-Eluting Bioresorbable Vascular Scaffold: The FANTOM II Study.” *JACC: Cardiovascular Interventions* 10 (18): 1832–38. <https://doi.org/10.1016/j.jcin.2017.07.033>.
- Bartkowiak-Jowska, Magdalena, Romuald Będziński, Anna Kozłowska, Jarosław Filipiak, and Celina Pezowicz. 2013. “Mechanical, Rheological, Fatigue, and Degradation Behavior of PLLA, PGLA and PDGLA as Materials for Vascular Implants.” *Meccanica* 48 (3): 721–31. <https://doi.org/10.1007/s11012-012-9626-2>.
- Beslikas, Theodore, Ioannis Gigis, Vasilios Goulios, John Christoforides, George Z. Papageorgiou, and Dimitrios N. Bikiaris. 2011. “Crystallization Study and Comparative in Vitro-in Vivo Hydrolysis of PLA Reinforcement Ligament.” *International Journal of Molecular Sciences* 12 (10): 6597–6618. <https://doi.org/10.3390/ijms12106597>.
- Bobel, Anna C., Stefan Lohfeld, Reyhaneh Neghabat Shirazi, and Peter E. McHugh. 2016. “Experimental Mechanical Testing of Poly (L-Lactide) (PLLA) to Facilitate Pre-Degradation Characteristics for Application in Cardiovascular Stenting.” *Polymer Testing* 54: 150–58. <https://doi.org/10.1016/j.polymertesting.2016.07.011>.
- Burkersroda, FrieDerike von, Luise Schedl, and Achim Gopferich. 2002. “Why Degradable Polymers Undergo Surface Erosion or Bulk Erosion.” *Biomaterials* 23: 4221–31.
- Byrne, Robert A, Giulio G Stefanini, Davide Capodanno, Yoshinobu Onuma, Andreas Baumbach, Javier Escaned, Michael Haude, Stefan James, Michael Joner, and Peter Ju. 2018. “Report of an ESC-EAPCI Task Force on the Evaluation and Use of Bioresorbable Scaffolds for Percutaneous Coronary Intervention: Executive Summary.” *European Heart Journal* 39 (July): 1591–1601. <https://doi.org/10.4244/EIJ20170912-01>.
- Canan, Timothy, and Michael S. Lee. 2010. “Drug-Eluting Stent Fracture: Incidence, Contributing Factors, and Clinical Implications.” *Catheterization and Cardiovascular Interventions* 75 (2): 237–45. <https://doi.org/10.1002/ccd.22212>.
- Cassese, Salvatore, Robert A. Byrne, Gjin Ndrepepa, Sebastian Kufner, Jens Wiebe, Janika Repp, Heribert Schunkert, Massimiliano Fusaro, Takeshi Kimura, and Adnan Kastrati. 2016. “Everolimus-Eluting Bioresorbable Vascular Scaffolds versus Everolimus-Eluting Metallic Stents: A Meta-Analysis of Randomised Controlled Trials.” *The Lancet* 387 (10018): 537–44. [https://doi.org/10.1016/S0140-6736\(15\)00979-4](https://doi.org/10.1016/S0140-6736(15)00979-4).
- Cheng, J, B Liu, Y H Wu, and Y F Zheng. 2013. “Comparative in Vitro Study on Pure Metals ( Fe , Mn , Mg , Zn and W ) as Biodegradable Metals” 29 (7): 619–27. <https://doi.org/10.1016/j.jmst.2013.03.019>.
- Chevalier, Bernard, Alexandre Abizaid, Didier Carrié, Norbert Frey, Matthias Lutz, Joachim Weber-Albers, Darius Dudek, et al. 2019. “Clinical and Angiographic Outcomes with a Novel Radiopaque Sirolimus-Eluting Bioresorbable Vascular Scaffold: The FANTOM II Study.” *Circulation: Cardiovascular Interventions* 12 (6): 1–8. <https://doi.org/10.1161/CIRCINTERVENTIONS.118.007283>.
- Dillon, Brian, Patrick Doran, Evert Fuenmayor, Andrew V. Healy, Noel M. Gately, Ian Major, and John G. Lyons. 2019. “Influence of Annealing and Biaxial Expansion on the Properties of Poly(l-Lactic



- Acid) Medical Tubing.” *Polymers* 11 (7). <https://doi.org/10.3390/polym11071172>.
- Duek, E. A.R., C. A.C. Zavaglia, and W. D. Belangero. 1999. “In Vitro Study of Poly(Lactic Acid) Pin Degradation.” *Polymer* 40 (23): 6465–73. [https://doi.org/10.1016/S0032-3861\(98\)00846-5](https://doi.org/10.1016/S0032-3861(98)00846-5).
- Elsawy, Moataz A., Ki Hyun Kim, Jae Woo Park, and Akash Deep. 2017. “Hydrolytic Degradation of Polylactic Acid (PLA) and Its Composites.” *Renewable and Sustainable Energy Reviews* 79 (June 2016): 1346–52. <https://doi.org/10.1016/j.rser.2017.05.143>.
- Fischer, E W, Hans J Sterzel, and G Wegner. 1973. “Investigation of the Structure of Solution Grown Crystals of Lactide Copolymers by Means of Chemical Reactions.” *Z. Polymere*. Vol. 251.
- Garg, Scot, Christos Bourantas, and Patrick W Serruys. 2013. “New Concepts in the Design of Drug-Eluting Coronary Stents.” *Nature Reviews Cardiology* 10 (5): 248–60. <https://doi.org/10.1038/nrcardio.2013.13>.
- Gonzalo, Nieves, Nieves Gonzalo, and Carlos Macaya. 2012. “Absorbable Stent: Focus on Clinical Applications and Benefits.” *Vascular Health and Risk Management*, February, 125. <https://doi.org/10.2147/VHRM.S22551>.
- Göpferich, Achim. 1996. “Mechanisms of Polymer Degradation and Erosion1.” *The Biomaterials: Silver Jubilee Compendium* 17 (2): 117–28. <https://doi.org/10.1016/B978-008045154-1.50016-2>.
- Hayman, Danika, Christie Bergerson, Samantha Miller, Michael Moreno, and James E. Moore. 2014. “The Effect of Static and Dynamic Loading on Degradation of PLLA Stent Fibers.” *Journal of Biomechanical Engineering* 136 (8). <https://doi.org/10.1115/1.4027614>.
- ISO. 2010. “International Standard 14283-2004 Implants for Surgery.” *ISO* 2010.
- Kastrati, A., D. Hall, and A. Schömig. 2000. “Long-Term Outcome after Coronary Stenting.” *Current Controlled Trials in Cardiovascular Medicine* 1 (1): 48–54. <https://doi.org/10.1186/CVM-1-1-048>.
- Katarzyna, Polak-Krasna, Ali Reza Abaei, Reyhaneh Neghabat Shirazi, Eoin Parle, Oliver Carroll, William Ronan, and Ted J Vaughan. 2021. “Physical and Mechanical Degradation Behaviour of Semi-Crystalline PLLA for Bioresorbable Stent Applications.” *Journal of the Mechanical Behaviour of Biomedical Materials*, 135938. <https://doi.org/10.1016/j.jmbbm.2021.104409>.
- Kereiakes, Dean J., Stephen G. Ellis, Christopher Metzger, Ronald P. Caputo, David G. Rizik, Paul S. Teirstein, Marc R. Litt, et al. 2017. “3-Year Clinical Outcomes With Everolimus-Eluting Bioresorbable Coronary Scaffolds: The ABSORB III Trial.” *Journal of the American College of Cardiology* 70 (23): 2852–62. <https://doi.org/10.1016/j.jacc.2017.10.010>.
- Kraak, Robin P., Mariëlla E.C.J. Hassell, Maik J. Grundeken, Karel T. Koch, Jose P.S. Henriques, Jan J. Piek, Jan Baan, et al. 2015. “Initial Experience and Clinical Evaluation of the Absorb Bioresorbable Vascular Scaffold (BVS) in Real-World Practice: The AMC Single Centre Real World PCI Registry.” *EuroIntervention* 10 (11): 1160–68. [https://doi.org/10.4244/EIJY14M08\\_08](https://doi.org/10.4244/EIJY14M08_08).
- Kufner, Sebastian, Michael Joner, Anna Thannheimer, Petra Hoppmann, Tareq Ibrahim, Katharina Mayer, Salvatore Cassese, et al. 2019. “Ten-Year Clinical Outcomes From a Trial of Three Limus-Eluting Stents With Different Polymer Coatings in Patients With Coronary Artery Disease: Results From the ISAR-TEST 4 Randomized Trial.” *Circulation* 139 (3): 325–33. <https://doi.org/10.1161/CIRCULATIONAHA.118.038065>.
- Lipinski, Michael J., Ricardo O. Escarcega, Nevin C. Baker, Hadiya A. Benn, Michael A. Gaglia,

- Rebecca Torguson, and Ron Waksman. 2016. "Scaffold Thrombosis after Percutaneous Coronary Intervention with ABSORB Bioresorbable Vascular Scaffold A Systematic Review and Meta-Analysis." *JACC: Cardiovascular Interventions* 9 (1): 12–24. <https://doi.org/10.1016/j.jcin.2015.09.024>.
- Liu, Guoming, Xiuqin Zhang, and Dujin Wang. 2014. "Tailoring Crystallization: Towards High-Performance Poly (Lactic Acid)." *Advanced Materials* 26 (40): 6905–11. <https://doi.org/10.1002/adma.201305413>.
- Luo, Qiyi, Xiangkun Liu, Zhonghua Li, Chubo Huang, Wen Zhang, Juan Meng, Zhaohua Chang, and Zezhao Hua. 2014. "Degradation Model of Bioabsorbable Cardiovascular Stents." *PLoS ONE* 9 (11): 1–9. <https://doi.org/10.1371/journal.pone.0110278>.
- Lyu, Su Ping, James Schley, Brian Loy, Deanna Lind, Christopher Hobot, Randall Sparer, and Darrel Untereker. 2007. "Kinetics and Time-Temperature Equivalence of Polymer Degradation." *Biomacromolecules* 8 (7): 2301–10. <https://doi.org/10.1021/bm070313n>.
- McKenna, Ciara G., and Ted J. Vaughan. 2020. "An Experimental Evaluation of the Mechanics of Bare and Polymer-Covered Self-Expanding Wire Braided Stents." *Journal of the Mechanical Behavior of Biomedical Materials* 103 (October 2019): 103549. <https://doi.org/10.1016/j.jmbbm.2019.103549>.
- Moussa, Issam D., Divyanshu Mohananey, Jorge Saucedo, Gregg W. Stone, Robert W. Yeh, Kevin F. Kennedy, Ron Waksman, Paul Teirstein, Jeffrey W. Moses, and Chuck Simonton. 2020. "Trends and Outcomes of Restenosis After Coronary Stent Implantation in the United States." *Journal of the American College of Cardiology* 76 (13): 1521–31. <https://doi.org/10.1016/j.jacc.2020.08.002>.
- Naseem, Raasti, Ligu Zhao, Senthil K. Eswaran, and Helen Willcock. 2020. "Characterization of Biodegradable Poly(L-Lactide) Tube over Accelerated Degradation." *Polymer Engineering and Science* 60 (7): 1430–36. <https://doi.org/10.1002/pen.25390>.
- Naseem, Raasti, Ligu Zhao, Vadim Silberschmidt, Yang Liu, Ollie Scaife, Helen Willcock, Senthil Eswaran, and Syed Hossainy. 2019. "Mechanical and Chemical Characterisation of Bioresorbable Polymeric Stent over Two-Year in Vitro Degradation." *Journal of Biomaterials Applications* 34 (1): 61–73. <https://doi.org/10.1177/0885328219839591>.
- Nuutinen, Juha Pekka, Claude Clerc, Raija Reinikainen, and Pertti Törmälä. 2003. "Mechanical Properties and in Vitro Degradation of Bioabsorbable Self-Expanding Braided Stents." *Journal of Biomaterials Science, Polymer Edition* 14 (3): 255–66. <https://doi.org/10.1163/156856203763572707>.
- Oliver, W C, and G M Pharr. 1992. "An Improved Technique for Determining Hardness and Elastic Modulus Using Load and Displacement Sensing Indentation Experiments." *Journal of Materials Research*. [http://www.journals.cambridge.org/abstract%7B\\_%7DS0884291400017039](http://www.journals.cambridge.org/abstract%7B_%7DS0884291400017039).
- Otsuka, Fumiyuki, Erica Pacheco, Laura E.L. Perkins, Jennifer P. Lane, Qing Wang, Marika Kamberi, Michael Frie, et al. 2014. "Long-Term Safety of an Everolimus-Eluting Bioresorbable Vascular Scaffold and the Cobalt-Chromium XIENCE v Stent in a Porcine Coronary Artery Model." *Circulation: Cardiovascular Interventions* 7 (3): 330–42. <https://doi.org/10.1161/CIRCINTERVENTIONS.113.000990>.
- Patel, Amisha, Tamim Nazif, Gregg W. Stone, and Ziad A. Ali. 2017. "Intraluminal Bioresorbable Vascular Scaffold Dismantling with Aneurysm Formation Leading to Very Late Thrombosis." *Catheterization and Cardiovascular Interventions* 89 (5): 876–79. <https://doi.org/10.1002/ccd.26913>.

Properties, Tyrocore. 2018. “Design of the Novel Tyrocore Polymer for the Next Generation of Thin Strut , Radiopaque Bioresorbable Scaffolds,” 3–4.

Qiu, T., R. He, C. Abunassar, S. Hossainy, and L. G. Zhao. 2018. “Effect of Two-Year Degradation on Mechanical Interaction between a Bioresorbable Scaffold and Blood Vessel.” *Journal of the Mechanical Behavior of Biomedical Materials* 78 (November 2017): 254–65. <https://doi.org/10.1016/j.jmbbm.2017.11.031>.

Räber, Lorenz, Salvatore Brugaletta, Kyohei Yamaji, Crochan J. O’Sullivan, Shuji Otsuki, Tobias Koppa, Masanori Taniwaki, et al. 2015. “Very Late Scaffold Thrombosis: Intracoronary Imaging and Histopathological and Spectroscopic Findings.” *Journal of the American College of Cardiology* 66 (17): 1901–14. <https://doi.org/10.1016/j.jacc.2015.08.853>.

Ramachandran, Karthik, Tiziana Di Luccio, Artemis Ailianou, Mary Beth Kossuth, James P. Oberhauser, and Julia A. Kornfield. 2018. “Crimping-Induced Structural Gradients Explain the Lasting Strength of Poly L-Lactide Bioresorbable Vascular Scaffolds during Hydrolysis.” *Proceedings of the National Academy of Sciences of the United States of America* 115 (41): 10239–44. <https://doi.org/10.1073/pnas.1807347115>.

Renouf-Glauser, Annette C., John Rose, David F. Farrar, and Ruth Elizabeth Cameron. 2005. “The Effect of Crystallinity on the Deformation Mechanism and Bulk Mechanical Properties of PLLA.” *Biomaterials* 26 (29): 5771–82. <https://doi.org/10.1016/j.biomaterials.2005.03.002>.

Serruys, Patrick W., Bernard Chevalier, Yohei Sotomi, Angel Cequier, Didier Carrié, Jan J. Piek, Ad J. Van Boven, et al. 2016. “Comparison of an Everolimus-Eluting Bioresorbable Scaffold with an Everolimus-Eluting Metallic Stent for the Treatment of Coronary Artery Stenosis (ABSORB II): A 3 Year, Randomised, Controlled, Single-Blind, Multicentre Clinical Trial.” *The Lancet* 388 (10059): 2479–91. [https://doi.org/10.1016/S0140-6736\(16\)32050-5](https://doi.org/10.1016/S0140-6736(16)32050-5).

Serruys, Patrick W., John A. Ormiston, Yoshinobu Onuma, Evelyn Regar, Nieves Gonzalo, Hector M. Garcia-Garcia, Koen Nieman, et al. 2009. “A Bioabsorbable Everolimus-Eluting Coronary Stent System (ABSORB): 2-Year Outcomes and Results from Multiple Imaging Methods.” *The Lancet* 373 (9667): 897–910. [https://doi.org/10.1016/S0140-6736\(09\)60325-1](https://doi.org/10.1016/S0140-6736(09)60325-1).

Shirazi, Reyhaneh Neghabat, Fawaz Aldabbagh, Andrea Erxleben, Yury Rochev, and Peter McHugh. 2014. “Nanomechanical Properties of Poly(Lactic-Co-Glycolic) Acid Film during Degradation.” *Acta Biomaterialia* 10 (11): 4695–4703. <https://doi.org/10.1016/j.actbio.2014.08.004>.

Singh, Achintya D., Aayush K. Singal, Agrima Mian, Samir R. Kapadia, David P. Hedrick, Anmar Kanaa’N, Jaikirshan J. Khatri, Rishi Puri, and Ankur Kalra. 2020. “Recurrent Drug-Eluting Stent In-Stent Restenosis: A State-of-the-Art Review of Pathophysiology, Diagnosis, and Management.” *Cardiovascular Revascularization Medicine* 21 (9): 1157–63. <https://doi.org/10.1016/j.carrev.2020.01.005>.

Song, Guangling, and Andrej Atrens. 2003. “Understanding Magnesium Corrosion. A Framework for Improved Alloy Performance.” *Advanced Engineering Materials* 5 (12): 837–58. <https://doi.org/10.1002/adem.200310405>.

Sorrentino, Sabato, Gennaro Giustino, Roxana Mehran, Anapoorna S. Kini, Samin K. Sharma, Michela Faggioni, Serdar Farhan, Birgit Vogel, Ciro Indolfi, and George D. Dangas. 2017. “Everolimus-Eluting Bioresorbable Scaffolds Versus Everolimus-Eluting Metallic Stents.” *Journal of the American College of Cardiology* 69 (25): 3055–66. <https://doi.org/10.1016/j.jacc.2017.04.011>.

- Stone, Gregg W., and Juan F. Granada. 2015. "Very Late Thrombosis After Bioresorbable Scaffolds." *Journal of the American College of Cardiology* 66 (17): 1915–17. <https://doi.org/10.1016/j.jacc.2015.08.863>.
- Tsuji, Hideto, and Yoshito Ikada. 2000. "Properties and Morphology of Poly(L-Lactide) 4. Effects of Structural Parameters on Long-Term Hydrolysis of Poly(L-Lactide) in Phosphate-Buffered Solution." *Polymer Degradation and Stability* 67 (1): 179–89. [https://doi.org/10.1016/S0141-3910\(99\)00111-1](https://doi.org/10.1016/S0141-3910(99)00111-1).
- Tsuji, Hideto, Akira Mizuno, and Yoshito Ikada. 2000. "Properties and Morphology of Poly(L-Lactide). III. Effects of Initial Crystallinity on Long-Term In Vitro Hydrolysis of High Molecular Weight Poly(L-Lactide) Film in Phosphate-Buffered Solution." *Journal of Applied Polymer Science* 77 (7): 1452–64. [https://doi.org/10.1002/1097-4628\(20000815\)77:7<1452::AID-APP7>3.0.CO;2-S](https://doi.org/10.1002/1097-4628(20000815)77:7<1452::AID-APP7>3.0.CO;2-S).
- Wang, Pei Jiang, Nicola Ferralis, Claire Conway, Jeffrey C. Grossman, and Elazer R. Edelman. 2018. "Strain-Induced Accelerated Asymmetric Spatial Degradation of Polymeric Vascular Scaffolds." *Proceedings of the National Academy of Sciences of the United States of America* 115 (11): 2640–45. <https://doi.org/10.1073/pnas.1716420115>.
- Wang, Qian, Gang Fang, Yinghong Zhao, Guohui Wang, and Tao Cai. 2017. "Computational and Experimental Investigation into Mechanical Performances of Poly-L-Lactide Acid (PLLA) Coronary Stents." *Journal of the Mechanical Behavior of Biomedical Materials* 65: 415–27. <https://doi.org/10.1016/j.jmbbm.2016.08.033>.
- Weir, N. A., F. J. Buchanan, J. F. Orr, and G. R. Dickson. 2004. "Degradation of Poly-L-Lactide. Part 1: In Vitro and in Vivo Physiological Temperature Degradation." *Proceedings of the Institution of Mechanical Engineers, Part H: Journal of Engineering in Medicine* 218 (5): 307–19. <https://doi.org/10.1243/0954411041932782>.
- Weir, N A, F J Buchanan, J F Orr, D F Farrar, and G R Dickson. 2004. "Degradation of Poly-L-Lactide. Part 2: Increased Temperature Accelerated Degradation." *Proceedings of the Institution of Mechanical Engineers, Part H: Journal of Engineering in Medicine* 218 (5): 321–30. <https://doi.org/10.1243/0954411041932809>.
- Wise, J., K. T. Gillen, and R. L. Clough. 1995. "An Ultrasensitive Technique for Testing the Arrhenius Extrapolation Assumption for Thermally Aged Elastomers." *Polymer Degradation and Stability* 49 (3): 403–18. [https://doi.org/10.1016/0141-3910\(95\)00137-B](https://doi.org/10.1016/0141-3910(95)00137-B).
- Yuan, Yuan, Xiaoyun Jin, Zhongyong Fan, Suming Li, and Zhiqian Lu. 2015. "In Vivo Degradation of Copolymers Prepared from L-Lactide, 1,3-Trimethylene Carbonate and Glycolide as Coronary Stent Materials." *Journal of Materials Science: Materials in Medicine* 26 (3): 1–9. <https://doi.org/10.1007/s10856-015-5384-8>.
- Zilberman, Meital, Kevin D. Nelson, and Robert C. Eberhart. 2005. "Mechanical Properties and in Vitro Degradation of Bioresorbable Fibers and Expandable Fiber-Based Stents." *Journal of Biomedical Materials Research - Part B Applied Biomaterials* 74 (2): 792–99. <https://doi.org/10.1002/jbm.b.30319>.

# Chapter 5

## Development, Implementation and Validation of a Phenomenological Degradation Model for a Polymeric Bioresorbable Scaffold

---

### 5.1. Introduction

Bioresorbable scaffolds (BRS) provide temporary mechanical support to the vessel in which they are implanted before the passive and physiological processes of the body lead to their gradual degradation. Through this degradation process, BRS have the potential to avoid some of the late-stage complications of drug eluting stents (DES) such as restenosis and thrombosis (Räber et al. 2015; Singh *et al.* 2020; Kan *et al.* 2016). Polymer BRS consisting of Poly-lactic acid (PLLA) and other proprietary polymers had initially shown promise, with short-term clinical outcomes of the Abbott Absorb (Serruys *et al.* 2009; Kraak *et al.* 2015), Igaki-Tamai BRS (Nishio *et al.* 2012) and Reva Medical Fantom (Chevalier et al. 2019; Abizaid *et al.* 2017) being non-inferior to permanent DES. However, more recent follow ups of polymer BRS have shown increased incidences of long-term complications when compared to permanent DES (Lipinski et al. 2016; Cassese *et al.* 2016; Serruys *et al.* 2016), such as increased rates of stent thrombosis and myocardial infarction. While the underlying reasons for the inferior late-stage performance of bioresorbable devices has largely been attributed to strut thickness, strut fracture upon loss of integrity of the scaffold backbone may also be a contributing factor (Byrne *et al.* 2018) and there is a clear need for robust predictions of device performance over their lifetime to better understand failure of these devices.

Semi-crystalline polymers typically degrade through the process of hydrolysis (Weir et al. 2004; Gleadall *et al.* 2014) in which water from the surrounding environment is absorbed and breaks down the ester bonds of the amorphous phase. Degradation results in molecular weight loss due to scission of the ester bonds (Vey *et al.* 2008; Weir *et al.* 2004) and can result in an increase in the measured crystallinity owing to biased cleavage of the ester bonds in the amorphous phase (Duek *et al.*, 1999) leading to complicated changes in mechanical performance. For these devices, the degradation kinetics and temporal evolution of these parameters can also vary substantially depending on polymer composition, processing parameters and a range of environmental factors, such as temperature, loading conditions and surrounding environment (Bergström 2015; Simamora and Chern 2006). As a consequence, experimental studies on PLLA have shown that degradation can have varying effects on mechanical properties, leading to deterioration in elastic modulus (Naseem *et al.* 2020; Duek, Zavaglia, and Belangero 1999), failure strain (Katarzyna *et al.* 2021; Renouf-Glauser *et al.* 2005; Tsuji and Ikada 2000, Chapter 4) or yield stress (Qiu *et al.*, 2018) to varying degrees. As a consequence, there are significant challenges to providing reliable modelling predictions of mechanical performance in the implanted environment. The majority of computational modelling studies on polymer BRS have focused on predicting the short-term performance of these devices. For example, many studies have simulated in vitro bench testing protocols (e.g. radial force, bending behaviour, crush resistance) to predict functional device properties (Bobel *et al.* 2015; Hoddy *et al.*, 2022) and predicted the implantation performance of BRS (Antonini, Poletti, *et al.* 2021; Debusschere *et al.* 2015). Unlike their metallic counterparts, the deployment behaviour of polymeric BRS are more sensitive to rate-dependent aspects of the procedure (e.g. inflation rate) and recent phenomenological models have been proposed to take into account these aspects when dealing with computational analysis of BRS (Antonini, Berti, *et al.* 2021; Antonini, Poletti, *et al.* 2021). However, the prediction of the long-term

performance of implanted polymer-based BRS presents significant challenges as the degradation process is influenced by many factors including loading rate, loading history, temperature and environmental conditions.

Due to long-time scales required to fully degrade PLLA, in the order of 2-3 years (Qiu et al. 2018; Naseem et al. 2019; Nishio et al. 2012), accelerated degradation protocols and development of computational degradation models, both physical and phenomenological, have been used to better understand the degradation of polymer BRS (Chapter 4). However, from the experimental work carried out in Chapter 4, there is complex evolving relationship between microstructural properties (e.g. molecular weight, degree of crystallinity) and the deterioration in mechanical properties (e.g. stiffness, strength, and ductility) during degradation. As a consequence, there are limited examples of physically-based computational models being used to predict aspects of the mechanical performance in bioresorbable devices undergoing degradation (Shine *et al.*, 2021; Shazly *et al.* 2012). Instead, predicting the long-term degradation performance of polymer based BRS devices have generally relied on phenomenological approaches to describe the degradation of the mechanical properties of the structure. These methods generally use a continuum damage mechanics framework to introduce phenomenological degradation variable(s) that operate on one, or several, of the constitutive material parameters to predict material degradation (Soares *et al.*, 2008; Luo *et al.* 2014; Amnieh *et al.* 2021). However, these approaches generally rely on substantial amounts of calibration for the model parameters (Boland *et al.* 2016) to capture effects observed during degradation and have rarely been validated beyond a limited set of circumstances. Furthermore, these approaches have been limited as they are not compatible with short-term constitutive models, which account for time dependent elastic and/or plastic behaviour during the deployment phase. There is a distinct need for consistency in the approaches used to predict

both short and long-term performance of polymer-based BRS, and to develop reliable model comparators that can independently evaluate the level of model credibility.

The aim of this chapter is to develop a robust computational phenomenological degradation framework that can predict short- and long-term degradation behaviour of a polymer BRS. The radial experimental behaviour of the non-commercial PLLA BRS in the previous chapter forms the basis for the model development, whereby both the short- and long-term performance of this device is predicted through a phenomenological elasto-viscoplastic degradation framework at a device level. Two separate model comparators are used in an effort to validate the developed model, whereby the non-commercial BRS is deployed within a silicone tube and subjected to an accelerated degradation protocol. Due to several distinct phenomena that take place in the early phase of degradation, an additional experimental validation is carried out by investigating the response of the non-commercial BRS under constant parallel plate compression loading for a time period of one week.

## **5.2. Methods**

### **5.2.1 Model Geometry**

The radial compression data from the non-commercial BRS investigated in Chapter 4 was used as a basis to calibrate the long-term degradation framework. A three-dimensional model of the BRS was created from two-dimensional drawings. This process used a repeating segment of the scaffold, which was drawn and meshed in Abaqus, bi-linearly patterned and then wrapped into a cylindrical coordinate system to create a fully expanded scaffold geometry. The BRS geometry was discretised with C3D8R (8-node linear brick, reduced integration, hourglass control) elements and is shown in Figure 5.1. For calibrating the model parameters of the degradation framework, a unit-cell geometry was used that had 23,928 C3D8R elements, as



shown in the inset to Figure 5.1. For the validation models, the entire scaffold geometry was used, which consisted of 187,260 C3D8R elements.

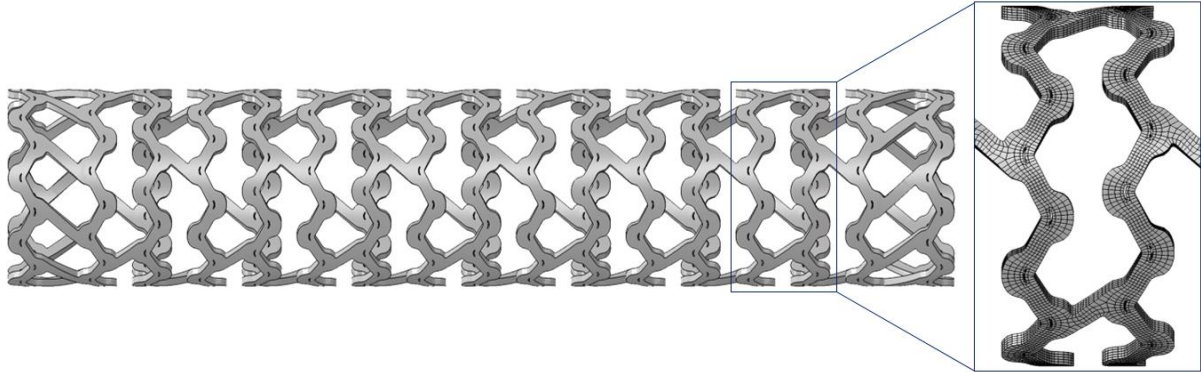


Figure 5.1. Schematic showing the non-commercial BRS geometry and zoomed image with the discretisation.

## 5.2.2 Material and Degradation Framework Description

In the implementation of the current phenomenological degradation framework, a set of degradation parameters ( $d_1$ ,  $d_2$ ,  $d_3$ ) are introduced that control the evolution of mechanical properties as a function of time ( $t$ ). This is implemented in a finite element framework through a continuum damage mechanics (CDM) based approach, whereby in the absence of yielding, the scalar damage variable  $d_1(t)$  is used to degrade the elastic response of the material over time such and is described by,

$$E(t) = E(1 - d_1) \quad (5-1)$$

The Johnson-Cook material model was chosen as the constitutive material model to describe the yield behaviour of the polymer BRS. Previous studies (Antonini, Poletti, *et al.* 2021; Antonini, Berti, *et al.* 2021; Wang *et al.* 2020) have suggested the use of elastic-viscoplastic material models to capture the rate-dependant loading behaviour demonstrated experimentally by PLLA. The Johnson-Cook model has the following form and is essentially a visco-plastic, or strain-rate dependent, version of the von Mises yield function, which is given by,

$$\bar{\sigma}_e = \left[ A + B(\bar{\epsilon}^{pl})^n \right] \left[ 1 + C \ln \left( \frac{\dot{\bar{\epsilon}}^{pl}}{\dot{\epsilon}_0} \right) \right] [1 - \hat{\theta}^m] \quad (5-2)$$

Where  $\bar{\sigma}_e$  is the material yield stress,  $\bar{\epsilon}^{pl}$  is the equivalent plastic strain,  $\dot{\bar{\epsilon}}^{pl}$  is the equivalent plastic strain rate and  $\dot{\epsilon}_0$  is the reference strain rate used to determine the model constants;  $A$ ,  $B$ ,  $C$ ,  $n$  and  $m$ . Here, the first bracketed term accounts for the yield and strain hardening effects, which are commonly described by a power law of this form. The second bracketed term accounts for the rate-dependence of the yield function, which here is driven by the  $\dot{\bar{\epsilon}}^{pl}$  equivalent plastic strain rate term. The final bracketed term in the Johnson-Cook model accounts possible temperature-dependence in the material response.

The phenomenological degradation framework enables the Johnson-Cook yield surface to evolve over time, by making use of the temperature-dependence term within the original model. This feature is used this to degrade the yield stress of the material over time, whereby equation ( 5-1 ) introduces the degradation parameter ( $d_2$ ) in place of  $\hat{\theta}$ ,

$$\bar{\sigma}(t) = \left[ A + B(\bar{\epsilon}^{pl})^n \right] \left[ 1 + C \ln \left( \frac{\dot{\bar{\epsilon}}^{pl}}{\dot{\epsilon}_0} \right) \right] [1 - d_2(t)] \quad (5-1)$$

Finally, failure of the material may be captured using a strain-based failure criteria described through Equation ( 5-7 ) implemented through the ductile damage framework in Abaqus. Damage initiation was controlled by the equivalent plastic strain, whereby damage initiation was described by a critical value of equivalent plastic strain  $\bar{\epsilon}^{pl}$  (according to the shear damage in the material. Degradation of the equivalent plastic strain at failure was controlled through,

$$\bar{\epsilon}^{pl}(t) = \bar{\epsilon}^{pl}(1 - d_3) \quad (5-2)$$

Damage evolution ( $\phi$ ) was implemented through a user-specified failure criterion, where upon damage initiation, the element linearly displaces a specified amount before failing. The evolution of this damage variable increases according to,

$$\phi = \frac{L\dot{\bar{\epsilon}}^{pl}}{\bar{u}_f^{pl}} = \frac{\dot{u}^{pl}}{u_f^{pl}} \quad (5-3)$$

Where  $L$  is the characteristic element length,  $\dot{\varepsilon}^{pl}$  is the plastic strain,  $\dot{u}^{pl}$  is the effective plastic displacement and  $\bar{u}_f^{pl}$  is the plastic displacement at failure. Once the damage variable reaches one, the material stiffness in that element will be fully damaged and is reduced to a zero stress state.

This phenomenological degradation framework was implemented through the Abaqus/Explicit finite element solver, whereby the degradation parameter  $d_2$  was controlled using a temperature field variable, while  $d_1$  and  $d_3$  are evolved within a user defined field subroutine (VUSDFLD) where a linear interpolation is used to obtain values of the dependant variable in the regions between the defined points for  $d_2$  and  $d_3$  is evolved through equation ( 5-2 ). Within each of the degradation parameter equations,  $d_i=0$  represented the case where the material parameter was in its un-degraded state, while  $d_i=1$  represented the case where that material property was fully degraded.

### 5.2.3 Model Verification – Single Element Test

To test the phenomenological degradation framework, a single element (C3D8R) measuring 1x1x1 mm element under axial tension was considered, over two steps: (i) a degradation step, whereby the degradation framework was implemented and (ii) a uniaxial loading step, whereby the unit cube was subjected to displacement-driven uniaxial tension of 0.5mm, applied through a reference point that was kinematically coupled to the element face. The load was applied at a rate of 0.05 mm/s. Four cases were considered, (i) the elastic modulus of the material was degraded by linearly decreasing the  $d_1$  parameter, (ii) the yield surface of the material was degraded by linearly decreasing the  $d_2$  parameter (iii) the overall failure strain of the material was degraded by linearly decreasing the  $d_3$  parameter, (iv) all parameters ( $d_1$ ,  $d_2$ ,  $d_3$ ) were degraded linearly in combination. In each of these cases, these parameters were decreased to 25%, of their original shown in Figure 5.2(a). The same baseline material parameters used for

the device were assumed for the unit cube (described in the following section). The stress and strain response from these simulations were then extracted from the reference point to verify the effects of the degradation model.

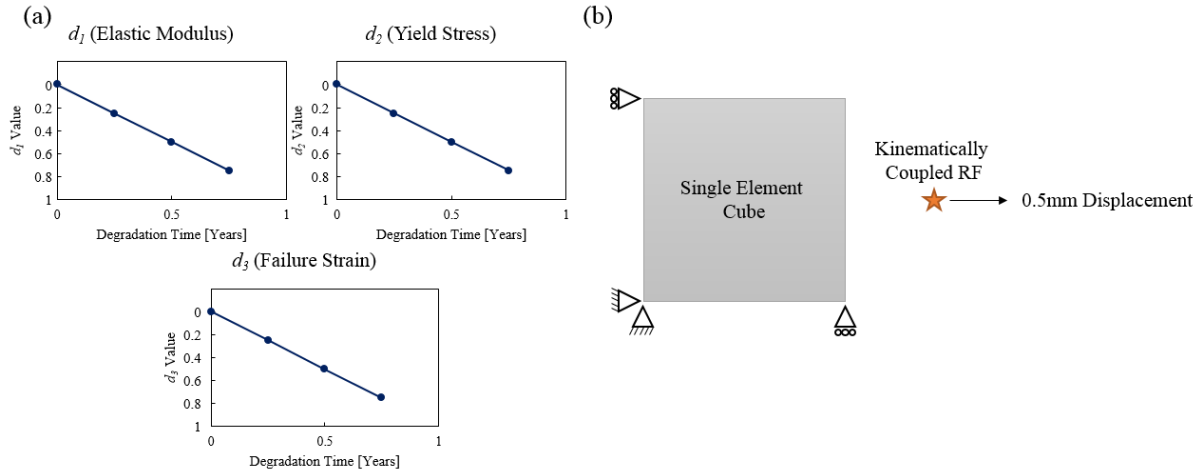


Figure 5.2. (a) Plots demonstrating how the various parameters were degraded over the verification on the unit cube. (b) Unit cube showing boundary conditions and load applied through the reference point.

#### 5.2.4 Crimping and Calibration of Initial Time Point

A reduced geometry consisting of two circumferential rings, shown in Figure 5.3(a) was used for the calibration of the initial and degraded time points. Here, the deployed geometry of the non-commercial BRS was received from collaborators, where a similar regime by Antonini, Poletti, *et al* (2021) was used to crimp and deploy the scaffold geometry. Here, a simplified and reduced balloon, as outlined in Antonini, Mandelli, *et al.* (2021) was modelled using an incompressible hyperelastic 1<sup>st</sup> order Ogden constitutive material model discretised with 3,960 M3D4R (4-node membrane element with reduced integration) elements. The parameters for the polymer BRS are shown in Table 5.1, while  $\mu = 80$  and  $\alpha = -15$  were the adopted material parameters for the balloon.

Table 5.1. Elastic and Johnson-Cook initial material parameters used for the non-commercial BRS.

BRS Model	Elastic Modulus (E) GPa	Poisson's Ratio ( $\nu$ )	Yield Stress ( $\sigma_y$ ) MPa	Johnson-Cook Parameters			Johnson-Cook Rate Dependant Hardening	
				A	B	n	C	$\dot{\epsilon}_0$
Johnson Cook	1.0	0.45	-	4.0	1.1	1.2	1.0	$5.0 \times 10^{-5}$

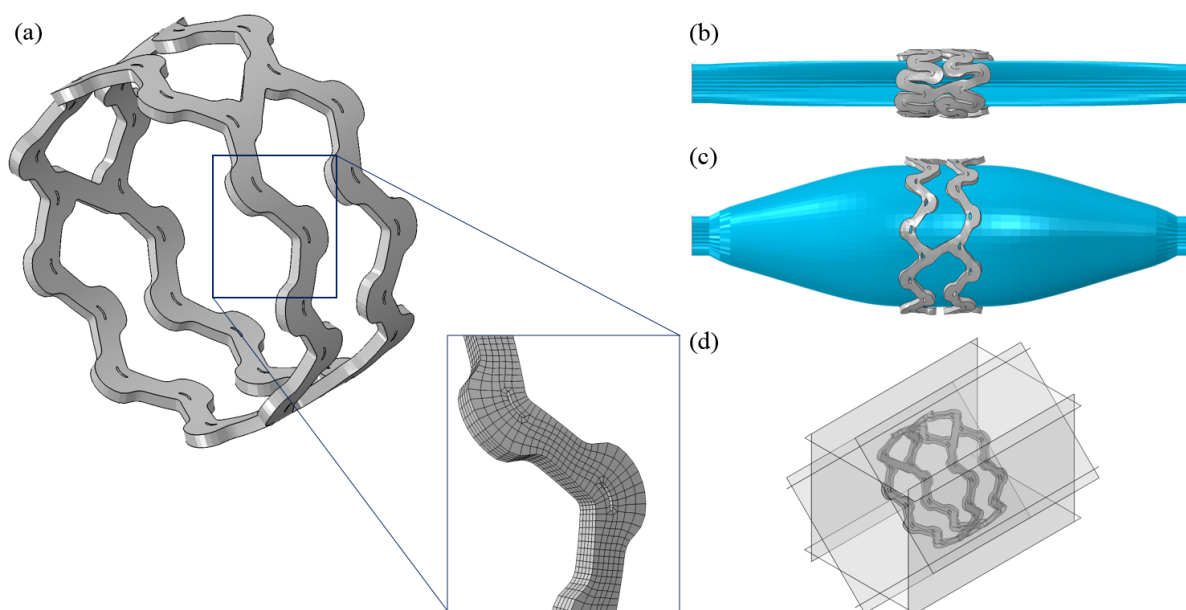


Figure 5.3. (a) Geometry of the non-commercial BRS, (2 rings of the whole scaffold) with details of the mesh. (b) BRS crimped onto the balloon. (c) BRS unit at maximum balloon inflation. (d) Initial configuration of the expanded BRS unit prior to radial crush step.

### 5.2.5 Degradation Framework Calibration

Calibration of the degraded radial tests was performed by simulating the experimental radial crush test (outlined in the previous chapter) and calibrating the material parameters in the phenomenological degradation framework until a matching radial response was achieved at each time point. Here, the reduced geometry model shown in Figure 5.3(a) was used for calibration of the parameters. Here, the stress and strain state was imported from the deployed configuration and 8 rigid plates were used to apply radial crimping to the BRS unit. The BRS was crimped from its freely-expanded diameter of 3.2 mm to a diameter of 2.4 mm over a period of 34s. It was held for a period of 30s and subsequently unloaded over a period of 34s. The Abaqus/Explicit solver was used for these radial crush tests, whereby mass scaling was used such that a target time increment of  $1 \times 10^{-5}$  was enforced. Contact conditions were defined between the BRS and rigid plates with a coefficient of friction set at  $\mu = 0.3$ . The radial reaction forces from the rigid plates were extracted from the reference points and summed to plot the overall radial force. From the observed experimental behaviour in Chapter 4, it was found that the BRS devices showed substantial strengthening in the first week of immersion. With this in

mind, the model parameter fitting required an initial strengthening of the response, which involved raising the value of  $A$  to 8.5MPa. The value for the equivalent plastic strain at failure values of un-fractured scaffolds determined from (Katarzyna *et al.* 2021) was 70% strain. To achieve a brittle failure the value chosen for  $\bar{u}_f^{pl}$  was small ( $\bar{u}_f^{pl} = 0.001$ ) to reduce the amount of displacement an element must experience before failing (see Equation ( 5-3 )). A summary of the baseline parameters that were considered are summarised here.

Table 5.2. Calibrated parameters for the elastic and Johnson-Cook material model for the day 7 time point.

BRS Model	Elastic Modulus (E) GPa	Poisson's Ratio ( $\nu$ )	Johnson-Cook Parameters			Johnson-Cook Rate Dependant Hardening		Equivalent Plastic Strain at Failure	$\bar{u}_f^{pl}$
			A	B	n	C	$\dot{\epsilon}_0$		
Day 7	1.3	0.45	8.5	1.1	1.2	1.0	$5.0 \times 10^{-5}$	0.7	0.001

Following this, a set of parameters were fit for the remainder of the degradation response, which required both  $d_1$  and  $d_3$  to change. Interestingly, after a small initial increase from day 0 to 7, the elastic response ( $d_1$ ) of the material remained largely unchanged. For the final fitted parameters, a third order polynomial was fitted to control the evolution of  $d_2$  over time, given by,

$$d_2 = 2.86 \times 10^{-7}t^3 - 2.99 \times 10^{-4}t^2 + 210t + 8.26 \quad (5-4)$$

where  $t$  is the simulation time. The initial and final  $d_3$  are defined corresponding to an un-degraded and fully degraded material and  $d_3$  is evolved through Equation (5.7). For this model, the degradation of the plastic strain at failure term was controlled by the third degradation variable, which was described over time by equation ( 5-7 ).

$$d_3(t) = \frac{\epsilon_{max}^{pl} - \epsilon_{min}^{pl}}{1 + e^{\left(t - \frac{t_{max}}{2}\right)^c}} + \epsilon_{min}^{pl} \quad (5-7)$$

Where  $\epsilon_{max}^{pl}$ ,  $\epsilon_{min}^{pl}$  are the equivalent plastic strain at failure of the un-degraded material and equivalent strain at failure of the fully degraded material,  $c$  is the slope and  $t_{max}$  the maximum degradation time. It was assumed that the material continued to degrade after day 146 such that by day 181 the material was fully degraded. Based on this fitting approach, Figure 5.4 shows

the how the calibrated degradation parameters evolved over the course of degradation. To assess the goodness of the model fit the least squares method was used, where a score of 0 would indicate a perfect fit.

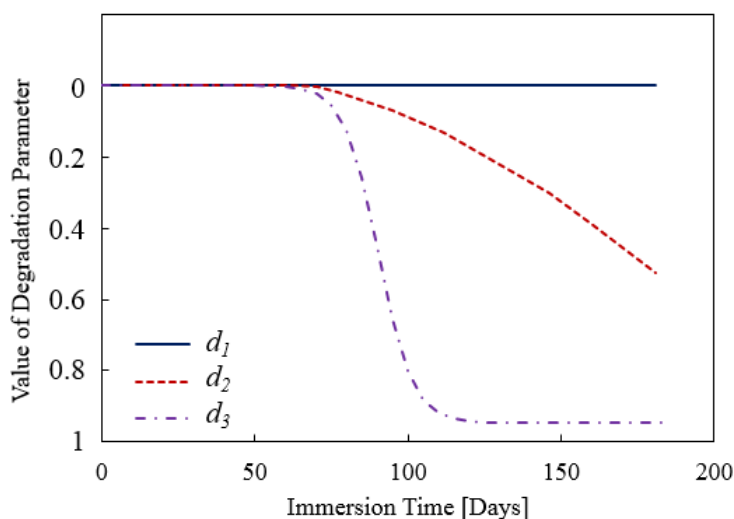


Figure 5.4. Plots demonstrating the evolution of the various degradation parameters calibrated to the response of the BRS during degradation.

### 5.2.6 Experimental Validation – Silicone Vessel Degradation and Parallel Plate Test

In an effort to validate the phenomenological degradation model, a non-commercial BRS was deployed within a silicone vessel and subjected to the same accelerated degradation protocol as the freely expanded BRS. The deployed BRS within the mock vessel was immersed into phosphate buffered saline (PBS) at 50°C for 181 days, with the pH monitored on a weekly basis such that pH remained at  $7.4 \pm 0.2$ . The silicone vessel consisted of a 3D printed idealised vessel printed with the polymer Agilus30 (Stratasys, MN, USA), with the geometry of the vessel shown in Figure 5.5(a) below. Prior to testing, several dog-bone samples of the Agilus30 material were subjected to a similar accelerated degradation protocol up to a period of 21 days and subjected to uniaxial tensile testing to ensure the mock vessel itself did not undergo significant alterations in mechanical response during immersion. Figure 5.5(b) shows that the mechanical response of the mock vessel material up to day 21 remained largely unchanged. Micro-computed tomography ( $\mu$ CT) imaging of the vessel with the inserted scaffold was performed (Scanco Medical AG, Nokomis, FL, USA) to take measurements of the internal

vessel diameter at various time points during the degradation process. The scan settings were 70 kVp with a 0.1 mm aluminium filter. For each scan, the vessel inner diameter (ID) was recorded at nine locations along the length of the vessel. The vessel ID was determined from an average of these measurements. As a control to the BRS device, a permanent metallic stent made of platinum chromium was also deployed within a mock vessel and subjected to the same accelerated degradation and scanned at the same time points. A straight vessel was not available for a direct comparison.

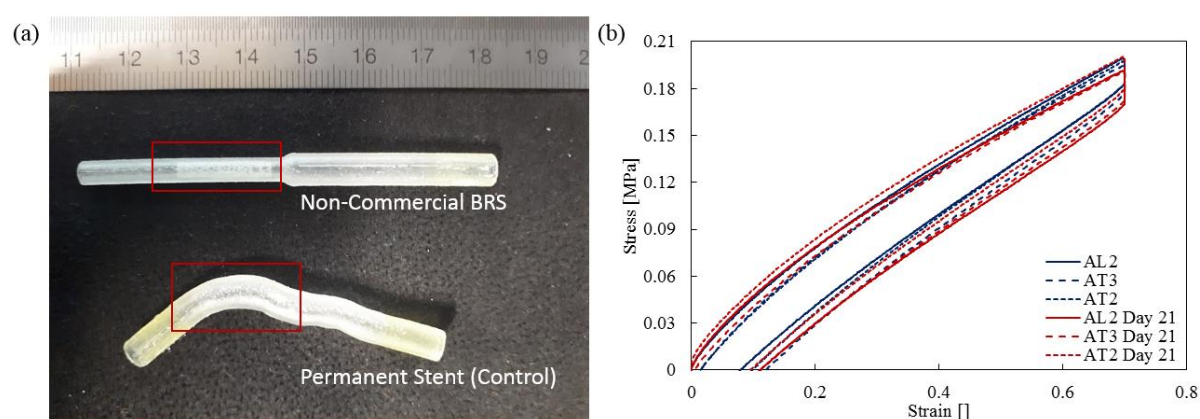


Figure 5.5. (a) Image of the silicone vessels used for validation, straight vessel with the implanted non-commercial BRS and curved vessel with implanted permanent stent used as a control. (b) Stress-strain plot showing initial and degraded response of the printed Agilus30 dog bones in different orientations showing that immersion in PBS has little effect on the Agilus30 material.

From the experimental results presented in Chapter 4, it was found that the BRS devices underwent distinct changes in mechanical properties in the first number of days of immersion testing. To investigate this short-term response, and as part of the validation process, a constant force parallel plate test was also performed on the PLLA BRS devices. A schematic of the experimental set up is shown in Figure 5.6(a). Here, the test sample was located in a bath of PBS, which had a temperature of 37°C that was maintained by pumping from a heated reservoir. A uniaxial compression load of 0.4 N load was applied (which resulted in a ≈5% reduction in diameter) between parallel plates, and this load was held constant for 8 days, with PBS solution maintained at 37°C throughout and the change in diameter recorded over the course of the test.



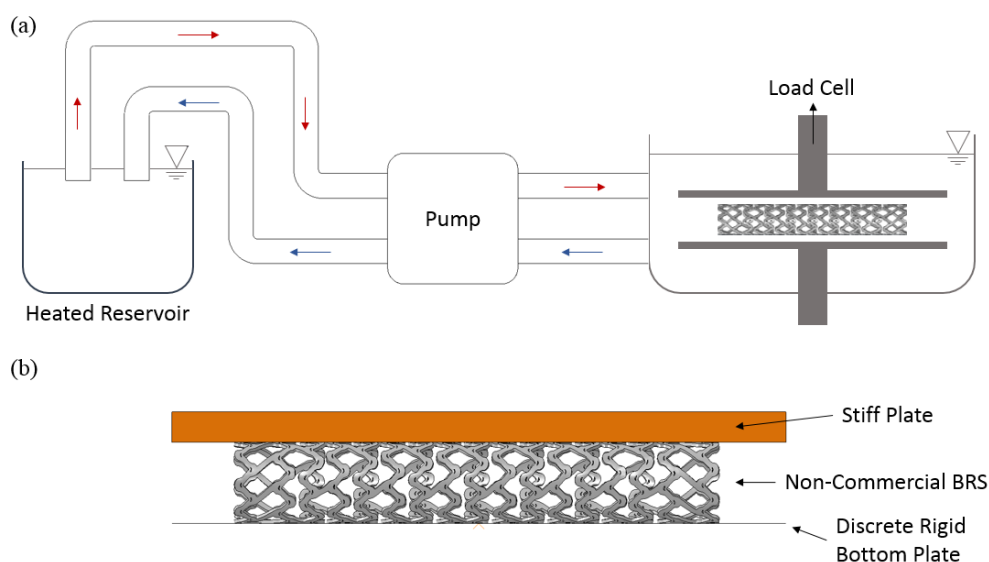


Figure 5.6 (a). Schematic of the experimental set-up for the parallel plate test on the non-commercial scaffold performed at 37°C. (b) Schematic showing the computational set-up to simulate the parallel plate experiment.

### 5.2.7 Computational Models of Mock Vessel Degradation and Parallel Plate Testing

A finite element model of the silicone vessel and non-commercial BRS was constructed, with a full sized non-commercial BRS, as shown in Figure 5.1, deployed within the narrow section of the vessel, as shown in Figure 5.7. The vessel consisted of 67,500 C3D8R elements. The vessel was modelled as an isotropic incompressible 1<sup>st</sup> order Neo-Hookean hyperelastic constitutive material model, whose parameters were determined from axial tensile testing of dog-bone and hoop specimens (Berti *et al.* 2021). A balloon pressure of 8atm was used to deploy the full BRS within the vessel, which was the same pressure as used in the experimental vessel deployment. The BRS was deployed over 24 s, held for 30 s and deflated over 5 s. The stages of crimping and deployment within the vessel are shown in Figure 5.7. The material parameters for the non-commercial BRS were those that were found during the calibration process. The Abaqus/Explicit solver was used to crimp, deploy and degrade the non-commercial BRS. A target time increment of  $1 \times 10^{-6}$  s was used for the simulations, where the time for each deployment time step was the same as the reduced geometries. The Abaqus/Explicit general surface contact was defined between the balloon and BRS and the BRS and the internal vessel walls with a penalty friction parameter of  $\mu = 0.3$ . The vessel and

balloon ends were constrained in all directions. Measurements of the ID were compared with the measurements taken from the  $\mu$ CT scans of the non-commercial BRS.

*Table 5.3. Hyperelastic Neo-Hookean material parameters used for the silicone vessel.*

$C_{10}$	$D_1$
0.096879	0.0

A finite element simulation for the experimental parallel crush test was also conducted. This simulation used the same crimp and deployment regime to freely-expand the BRS as used for the mock vessel simulation. The set-up for this simulation can be seen in Figure 5.6(b). The BRS was placed between a discrete rigid plate and a moveable plate which was very stiff in comparison to the BRS, having an elastic modulus of 200 GPa. A pressure load was applied to the top surface of the top plate of 0.005 MPa applied over a surface area of 80 mm<sup>2</sup>. The load was applied over a similar period as the experiment of 600 s and the load held for a period of 259,200 s (72 hrs). The diameter versus time was monitored over this period and compared against the experimental results. For this simulation, the Abaqus/Explicit solver was used with a target time increment of 0.1 s. To investigate the effects of the material properties evolving during this time period, which was observed experimentally (e.g. strengthening), three simulations were considered; (i) a test with no change to the material properties over the hold period, (ii) a test where the  $A$  parameter of the Johnson-Cook model was increased by a factor of two over the hold period and (iii) a test where  $A$  parameter of the Johnson-Cook was reduced by a factor of two over the hold period. The  $A$  parameter controls the yield surface of the Johnson-Cook model, with these changes essentially increasing or decreasing the radial strength of the BRS device.

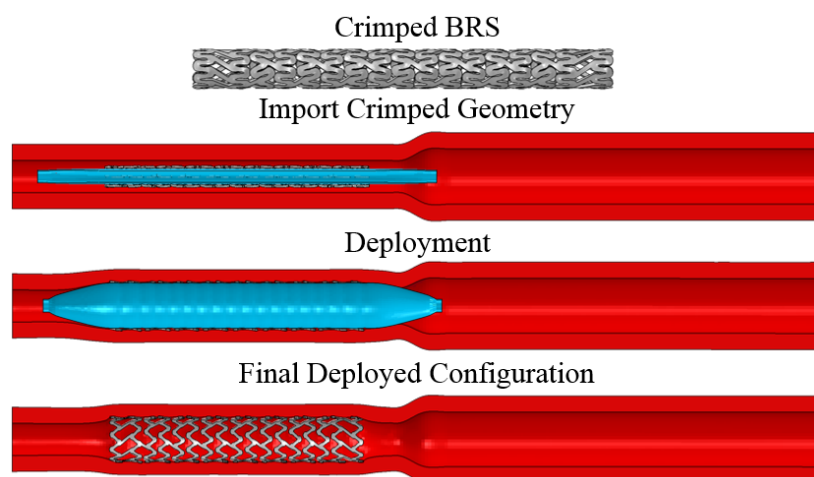


Figure 5.7. Schematic of the computational model showing the crimping and deployment process within the simulated silicone vessel.

## 5.3. Results

### 5.3.1. Degradation Framework Implementation

Figure 5.8(a) shows the predicted stress-strain behaviour on a single element for the material where  $d_1$  parameter that controls the elastic response was reduced. Figure 5.8(b) shows the predicted stress-strain behaviour for the material where the  $d_2$  parameter that controls the Johnson-Cook yield surface was evolved. Figure 5.8(c) show the predicted stress-strain behaviour for material where  $d_3$ , which controls the failure strain was decreased. Finally, Figure 5.8(d) shows the predicted stress-strain behaviour for material where degradation model includes reductions in all three parameters ( $d_1$ ,  $d_2$ ,  $d_3$ ). These results demonstrate the capacity of the mechanical degradation model to capture wide-ranging behaviour for the Johnson-Cook degradation framework, which could be applied to many potential polymer material systems and behaviours.

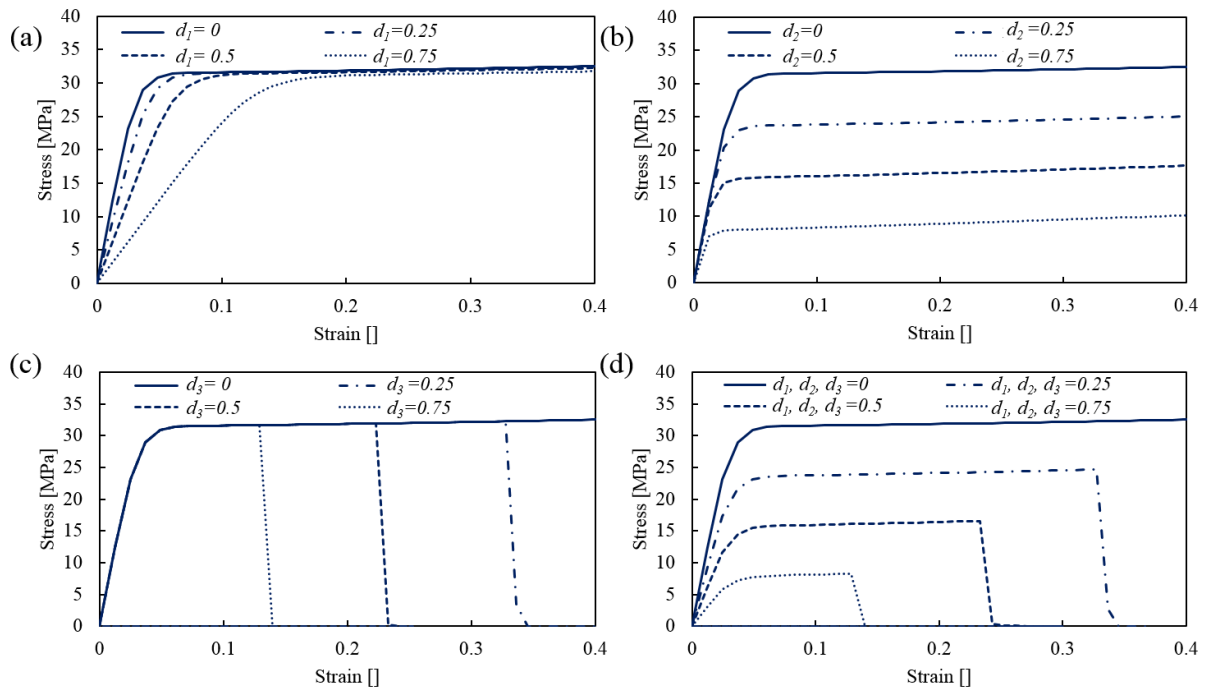


Figure 5.8. Stress Strain plots showing the degradation model's capability in controlling the following mechanical parameters (a)  $d_1$ , (b)  $d_2$ , (c)  $d_3$  and (d) combined degradation ( $d_1$ ,  $d_2$ ,  $d_3$ ).

### 5.3.2. Degradation Framework Calibration Results

The averaged radial force response for each experimental time point and the computational match is shown in Figure 5.9. The radial response at day 0 shows a linear increase and plateau region upon loading, a relaxation period during the hold and unloading with a permanent deformation of the BRS. In the first 7 days, the BRS exhibited a large increase in radial strength and a smaller increase in radial stiffness, which resulted in the radial strength almost doubling. The increased stiffness and strength of the degraded time points resulted in a 30% increase in the elastic modulus and 100% increase in yield strength. This increased strength was generally maintained until day 77. Figure 5.9(b) shows the experimental response and resulting model fit for days 7 and 21. Here, there is a slight difference in the starting diameter of the BRS due to a small amount of shrinkage taking place in the experimental sample. Despite this, there is an excellent match between predicted response and experimental response of the BRS throughout the loading regime. Here, the calibrated computational model correctly captures the stiffness response, yield plateau and overall radial strength of the BRS during the loading phase. At maximum crimp, the computational model correctly predicted a reduction in the

radial force during the hold period of 30 seconds, which resulted from the viscoelastic response of the material model. Following this, model prediction generally captures the unloading phase of the radial test, although slight differences are observed in the final crimped diameter that resulted due to permanent deformation of the scaffold. The general behaviour of the device remained largely similar until day 77. Beyond this, at day 112 the experimental response showed a reduction in ductility, with a decreased radial strength visible in Figure 5.9(e), which also coincided with a drop in the radial force after the peak load was reached, which is indicative of damage taking place. Again, the computational model captures the features of this response very well, with the substantial reduction in radial strength enabled by an increased damage parameter  $d_2$ . Beyond this yield point, the implemented damage model correctly captures the drop in radial force during the crimp phase and, again, captures the drop in load during the hold phase at maximum crimp followed by unloading. At day 146, the radial response is degraded further with additional reductions in the radial strength and very low ductility, which is captured by the computational model due to the high value of  $d_3$  at this time point. Using the least squares method to assess the fit of the calibrated model, Table 5.3 it is shown that for days 0, 77, 112 and 146 a good match is achieved. Due to the offset in the initial diameter for days 7, 21, 49 and 54 the fit is not as good. However, despite this, the slope and maximum radial strength is still in good agreement with the experimental time points.

Table 5.3. Least square fit for the calibrated model versus the experimental radial force curves.

Day	0	7, 21	49, 54	77	112	146
Least squares residual (N/mm)	0.236	1.236	1.819	0.522	0.091	0.551

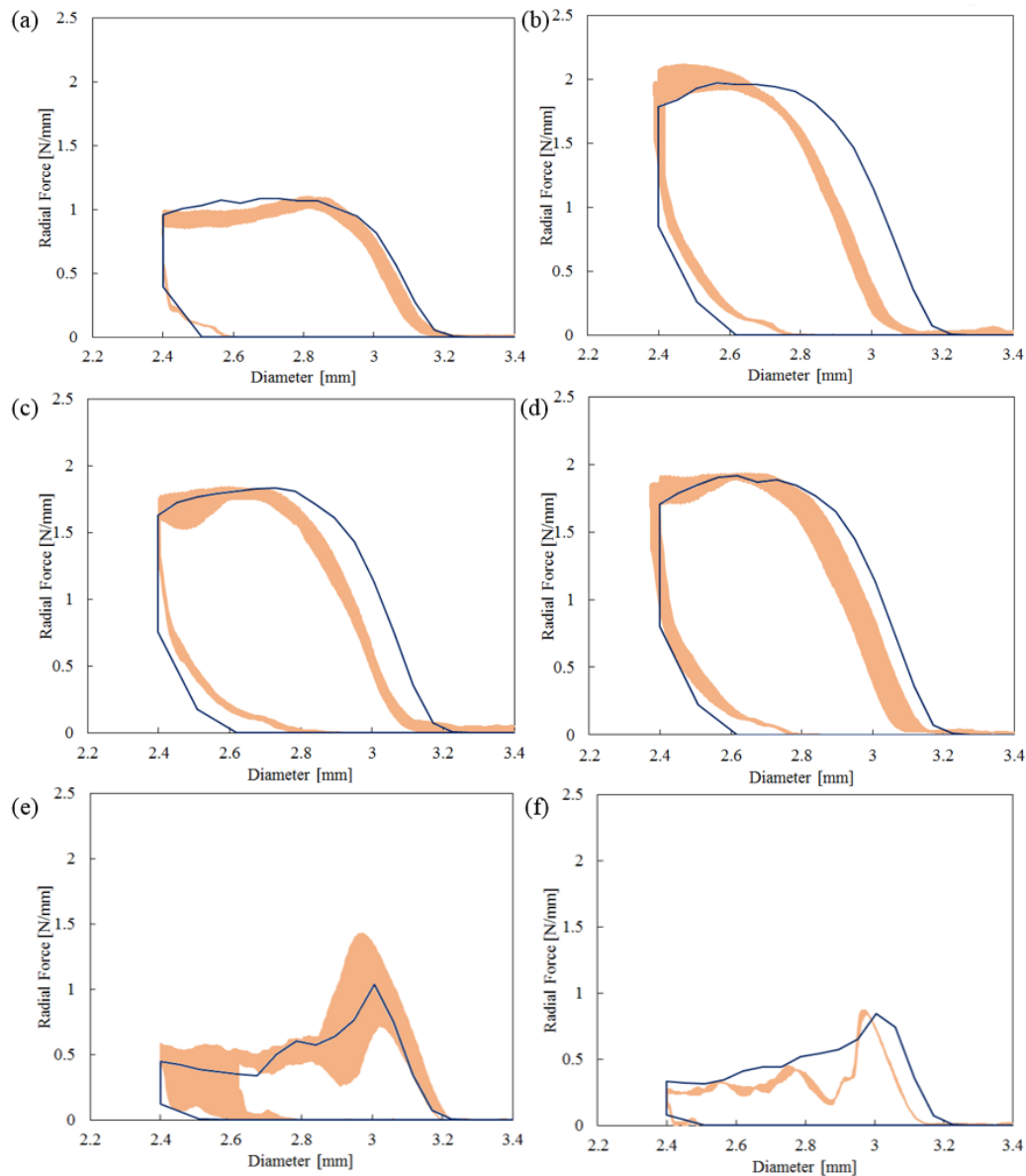


Figure 5.9. Normalised and averaged radial force-diameter curves comparing the experimental and calibrated computational model results, shaded areas represent the range of experimental curves. (a) Day 0, (b) Days 7, 21 (c) Days 49 and 54, (d) Days 62 and 77, (e) Day 112 and (f) Day 146.

Contour plots of the BRS during the radial crush simulation at a diameter of 2.7 mm shown in Figure 5.10 below. Here, higher levels of stress are evident between days 7 and 77 compared to day 0, whereby Figure 5.10(a)-(d) correspond to the increase in the yield stress and radial performance seen in the previous chapter. Beyond day 77, the contour plots in Figure 5.10(f-h) show lower stresses in the BRS, with several damaged elements observed in the hinge regions due to ductile damage model (not shown). This corresponds to a decrease in the radial performance seen in Figure 5.10 below.

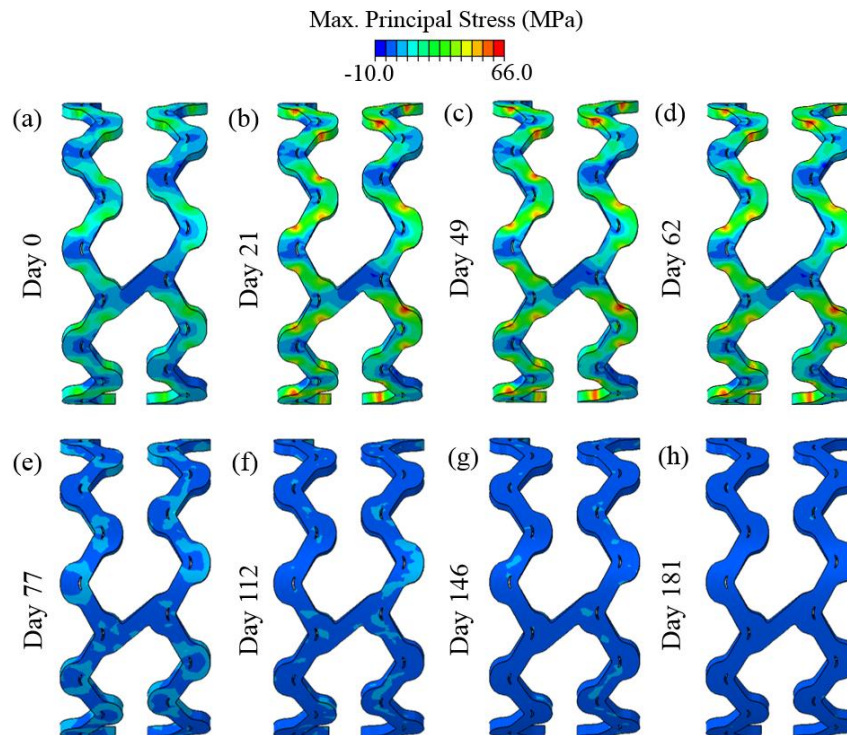


Figure 5.10. Contour plots showing maximum principal stress of the BRS during crimping at a diameter of 2.7mm at various stages of the degradation process. Plots showing: (a) Day 0. (b) Day 21. (c) Day 49. (d) Day 62. (e) Day 77. (f) Day 112. (g) Day 146. (h) Day 181.

Figure 5.11 shows the evolution in the normalised radial strength and stiffness for the experimental and calibrated computational model. Here, the computational model captures the key device-level properties over the course of degradation. The BRS experiences an increase in radial strength that is maintained until day 77. A large drop in radial strength was observed between days 77 and 112, which is predicted by the computational model. The BRS stiffness also increases from day 0 and is largely maintained until day 146. This sudden decrease corresponded with fracture of the scaffold on day 112.

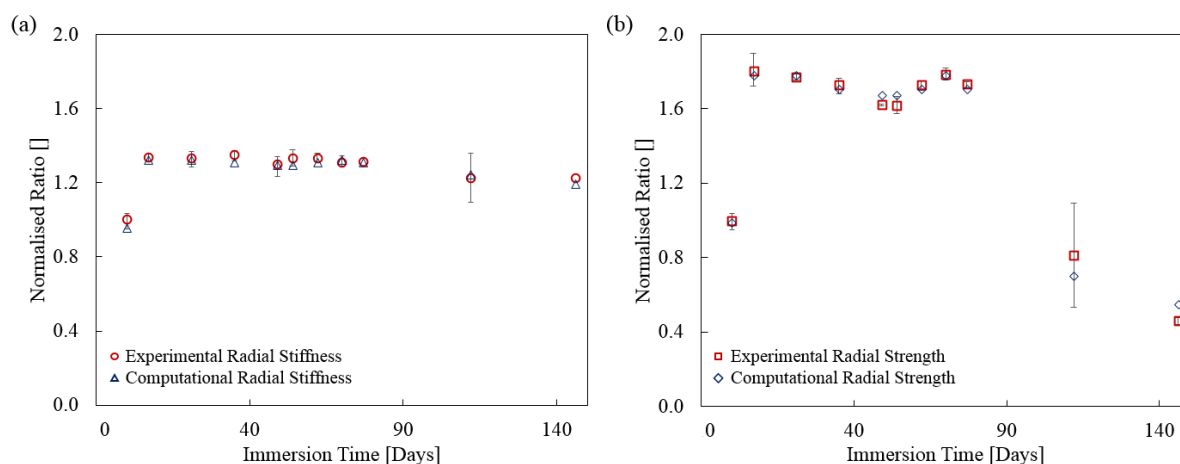


Figure 5.11. Evolution of normalised scaffolds (a) radial strength and (b) stiffness over the course of the study for the experimental radial testing and the calibrated computational model, error bars denote max and min values from the experimental testing.

### 5.3.3. Degradation Framework Validation Results

#### 5.3.3.1 Silicone Vessel

From implantation of the BRS in the silicone mock vessel, the ID was recorded from  $\mu$ CT scanning of the non-commercial BRS and permanent stent over the course of the accelerated degradation period of 180 days, with results shown in Figure 5.12(a). Here, the experimental results show a large initial drop in the measured lumen diameter between days 0 and 7. After 90 days, the lumen diameter was close to the original un-expanded diameter of the mock vessel. On the other hand, there was no diameter change observed for the permanent stent during the accelerated degradation test. Figure 5.12(b) shows  $\mu$ CT composite images from the final time point (Day 181) and an intermediary time point (Day 80). Some discontinuities are visible in the scans of Day 181 suggesting that the BRS had fractured. Figure 5.12(a) also shows the predicted lumen diameter from the computational degradation simulations. Here, the computational simulations predicted that the lumen diameter was maintained until approximately day 140, at which point the lumen diameter decreases. Contour plots showing the maximum principal stress and contact stress of the BRS and silicone vessel over the simulated degradation period are shown in Figure 5.13. They show a decrease in the overall stress and strain within the BRS and the change in diameter of the vessel and BRS is also visible



towards the final degradation stages (Day 181). Here, the radial strength and radial stiffness of the BRS device was fully maintained in the early stages of the degradation process, until eventually reductions in radial strength and increased brittleness were observed. With these calibrated parameters, it would be expected that the BRS device should maintain the lumen diameter of the vessel in the experiment, as the model has predicted in Figure 5.12(a), it should be noted that this only captures the change in diameter after the deployment and acute recoil post deployment has already occurred. However, there was a substantial reduction in vessel diameter observed in the early phase of the experiment, which does not align with the radial performance data available.

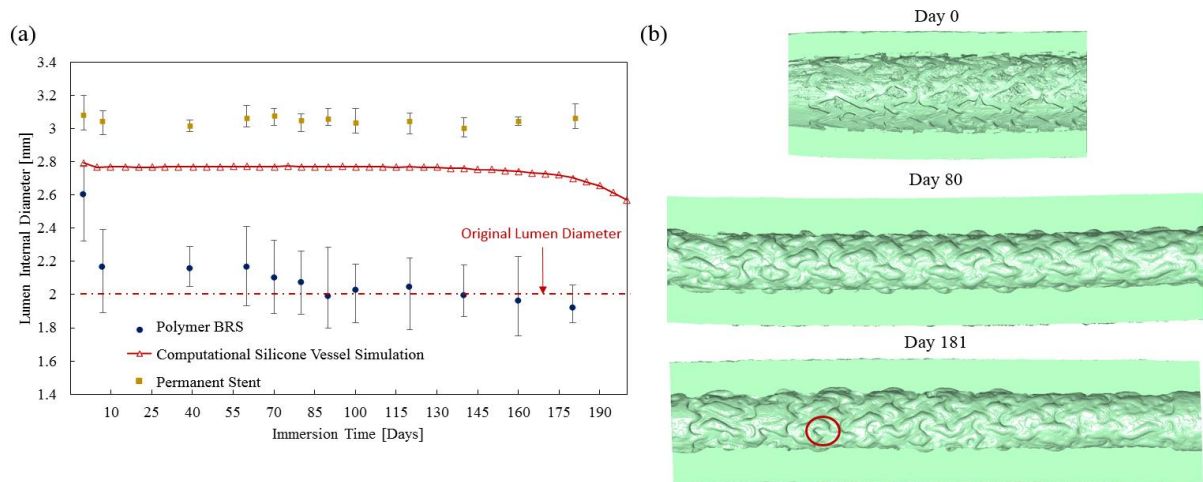


Figure 5.12. Plot showing evolution of inner diameter for the non-commercial BRS with max and min values implanted in the silicone vessel and degraded for 181 days at 50°C in PBS compared against the computational match of the non-commercial BRS. Also shown is the permanent stent as the control with max and min values.

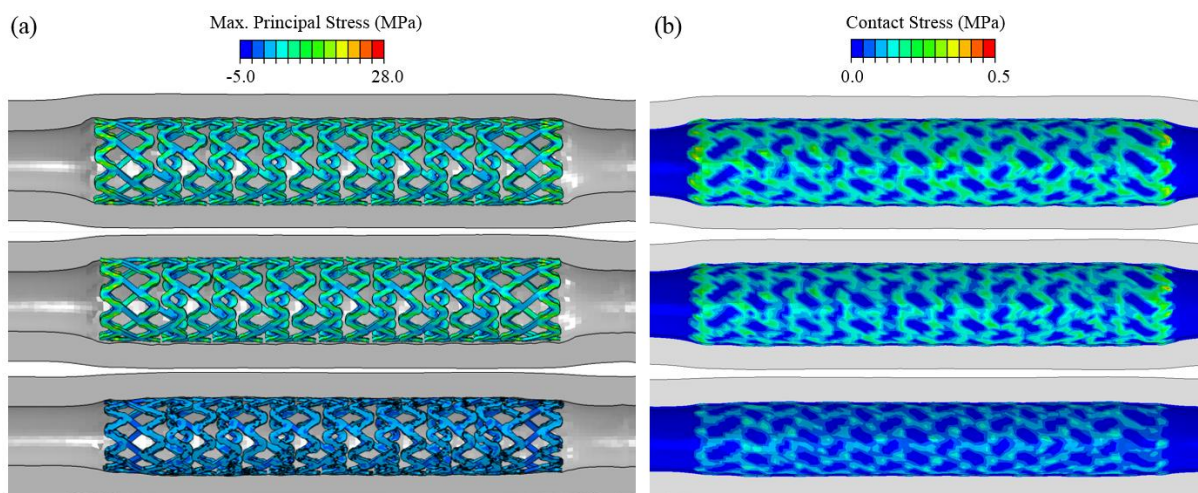


Figure 5.13. Contour plots showing (a) maximum principal stress and (b) contact stress within the BRS and vessel over the simulated degradation period. Top row showing Day 0, middle row showing Day 100 and the final row showing Day 181.

### 5.3.3.2 Parallel Plate Compression

To further investigate this short-term degradation response, a constant force parallel plate test was also performed on the PLLA BRS devices, whereby a constant load of 0.4 N was applied over a period of 8 days while immersed in PBS at 37°C. Figure 5.14 shows the resulting BRS diameter versus time for the first 72 hours. Here, the initial load was applied monotonically, with the time point at which maximum load being reached identified as a red dashed line on the graph. Here, the parallel plate crush test resulted in a substantial reduction of the BRS diameter in the first 8 hours of load application, corresponding to a significant creep response of the device. This behaviour was similar to that observed in the silicone vessel, where a substantial diameter reduction was observed in first 24 hours of immersion at 50°C. Figure 5.14 also shows the results from the computational simulations, whereby there is only a small creep response evident and only a slight reduction in diameter. These computational simulations also examined how altering the yield stress in this phase (which was observed in radial experiments) would affect the response. Here, increasing and decreasing the yield stress during this period only resulted in very slight changes in the diameter of the BRS in the later stages of the test.

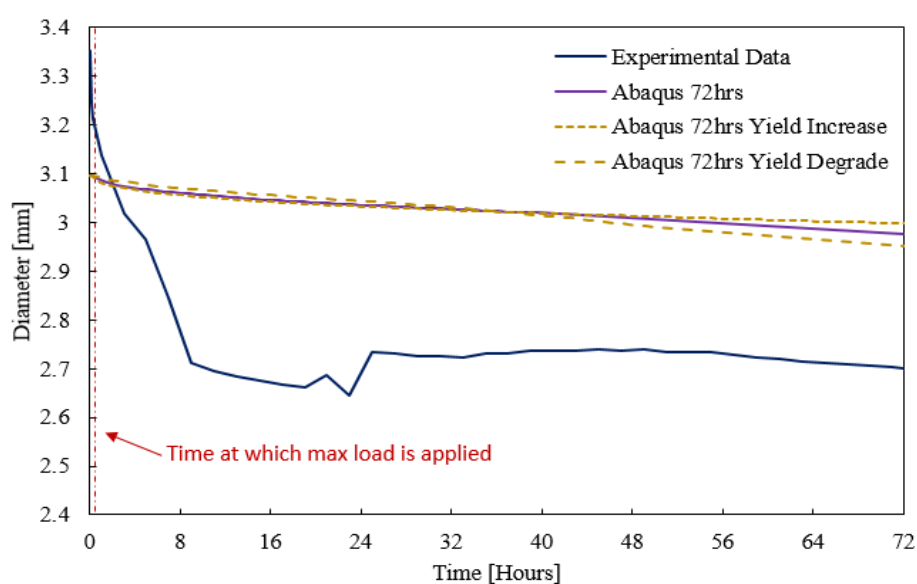


Figure 5.14. Time versus diameter curves of the non-commercial BRS comparing the computational and experimental creep testing. Plot also demonstrates behaviour of changing the yield stress under a constant load. Max load was achieved after a period of 10 minutes.

## 5.4. Discussion

In this chapter, a phenomenological degradation framework was developed to predict the short-term performance and the long-term degradation behaviour of a polymer BRS. The Johnson-Cook degradation model was implemented within the Abaqus finite element framework and showed distinct flexibility in the mechanical responses that could be captured, with each of the elastic, yield and post-yield behaviour controllable. The model parameters of the degradation model were calibrated based on the freely-expanded performance of a non-commercial BRS, with the degradation model accurately capturing short-term deployment behaviour and the long-term degradation response under radial loading. To the author's knowledge, this is the first instance of a damage model simulating the embrittlement and resulting radial performance of a polymer BRS. In an effort to validate the degradation framework, parallel plate crush test and deployment of the non-commercial BRS within a silicone vessel subjected to the same accelerated degradation protocol as presented in Chapter 4. These tests were complimented with computational simulations to apply the degradation framework calibrated on the freely expanded and degraded BRS. However, both of these tests showed distinct creep behaviour in the early stages of the degradation response, where the diameter of the BRS was reduced within the first seven days in the case of the silicone vessel and in the first 4 hours for the parallel plate test. In both the experiment and computational cases, recording of the changes in diameter were performed after the deployment and acute recoil stage. This was not captured by the computational model and suggests that a further understanding of the creep performance of these devices is required, both experimentally and computationally to enable future BRS development.

A major challenge in polymer degradation modelling has been that the physical processes that are responsible for impaired mechanical performance are not fully understood, which means that predictive models have generally relied on capturing the phenomenology of degradation

(Luo *et al.* 2014; Qiu *et al.* 2018). Phenomenological approaches can be very effective in predicting complex processes, but they rely on the problem being well-described and replicable, and the availability of sufficient experimental data that adequately describe material performance. Until now, many existing computational degradation models have been limited by the fact that they do not completely capture the mechanical effects of degradation seen experimentally (Qiu *et al.* 2018; Shine *et al.* 2021) or have been calibrated to a narrow range of mechanical data, which has enabled simplifications in their model form, whereby degradation has been simulated by operating on a single material parameter such as elastic modulus (Shine *et al.* 2021) or yield stress (Qiu *et al.* 2018; Luo *et al.* 2014). The degradation model presented in this study shows distinct flexibility in the range of mechanical responses that can be captured, with each of the elastic, yield and post-yield behaviour adaptable to almost any material response. Furthermore, the implementation of this model was compatible with the elasto-viscoplastic framework required to accurately predict the deployment behaviour of these BRS devices, Table 5.3. This degradation model was fully compatible with the constitutive behaviour of the short-term response, with the model capturing the free-expansion and implantation of BRS within a vessel, in addition to capturing the loading, hold and unloading phases of the radial response at each time point during the degradation phase. Furthermore, the model showed captured the ductile to brittle transition of the BRS that occurred in the later stages of degradation in these devices and found to occur in other similar material/devices.

While the model framework was effective in predicting the radial behaviour of the BRS following a static degradation protocol, the mechanical behaviour of PLLA is significantly affected when other loading conditions were considered. In an effort to validate this degradation model, an *in vitro* comparator was established, whereby a non-commercial BRS device was deployed into a silicone mock vessel and subjected to accelerated degradation conditions. While the computational degradation model predicted that the mock vessel would

maintain its internal diameter until the later stages of degradation (see Figure 5.14(a)), the experimental vessel showed a reduction in diameter in the early stages of the experiment. Here, the constant prolonged load applied by the silicone vessel appears to have resulted in a creep response of the BRS device that was not seen during the hold phase of the experimental radial testing. This was not captured by the computational model as it was calibrated to the static degradation behaviour of the freely expanded BRS device. The creep behaviour could have implications for the performance of PLLA BRS devices *in vivo* as a re-narrowing of the vessel could occur within a short timeframe of the initial deployment. While this creep behaviour has been noted previously for a different device, most notably in the initial clinical trials of polymer BRS where recoil was noted immediately after implantation, it was partially rectified through changes in deployment techniques (Bangalore et al. 2017). It would appear that other polymer BRS devices have not suffered from these effects in clinical studies and for the Abbot Absorb device, in particular it was late-stage performance where problems were encountered. When deploying such devices *in vivo*, it is very likely that during the deployment and any pre-/post-angioplasty steps that the vessel itself and possibly the plaque undergoes damage and/or plasticity that results in permanent deformation (Akyildiz, Barrett, and Gijssen 2021), which may reduce the overall elastic strain acting on a device. While the silicon vessel used here has previously been used to validate the short-term deployment performance of permanent stents (Berti et al. 2021), and the BRS devices here, these hyperelastic mock vessels may not be suitable for the validation of the long-term degradation performance of polymer BRS. It should be noted that the reduction in vessel diameter in the early stages of degradation occurred despite the fact that the static radial strength was found to increase two-fold in the first seven days of the accelerated degradation experiment. This increase in radial strength is typically attributed to an increase in chain mobility caused by ingress of water molecules allowing for a recrystallization of the polymer (Vyavahare, Ng, and Hsu 2014). While the initial aim of the

parallel plate test was to investigate how this increased radial strength affected the performance, it was again evident that the application of a constant load resulted in the same loss in diameter of the scaffolds in the early phases of these tests. In the corresponding computational simulation, altering the yield stress of the PLLA (and associated radial strength of the device) had little effect on the behaviour, with the experimental response dominated by the creep effect during the hold period of the simulation. This study further highlights the importance of considering the environmental and loading condition for the *in vitro* assessment of polymer BRS.

This study has certain limitations in that, despite the fact the degradation model was found to predict the static degradation performance of the polymer BRS accurately, the efforts to validate the model showed that static material characterisation (and modelling) may not represent the typical in-service conditions of these devices. While many other studies have used similar static approaches as inputs to their degradation modelling framework, this study is one of the few studies to make the effort to independently validate the developed model framework. This also clearly highlights that it is not possible to calibrate BRS samples that were degraded under static conditions. To extend this model framework further, it is clear that more experimental data is needed on the long-term creep response of these devices, with degradation protocols requiring that BRS devices are tested under non-static conditions. From the model developed, the inclusion of either visco-elastic or load-dependent degradation would be relatively easy to implement. In fact, the main challenge here is having a full understanding of the material behaviour. Another limitation is the use of a phenomenological model to predict the long-term degradation behaviour of a polymer BRS. While these models may not capture the physical degradation, such as the scission of chain bonds that occurs within the polymer itself during degradation, they do capture the overall effects of degradation at a device level and can provide some indication of how a PLLA BRS may perform over its lifespan while it is

implanted. In addition, accounting for microscopic changes within the bulk polymer due to degradation at a device level would be extremely computationally expensive. Furthermore, several of the effects observed may have been linked to the elevated temperature (50°C) of the accelerated degradation protocol, with the diameter loss in the silicone vessel perhaps more substantial due the larger creep response likely at higher temperatures (Bartkowiak-Jowska et al. 2013). Finally, the large maximum and minimum error bars on the BRS measurements from the silicone vessels are due to the vessel being ovular rather than circular. This feature is also responsible for the measurements showing the vessel diameter dropping below the starting diameter.

## **5.5. Conclusions**

A phenomenological finite element based degradation framework was developed to predict the short-term performance of several key aspects from the long-term degradation behaviour of a PLLA BRS. The degradation model predicted the elastic, yield and post-yield response of the PLLA BRS, including ductile to brittle transition in late-stage degradation. Based on the calibration to the radial response of the device following static degradation, it was found that the calibrated parameters were only useful in predicting the static response of the PLLA BRS. Upon implantation in a silicone vessel or on the application of constant load, the PLLA BRS showed substantial amounts of creep behaviour in the early stages of immersion, which was not captured by the model. This highlights a distinct need to carefully consider the creep performance of polymer BRS in subsequent experimental and computational degradation studies.

## 5.7. References

- Abizaid, Alexandre, Didier Carrié, Norbert Frey, Matthias Lutz, Joachim Weber-Albers, Darius Dudek, Bernard Chevalier, et al. 2017. “6-Month Clinical and Angiographic Outcomes of a Novel Radiopaque Sirolimus-Eluting Bioresorbable Vascular Scaffold: The FANTOM II Study.” *JACC: Cardiovascular Interventions* 10 (18): 1832–38. <https://doi.org/10.1016/j.jcin.2017.07.033>.
- Akyildiz, Ali C., Hilary E. Barrett, and Frank J.H. Gijssen. 2021. *Identification of Coronary Plaque Mechanical Properties from Ex Vivo Testing. Biomechanics of Coronary Atherosclerotic Plaque: From Model to Patient*. Elsevier. <https://doi.org/10.1016/B978-0-12-817195-0.00018-4>.
- Amnieh, Sasan Khalaj, Mohammad Mashayekhi, Ehsan Shahnooshi, Mehdi Tavafooghi, and Peiman Mosaddegh. 2021. “Biodegradable Performance of PLA Stents Affected by Geometrical Parameters : The Risk of Fracture and Fragment Separation.” *Journal of Biomechanics* 122: 110489. <https://doi.org/10.1016/j.jbiomech.2021.110489>.
- Antonini, Luca, Francesca Berti, Benedetta Isella, Dipok Hossain, Lorenzo Mandelli, Giancarlo Pennati, and Lorenza Petrini. 2021. “From the Real Device to the Digital Twin: A Coupled Experimental-Numerical Strategy to Investigate a Novel Bioresorbable Vascular Scaffold.” *Plos One* 16 (6): e0252788. <https://doi.org/10.1371/journal.pone.0252788>.
- Antonini, Luca, Lorenzo Mandelli, Francesca Berti, Giancarlo Pennati, and Lorenza Petrini. 2021. “Validation of the Computational Model of a Coronary Stent : A Fundamental Step towards in Silico Trials.” *Journal of the Mechanical Behavior of Biomedical Materials* 122 (April): 104644. <https://doi.org/10.1016/j.jmbbm.2021.104644>.
- Antonini, Luca, Gianluca Poletti, Lorenzo Mandelli, Gabriele Dubini, Giancarlo Pennati, and Lorenza Petrini. 2021. “Comprehensive Computational Analysis of the Crimping Procedure of PLLA BVS : Effects of Material Viscous-Plastic and Temperature Dependent Behavior.” *Journal of the Mechanical Behavior of Biomedical Materials* 123 (April): 104713. <https://doi.org/10.1016/j.jmbbm.2021.104713>.
- Bangalore, Sripal, Hiram G. Bezerra, David G. Rizik, Ehrin J. Armstrong, Bruce Samuels, Srihari S. Naidu, Cindy L. Grines, et al. 2017. “The State of the Absorb Bioresorbable Scaffold: Consensus From an Expert Panel.” *JACC: Cardiovascular Interventions* 10 (23): 2349–59. <https://doi.org/10.1016/j.jcin.2017.09.041>.
- Bergström, Jörgen. 2015. “Determination of Material Parameters from Experimental Data.” *Mechanics of Solid Polymers*, 437–46. <https://doi.org/10.1016/b978-0-323-31150-2.00009-1>.
- Berti, Francesca, Luca Antonini, Gianluca Poletti, Constantino Fiuza, Ted J. Vaughan, Francesco Migliavacca, Lorenza Petrini, and Giancarlo Pennati. 2021. “How to Validate in Silico Deployment of Coronary Stents: Strategies and Limitations in the Choice of Comparator.” *Frontiers in Medical Technology* 3 (August). <https://doi.org/10.3389/fmedt.2021.702656>.
- Bobel, A. C., S. Petisco, J. R. Sarasua, W. Wang, and P. E. McHugh. 2015. “Computational Bench Testing to Evaluate the Short-Term Mechanical Performance of a Polymeric Stent.” *Cardiovascular Engineering and Technology* 6 (4): 519–32. <https://doi.org/10.1007/s13239-015-0235-9>.
- Boland, Enda L., Rosa Shine, Nicola Kelly, Caoimhe A. Sweeney, and Peter E. McHugh. 2016. “A Review of Material Degradation Modelling for the Analysis and Design of Bioabsorbable Stents.” *Annals of Biomedical Engineering* 44 (2): 341–56. <https://doi.org/10.1007/s10439-015-1413-5>.
- Byrne, Robert A, Giulio G Stefanini, Davide Capodanno, Yoshinobu Onuma, Andreas Baumbach, Javier Escaned, Michael Haude, Stefan James, Michael Joner, and Peter Ju. 2018. “Report of an ESC-EAPCI Task Force on the Evaluation and Use of Bioresorbable Scaffolds for Percutaneous Coronary Intervention : Executive Summary,” no. July 2014: 1591–1601. <https://doi.org/10.4244/EIJ20170912-01>.



- Cassese, Salvatore, Robert A. Byrne, Gjin Ndrepepa, Sebastian Kufner, Jens Wiebe, Janika Repp, Heribert Schunkert, Massimiliano Fusaro, Takeshi Kimura, and Adnan Kastrati. 2016. “Everolimus-Eluting Bioresorbable Vascular Scaffolds versus Everolimus-Eluting Metallic Stents: A Meta-Analysis of Randomised Controlled Trials.” *The Lancet* 387 (10018): 537–44. [https://doi.org/10.1016/S0140-6736\(15\)00979-4](https://doi.org/10.1016/S0140-6736(15)00979-4).
- Chevalier, Bernard, Alexandre Abizaid, Didier Carrié, Norbert Frey, Matthias Lutz, Joachim Weber-Albers, Darius Dudek, et al. 2019. “Clinical and Angiographic Outcomes with a Novel Radiopaque Sirolimus-Eluting Bioresorbable Vascular Scaffold: The FANTOM II Study.” *Circulation: Cardiovascular Interventions* 12 (6): 1–8. <https://doi.org/10.1161/CIRCINTERVENTIONS.118.007283>.
- Debusschere, Nic, Patrick Segers, Peter Dubruel, Benedict Verhegghe, and Matthieu De Beule. 2015. “A Finite Element Strategy to Investigate the Free Expansion Behaviour of a Biodegradable Polymeric Stent.” *Journal of Biomechanics* 48 (10): 2012–18. <https://doi.org/10.1016/j.jbiomech.2015.03.024>.
- Duek, E. A.R., C. A.C. Zavaglia, and W. D. Belangero. 1999. “In Vitro Study of Poly(Lactic Acid) Pin Degradation.” *Polymer* 40 (23): 6465–73. [https://doi.org/10.1016/S0032-3861\(98\)00846-5](https://doi.org/10.1016/S0032-3861(98)00846-5).
- Fiuza, Constantino, Katarzyna Polak-Krasna, Luca Antonini, Lorenza Petrini, Oliver Carroll, William Ronan, and Ted J Vaughan. 2022. “An Experimental Investigation into the Physical, Thermal and Mechanical Degradation of a Polymeric Bioresorbable Scaffold.” *Journal of the Mechanical Behavior of Biomedical Materials* 125 (November 2021): 1–9. <https://doi.org/10.1016/j.jmbbm.2021.104955>.
- Gleadall, Andrew, Jingzhe Pan, Marc Anton Krufft, and Minna Kellomäki. 2014. “Degradation Mechanisms of Bioresorbable Polyesters. Part 1. Effects of Random Scission, End Scission and Autocatalysis.” *Acta Biomaterialia* 10 (5): 2223–32. <https://doi.org/10.1016/j.actbio.2013.12.039>.
- Hoddy, Ben, Naveed Ahmed, Kadem Al-lamee, Nial Bullett, and Neil W. Bressloff. 2022. “Exploring a Parallel Rheological Framework to Capture the Mechanical Behaviour of a Thin-Strut Polymeric Bioresorbable Coronary Scaffold.” *Journal of the Mechanical Behavior of Biomedical Materials* 130 (December 2021): 105154. <https://doi.org/10.1016/j.jmbbm.2022.105154>.
- Kan, Jing, Zhen Ge, Jun Jie Zhang, Zhi Zhong Liu, Nai Liang Tian, Fei Ye, Sui Ji Li, et al. 2016. “Incidence and Clinical Outcomes of Stent Fractures on the Basis of 6,555 Patients and 16,482 Drug-Eluting Stents From 4 Centers.” *JACC: Cardiovascular Interventions* 9 (11): 1115–23. <https://doi.org/10.1016/j.jcin.2016.02.025>.
- Katarzyna, Polak-Krasna, Ali Reza Abaei, Reyhaneh Neghabat Shirazi, Eoin Parle, Oliver Carroll, William Ronan, and Ted J Vaughan. 2021. “Physical and Mechanical Degradation Behaviour of Semi-Crystalline PLLA for Bioresorbable Stent Applications.” *Journal of the Mechanical Behaviour of Biomedical Materials*, 135938. <https://doi.org/10.1016/j.jmbbm.2021.104409>.
- Kraak, Robin P., Mariëlla E.C.J. Hassell, Maik J. Grundeken, Karel T. Koch, Jose P.S. Henriques, Jan J. Piek, Jan Baan, et al. 2015. “Initial Experience and Clinical Evaluation of the Absorb Bioresorbable Vascular Scaffold (BVS) in Real-World Practice: The AMC Single Centre Real World PCI Registry.” *EuroIntervention* 10 (11): 1160–68. [https://doi.org/10.4244/EIJY14M08\\_08](https://doi.org/10.4244/EIJY14M08_08).
- Lipinski, Michael J., Ricardo O. Escarcega, Nevin C. Baker, Hadiya A. Benn, Michael A. Gaglia, Rebecca Torguson, and Ron Waksman. 2016. “Scaffold Thrombosis after Percutaneous Coronary Intervention with ABSORB Bioresorbable Vascular Scaffold A Systematic Review and Meta-Analysis.” *JACC: Cardiovascular Interventions* 9 (1): 12–24. <https://doi.org/10.1016/j.jcin.2015.09.024>.
- Luo, Qiyi, Xiangkun Liu, Zhonghua Li, Chubo Huang, Wen Zhang, Juan Meng, Zhaohua Chang, and Zezhao Hua. 2014. “Degradation Model of Bioabsorbable Cardiovascular Stents.” *PLoS ONE* 9 (11): 1–9. <https://doi.org/10.1371/journal.pone.0110278>.
- Naseem, Raasti, Ligu Zhao, Senthil K. Eswaran, and Helen Willcock. 2020. “Characterization of

Biodegradable Poly(L-Lactide) Tube over Accelerated Degradation.” *Polymer Engineering and Science* 60 (7): 1430–36. <https://doi.org/10.1002/pen.25390>.

Naseem, Raasti, Ligu Zhao, Vadim Silberschmidt, Yang Liu, Ollie Scaife, Helen Willcock, Senthil Eswaran, and Syed Hossainy. 2019. “Mechanical and Chemical Characterisation of Bioresorbable Polymeric Stent over Two-Year in Vitro Degradation.” *Journal of Biomaterials Applications* 34 (1): 61–73. <https://doi.org/10.1177/0885328219839591>.

Nishio, Soji, Kunihiko Kosuga, Keiji Igaki, Masaharu Okada, Eisho Kyo, Takafumi Tsuji, Eiji Takeuchi, et al. 2012. “Long-Term (>10 Years) Clinical Outcomes of First-in-Human Biodegradable Poly-L-Lactic Acid Coronary Stents: Igaki-Tamai Stents.” *Circulation* 125 (19): 2343–52. <https://doi.org/10.1161/CIRCULATIONAHA.110.000901>.

Qiu, T., R. He, C. Abunassar, S. Hossainy, and L. G. Zhao. 2018. “Effect of Two-Year Degradation on Mechanical Interaction between a Bioresorbable Scaffold and Blood Vessel.” *Journal of the Mechanical Behavior of Biomedical Materials* 78 (November 2017): 254–65. <https://doi.org/10.1016/j.jmbbm.2017.11.031>.

Räber, Lorenz, Salvatore Brugaletta, Kyohei Yamaji, Crochan J. O’Sullivan, Shuji Otsuki, Tobias Koppa, Masanori Taniwaki, et al. 2015. “Very Late Scaffold Thrombosis: Intracoronary Imaging and Histopathological and Spectroscopic Findings.” *Journal of the American College of Cardiology* 66 (17): 1901–14. <https://doi.org/10.1016/j.jacc.2015.08.853>.

Renouf-Glauser, Annette C., John Rose, David F. Farrar, and Ruth Elizabeth Cameron. 2005. “The Effect of Crystallinity on the Deformation Mechanism and Bulk Mechanical Properties of PLLA.” *Biomaterials* 26 (29): 5771–82. <https://doi.org/10.1016/j.biomaterials.2005.03.002>.

Serruys, Patrick W., Bernard Chevalier, Yohei Sotomi, Angel Cequier, Didier Carrié, Jan J. Piek, Ad J. Van Boven, et al. 2016. “Comparison of an Everolimus-Eluting Bioresorbable Scaffold with an Everolimus-Eluting Metallic Stent for the Treatment of Coronary Artery Stenosis (ABSORB II): A 3 Year, Randomised, Controlled, Single-Blind, Multicentre Clinical Trial.” *The Lancet* 388 (10059): 2479–91. [https://doi.org/10.1016/S0140-6736\(16\)32050-5](https://doi.org/10.1016/S0140-6736(16)32050-5).

Serruys, Patrick W., John A. Ormiston, Yoshinobu Onuma, Evelyn Regar, Nieves Gonzalo, Hector M. Garcia-Garcia, Koen Nieman, et al. 2009. “A Bioabsorbable Everolimus-Eluting Coronary Stent System (ABSORB): 2-Year Outcomes and Results from Multiple Imaging Methods.” *The Lancet* 373 (9667): 897–910. [https://doi.org/10.1016/S0140-6736\(09\)60325-1](https://doi.org/10.1016/S0140-6736(09)60325-1).

Shazly, Tarek, Vijaya B. Kilachalama, Jahid Ferdous, James P. Oberhauser, Syed Hossainy, and Elazer R. Edelman. 2012. “Assessment of Material By-Product Fate from Bioresorbable Vascular Scaffolds.” *Annals of Biomedical Engineering* 40 (4): 955–65. <https://doi.org/10.1007/s10439-011-0445-8>.Assessment.

Shine, Connor J, Peter E Mchugh, and William Ronan. 2021. “Impact of Degradation and Material Crystallinity on the Mechanical Performance of a Bioresorbable Polymeric Stent.” *J Elast.* <https://doi.org/10.1007/s10659-021-09835-7>.

Simamora, Pahala, and Wendy Chern. 2006. “Poly-L-Lactic Acid: An Overview.” *Journal of Drugs in Dermatology : JDD* 5 (5): 436–440. <http://europepmc.org/abstract/MED/16703779>.

Singh, Achintya D., Aayush K. Singal, Agrima Mian, Samir R. Kapadia, David P. Hedrick, Anmar Kanaa’N, Jaikirshan J. Khatri, Rishi Puri, and Ankur Kalra. 2020. “Recurrent Drug-Eluting Stent In-Stent Restenosis: A State-of-the-Art Review of Pathophysiology, Diagnosis, and Management.” *Cardiovascular Revascularization Medicine* 21 (9): 1157–63. <https://doi.org/10.1016/j.carrev.2020.01.005>.

Soares, João S., James E. Moore, and Kumbakonam R. Rajagopal. 2008. “Constitutive Framework for Biodegradable Polymers with Applications to Biodegradable Stents.” *ASAIO*, 295–301. <https://doi.org/10.1097/MAT.0b013e31816ba55a>.

Tsuji, Hideto, and Yoshito Ikada. 2000. "Properties and Morphology of Poly(L-Lactide) 4. Effects of Structural Parameters on Long-Term Hydrolysis of Poly(L-Lactide) in Phosphate-Buffered Solution." *Polymer Degradation and Stability* 67 (1): 179–89. [https://doi.org/10.1016/S0141-3910\(99\)00111-1](https://doi.org/10.1016/S0141-3910(99)00111-1).

Tsuji, Hideto, Akira Mizuno, and Yoshito Ikada. 2000. "Properties and Morphology of Poly(L-Lactide). III. Effects of Initial Crystallinity on Long-Term *In Vitro* Hydrolysis of High Molecular Weight Poly(L-Lactide) Film in Phosphate-Buffered Solution." *Journal of Applied Polymer Science* 77 (7): 1452–64. [https://doi.org/10.1002/1097-4628\(20000815\)77:7<1452::AID-APP7>3.0.CO;2-S](https://doi.org/10.1002/1097-4628(20000815)77:7<1452::AID-APP7>3.0.CO;2-S).

Vey, Elisabeth, Caroline Roger, Liz Meehan, Jonathan Booth, Mike Claybourn, Aline F. Miller, and Alberto Saiani. 2008. "Degradation Mechanism of Poly(Lactic-Co-Glycolic) Acid Block Copolymer Cast Films in Phosphate Buffer Solution." *Polymer Degradation and Stability* 93 (10): 1869–76. <https://doi.org/10.1016/j.polymdegradstab.2008.07.018>.

Vyavahare, Omkar, David Ng, and Shaw Ling Hsu. 2014. "Analysis of Structural Rearrangements of Poly(Lactic Acid) in the Presence of Water." *Journal of Physical Chemistry B* 118 (15): 4185–93. <https://doi.org/10.1021/jp500219j>.

Wang, Pei-jiang, Francesca Berti, Luca Antonini, Farhad Rikhtegar Nezami, Lorenza Petrini, Francesco Migliavacca, and Elazer R. Edelman. 2020. "Multimodal Loading Environment Predicts Bioresorbable Vascular Scaffolds' Durability." *Annals of Biomedical Engineering*.

Weir, N. A., F. J. Buchanan, J. F. Orr, and G. R. Dickson. 2004. "Degradation of Poly-L-Lactide. Part 1: *In Vitro* and *In Vivo* Physiological Temperature Degradation." *Proceedings of the Institution of Mechanical Engineers, Part H: Journal of Engineering in Medicine* 218 (5): 307–19. <https://doi.org/10.1243/0954411041932782>.

# Chapter 6

## A Computational Investigation into the Effect of Scaffold Geometry and Degradation Parameters on the Long-Term Degradation Performance

---

### 6.1. Introduction

Bioresorbable scaffolds (BRS) were envisaged to become the next step in percutaneous coronary interventions (PCI), with the ability to be fully resorbed into the patient vessel once healing was complete. However, it has been found that the implantation of polymer BRS has led to excessive late-stent thrombosis compared with conventional metal drug eluting stents (DES) (Byrne *et al.* 2018). One of the possible causes for poor late-stage performance was attributed to loss of integrity of the polymer backbone causing an alteration in the blood flow and possible prolapse of struts into the lumen and also the thick stent struts protruding into the vessel. It is well established that stent geometry and strut dimensions affect the performance of endovascular devices, where thinner strut cross sections perform better than thicker strut profiles *in vivo* (Foin *et al.* 2014). Thinner struts generally cause less alteration to local hemodynamics, leading to a reduction in the risk of restenosis and thrombosis and also allow for faster re-endothelisation (Byrne *et al.* 2018). However, polymer BRS materials are inherently less stiff than their metallic counterparts and have tended to have higher thickness struts to achieve the required radial properties. There has still been a substantial variation in the strut thickness of polymer BRS, with a variety of stent designs also used. To date, computational design optimisation studies (Migliavacca *et al.* 2002; Pant *et al.* 2011; Pant, Bressloff, and Limbert 2012) on stent geometry performed on various stent designs and on

early metallic DES by (Migliavacca *et al.* 2002) have shown the importance of strut width, where stents with low stent-to-artery surface ratios have higher levels of radial and foreshortening in DES. Grogan *et al.*, (2013) investigated metallic BRS to better understand the effect of stent cross-sections and hinge profiles on short- and long-term performance of metallic BRS. It was found maximising strut width leads to a favourable initial and long-term stiffness, which would likely contribute to improved long-term degradation performance. Although, it was also found that there was no substantial advantage to varying the cross-section shape/profile on the mechanical short and long-term performance. While a number of studies have been performed on the optimisation of metal and polymer BRS for the initial mechanical performance, there seems to be a lack of studies that consider the optimisation of scaffold geometry and its role in the long-term degradation performance.

Degradation of aliphatic polyesters used in BRS applications is known to progress through the process of hydrolysis (Göpferich 1996) where the mechanisms of degradation are covered in detail in Chapter 2. Polymers that undergo recrystallization during degradation are able to maintain their elastic modulus and tend to have increased strength, but have reduced ductility (Tsuji and Ikada 1995). Numerous experimental studies examining sample geometries, such as films (Tsuji and Ikada 2000; Vey *et al.* 2012; Weir *et al.* 2004), dog-bones (Kimble and Bhattacharyya 2015; Katarzyna *et al.* 2021), pins (Duek, Zavaglia, and Belangero 1999) and tubes (Naseem *et al.* 2020), have evaluated the response of PLLA undergoing degradation. It has been found that degradation affects mechanical properties in a number different ways, with a number of mechanical properties affected and found to deteriorate differently depending on the PLLA formulation. Thermal and molecular weight analysis from these studies also demonstrate the decrease in molecular weight and increase in crystallinity over the course of the degradation period. The complex and varied changes that take place during polymer

---

degradation lead to great complexity in designing polymer BRS, in particular when both short- (e.g. deployment) and long-term degradation behaviour are to be considered.

Computational degradation models have generally used continuum damage mechanics frameworks to introduce phenomenological degradation variable(s) that operate on one, or several, of the constitutive material parameters to predict material degradation. Degradation variables are implemented as a function of time and describe the severity of degradation at a material point. While there are key differences in model implementation across computational degradation models, their general principles assume that degradation leads to a reduction in one or more material properties. Apart from differences in the underlying constitutive description of the virgin material, the underlying assumption(s) of how degradation actually affects material behaviour across these models is vastly different. Many computational degradation models only consider evolution in a single mechanical parameter (T. Qiu et al. 2018; Soares, Moore, and Rajagopal 2010) compared to what has been shown experimentally. While studies provide a certain amount of reasoning for their model form, generally attributing it to the observed experimental behaviour, the physical basis for these differences in model implementation is generally not clear. It would appear that several models happen to be effective in reducing the load-bearing capacity of the device. While this might re-create the observed response of the device under certain loading conditions, the justification of the model form is not provided, and it is difficult to see how they could be applied beyond a limited range of circumstances. This was partially observed in Chapter 5, whereby the degradation model framework was calibrated based on static degradation data, but was unable to capture several effects that were observed experimentally under constant loading conditions. Although the degradation model developed in Chapter 5 could only capture the static response of polymer BRS, it still provides a suitable framework to study the behaviour of these devices as it can

predict short-term deployment behaviour and a wide range of possible degradation responses, including elastic, yield and post-yield behaviour.

The objective of this study is to systematically investigate the role of geometric and material properties on the short- and long-term degradation performance of polymer BRS. In particular, the role of polymer BRS design is investigated in detail to understand how it affects the deployment behaviour and subsequent degradation performance. The effect of material behaviour is also investigated, whereby a parameter study of the degradation model parameters is carried out to understand long-term degradation performance.

## **6.2. Methods**

### **6.2.1. Study Design**

This study consists of three parts, whereby the first investigates the long-term degradation behaviour of a generic polymer BRS geometry (based on the Abbott Absorb design) in both freely expanded and artery expanded configurations. The effect of individually degrading various material parameters (e.g. elastic modulus, yield strength, strain to failure and a combination of these three mechanical parameters) and its effects on the radial performance is investigated. The second section investigates the role of scaffold width on the short- and long-term performance of polymer BRS. In this section the effect on the short-term performance including crimp, deployment and radial performance with varying strut width is investigated. Finally, two separate scaffold geometries (Abbott Absorb and a non-commercial BRS) are compared by expanding them within an idealised artery, where the short- and long-term performance are investigated using established material properties determined from Chapter 4 and 5 (non-commercial BRS) and from the literature (Abbott Absorb).

### 6.2.2. Model Geometries

In the parametric studies, the balloon expandable polymer BRS used were representative of the Abbott Absorb and a non-commercial polymer BRS. The Absorb geometry consisted of three peaks and valleys per unit, with three connecting vertical axial struts for each ring. The non-commercial BRS consisted of six peaks and valleys per unit connected diagonally with three axial struts for each ring (see Figure 6.1). To reduce computational cost, reduced models consisting of two circumferential rings were considered for this analysis. The BRS models were discretized using 10,560 and 27,990 C3D8R hexahedral elements for the Absorb and non-commercial BRS respectively, with four elements across the thickness of the scaffold. Figure 6.1 shows the geometry and discretized BRS used for the simulation. A verification of these reduced models was carried out by establishing that they exhibited similar behaviour to a full-sized model of the Absorb and non-commercial BRS, under both crimping and free expansion.

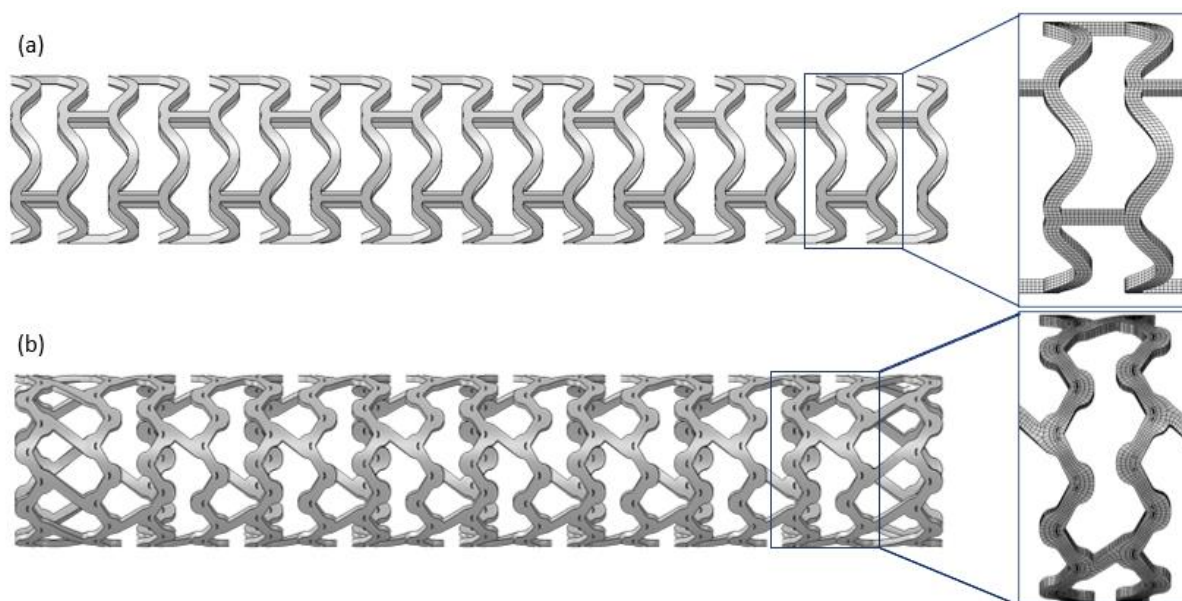


Figure 6.1. BRS geometries of the (a) Abbott Absorb and (b) Non-commercial BRS used in this study with the meshes used to discretise the BRS devices.


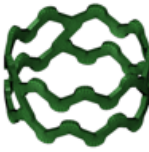



#### 6.2.2.1. Scaffold Geometric Parameter Study

To investigate the role of geometric effects on the short- and long-term performance, the width of the generic BRS devices were varied and considered as a ratio of the strut thickness. Four width to thickness ratios (WTR) were investigated: WTR=1, WTR = 1.17, WTR = 1.45 and



WTR = 1.6. Thickness is defined as the dimension in the radial direction and width as the dimension in the circumferential direction. Here, the WTR = 1.17 geometry had similar dimensions to the original Abbot Absorb design, while WTR = 1.6 had a similar configuration to the non-commercial BRS presented in Chapter 5. Table 6.1 summarises the attributes of the BRS used in this study along with the dimensions of the BRS cross-sections. Note that the discretization of each of the WTR BRS contained the same number of elements in each model.

Table 6.1. Overview of the geometries, cross sections and internal diameter of the vascular BRS used for the simulations used in this study.

Geometry Name	Absorb (WTR 1.17)	Non-Commercial BRS	WTR 1.0	WTR 1.45	WTR 1.6
Width-Thickness Ratio (WTR)	1.17	1.6	1.0	1.45	1.6
Geometry					
Cross Section TxW (µm)	157.5 x 184.275	115.5 x 184	157.5 x 157	157.5 x 228.375	157.5 x 252
Diameter (mm)	3.0	3.0	3.0	3.0	3.0

### 6.2.2.2. Balloon Geometry

A tri-folded balloon, meshed with 11,242 3-node triangular membrane (M3D3) elements was used for device expansion using a similar construction approach to Avanzini *et al* (Avanzini and Battini 2018). Figure 6.2 demonstrates the construction steps of the tri-folded balloon geometry used for deployment of the reduced BRS. The three leaflets were formed using semi-circular rigid tools; an internal pressure was applied to maintain the shape while a second set of sigmoidal shaped tools folded the leaflets into a tri-folded configuration. The same method of generating the balloon geometry was used to construct the balloon used for expanding the full BRS geometries.

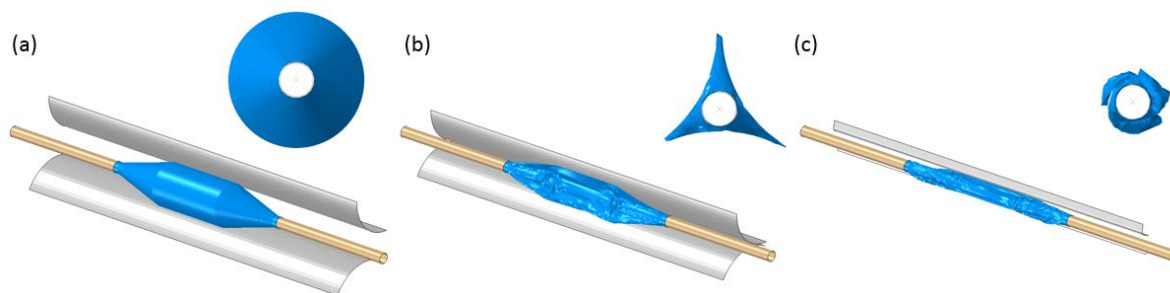


Figure 6.2. Schematic showing the process of the formation of a tri-folded balloon and rigid tools used to form and fold the leaflets. (a) Application of the rigid tools to form three leaflets, (b) application of pressure to hold tri-folded shape and (c) rotation of tools to fold the leaflets such that the balloon can fit within the crimped geometry of a vascular BRS.

### 6.2.2.3. Vessel Geometry

An idealised vessel section was considered for deployment of the BRS designs, as shown in Figure 6.3. The characteristic dimensions of this vessel were derived from a patient-specific vessel geometry obtained from the InSilc artery database (“INSILC Cloud” 2018), with further reading on the vessel reconstruction methods available in Vukicevic et al (Vukicevic et al. 2018). The reduced section was meshed using 20,740 hexahedral (C3D8R) elements, whereby this vessel was extended for the full-sized BRS, which consisted of 28,800 C3D8R elements. The blood vessel had an internal diameter of 1.87 mm with the section divided into three layers consisting of the intima, media and adventitia. The thickness of each layer taken from the most occluded section of a patient specific arterial model. The thickness for each layer was 0.89 mm, 0.28 mm and 0.3 mm for the intima, media and adventitia, respectively.

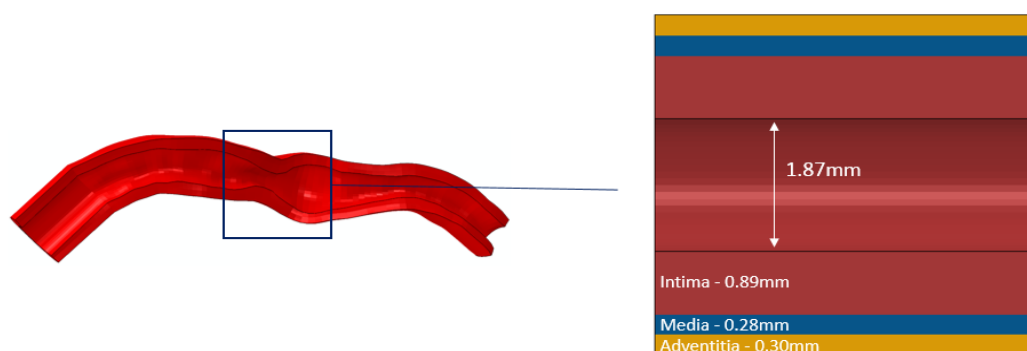


Figure 6.3. Schematic showing the patient specific arterial model and the artery section used in this study derived from and the widths of the different arterial layers.

### 6.2.3. Constitutive Material Models

#### 6.2.3.1 BRS Constitutive Material Models

The short-term BRS constitutive material model used for the WTR and degradation sections of this study was based on an elastic-plastic match of the Johnson-Cook model framework presented in the previous Chapter. Here, the chosen parameters consisted of a rate-independent calibration of the previous model, see Table 6.2 at a strain rate of 0.1 mm/s. The time-dependency was removed so that the effects of the degradation could be analysed without viscous effects. In the third section of this study, material properties for the Absorb BRS are shown in Table 6.2. Here, the non-commercial BRS was modelled using an elastic visco-plastic material using the Johnson Cook model frame-work as outlined in the previous chapter, again summarised in Table 6.2below.

*Table 6.2. Elastic and Johnson-Cook material parameters used for the non-commercial and Absorb BRS.*

BRS Model	Elastic Modulus (E) GPa	Poisson's Ratio ( $\nu$ )	Yield Stress ( $\sigma_y$ ) MPa	Johnson-Cook Parameters			Johnson-Cook Rate Dependant Hardening	
				A	B	n	C	$\dot{\epsilon}_0$
Non-Commercial BRS	1.0	0.45	-	4.0	1.1	1.2	1.0	$5.0 \times 10^{-5}$
Abbott Absorb TWR	1.665	0.45	-	5.0	30.0	1.97	1.5	$2.0 \times 10^{-5}$
Parameter Study	1.25	0.45	34.0	-	-	-	-	-

#### 6.2.3.2 Balloon and Artery Constitutive Properties

The balloon material was modelled using a 1<sup>st</sup> order Ogden hyperelastic material with the material parameters obtained from (Antonini, Mandelli, et al. 2021). An isotropic hyperelastic constitutive model was used to model the different arterial layers. The constitutive law used was a 6<sup>th</sup> order reduced polynomial strain energy density function, with the material coefficients obtained from (Gervaso et al. 2008) with the coefficients calibrated from experimental testing performed on arterial tissue by Holzapfel et al (Holzapfel et al. 2005). Table 6.3 reports the coefficients for each layer. Note that for the full sized BRS simulations

the vessel geometry was extended to accommodate the full sized BRS geometry and balloon, the material parameters remain the same.

Table 6.3. Material coefficients for the 6<sup>th</sup> order reduced polynomial strain energy density function for the intima, media and adventitia vessel layers.

	$C_{10}$	$C_{20}$	$C_{30}$	$C_{40}$	$C_{50}$	$C_{60}$
Intima	$6.79 \times 10^{-3}$	0.54	-1.11	10.65	-7.27	1.63
Media	$6.52 \times 10^{-3}$	$4.89 \times 10^{-2}$	$9.26 \times 10^{-3}$	0.76	-0.43	$8.69 \times 10^{-2}$
Adventitia	$8.27 \times 10^{-3}$	$1.20 \times 10^{-2}$	0.52	-5.63	21.44	0.00

### 6.2.3.3 Degradation Models and Parameter Study

To investigate the effect of various material parameters degrading on the freely expanded and arterial performance of the BRS, the degradation framework presented in Chapter 5 was used and adapted for use with an elastic-plastic material. This framework meant that the elastic, yield and post-yield behaviour could be manipulated according to Equations ( 5-1 ), ( 5-1 ) and ( 5-2 ). As outlined in the previous chapter, degradation was implemented through a user defined subroutine (VUSDFLD). The degradation parameters  $d_i(t)$  control how each of the mechanical properties is degraded, namely elastic modulus ( $d_1$ ), yield stress ( $d_2$ ), failure strain ( $d_3$ ). A field variable controlled with Equation ( 6-1 ) and implemented through the VUSDFLD relates the evolution of the  $d$  parameters to the material parameter being degraded. For this study, the evolutions of the degradation parameters followed an arbitrary degradation curve governed by the following sigmoidal function, described by,

$$d_i(t) = \frac{d_{t_0} - d_{t_{max}}}{1 + e^{\left(\frac{t-t_{max}}{2}\right)^c}} + d_{t_{max}} \quad (6-1)$$

where  $d_{t_0}$  is the value of the parameter being degraded at time zero,  $d_{t_{max}}$  is the value of the parameter at full degradation and  $t$  is the simulation time. Figure 6.4 shows the evolution of  $d_i(t)$  for each of the material parameters. An arbitrary degradation curve was chosen for each parameter independent of the behaviours shown in previous chapters. This was used for the variation of the degradation parameters and WTR study. Once the failure strain was exceeded damage was implemented through the ductile damage model in Abaqus CAE, see Equation ( 5-3 ) where the displacement to failure,  $\bar{u}_f^{pl}$  was kept at a value of 0.01. For each degradation

simulation at  $t = 0$  the material was un-degraded and at  $t = 1$  the material was fully degraded.

A degradation period of one year was arbitrarily selected for the simulated degradation.

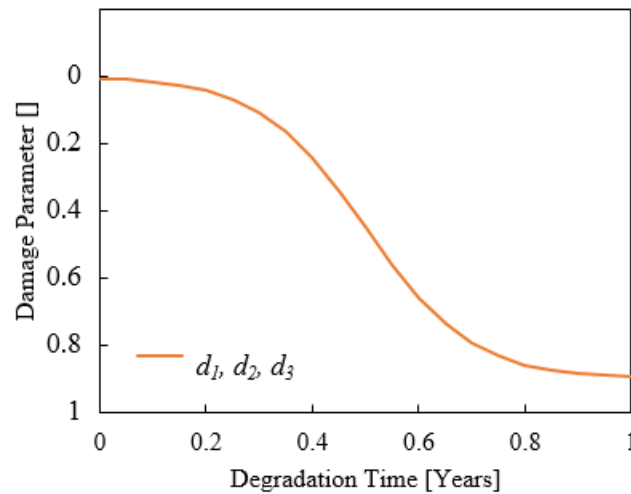


Figure 6.4. Plots demonstrating the evolution of the various material properties,  $d_1$  (elastic modulus),  $d_2$  (yield stress) and  $d_3$  (failure strain).

For the third part of this study, the degradation framework as outlined in the previous chapter was used to degrade the non-commercial and Absorb BRS. For the non-commercial BRS the degradation model parameters are the same as those calibrated in Chapter 5. For the Absorb BRS, some alterations to the framework were made. Experimental degradation of the Abbott Absorb performed by (T. Qiu et al. 2018) found that only the yield stress was affected by the degradation. To replicate this behaviour, only the  $d_2$  parameter was evolved over time to capture the effects of degradation as found by Qiu *et al.* Figure 6.5 shows the evolution of the degradation parameters for both the non-commercial and Absorb BRS. This differs from the Figure 6.4 as these degradation parameters are defined on experimental results for the represented devices.

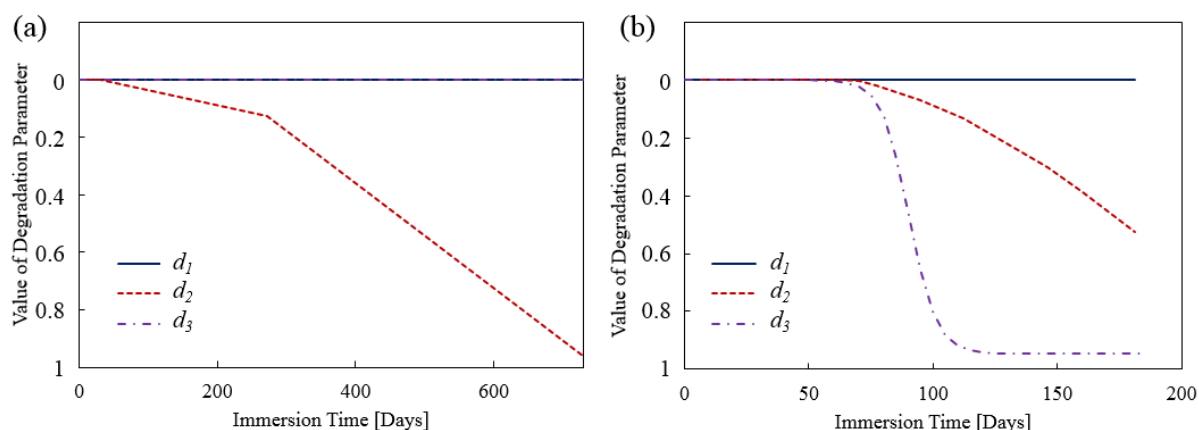


Figure 6.5. Plots demonstrating the evolution of the various material properties,  $d_1$  (elastic modulus),  $d_2$  (yield stress) and  $d_3$  (failure strain) for the (a) Abbott Absorb and (b) non-commercial BRS.

#### 6.2.4. Simulation Workflow

Crimping of the various BRS geometries was performed using 16 discrete rigid plates. The plates were meshed using 160 4-noded 3D bilinear rigid quadrilateral elements (R3D4). The BRS devices were crimped to a diameter of 1.67 mm to conform to a balloon of this size. It should be noted that clinically this represents a large crossing profile, typically crossing profiles for coronary stents are less than 1 mm. Deployment was performed using the tri-folded balloon, by inflating the geometry and applying a pressure of 8atm to the internal balloon surface over a time step of 1.6 s. The balloon was then deflated by removing the pressure load, with the BRS allowed to recoil over a time step of 0.4 s. This deployment strategy was employed for both the freely-expanded and artery expansion simulations for all BRS geometries. A coefficient of friction of 0.3 was adopted for the balloon-BRS and BRS-vessel contact. Abaqus explicit finite element solver was used for all the simulations with a target time increment of  $1 \times 10^{-6}$  s. The radial response of the scaffolds was evaluated in their un-degraded and degraded states, by simulating a radial crush test on the devices using 16 discrete rigid plates (Figure 6.6). A displacement was applied to the plates to reduce the diameter of the scaffolds from the deployed diameter of 3.7 mm to 1.6 mm. The radial strength and stiffness taken were measured from the resulting radial curves. As outlined previously the radial stiffness was defined as the slope of the initial linear portion of the loading curve. The radial strength was defined as a

parallel line and 0.1 mm offset from the stiffness. The strength is defined as the intersection between this offset line and the loading curve. For the full sized BRS the same regime for crimping and deployment as outlined in the previous chapter was adopted for the non-commercial BRS, (Antonini, Poletti, et al. 2021). Crimping and deployment of the Absorb was performed as per (T. Qiu et al. 2018). Both BRS were deployed in a vessel of length 30 mm, consisting of the same layer geometry as outlined in Figure 6.6(b).

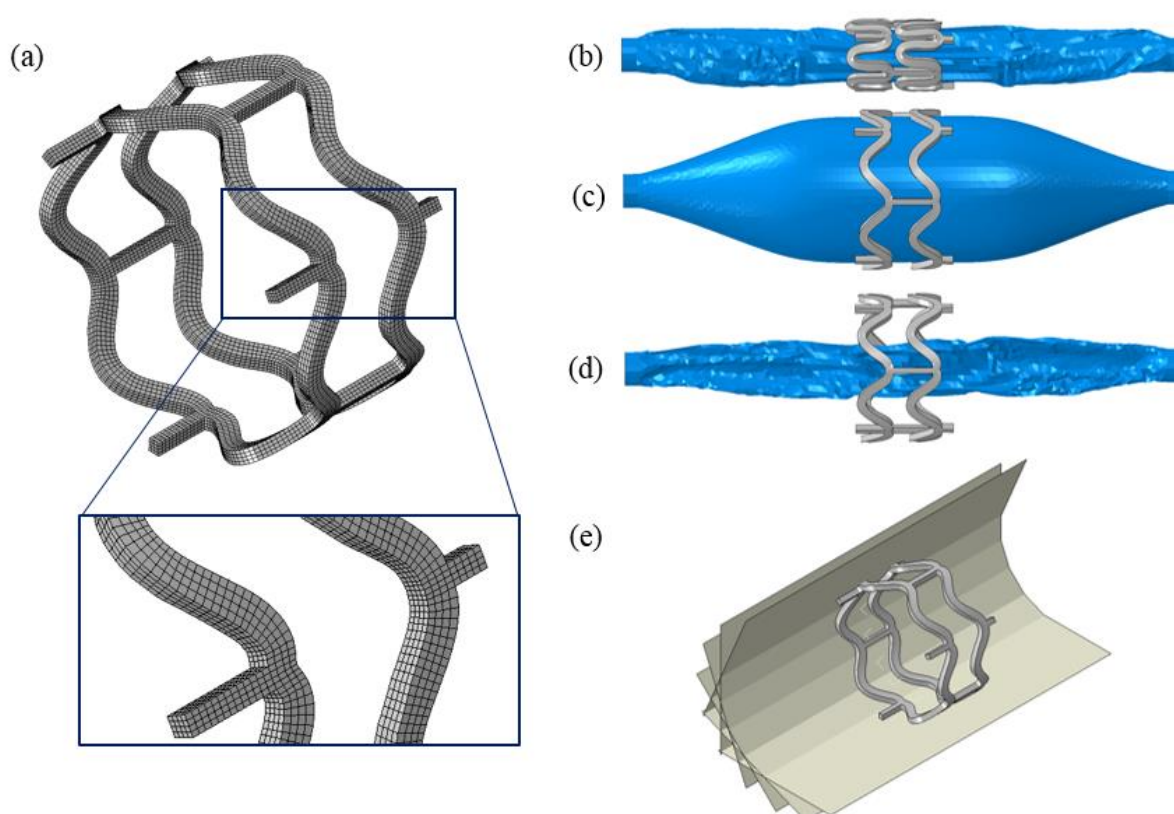


Figure 6.6 (a) Discretised Absorb geometry showing a zoomed image of the mesh used for analysis, (b-e) Schematic of the various stages of the simulation from crimping, deployment, post recoil and radial crush.

### 6.2.5. Post Processing

A number of relevant clinical and mechanical performance parameters for both short- and long-term properties of the BRS were determined from the vessel and freely expanded models. Several clinically relevant parameters (Auricchio et al. 2011) were selected: (i) the smallest area within the scaffolded region known as the minimal lumen area (MLA), (ii) lumen gain (LG) or the area compared pre and post stenting and (iii) area covered by the scaffold struts known as vessel coverage (VC). A schematic detailing how these metrics were measured is

shown in Figure 6.7. Mechanical performance parameters such as radial strength, stiffness, recoil and freely expanded diameter were also evaluated. The pressure diameter curves from inflating the devices were also computed.

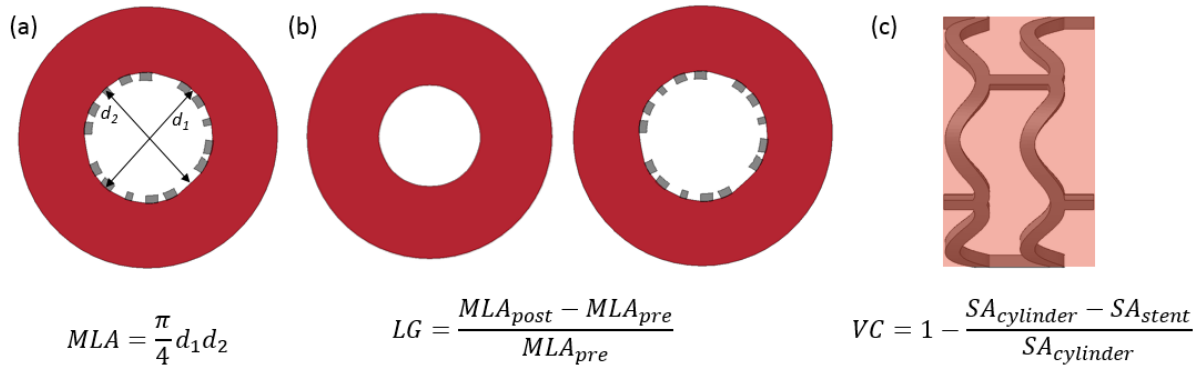


Figure 6.7. Schematic showing how key output parameters were computed, (a) Minimum lumen area (MLA), (b) Lumen gain (LG) and (c) Vessel coverage (VC).

## 6.3. Results

### 6.3.1. Effect of Degradation Parameters on Scaffold Performance

Figure 6.8 shows the radial response of the baseline BRS geometry that had a WTR= 1.17 (similar to Abbot Absorb), when subject to degradation through deterioration of the (i) elastic modulus (Figure 6.8(a)), (ii) yield stress (Figure 6.8(b)), (iii) failure strain (Figure 6.8(c)) and (iv) combined (Figure 6.8(d)). The values for radial force are normalised against the length of the scaffold section. Each of these material parameters controls an aspect of the radial response curve from these simulated mechanical tests. In Figure 6.8, the non-degraded scaffold response follows a typical radial response for a balloon expandable scaffold. This is characterised by a toe region, where contact is made between the radial test plates and the scaffold, which is followed by a linear region during elastic loading, a plateau region during plastic yielding and unloading along a slope that is generally similar to the loading curve. Figure 6.8 shows that the radial stiffness and strength are controlled by the elastic modulus and yield strength, while the length of the plateau region is controlled by the  $d_3$  degradation parameter. Figure 6.8(e) and Figure 6.8(f) show that degradation of elastic modulus reduces both the radial strength and



stiffness to a similar extent during degradation. Figure 6.8(d) shows combined degradation completely degrades the mechanical support of the vessel compared with degrading the parameters individually. It should be noted that while there is small visual difference in the radial stiffness in Figure 6.8(b), quantitatively measuring the slope shows the differences shown in Figure 6.8(f). As it is a post-yield property, degradation of the strain-to-failure has no effect on the stiffness of the BRS, as shown in Figure 6.8(c, f). However, at later time-points ( $t > 7$  months), the radial strength of the scaffold is gradually reduced by the deteriorating strain-to-failure.

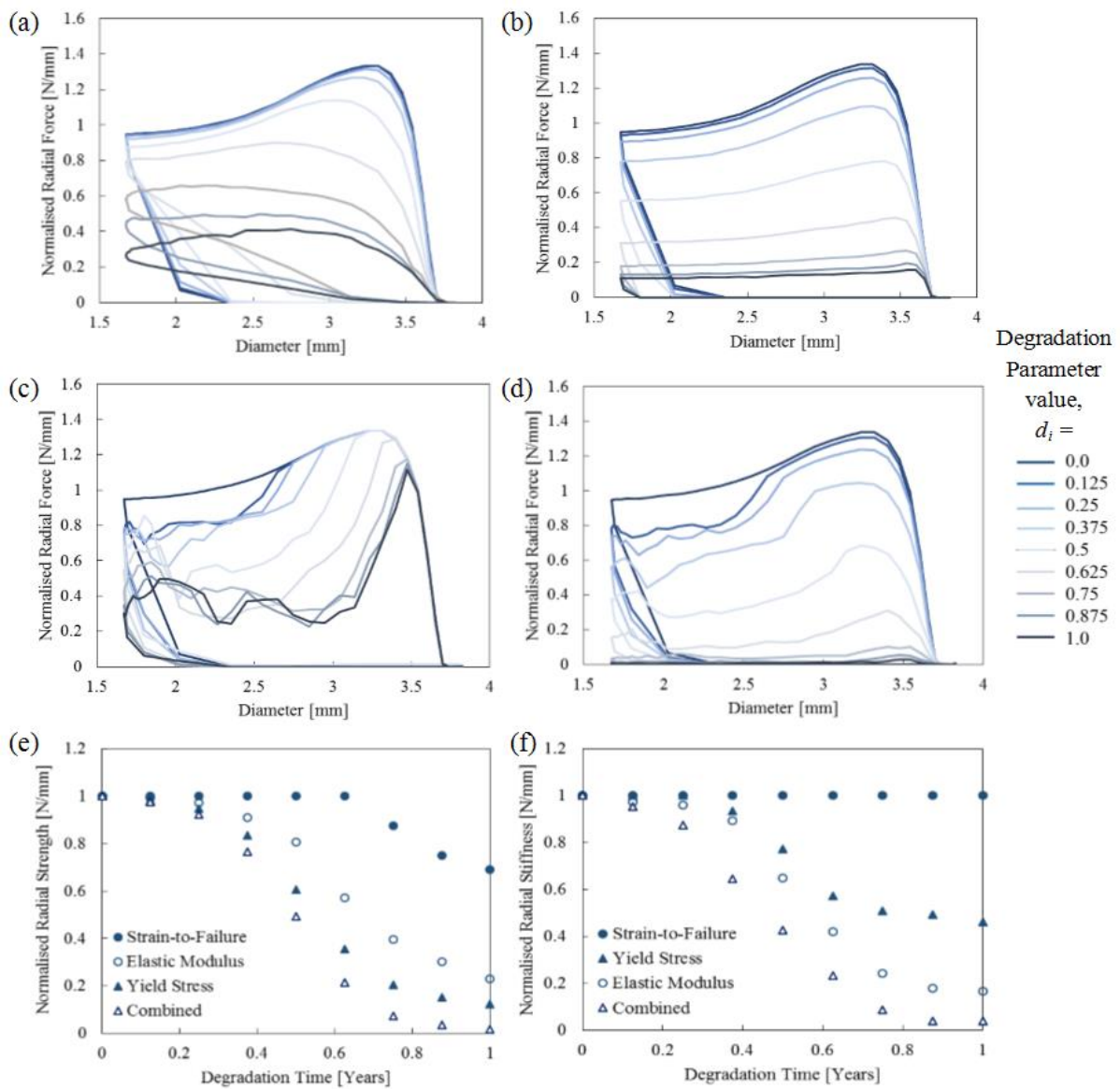


Figure 6.8. Normalised radial force versus diameter curves for a generic polymer BRS showing the effect of degrading the (a) elastic modulus, (b) yield strength, (c) failure strain, (d) combined and (e) evolution in radial strength and (f) evolution in the radial stiffness over the degradation period.

The effect of degrading each of these individual material parameters on the implanted performance of the BRS is shown in Figure 6.9. It shows that reductions in the yield strength or elastic modulus of the BRS lead to gradual reduction in the MLA of the scaffolded vessel over time. Interestingly, it was found that degradation of yield strength results in a greater reduction in MLA, compared the same relative degradation of elastic modulus. This suggests that post-yield elastic and plastic properties of the scaffold provide a greater contribution to the MLA, compared to the elastic component alone. Reduction of the strain-to-failure has little to no effect on the lumen area over time for the static vessel. As expected, a combined degradation approach results in the lowest MLA.

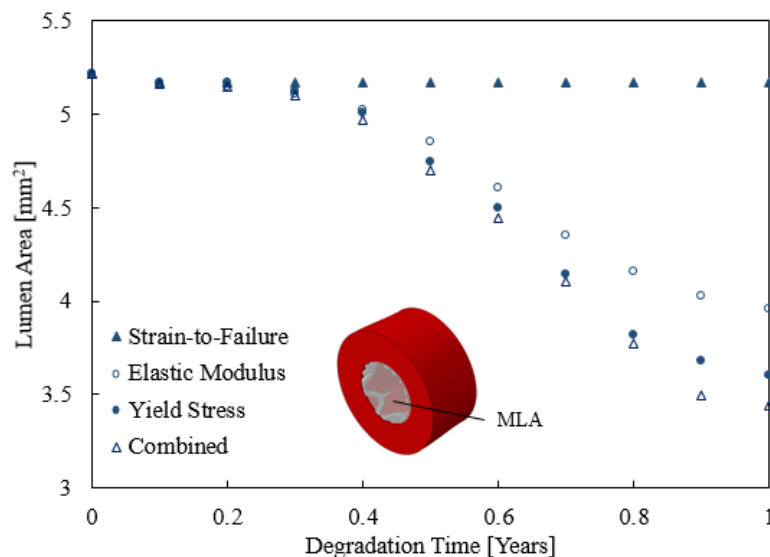


Figure 6.9. Effect of degradation of different parameters on the normalised minimal lumen area for a static vessel.

### 6.3.2. Effect of Geometric Parameters on Short and Long-Term Performance

#### 6.3.2.1 Crimp Performance

Contour plots of the crimping processes show the maximum principal stress and equivalent plastic strain distribution within the BRS sections, with an increasing maximum stress and plastic strain observed with increasing WTR, as shown in Figure 6.10. The width of the struts also affected the minimum crimped diameter possible for a given geometry, which can be seen in Figure 6.10. Measuring from the midpoint of the struts the average clearance between the struts at this diameter is 0.288 mm and 0.186 mm for WTR1 and 1.6 respectively.

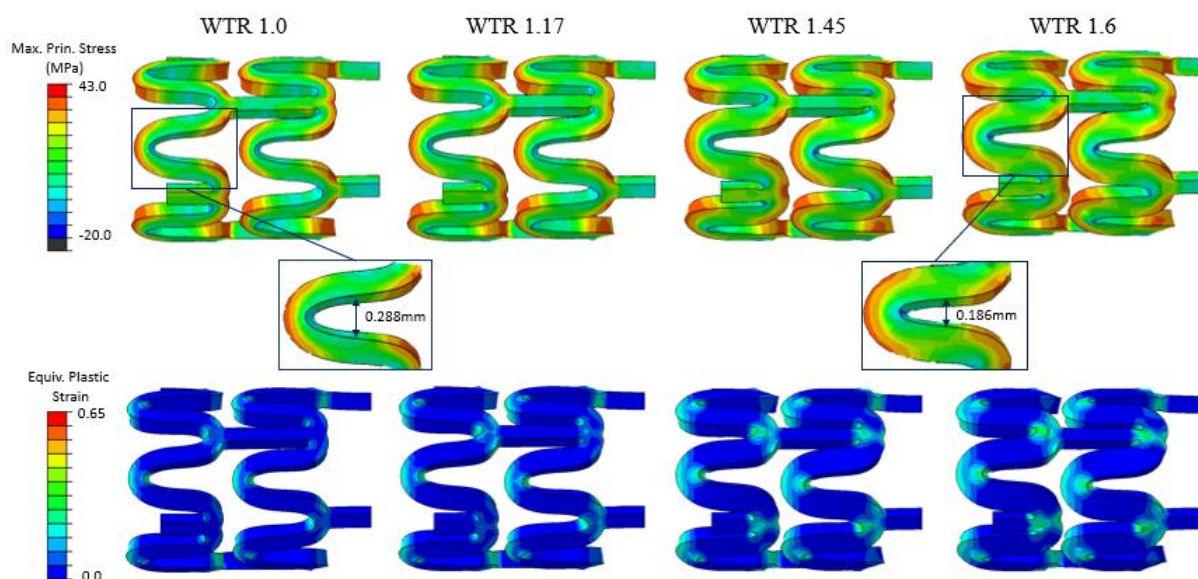


Figure 6.10. Contour plots of the different WTRBRS showing the maximum principal stress and equivalent plastic strain distributions at full crimp. Note each of the BRS was crimped to the same diameter.

### 6.3.2.2 Deployment

The pressure-diameter curves for the free expansion of the BRS are shown in Figure 6.11, where the outer diameter of the BRS is plotted against the balloon pressure. Here, the inflation process is represented on the left-hand side of the graph (0-0.8 MPa), while the deflation/recoil process is represented on the right-hand side of the graph (0.8 – 0 MPa). The pressure-diameter curves for free expansion generally have a bi-linear form. Initially, the BRS are easy to deploy as the plastic hinges are opened. This is followed by a notable change in slope as the hinges become more difficult to deform as they go past their original un-crimped diameter and the original balloon diameter is achieved. The plot shows that higher WTR values require higher pressures to achieve a diameter greater than 3 mm. For the vessel deployment cases, a similar bi-linear behaviour is observed, however it is less distinct than the freely expanded case. The final diameter for each of the BRS show WTR=1 and WTR=1.17 achieving the highest freely expanded and vessel expanded diameter at maximum inflation. Recoil of the BRS for both freely expanded and vessel cases for each of the WTRBRS is shown below in the latter half of Figure 6.11 and in Figure 6.12 below. The freely expanded cases show less recoil to those BRS deployed within the vessel. It shows that in the freely expanded case the lower WTR device

have lower recoil. However, the opposite is shown when deployed in a vessel where the higher WTR devices show less recoil and resulted in a larger lumen area post deployment. However, the lowest WTR= 1.0, which had the narrowest struts had a recoil of almost 18.7% when implanted in the vessel, which resulted in the smallest resulting lumen diameter.

Table 6.4. Recoil for the various WTR BRS under free expansion and expansion within a vessel.

Deployment Condition	Recoil (%)			
	WTR 1.0	WTR 1.17	WTR 1.45	WTR 1.6
Freely Expanded	3.64	4.33	4.47	5.95
Vessel	18.7	15.1	13.3	8.46

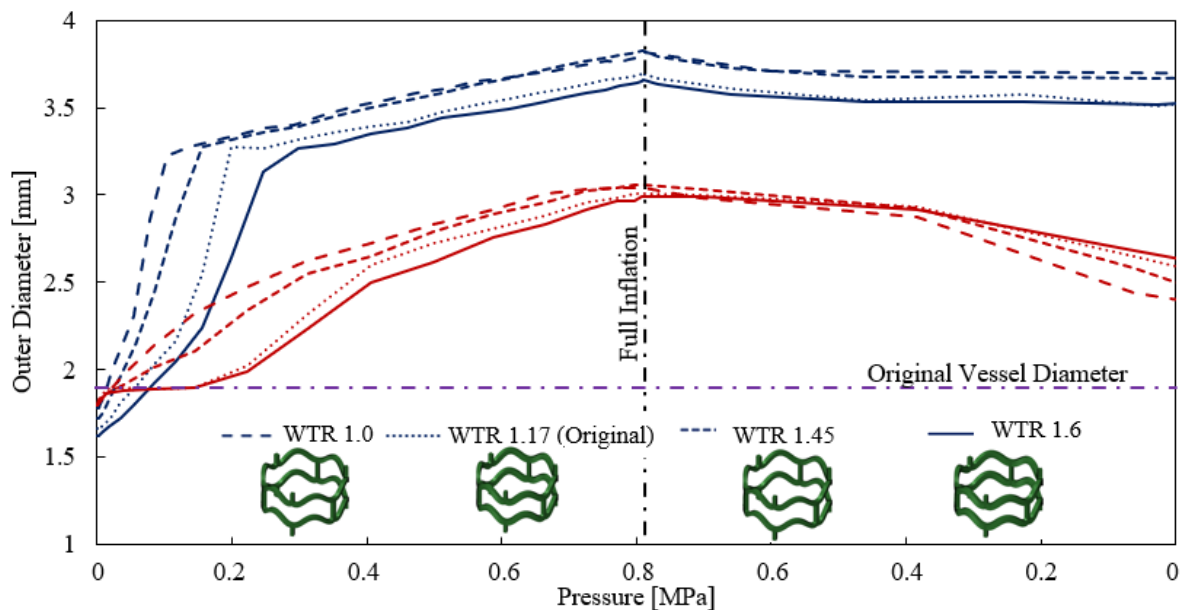


Figure 6.11. Diameter vs pressure curves for varying WTR under free expansion (Blue) and expansion within the vessel (Red) conditions followed by the recoil in each condition.

Contour plots of the deployment processes show the maximum principal stress and equivalent plastic strain distribution within the BRS, with a higher maximum stress and plastic strain observed with increasing WTR as expected, this is shown in Figure 6.12 below.

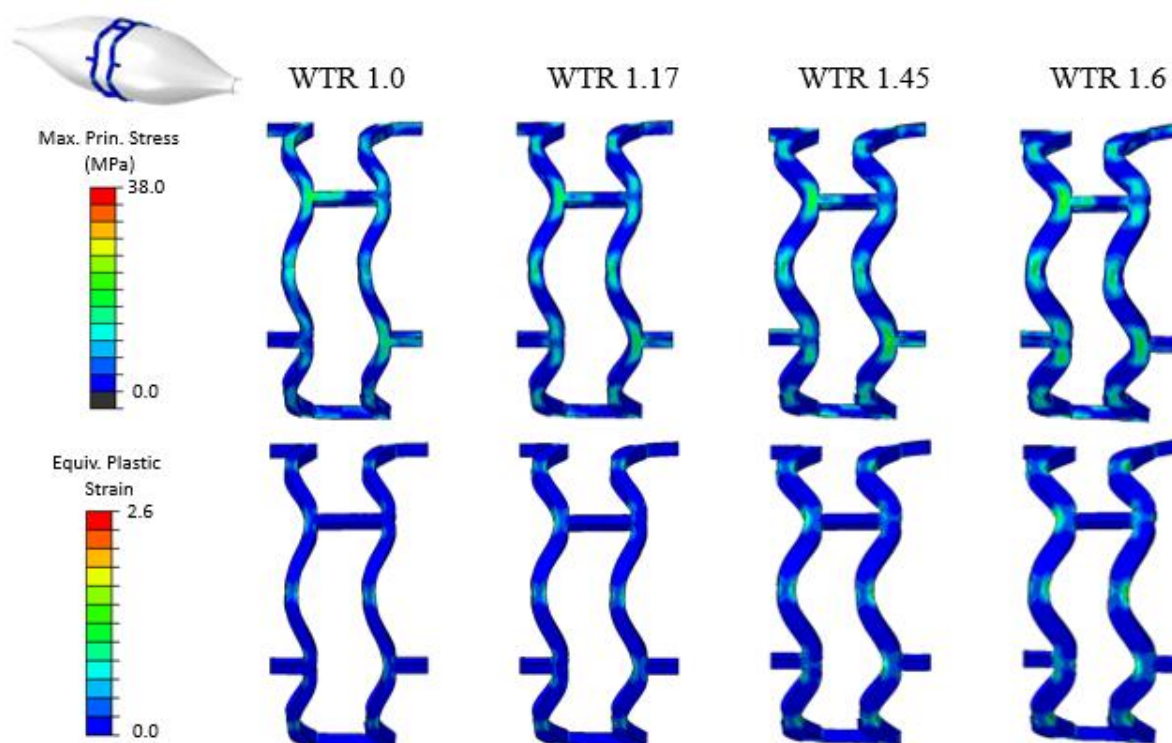


Figure 6.12. Contour plots of the different WTRBRS showing the maximum principal stress and equivalent plastic strain distributions at full deployment under free expansion.

### 6.3.2.3 Radial Performance

The effect of various WTR on the short- and long-term performance of BRS was investigated through freely-expanded and artery-expanded BRS. Figure 6.13 demonstrates the effect of the WTR on the radial crush performance, where an initial loading region is followed by a plateau and unloading. A square cross section, WTR=1 in this case results in a lower strength and stiffness compared with the original WTR=1.17. In terms of radial strength, increases in WTR result in an increase in the initial radial strength. A similar trend was found for the radial stiffness with higher WTR shaving higher radial stiffness, although this results in only modest increases (compared to those observed for radial strength). This shows that wider struts have higher radial strength over narrower struts.

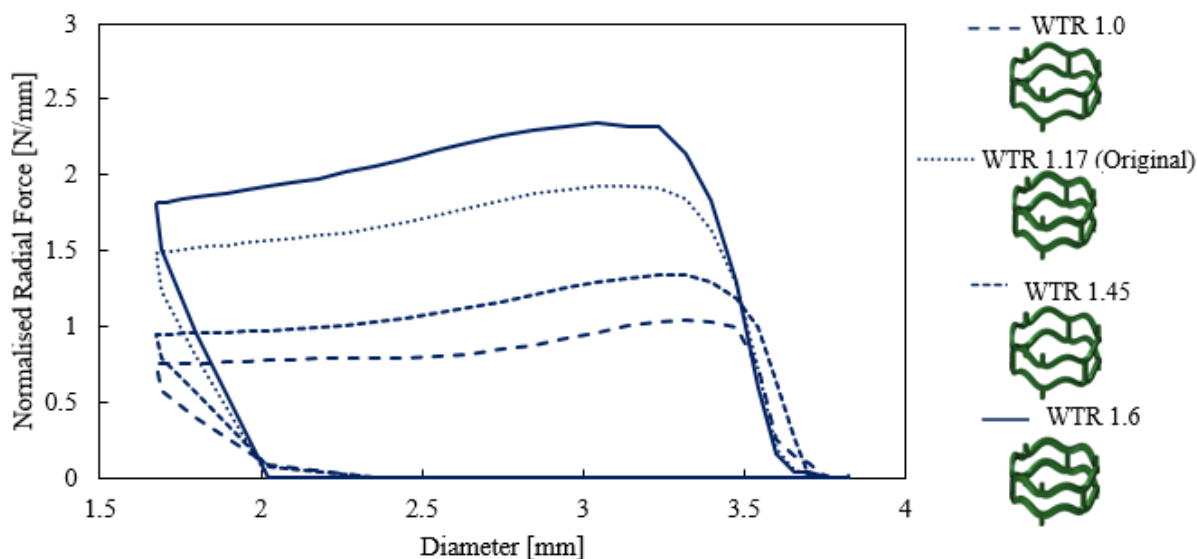


Figure 6.13. Computational radial force versus diameter curves for varying WTR.

Degradation of the WTRBRS was performed using a combined approach, whereby the  $d_1$ ,  $d_2$ , and  $d_3$  were degraded simultaneously. The effect of this combined degradation approach on the radial response is shown below in Figure 6.14(a) for WTR= 1.17. Here, there is a successive decrease in the radial strength, stiffness and also reduction in the plateau region of the curves. Figure 6.14(b) and (c) shows the evolution of radial strength and stiffness during the degradation period for each of the WTR ratios considered. It is evident from Figure 6.14(b) there is a substantial increase in the radial strength as a result of WTR, however it only provides a modest increase in long-term degradation performance. Figure 6.14(d) shows the long-term degradation response to changes in lumen area. The BRS show that larger WTR results in higher minimal lumen areas in the implanted artery upon scaffold deployment. While larger WTR provide higher vessel patency upon deployment, the onset of degradation decreases the lumen area and the benefits of a larger WTR are only seen in the initial period. For example, in the lowest and higher WTRs considered, they return to a MLA = 4.5 mm<sup>2</sup> after 5 months and 7 months respectively.



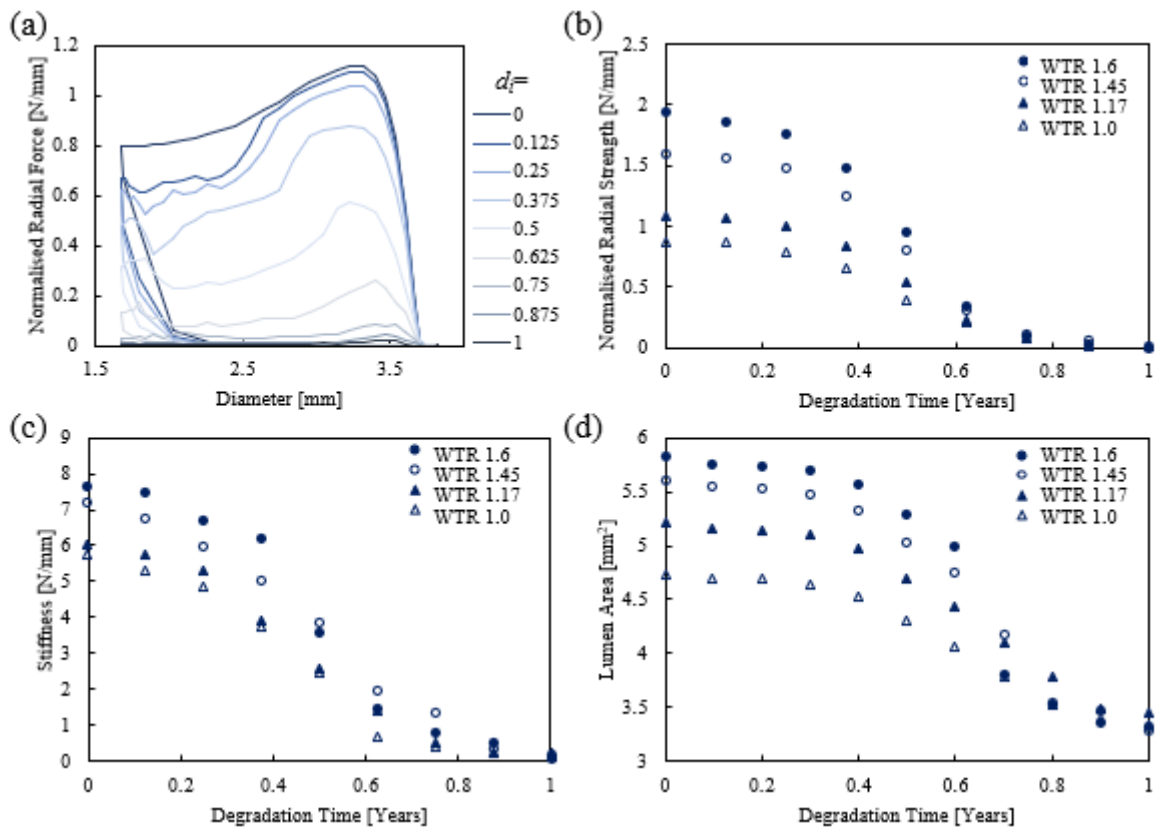


Figure 6.14. (a) Radial force versus diameters curves for WTR= 1.17 showing the effect of combined degradation on the radial response, (b) Effect of WTR on the radial strength response during the combined degradation, (c) Effect of WTR on the radial stiffness response during the combined degradation and (d) Effect of WTR on the long-term lumen area response during the combined degradation.

Figure 6.15 below shows a decrease in the artery stress with decreasing WTR. It also shows the long-term effect of degradation of the implanted BRS on the artery with a decrease in artery stress shown over the degradation period. Coupled with the decrease in the lumen area over the course of the degradation period shown in Figure 6.14(d) is a reduction in the stress distribution within the artery. The reduction in cross-sectional area is also visible in the contour plots.

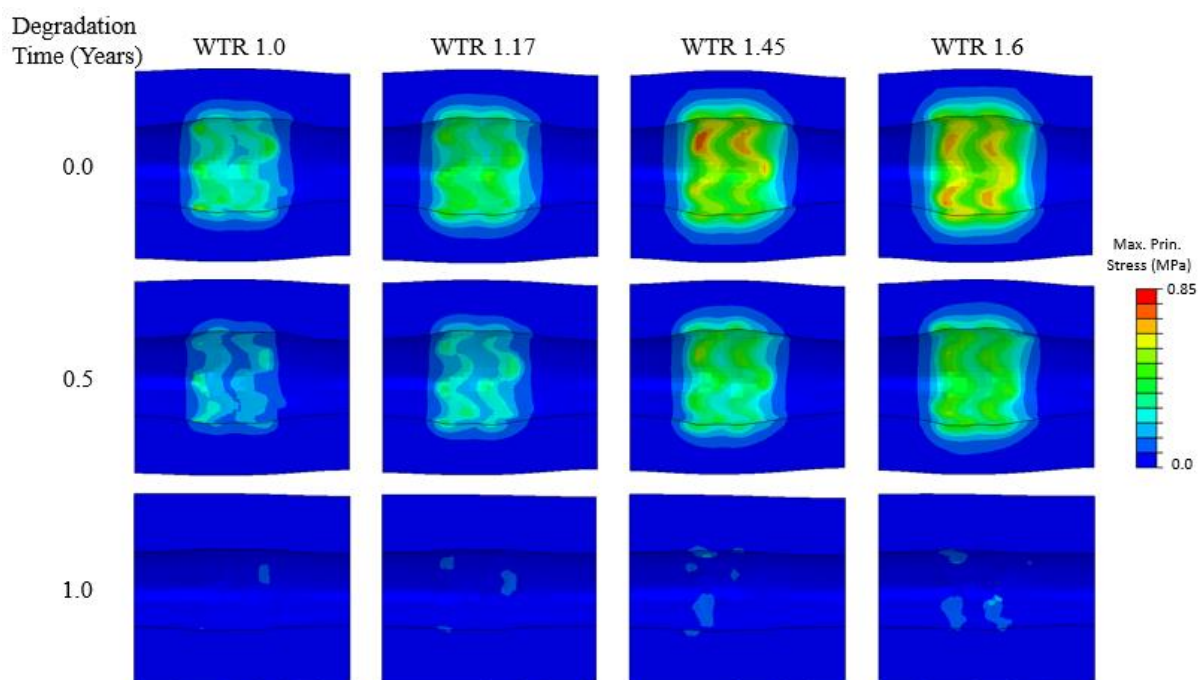


Figure 6.15. Contour plots showing the stress distribution in the artery after deployment and at varying stages of the degradation process for the combined degradation of the WTRBRS.

Finally, a summary on the effects of the WTR on the short-term performance in both freely expanded and artery expanded configurations is presented in Figure 6.16 below, results are compared against the original WTR1.17. Varying the width of the BRS increases the radial strength and stiffness, with the most notable being radial strength. Thicker struts resulted in higher freely expanded recoil compared with the reference WTR and a resulting smaller final diameter in the freely expanded models. Within the artery the higher WTR BRS performed better than the lower WTR BRS with a higher lumen area and radial gain after deployment and less recoil on account of the higher radial strength.



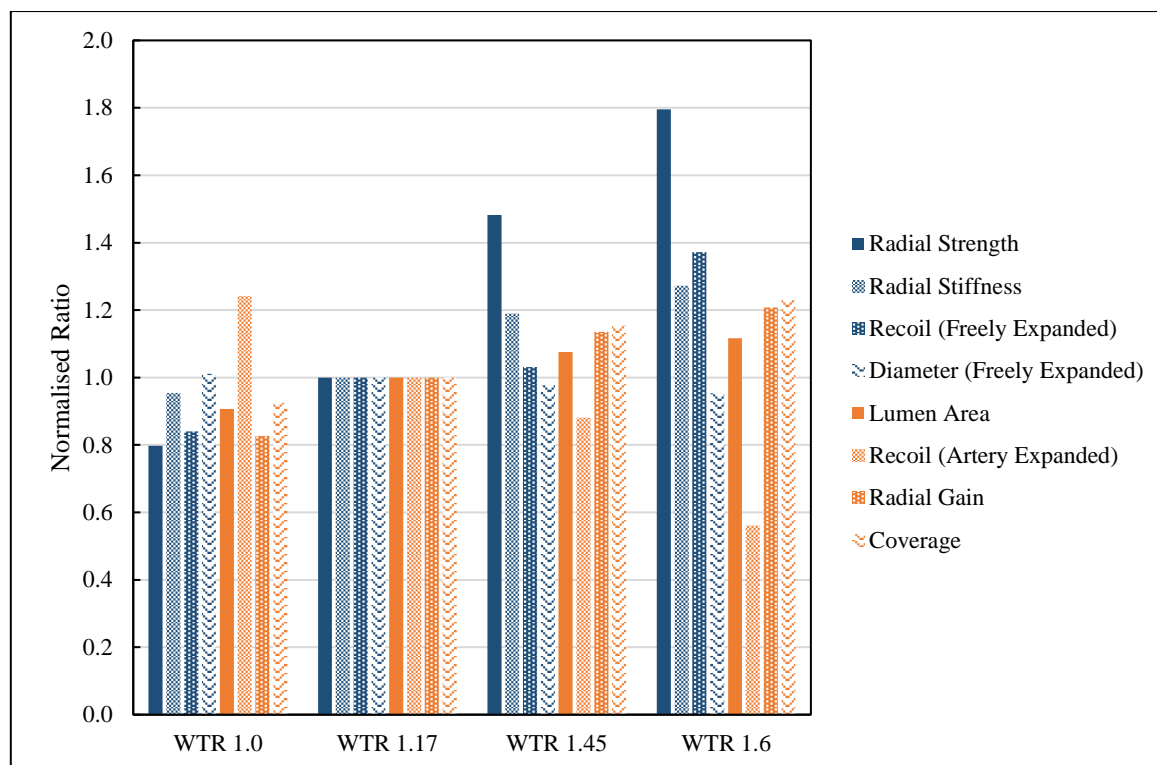


Figure 6.16. Bar chart showing the effect varying the TWR has on the short-term performance of a polymer BRS. All results have been normalised against the original WTR of 1.17.

### 6.3.3. Comparison of Absorb and Non-Commercial Scaffolds

The Absorb and non-commercial BRS were deployed within a simplified straight artery geometry to compare their short and long-term performance. Figure 6.17 compares the pressure-diameter curves for the two BRS. Again, the inflation process is represented on the left-hand side of the graph (0-0.8/1.4 MPa), while the deflation/recoil process is represented on the right-hand side of the graph (0.8/1.4 – 0 MPa). The Absorb BRS shows a similar bi-linear behaviour to the BRS sections already shown during inflation. However, the non-commercial BRS shows a different behaviour, with a progressive stiffening during inflation and a hold period after the initial inflation contributing to an increase in the final diameter. The non-commercial BRS had a lower recoil of 11.02% and a larger initial MLA, 5 mm<sup>2</sup> versus the Absorb BRS which had a recoil of 16.74% and a MLA of 4.8 mm<sup>2</sup>.

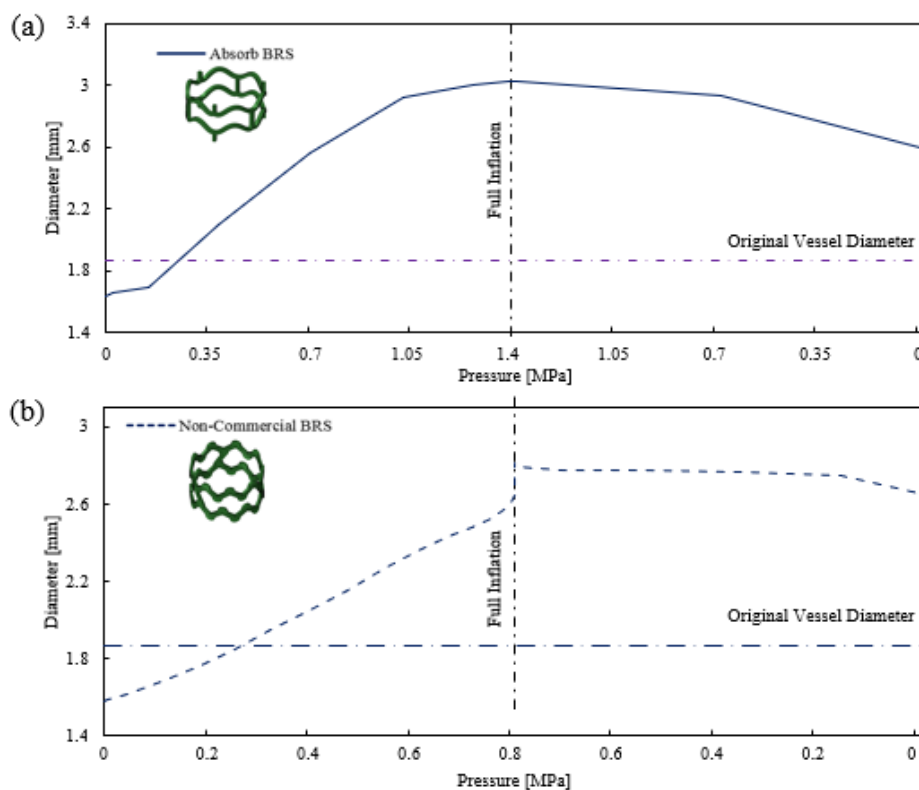


Figure 6.17. Pressure versus diameter curves for the (a) Absorb and (b) non-commercial BRS.

Subjecting these BRS to two years as per Qiu *et al* (2018) and Chapter 5, simulated degradation shows a reduction in the lumen area over time for the Absorb BRS. A greater reduction in the MLA was noted for the Absorb compared with the non-commercial BRS, Figure 6.18. The non-commercial BRS maintained its deployed diameter until month 17 where it began to decrease, a larger decrease is noted in months 22-24 where the BRS becomes more brittle. The reduction in MLA for the Absorb continues to decrease throughout the degradation period. The difference between the two scaffolds is primarily due to the difference in what parameters and the extent to which parameters are degraded. With the non-commercial BRS, only the failure-strain is significantly affected. While Qiu *et al* found the yield stress of the material to be primarily affected by degradation. As shown previously in this chapter, degradation of the yield stress greatly affects the ability of a BRS to maintain the deployed diameter within a vessel.

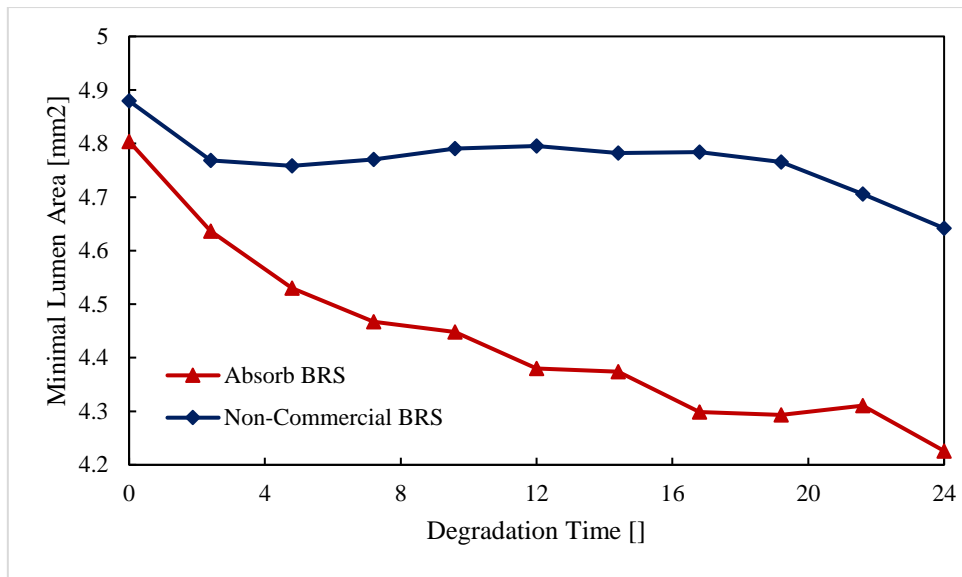


Figure 6.18. MLA loss for the simulated degradation of the Absorb and non-commercial BRS over a simulated two-year period.

Figure 6.19(a) and (b) shows stress contour of the post deployment for the Absorb and non-commercial BRS within the simplified vessel geometry and at the end of a two-year simulated degradation. Both show a reduction in stress through the BRS caused by the degradation. There is also a visible reduction in lumen diameter for the Absorb BRS, Figure 6.19(a).

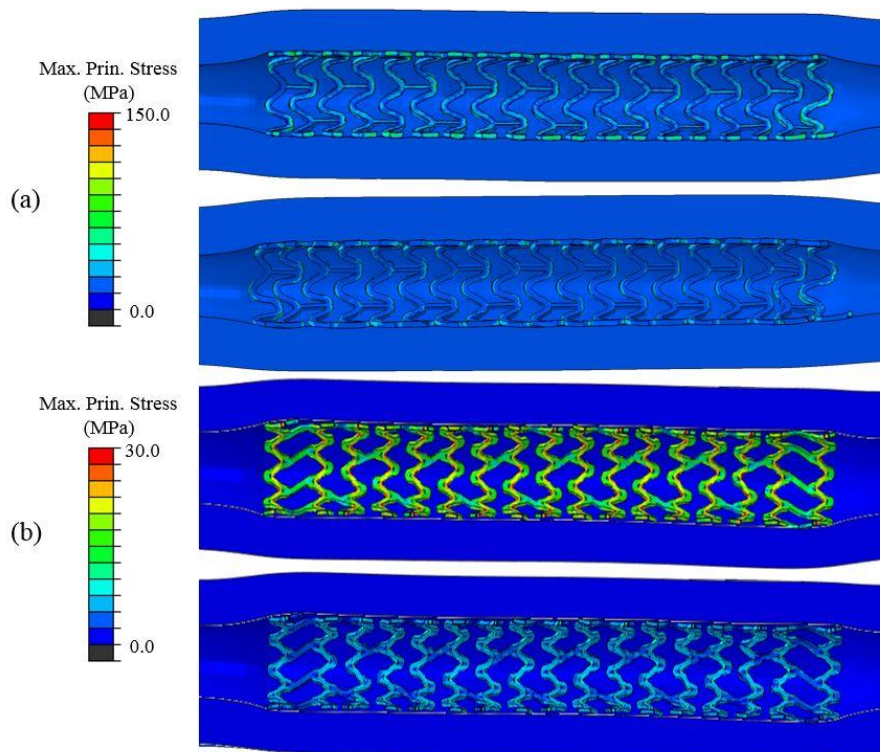


Figure 6.19. Contour plots showing the max principal stress within the (a) Abbott Absorb and (b) non-commercial BRS after deployment and after two-year simulated degradation.

The stress within the artery after deployment and degradation for both BRS is shown in Figure 6.20. It is interesting to note that the wider strut non-commercial BRS imparts a higher stress to the wall than the less wide Absorb. It is also noted that the wider non-commercial BRS held the artery at a larger lumen area to the Absorb, as was seen in the WTR study above. The stress in both BRS reduces over the degradation period.

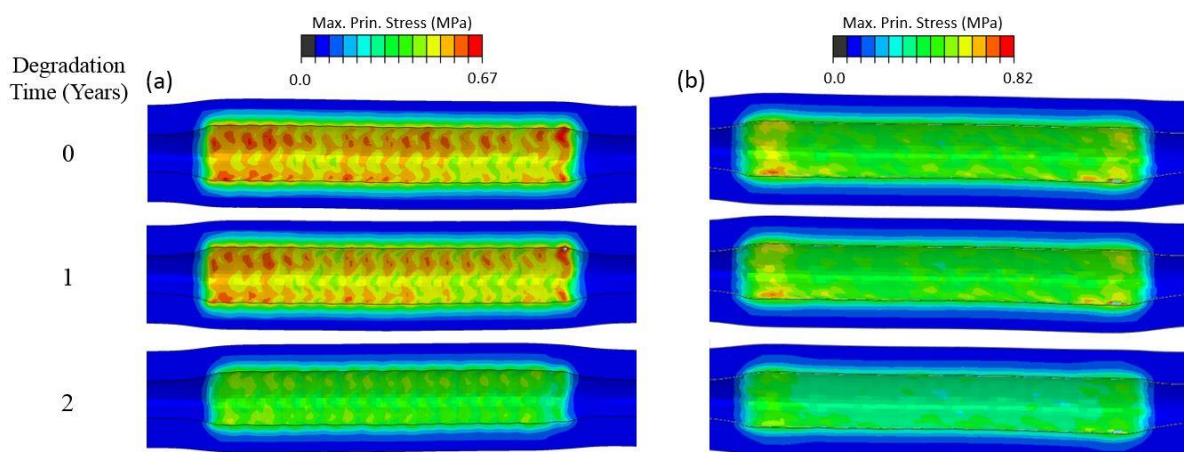


Figure 6.20. Contour plots comparing the maximum principal stress distribution within the simplified vessel geometry for the (a) Abbott Absorb and (b) non-commercial BRS over the two-year simulated degradation period.

## 6.4. Discussion

In this chapter, the role of scaffold design and material properties on the short- and long-term degradation performance of polymer BRS was investigated. In general, it was found that the geometric design of the BRS can substantially affect the short-term performance, including deployment, recoil and baseline radial properties of the scaffold. However, it was found that the width does not have a major impact on the long-term performance during degradation. While the initial radial performance of a scaffold design may be higher due to geometric features, this performance was only maintained for short time periods compared to baseline designs, with degradation performance largely similar across devices in the medium-term. This indicates that “material design” is the primary aspect that can be targeted to enhance the degradation performance of BRS.

Experimental studies investigating the performance of PLLA have shown that degradation affects mechanical properties in different ways, with elastic modulus (Naseem et al. 2020; Duek, Zavaglia, and Belangero 1999), yield stress (Tsuji and Ikada 2000) and failure strain (Katarzyna et al. 2021) found to deteriorate differently depending on the material formulation. As a consequence, previous computational degradation frameworks have used different model forms, to capture specific aspects of PLLA degradation, with many assuming that degradation only deteriorates the elastic response (Soares, Moore, and Rajagopal 2010), while others assuming that degradation affects only the yield (T. Qiu et al. 2018), hardening (Vieira et al. 2011) or elongation properties (Luo et al. 2014). In this chapter, the degradation framework was used to explore in detail the effects of degradation model form on the overall behaviour of freely expanded and implanted on a generic polymer BRS geometry. It was found a model form that degraded the material elastic modulus resulted in lower radial stiffness and radial strength at device level. Similarly, a model form that degraded the material yield stress resulted in lower radial stiffness and radial strength at device level, but through a distinctly different loading profile. As a consequence, it was found that degrading either the elastic modulus or yield stress could provide similar predictions in lumen area reduction during degradation. This implies that several different model forms may be effective in capturing the observed degradation performance of polymer BRS but may not necessarily capture the material level changes occurring. This type of model calibration may limit the application of certain models to wider sets of circumstances. To maximise the lumen area during long-term degradation of a BRS, the polymer should not experience deterioration of either elastic or yield properties. This was demonstrated by the comparison of the two BRS, the Abbott Absorb and a non-commercial BRS using their as reported constitutive material models. The deployment and subsequent degradation of these two different BRS highlight the results in the previous sections where

reduction in the yield stress ( $d_2$ ) causes a reduction in the lumen area while in a static vessel and reduction in failure strain ( $d_3$ ) will maintain the deployed diameter.

The effects of varying the strut width and its effects on the long-term degradation performance were investigated in the second section of this chapter. Increasing the strut width was shown to increase the short-term performance in terms of increasing radial strength and stiffness at a cost of slightly higher recoil, 5.95% compared with 3.64% for the WTR=1.6 and WTR=1.0 respectively for the freely expanded cases. However, when deployed within a vessel the higher WTR maintained a larger MLA experiencing much less recoil than the lower MLA BRS, despite not achieving the same maximum diameter at maximum inflation pressure. Other computational scaffold studies have also shown strut width to improve radial performance (Grogan, Leen, and McHugh 2013; Migliavacca *et al.* 2002). While increasing the strut width does result in improvements in the initial deployment performance, larger strut dimensions are viewed upon negatively in a clinical setting (Foin *et al.* 2014), where thinner struts and smaller crossing profiles are generally favoured. In terms of long-term performance, wider struts result in higher initial starting points for radial strength and stiffness as expected. However wider struts showed a of higher rate of strength and stiffness reduction, Figure 6.14(c-d). This was noted in particular for the highest WTR, where the radial stiffness loss and minimum lumen area dropped below that of WTR1.45. This could be attributed to higher strains within the BRS structure compared with lower WTR, contributing a larger number of elements that could fail from the applied combined degradation. While increasing the strut width improved the overall short-term performance, no real improvements were observed in terms of long-term degradation performance. Indicating that the long-term behaviour is primarily controlled through the initial material design and chemical make-up.

The third section investigated the long-term performance of two BRS, the well-studied Abbott Absorb and a non-commercial BRS. The narrower Absorb experienced more recoil after

deployment than the non-commercial BRS, with recoils of 16.74% and 11.02% respectively. Typically recoil of less than 10% is desirable in coronary stents (“FDA PMA Review Process” 2021). This resulted in the wider non-commercial BRS maintaining a larger MLA compared with the Absorb BRS, this is not unexpected owing to the WTR study showing wider struts experience recoil once deployed within a vessel. The wider non-commercial BRS also imparted a higher stress to the vessel walls after deployment, this is seen as disadvantageous owing to a more aggressive neo-intimal growth response (Foin *et al.* 2014). The Absorb experienced a loss in MLA over the course of the degradation period while the non-commercial did not, this was attributed to the method of degradation, where the Absorb was degraded through an evolution in the yield stress as prescribed by (T. Qiu *et al.* 2018) and the non-commercial BRS degraded primarily through a loss in the failure strain. Results from the previous sections demonstrated that for a static vessel a reduction in the strain-to-failure does not show any loss in lumen area compared with losses in elastic modulus and yield stress.

The primary limitation of this study is the exclusion of a creep response in the long-term degradation simulations, as identified in the previous chapter. The creep response was neglected owing to a lack of data on creep performance of other BRS and the focus of this study on the effects of the degradation parameters and geometrical changes. Other limitations of this study include the use of an elastic-plastic constitutive material model. Many polymer materials exhibit rate dependant behaviour (Bobel *et al.* 2016), however to simplify the analysis and focus on the affects of degradation and geometrical changes on the BRS devices a more straight forward material model was employed. Future work could include time dependence to see if this effects the long-term degradation response and a material model to account for the creep response. A limitation in the strut width study was the negligence of the maximum strain experienced by increasing the strut width, increasing the strut width also increases the strain in the BRS which could also exceed the ultimate strain for the material. The degradation models

that include the artery do not include neo-intimal growth or vessel remodelling. Experiments have shown that encapsulation of the tissue around the BRS changes the rate of degradation. Accounting for these phenomena is important in future predictions of BRS performance and may lead to a further decrease in the predicted MLA.

## **6.5. Conclusions**

This chapter investigated the role of degrading several mechanical parameters both individually and combined to find their effects on the long-term performance of a polymer BRS using the degradation framework outlined in Chapter 5. Computational radial testing showed that radial strength and stiffness are not uniquely controlled through the yield strength and elastic modulus. The role of strut width was investigated to find the effect simple geometric changes can have on the long-term performance of a polymer BRS. It was shown that increases in strut width vastly improve the initial BRS performance in terms of radial strength and recoil within an artery. However, long-term predictions suggest that at least for changes in strut width, greater degradation performance is determined through changes in the material composition and processing as opposed to optimising the geometry which is seen to have more of an impact on the short-term performance. Whereas “material design” is really the only aspect that can be targeted to enhance the degradation performance of polymer BRS.



## 6.7. References

- Antonini, Luca, Lorenzo Mandelli, Francesca Berti, Giancarlo Pennati, and Lorenza Petrini. 2021. “Validation of the Computational Model of a Coronary Stent : A Fundamental Step towards in Silico Trials.” *Journal of the Mechanical Behavior of Biomedical Materials* 122 (April): 104644. <https://doi.org/10.1016/j.jmbbm.2021.104644>.
- Antonini, Luca, Gianluca Poletti, Lorenzo Mandelli, Gabriele Dubini, Giancarlo Pennati, and Lorenza Petrini. 2021. “Comprehensive Computational Analysis of the Crimping Procedure of PLLA BVS : Effects of Material Viscous-Plastic and Temperature Dependent Behavior.” *Journal of the Mechanical Behavior of Biomedical Materials* 123 (April): 104713. <https://doi.org/10.1016/j.jmbbm.2021.104713>.
- Auricchio, F., M. Conti, M. De Beule, G. De Santis, and B. Verheghe. 2011. “Carotid Artery Stenting Simulation: From Patient-Specific Images to Finite Element Analysis.” *Medical Engineering and Physics* 33 (3): 281–89. <https://doi.org/10.1016/j.medengphy.2010.10.011>.
- Avanzini, A., and D. Battini. 2018. “FEM Simulation of Subintimal Angioplasty for the Treatment of Chronic Total Occlusions.” *Mathematical Problems in Engineering* 2018. <https://doi.org/10.1155/2018/2648910>.
- Bobel, Anna C., Stefan Lohfeld, Reyhaneh Neghabat Shirazi, and Peter E. McHugh. 2016. “Experimental Mechanical Testing of Poly (L-Lactide) (PLLA) to Facilitate Pre-Degradation Characteristics for Application in Cardiovascular Stenting.” *Polymer Testing* 54: 150–58. <https://doi.org/10.1016/j.polymertesting.2016.07.011>.
- Byrne, Robert A, Giulio G Stefanini, Davide Capodanno, Yoshinobu Onuma, Andreas Baumbach, Javier Escaned, Michael Haude, Stefan James, Michael Joner, and Peter Ju. 2018. “Report of an ESC-EAPCI Task Force on the Evaluation and Use of Bioresorbable Scaffolds for Percutaneous Coronary Intervention : Executive Summary,” no. July 2014: 1591–1601. <https://doi.org/10.4244/EIJ20170912-01>.
- Duek, E. A.R., C. A.C. Zavaglia, and W. D. Belangero. 1999. “In Vitro Study of Poly(Lactic Acid) Pin Degradation.” *Polymer* 40 (23): 6465–73. [https://doi.org/10.1016/S0032-3861\(98\)00846-5](https://doi.org/10.1016/S0032-3861(98)00846-5).
- “FDA PMA Review Process.” 2021. *Fda.Gov*. <https://www.fda.gov/medical-devices/premarket-approval-pma/pma-review-process>.
- Fiuzza, Constantino, Katarzyna Polak-Krasna, Luca Antonini, Lorenza Petrini, Oliver Carroll, William Ronan, and Ted J Vaughan. 2022. “An Experimental Investigation into the Physical , Thermal and Mechanical Degradation of a Polymeric Bioresorbable Scaffold.” *Journal of the Mechanical Behavior of Biomedical Materials* 125 (November 2021): 1–9. <https://doi.org/10.1016/j.jmbbm.2021.104955>.
- Foin, Nicolas, Renick D. Lee, Ryo Torii, Juan Luis Guitierrez-Chico, Alessio Mattesini, Sukhjinder Nijjer, Sayan Sen, et al. 2014. “Impact of Stent Strut Design in Metallic Stents and Biodegradable Scaffolds.” *International Journal of Cardiology*. <https://doi.org/10.1016/j.ijcard.2014.09.143>.
- Gervaso, Francesca, Claudio Capelli, Lorenza Petrini, Simone Lattanzio, Luca Di Virgilio, and Francesco Migliavacca. 2008. “On the Effects of Different Strategies in Modelling Balloon-Expandable Stenting by Means of Finite Element Method.” *Journal of Biomechanics* 41 (6): 1206–12. <https://doi.org/10.1016/j.jbiomech.2008.01.027>.
- Göpferich, Achim. 1996. “Mechanisms of Polymer Degradation and Erosion1.” *The Biomaterials: Silver Jubilee Compendium* 17 (2): 117–28. <https://doi.org/10.1016/B978-008045154-1.50016-2>.
- Grogan, James A., Sean B. Leen, and Peter E. McHugh. 2013. “Optimizing the Design of a Bioabsorbable Metal Stent Using Computer Simulation Methods.” *Biomaterials* 34 (33): 8049–60. <https://doi.org/10.1016/j.biomaterials.2013.07.010>.
- Hoddy, Ben, Naveed Ahmed, Kadem Al-lamee, Nial Bullett, and Neil W. Bressloff. 2022.

“Exploring a Parallel Rheological Framework to Capture the Mechanical Behaviour of a Thin-Strut Polymeric Bioresorbable Coronary Scaffold.” *Journal of the Mechanical Behavior of Biomedical Materials* 130 (December 2021): 105154. <https://doi.org/10.1016/j.jmbbm.2022.105154>.

Holzapfel, Gerhard A., Gerhard Sommer, Christian T. Gasser, and Peter Regitnig. 2005. “Determination of Layer-Specific Mechanical Properties of Human Coronary Arteries with Nonatherosclerotic Intimal Thickening and Related Constitutive Modeling.” *American Journal of Physiology-Heart and Circulatory Physiology* 289 (5): H2048–58. <https://doi.org/10.1152/ajpheart.00934.2004>.

“INSILC Cloud.” 2018. *Insilc.Eu*. <https://insilc.eu/insilc-cloud/>.

Katarzyna, Polak-Krasna, Ali Reza Abaei, Reyhaneh Neghabat Shirazi, Eoin Parle, Oliver Carroll, William Ronan, and Ted J Vaughan. 2021. “Physical and Mechanical Degradation Behaviour of Semi-Crystalline PLLA for Bioresorbable Stent Applications.” *Journal of the Mechanical Behavior of Biomedical Materials*, 135938. <https://doi.org/10.1016/j.jmbbm.2021.104409>.

Kimble, Lloyd Dylan, and Debes Bhattacharyya. 2015. “In Vitro Degradation Effects on Strength, Stiffness, and Creep of PLLA/PBS: A Potential Stent Material.” *International Journal of Polymeric Materials and Polymeric Biomaterials* 64 (6): 299–310. <https://doi.org/10.1080/00914037.2014.945203>.

Luo, Qiyi, Xiangkun Liu, Zhonghua Li, Chubo Huang, Wen Zhang, Juan Meng, Zhaohua Chang, and Zezhao Hua. 2014. “Degradation Model of Bioabsorbable Cardiovascular Stents.” *PLoS ONE* 9 (11): 1–9. <https://doi.org/10.1371/journal.pone.0110278>.

Migliavacca, Francesco, Lorenza Petrini, Maurizio Colombo, Ferdinando Auricchio, and Riccardo Pietrabissa. 2002. “Mechanical Behavior of Coronary Stents Investigated through the Finite Element Method.” *Journal of Biomechanics* 35 (6): 803–11. [https://doi.org/10.1016/S0021-9290\(02\)00033-7](https://doi.org/10.1016/S0021-9290(02)00033-7).

Milosevic, Miljan, Milos Anic, Dalibor Nikolic, Vladimir Geroski, Bogdan Milicevic, Milos Kojic, and Nenad Filipovic. 2021. “Application of in Silico Platform for the Development and Optimization of Fully Bioresorbable Vascular Scaffold Designs.” *Frontiers in Medical Technology* 3 (October): 1–13. <https://doi.org/10.3389/fmedt.2021.724062>.

Naseem, Raasti, Ligu Zhao, Senthil K. Eswaran, and Helen Willcock. 2020. “Characterization of Biodegradable Poly(l-Lactide) Tube over Accelerated Degradation.” *Polymer Engineering and Science* 60 (7): 1430–36. <https://doi.org/10.1002/pen.25390>.

Naseem, Raasti, Ligu Zhao, Vadim Silberschmidt, Yang Liu, Ollie Scaife, Helen Willcock, Senthil Eswaran, and Syed Hossainy. 2019. “Mechanical and Chemical Characterisation of Bioresorbable Polymeric Stent over Two-Year in Vitro Degradation.” *Journal of Biomaterials Applications* 34 (1): 61–73. <https://doi.org/10.1177/0885328219839591>.

Otsuka, Fumiyuki, Erica Pacheco, Laura E.L. Perkins, Jennifer P. Lane, Qing Wang, Marika Kamberi, Michael Frie, et al. 2014. “Long-Term Safety of an Everolimus-Eluting Bioresorbable Vascular Scaffold and the Cobalt-Chromium XIENCE v Stent in a Porcine Coronary Artery Model.” *Circulation: Cardiovascular Interventions* 7 (3): 330–42. <https://doi.org/10.1161/CIRCINTERVENTIONS.113.000990>.

Pant, Sanjay, Neil W. Bressloff, and Georges Limbert. 2012. “Geometry Parameterization and Multidisciplinary Constrained Optimization of Coronary Stents.” *Biomechanics and Modeling in Mechanobiology* 11 (1–2): 61–82. <https://doi.org/10.1007/s10237-011-0293-3>.

Pant, Sanjay, Georges Limbert, Nick P. Curzen, and Neil W. Bressloff. 2011. “Multiobjective Design Optimisation of Coronary Stents.” *Biomaterials* 32 (31): 7755–73. <https://doi.org/10.1016/j.biomaterials.2011.07.059>.

Qiu, T., R. He, C. Abunassar, S. Hossainy, and L. G. Zhao. 2018. “Effect of Two-Year Degradation on

Mechanical Interaction between a Bioresorbable Scaffold and Blood Vessel.” *Journal of the Mechanical Behavior of Biomedical Materials* 78 (November 2017): 254–65. <https://doi.org/10.1016/j.jmbbm.2017.11.031>.

Qiu, T. Y., M. Song, and L. G. Zhao. 2018. “A Computational Study of Crimping and Expansion of Bioresorbable Polymeric Stents.” *Mechanics of Time-Dependent Materials* 22 (2): 273–90. <https://doi.org/10.1007/s11043-017-9371-y>.

Shine, Connor J, Peter E Mchugh, and William Ronan. 2021. “Impact of Degradation and Material Crystallinity on the Mechanical Performance of a Bioresorbable Polymeric Stent.” *J Elast.* <https://doi.org/10.1007/s10659-021-09835-7>.

Soares, João S., James E. Moore, and Kumbakonam R. Rajagopal. 2010. “Modeling of Deformation-Accelerated Breakdown of Polylactic Acid Biodegradable Stents.” *Journal of Medical Devices, Transactions of the ASME* 4 (4). <https://doi.org/10.1115/1.4002759>.

Tsuji, Hideto, and Yoshito Ikada. 1995. “Properties and Morphologies of Poly(L-Lactide): 1. Annealing Condition Effects on Properties and Morphologies of Poly(L-Lactide).” *Polymer* 36 (14): 2709–16. [https://doi.org/10.1016/0032-3861\(95\)93647-5](https://doi.org/10.1016/0032-3861(95)93647-5).

Tsuji, Hideto, and Yoshito Ikada. 2000. “Properties and Morphology of Poly(L-Lactide) 4. Effects of Structural Parameters on Long-Term Hydrolysis of Poly(L-Lactide) in Phosphate-Buffered Solution.” *Polymer Degradation and Stability* 67 (1): 179–89. [https://doi.org/10.1016/S0141-3910\(99\)00111-1](https://doi.org/10.1016/S0141-3910(99)00111-1).

Vey, Elisabeth, Caroline Rodger, Liz Meehan, Jonathan Booth, Mike Claybourn, Aline F. Miller, and Alberto Saiani. 2012. “The Impact of Chemical Composition on the Degradation Kinetics of Poly(Lactic-Co-Glycolic) Acid Copolymers Cast Films in Phosphate Buffer Solution.” *Polymer Degradation and Stability* 97 (3): 358–65. <https://doi.org/10.1016/j.polymdegradstab.2011.12.010>.

Vieira, A. C., J. C. Vieira, J. M. Ferra, F. D. Magalhães, R. M. Guedes, and A. T. Marques. 2011. “Mechanical Study of PLA-PCL Fibers during in Vitro Degradation.” *Journal of the Mechanical Behavior of Biomedical Materials* 4 (3): 451–60. <https://doi.org/10.1016/j.jmbbm.2010.12.006>.

Vukicevic, Arso M., Serkan Çimen, Nikola Jagic, Gordana Jovicic, Alejandro F. Frangi, and Nenad Filipovic. 2018. “Three-Dimensional Reconstruction and NURBS-Based Structured Meshing of Coronary Arteries from the Conventional X-Ray Angiography Projection Images.” *Scientific Reports* 8 (1): 1–20. <https://doi.org/10.1038/s41598-018-19440-9>.

Wang, Pei-jiang, Francesca Berti, Luca Antonini, Farhad Rikhtegar Nezami, Lorenza Petrini, Francesco Migliavacca, and Elazer R. Edelman. 2020. “Multimodal Loading Environment Predicts Bioresorbable Vascular Scaffolds’ Durability.” *Annals of Biomedical Engineering*.

Weir, N. A., F. J. Buchanan, J. F. Orr, and G. R. Dickson. 2004. “Degradation of Poly-L-Lactide. Part 1: In Vitro and in Vivo Physiological Temperature Degradation.” *Proceedings of the Institution of Mechanical Engineers, Part H: Journal of Engineering in Medicine* 218 (5): 307–19. <https://doi.org/10.1243/0954411041932782>.

# Chapter 7

## Concluding Remarks and Future Perspectives

---

### 7.1 Summary of Key Contributions

While polymer bioresorbable scaffolds (BRS) have shown great initial promise in addressing limitations of their permanent DES counterparts (Nishio *et al.*, 2012; Abizaid *et al.*, 2017), clinical trials have shown poor long-term performance when compared to permanent stents (Byrne *et al.*, 2018). As a consequence, the wider implementation of bioresorbable endovascular medical devices has faced significant challenges, with the future of polymer BRS devices in particular quite uncertain, with discontinuation of Abbot Absorb and other commercial programmes (Densford 2017) slowing development. While these polymer BRS devices still present exciting potential advantages over permanent stents (Welch *et al.*, 2019), the under-lying reasons for their poor clinical performance in coronary applications is attributed to thick stent struts, although much evidence has suggested that failures were as a consequence of physical and/or mechanical performance. In the context of overall BRS performance, these aspects are a function of both the underlying polymer material and the functional design of the device itself, which provided the key motivation for this thesis.

The overall contribution of this thesis has been to present a detailed biomechanical investigation that provides new insights into the long-term mechanical behaviour of polymer BRS. These studies have provided much needed experimental data to the biomechanics community that systematically evaluates the long-term mechanical performance of polymer BRS. Furthermore, this work has developed a phenomenological degradation model

implemented within the Abaqus finite element framework that can predict both the short-term deployment behaviour and the long-term quasi-static behaviour of polymer BRS. The key scientific contributions have been to show that polymer BRS are highly effective in maintaining their radial stiffness and strength during short- and medium-term degradation but undergo a ductile to brittle transition in later stages of degradation. This highlights a possible reason for polymer BRS poor long-term performance in clinical settings. Furthermore, it was observed that polymer BRS in an *in vitro* setting under constant load experience a large amount of creep in the early phases of degradation, further complicating future assessment for the prediction of long-term behaviour. This extensive creep has not been widely seen in the literature. It was found that increasing the width of the geometry of the polymer BRS generally improved the short-term deployment performance; with design changes only providing modest benefits for the long-term degradation behaviour. Therefore, to improve the overall clinical performance of polymer BRS, the following should be considered; development of the constitutive polymer itself, or entirely new materials are required, refinement in the polymer production and processing and finally thinner struts would allow faster re-endothelisation and resorption, potentially avoiding fracture due to reduction in material integrity. This section below outlines in more detail the key contributions and main findings from each of these studies.

Chapter 4 presented an experimental evaluation on the effects of degradation on the mechanical, thermal and physical performance for two polymer BRS, the REVA Fantom Encore and a non-commercial PLLA BRS. This study represents the first systematic evaluation of these BRS under long-term accelerated degradation that evaluated both mechanical and physical aspects for degradation of these devices (Chapter 4). In the early stages of degradation, it was found that both BRS devices showed substantial increases in radial strength and stiffness, despite a substantial reduction in molecular weight. Beyond this, the radial stiffness and strength of the devices were maintained, despite a continued loss in molecular weight, with

limited mass loss was observed in this period. Throughout each of these phases, there was a steady increase in the relative crystallinity, and only minor changes in glass transition and melt temperatures. In the final phases of degradation, the load-bearing capacity of the BRS devices showed continued reduction, with decreases in radial stiffness and strength, and drastic reduction in the work-to-fracture of the devices, with devices from some of the later time-points too brittle to test. This ductile to brittle transition suggest that BRS device could exhibit substantially brittle behaviour after ~one year of implantation.

In Chapter 5, a computational degradation framework was developed that could predict short-term deployment performance and several key long-term degradation effects that were observed in the experimental work completed in Chapter 4. Through a calibration process, the degradation model was able to capture loading, holding and unloading phases of the radial response at each time point, and in particular captured the ductile to brittle transition that occurred in the later stages of degradation. In an effort to validate the degradation framework a non-commercial BRS was deployed within an additively manufactured silicone vessel and subjected to the same accelerated degradation protocol as Chapter 4. In addition to this, a parallel plate crush test to assess if there was an increase in diameter corresponding to the increase in radial strength seen in Chapter 4 was also performed. Both of these experimental tests showed the BRS to experience a large amount of creep, which was unexpected. In the case of the silicone vessel, this resulted in a 70% loss in lumen diameter within the first seven days of immersion. In the case of the parallel plate test a loss of 20% in diameter was recorded. The degradation framework calibrated from the radial crush testing was not able to capture this initial decrease in diameter, where the simulated degradation showed a decrease in diameter only in the later stages of the simulated degradation.

Chapter 6 examined role of both material and geometric properties on both the short- and long-term performance of polymer BRS. It was found the geometric parameters of the BRS were

mainly responsible for the short-term deployment characteristics and had little effect on overall degradation performance. In particular, it was found that higher strut widths resulted in substantially higher radial strength and minimal lumen areas when such geometries were implanted within a vessel. However, this more favourable performance in the short-term only lead to modest benefits in the long-term performance of the devices. Furthermore, this Chapter provided detailed insight into the specific roles of material parameters in dictating the overall degradation response. It was found that the radial strength and stiffness were not exclusively controlled by the yield stress and elastic modulus, respectively with both parameters contributing to these features. The degradation of these parameters was also explored in terms of vessel performance, with yield stress having the largest impact of the minimum lumen area loss. Thus, leading to the conclusion that at least in terms of strut width long-term performance is controlled through the material formulation as opposed to dimensional changes within the BRS.

Chapter 7 served as a demonstration for the degradation framework developed in Chapter 5 as part of an *in silico* platform. With the difficulty and expense of traditional clinical trials there is a push from the scientific community for computational testing and evaluation to form a larger part for the assessment of the safety and efficacy of medical devices. The InSilc platform is an *in silico* clinical trial platform for the design and development of coronary stents both permanent and bioresorbable. This platform consisted of a number of modules including crimping and deployment, degradation, fluid dynamics and drug perfusion modules. This platform allows for the efficient assessment of various scenarios that can compare the performance of BRS devices or designs in different patient anatomies. While the platform demonstrated the integration of the degradation framework developed in Chapter 5, there are still several key aspects of the degradation model that require robust validation. However, such

a platform could still provide very meaningful outputs and provide insight into device performance during the development phases of coronary stent development.

## 7.2 Future Recommendations

The work presented in this thesis represents a step towards understanding the mechanical behaviour of polymer BRS while undergoing degradation. A major contribution has demonstrated that polymer BRS experience creep behaviour while under a constant load. While excessive recoil has been reported upon initially with Abbott Absorb BRS (Bangalore *et al.*, 2017). The short-term recoil/creep shown here has not been accounted for or documented well in great detail clinically. Future work should explore this short-term effect and it highlights a clear need for the development of degradation protocols that enable the application of loading during degradation. Until now, the vast majority of experimental work has been carried out using static protocols, with the results in this thesis highlighting the limitations associated with these approaches. Furthermore, it was shown that an increase in radial performance is experienced by polymer BRS within the initial stages of the degradation process, with later stages of the degradation process resulting in the BRS become exceedingly brittle. This could provide an explanation as to poor long-term clinical performance, where excess late stent thrombosis has been reported for polymer BRS (Byrne *et al.*, 2018). Further work is required in terms of tuning the degradation characteristics of polymers used in coronary BRS applications such that the degraded BRS does not pose such a fracture risk. The computational degradation framework developed in Chapter 5 enables accurate predictions of the freely expanded mechanical performance of the PLLA BRS over the duration of offering mechanical support to a vessel and provide a reference for future computational degradation modelling. However, an attempt at validating the degradation framework showed a mismatch between the freely expanded polymer BRS and those subjected to a constant load (through implantation within a silicone vessel and a parallel plate crush test). It was found that the polymer BRS



experienced a large amount of creep which the degradation framework did not account for and indeed many models used for PLLA in the literature do not account for. This aspect is critical in determining the long-term implanted performance, where this behaviour should be accounted for in future computational modelling of polymer BRS. Indeed, this finding further complicates the development of models predicting the long-term performance of polymer BRS if creep, fatigue and degradation are to be accounted for. Generally, there remains little consistency across the literature in how computational models for polymer BRS are simulated and validated. With a large variety of material models used to represent PLLA, more work required in terms of validation for polymer BRS materials and new validation strategies required for polymer BRS validation. Future computational modelling should adopt models that account for the viscous nature of polymers. While the publication of the ASME V&V 40 guidance is greatly welcomed, for polymer BRS a guidance on the assessment of mechanical performance coupled with its physical characterisation over the lifetime of the BRS is needed. To assess the credibility of current degradation models, *in vivo* studies should be performed alongside their *in silico* counterparts. While the results from Chapter 6 suggest that enhancing long-term degradation performance lies with controlling the synthesis of the polymer backbone, only a single aspect of the scaffold geometry was considered in this study. Future work should consider other aspects of scaffold geometry design to facilitate the long-term performance, such as exploring different geometries.

Finally, there is much work ongoing in the development of polymer BRS and characterisation of polymer degradation and its effects at a device level, where efforts are focussed on improving material characteristics (McMahon *et al.*, 2018; Zong *et al.*, 2022). While these will contribute to a greater understanding of polymer BRS and how degradation effects the long-term performance, further clinical data coupled with robust guidance on the evaluation of polymer BRS throughout the whole lifecycle of the device is needed. Despite these challenges,

fully bioresorbable devices still show potential as an alternative to permanent metallic stents, although they may have higher chances of success in certain peripheral applications, where the failure rates of permanent devices can be much higher than the coronary space (Gökgöl *et al.* 2021).

### 7.3 References

- Abizaid, Alexandre, Didier Carrié, Norbert Frey, Matthias Lutz, Joachim Weber-Albers, Darius Dudek, Bernard Chevalier, et al. 2017. “6-Month Clinical and Angiographic Outcomes of a Novel Radiopaque Sirolimus-Eluting Bioresorbable Vascular Scaffold: The FANTOM II Study.” *JACC: Cardiovascular Interventions* 10 (18): 1832–38. <https://doi.org/10.1016/j.jcin.2017.07.033>.
- Bangalore, Sripal, Hiram G. Bezerra, David G. Rizik, Ehrin J. Armstrong, Bruce Samuels, Srihari S. Naidu, Cindy L. Grines, et al. 2017. “The State of the Absorb Bioresorbable Scaffold: Consensus From an Expert Panel.” *JACC: Cardiovascular Interventions* 10 (23): 2349–59. <https://doi.org/10.1016/j.jcin.2017.09.041>.
- Byrne, Robert A, Giulio G Stefanini, Davide Capodanno, Yoshinobu Onuma, Andreas Baumbach, Javier Escaned, Michael Haude, Stefan James, Michael Joner, and Peter Ju. 2018. “Report of an ESC-EAPCI Task Force on the Evaluation and Use of Bioresorbable Scaffolds for Percutaneous Coronary Intervention: Executive Summary.” *European Heart Journal* 39 (July): 1591–1601. <https://doi.org/10.4244/EIJ20170912-01>.
- Densford, Fink. 2017. “Boston Scientific to End Renuvia Bioresorbable Coronary Stent Program.” *Massdevice.Com*. <https://www.massdevice.com/boston-scientific-end-renuvia-bioresorbable-coronary-stent-program/>.
- Fiuza, Constantino, Katarzyna Polak-Krasna, Luca Antonini, Lorenza Petrini, Oliver Carroll, William Ronan, and Ted J Vaughan. 2022. “An Experimental Investigation into the Physical, Thermal and Mechanical Degradation of a Polymeric Bioresorbable Scaffold.” *Journal of the Mechanical Behavior of Biomedical Materials* 125 (November 2021): 1–9. <https://doi.org/10.1016/j.jmbbm.2021.104955>.
- Gökgöl, Can, Yasushi Ueki, Daniel Abler, Nicolas Diehm, Rolf P. Engelberger, Tatsuhiko Otsuka, Lorenz Räber, and Philippe Büchler. 2021. “Towards a Better Understanding of the Posttreatment Hemodynamic Behaviors in Femoropopliteal Arteries through Personalized Computational Models Based on OCT Images.” *Scientific Reports* 11 (1): 1–12. <https://doi.org/10.1038/s41598-021-96030-2>.
- McMahon, Sean, Nicky Bertollo, Eoin D.O’ Cearbhaill, Jochen Salber, Luca Pierucci, Patrick Duffy, Thomas Dürig, Vivian Bi, and Wenxin Wang. 2018. “Bio-Resorbable Polymer Stents: A Review of Material Progress and Prospects.” *Progress in Polymer Science* 83: 79–96. <https://doi.org/10.1016/j.progpolymsci.2018.05.002>.
- Nishio, Soji, Kunihiko Kosuga, Keiji Igaki, Masaharu Okada, Eisho Kyo, Takafumi Tsuji, Eiji Takeuchi, et al. 2012. “Long-Term (>10 Years) Clinical Outcomes of First-in-Human Biodegradable Poly-L-Lactic Acid Coronary Stents: Igaki-Tamai Stents.” *Circulation* 125 (19): 2343–52. <https://doi.org/10.1161/CIRCULATIONAHA.110.000901>.
- Welch, Tre R., Alan W. Nugent, and Surendranath R. Veeram Reddy. 2019. “Biodegradable Stents for Congenital Heart Disease.” *Interventional Cardiology Clinics* 8 (1): 81–94. <https://doi.org/10.1016/j.iccl.2018.08.009>.
- Zong, Jiabin, Quanwei He, Yuxiao Liu, Min Qiu, Jiehong Wu, and Bo Hu. 2022. “Advances in the Development of Biodegradable Coronary Stents: A Translational Perspective.” *Materials Today Bio* 16 (June). <https://doi.org/10.1016/j.mtbio.2022.100368>.

# Appendix Chapter

## Demonstration of an In-Silico Platform for the Design and Development of Vascular Scaffolds – Degradation Module

---

### 8.1. Introduction

Currently, the pathway to market for vascular stents, either permanent or bioresorbable, consists of rigorous bench testing followed by pre-clinical animal testing and finally human clinical trials to demonstrate the safety and efficacy of the product or device in development (Sastry, 2014; Byrne *et al.*, 2015). A heavy reliance in the development pathway is placed on experimental testing, with only a small component of pre-clinical testing requirements employing computational methods (FDA, 2010). Typically, extensive prototyping using trial-and-error approaches is required in the early stages of development to establish functional performance. However, despite this, it is not uncommon for devices to experience failures in the later stages of this pathway, during animal testing, clinical trials or in the worst case the post-market surveillance phase. These failures increase time to market, which is typically several years for a coronary stent including seeking the application of premarket approval for the FDA ('FDA PMA Review Process', 2021), and mean that significant costs can be incurred during animal and human studies to validate and prove the safety of the devices. In designing a new coronary stent, there are several key aspects of performance that the device must fulfil. The stent must have sufficient structural integrity to open the diseased artery, while avoiding any damage to the surrounding tissue, and have sufficient flexibility to facilitate deliverability and conformation to lesion sites. Once implanted, the stent should restore natural blood flow

patterns to the coronary arteries and avoid unwanted re-narrowing of the vessel due to in-stent restenosis (Singh *et al.*, 2020). This presents a very challenging design problem, particularly as these functions must be fulfilled across a diverse patient population, whose coronary anatomies vary significantly. In-Silico Clinical Trials (ISCT) have the potential to address these aspects and effectively reduce the size and duration of animal and clinical studies, lower development costs and reduce the overall time-to-market for devices (Viceconti *et al.*, 2019). Over recent years, significant advancements in multi-scale, multi-physics and image-based modelling capabilities mean that computational modelling can effectively model various aspects of in vivo performance of medical devices. Recently, the InSilc project has developed an ISCT platform for coronary stents by using integrated computational models to provide detailed predictions of implanted BRS performance. The overall project vision was to develop a set of integrated modules that provide predictions of stent performance in the pre-operative, short-, medium- and long-term phases of the device lifetime. The platform included detailed predictions of functional device performance through *in silico* bench testing, predictions of device deployment, fluid dynamics, drug delivery and myocardial perfusion (‘INSILC Cloud’, 2018). As part of the InSilc project, the “Degradation Module” was developed as part of this thesis to provide predictions of the long-term performance of several candidate vascular scaffolds. The Degradation Module uses the constitutive phenomenological degradation models that were developed in Chapter 5 to predict the long-term performance of implanted scaffolds. This approach affords the InSilc platform the unique opportunity to pose a wide range of “what if” questions to explore stent performance through different virtual scenarios. This could facilitate useful insight in device behaviour during the design and development phase of coronary stents.

The objective of this Chapter is to describe (i) the development of the InSilc Degradation Module, (ii) its integration into the InSilc ISCT workflow and (iii) to present a number of

virtual use-cases or “scenarios” to demonstrate its functionality. For the latter component, three separate scenarios were considered that allowed the implanted performance of different stents and stent designs to be compared across several arterial configurations. The results were then used to generate clinically relevant outputs and assess the long-term performance.

## 8.2. Methods

### 8.2.1. InSilc Platform

#### 7.2.1.1 InSilc Workflow

The InSilc platform consists of several integrated modules to provide detailed predictions of implanted device performance. These integrated modules provide predictions of stent performance, functionalities and operation in the pre-operative, short-, medium- and long-term phases of the device lifetime. The integrated workflow is summarised schematically in Figure 7.1 where an ISCT begins with selection of a virtual patient (or patients) from the virtual population. Following this, the deployment module enables a device to be deployed within straight or bifurcated stenosed patient-specific vessels (from the virtual population) to characterise the short-term performance. The deformed configuration from this module then feeds into the degradation, fluid dynamics, drug delivery and myocardial modules, which together predict the medium- to long-term performance. Further detail on each module is provided in Table 7.1.

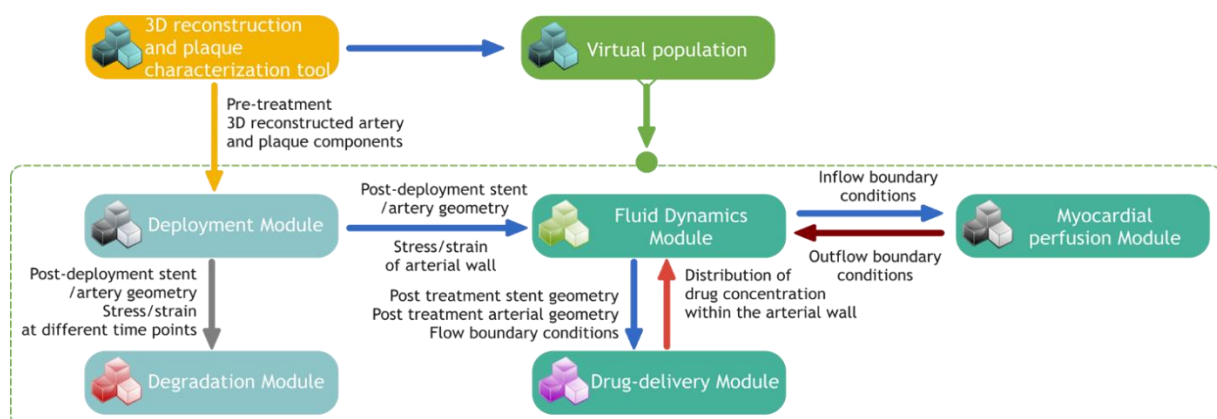


Figure 7.1. Overview of InSilc Degradation Module architecture and required inputs.

Table 7.1. Summary of the primary function of the various main and support modules of the InSilc ISCT Platform.

Module	Summary
Mechanical Modelling Module	The Mechanical modelling module enables virtual <i>in vitro</i> bench testing of coronary stents. Used early in the design process to quickly compare the functional mechanical performance of different stent designs. It includes <i>in silico</i> bench testing for dimensional verification, foreshortening, dog-boning, radial force, local compression, and crush resistance with parallel plates, three point bending and fatigue.
3D reconstruction and plaque characterization tool	The 3D reconstruction and plaque characterization tool is an integrated software that accurately reconstructs parts of the arterial tree including the lumen, the outer wall, as well as plaque. This allows a wide range of patient anatomies to be considered, from straight vessels to more complex tortuous lesions.
Deployment Module	Virtual positioning and deployment of stents within single and bifurcated stenosed patient specific arteries is captured. The results of this module will provide indications on the short-term behaviour. Also, the coupling with other in silico modules, Fluid Dynamics module and Degradation module, will provide valuable information in medium/long term.
Fluid Dynamics Module	The fluid dynamics of the implanted scaffolds are examined at different length scales. The first level concerns characterization of the macroscopic flow phenomena where the scaffold is implanted. For the macroscopic approach, blood is treated as a continuum, and the velocity and shear stress patterns in the stent will be computed. The second level is flow patterns on a microscopic scale, where blood is not treated as a continuum on this.
Degradation Module	In polymer-based degradation, continuum damage mechanics approaches have been developed that capture the effect of polymer chain scission through a degradation damage variable that operates on materials parameters of the chosen constitutive law. Similarly, metal-based corrosion has been captured through continuum damage mechanics, whereby a corrosion kinetic parameter controls the load-bearing capacity of surface elements.
Myocardial Perfusion	The Myocardial perfusion module allows for more realistic simulation of post-operative coronary flow in patients by describing the local response of the cardiac muscle and the coronary autoregulation system. This module can predict the degree to which the stent will enable re-perfusion of the coronary arteries following implantation.
Drug Delivery	Taking the outputs from the deployment and fluid dynamics modules, the diffusion of the anti-proliferative drugs will be modelled. The arterial wall geometry is meshed, and a flow solver used to model the transluminal flow of plasma.

## 8.2.2. InSilc Degradation Module – General Overview

### 7.2.2.1 Input from other InSilc Modules

The Degradation Module follows the Deployment Module, which is used to predict the implanted configuration of the relevant device and artery. The post-deployment stent/artery geometry and the material stress and strain history at all model integration points are imported from the Deployment Module and form the starting point for the Degradation Module. This is transferred in the form of either Output Database (.odb) and/or input (.inp) file formats. This approach ensures that the model parameters are derived directly from the InSilc Deployment Module, with continuity maintained in the discretisation/mesh, element type, underlying constitutive model, stress state, and the numerical parameters that control the solution process (e.g. step times, mass scaling etc.) allowing for a consistent predictive mechanical framework.

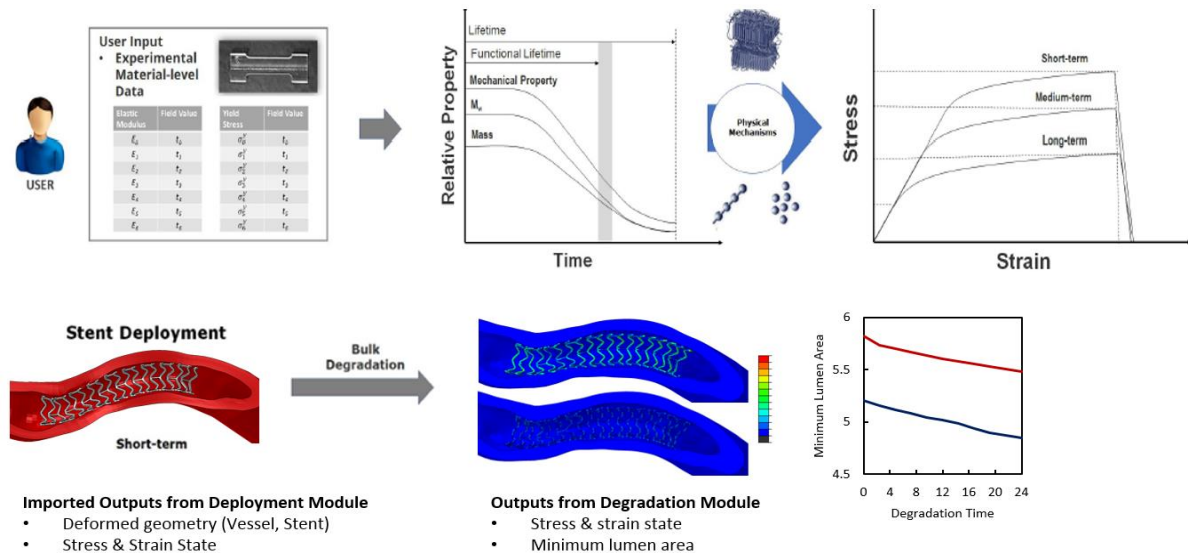


Figure 7.2. Schematic showing the InSilc Degradation Module workflow from experimental material characterisation to prediction of the long-term stent behaviour and Degradation Module outputs.

The Degradation Module uses the degradation framework developed in Chapter 5, which offered distinct flexibility that has the capacity to capture a wide-ranging behaviour for a range of potential material systems, as represented schematically below in Figure 7.2. Despite the limitations observed in the short-term creep response, the developed framework still provides an indication of the isolated device degradation performance. The degradation modelling framework can be implemented by considering the polymer behaviour to be either rate-dependent or rate-independent, implemented using elastic-plastic and elastic-visco-plastic (Johnson-Cook plasticity) constitutive laws. The Degradation Module also offers visco-elastic-plastic options through a parallel rheological framework (PRF) model, which was not described as part of this thesis. It should be noted that the different material models were used to best capture the experimental or literature observed behaviour of the represented BRS and also to act as a demonstration of the platform.

Table 7.2. Summary of Constitutive Models in InSilc Degradation Module.

Material	Constitutive Model
PLLA Non-Commercial BRS	<b>Johnson-Cook:</b> The InSilc degradation framework uses the isothermal condition of the Johnson-Cook model and introduces a series of degradation damage parameters ( $d_1, d_2, d_3$ ) that control the evolution of key material properties.
Tyrocore™ REVA Medical Fantom Encore	<b>Parallel Rheological Framework (PRF)*:</b> The PRF model describes nonlinear viscoelastic-elastoplastic material behavior. The InSilc degradation framework introduces time-dependent damage parameters.



<b>PLLA Abbot ABSORB BVS</b>	<b>Elastic-Plastic:</b> A series of field-dependent variables are introduced to control the evolution of material properties as a function of time during the analysis. This behavior has already been described in Chapter 6, using similar damage parameters ( $d_1, d_2, d_3$ ) to control material degradation.
------------------------------	---

\* Not addressed in this thesis

### 7.2.2.3 Results and Clinical Endpoints

Based on this, the InSilc degradation module predicts the implanted configuration of the device and artery over the defined time period of degradation. Stent-artery configurations and the material stress/strain history within the device and the artery is predicted. The detailed biomechanical output provided here may be related to several clinical endpoints relevant to implanted stents, mainly related to the Minimal Lumen Area (MLA). All outputs from the InSilc Degradation (and other modules) have been integrated into a single web-based cloud platform that enables the users to set up, monitor and analyse the results of virtual clinical trials and bench tests ('INSILC Cloud', 2018).

## 8.2.3. InSilc Scenarios – Simulation Setup and Clinical Outputs

### 7.2.3.1 Virtual Scenarios

This Chapter considers three set of virtual “scenarios” to demonstrate the functionality of the platform that allowed the implanted performance of different stents and stent designs to be compared across several arterial configurations. These scenarios were defined as follows, which are also summarised in Table 7.3 and schematically showed in Figure 7.3 below.

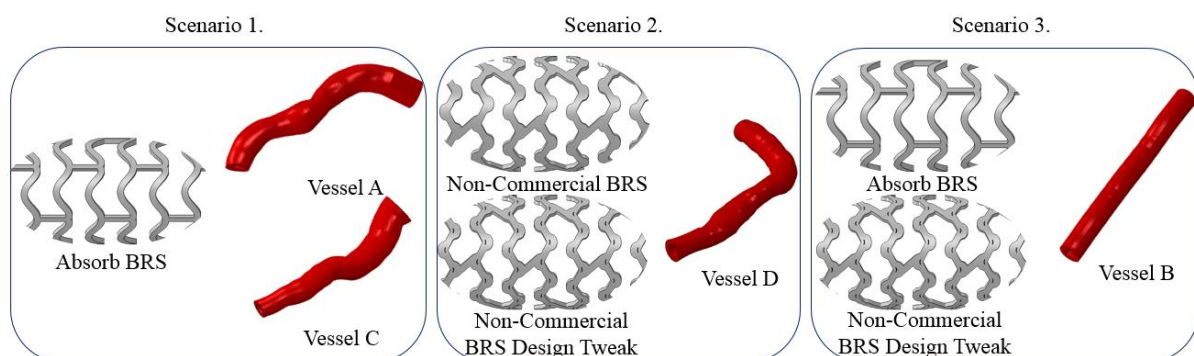


Figure 7.3. Schematic showing the BRS and the vessel geometries in which they are implanted.

**Scenario 1 - Compare Patient Anatomy:** The performance of the Abbott Absorb in treating two separate patient-specific vessel anatomies is compared in this scenario. While both these

cases use the same BRS geometry, the BRS deployed in vessel C is 5mm longer than the BRS used in vessel A, such that it covers the stenosed region.

**Scenario 2 - Compare Stent Designs:** Two non-commercial prototype BRS scaffolds were considered that have similar characteristic dimensions, although one of the scaffolds contains a design change which consists of the slots show in previous chapters filled in, see Figure 7.3. The removal of this slots was performed to investigate the slots effect on the deployment stress and strain state within the hinge regions of the BRS. Both scaffolds are deployed in a virtual artery based on an animal case (Vessel D).

**Scenario 3 - Compare Different Stents:** The Abbott Absorb BRS and non-commercial BRS were deployed within a virtual artery based on an animal case (Vessel B) and long-term performance compared.

*Table 7.3. InSilc scenarios covered in this chapter investigating the effects of degradation.*

Vessel ID	BRS Deployed	Scenario Code	Scenario No.
A	Abbott Absorb (Ab)	EMC001-Ab	1
C	Abbott Absorb (Ab)	EMC018-Ab	
D	Non-commercial scaffold (PP-F0)	LCX1909-PP-F0	2
D	Non-commercial scaffold, design tweak (PP-F1)	LCX1909-PP-F1	
B	Non-commercial scaffold, design tweak (PP-F1)	LAD1785-PP-F1	3
B	Abbott Absorb (Ab)	LAD1785-Ab	

### 7.2.3.2 Stent and Vessel Geometries

The BRS modelled in these degradation scenarios include the Abbott Absorb, and two non-commercial polymer BRS. A number of patient-specific human and animal vessels were reconstructed and used in these scenarios. Reconstruction of the virtual patients was performed by project collaborators, Foundation for Research and Technology Hellas (FORTH). The four coronary vessel geometries used across these scenarios are shown in Figure 7.3 above. Reconstruction of the vessels was performed using a genetic algorithm optimizer to determine the calibration parameters across x-ray angiography views and find the vessel centre line. The x-ray angiography was performed using two projections to determine the vessel path in 3D

space. Meshing of the vessels was performed using the non-uniform rational B-spline (NURBS) method. Further reading of the vessel reconstruction process is available in (Vukicevic *et al.*, 2018). Each of the scaffolds was discretised using hexahedral reduced integration elements (C3D8R). The deployment of these scenarios was performed by the Deployment Module owner Politecnico di Milano (POLIMI). The process for deploying is described in detail here (Poletti *et al.* 2022), and followed various BRS instructions for use (IFU) for each device. This first consisted of a crimping simulation where BRS were crimped into straight configurations. The site of implantation was pre-dilated before the BRS was deployed using a simplified balloon. The BRS was held at maximum pressure to allow for stress relaxation in the polymer BRS before deflating.

To apply the degradation framework developed in this thesis, the stress/strain state was imported from the deployment module. An initial state predefined field was set up to import the deformed mesh (vessel and stent), material models and stress/strain state from the output database file (.odb) produced by the Deployment Module. Information was also extracted from the restart file (.res) for the step number and total simulation time. For all simulations, model parameters must be compatible with the new simulation to ensure that equilibrium was maintained at the beginning of the degradation simulation. This meant that the initial constitutive law, mass scaling parameters and boundary conditions initially applied to the degradation model should be consistent with the final time step predicted by the Deployment module. In each of the scenarios, the proximal and distal ends of arteries were constrained in all directions during the degradation simulation. Sufficient space was allowed between the ends of the scaffold and the ends of the vessel such that the expansion of the BRS did not suffer from any edge-effects. The analysis considered a general explicit contact formulation using a friction coefficient of 0.3 applied between the BRS-vessel contacts. A target time increment of  $1 \times 10^{-5}$  was applied to the degradation simulations.

### 7.2.3.3 Constitutive Material Models

The short-term mechanical behaviour of the PLLA BRS were modelled using the Johnson-Cook elastic-visco-plastic constitutive material model. The parameters for the different BRS are outlined in Table 7.4. Here, the material parameters for the non-commercial BRS were obtained from a number of bench-top tests on curved dog-bone samples laser-cut from PLLA tubes completed as part of the data acquisition of the Mechanical Modelling Module. The parameters for the Abbot Absorb device were determined by (Antonini *et al.*, 2021). Arbitrary melt and transition temperatures were selected for the purpose of degrading the plastic response.

Table 7.4. Material parameters for the constitutive material behaviour of the PLLA used in the BRS simulations.

BRS Model	Elastic Modulus (E) GPa	Poisson's Ratio ( $\nu$ )	Johnson-Cook Parameters						Johnson-Cook Rate Dependant Hardening	
			A	B	n	m	Tm	Tt	C	$\dot{\epsilon}_0$
Non-Commercial BRS	1.665	0.45	2.0	3.0	1.2	1	60	20	2.0	$2.0 \times 10^{-4}$
Abbott Absorb	1.665	0.45	5.0	30.0	1.97	1	60	20	1.5	$2.0 \times 10^{-5}$

The long-term degradation behaviour of the Absorb and non-commercial BRS was predicted using the degradation framework as developed in Chapter 5. A number of degradation parameters ( $d_1$ ,  $d_2$ ,  $d_3$ ) capable of controlling the elastic modulus, yield stress and failure strain were evolved through Equations ( 5-1 ), ( 5-1 ) and ( 5-2 ). The evolution of each of these parameters is shown below in Figure 7.4.

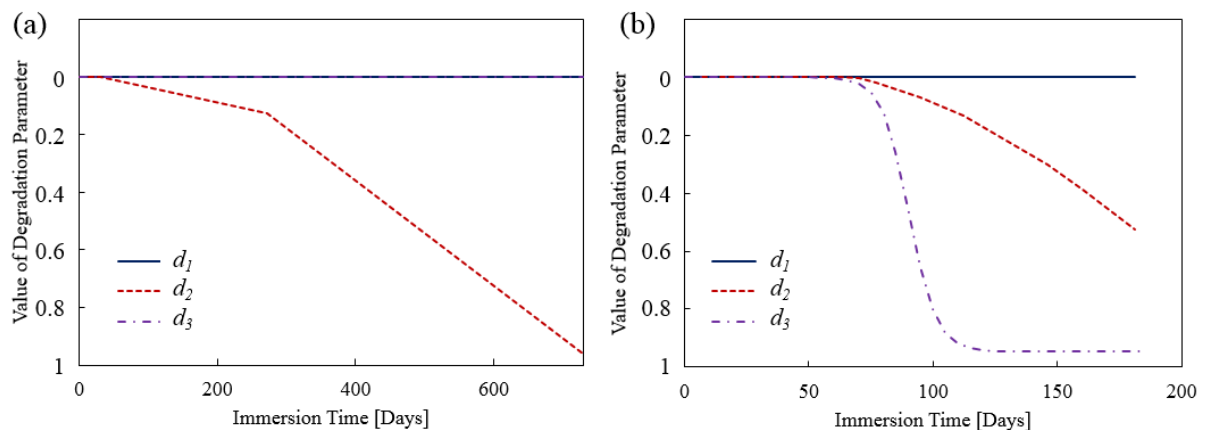


Figure 7.4. Plots demonstrating the evolution of the various degradation parameters  $d_1$  (elastic modulus),  $d_2$  (yield stress) and  $d_3$  (failure strain) for (a) Abbott Absorb and (b) non-commercial BRS.

A three-layer model was used to represent human vessels. Both media and adventitia vessel layers were represented 6<sup>th</sup> order reduced polynomial strain energy density function, with parameters summarised in Table 7.5. The third layer consisted of an intima and plaque region which were represented using a Neo-Hookean hyperelastic law, with parameters summarised in Table 7.5. Elastic-plastic material properties used to represent the material response of animal vessels B and D, with parameters summarised in Table 7.6 values for material properties were calibrated through experimental testing performed by project collaborator FORTH.

Table 7.5. Material coefficients for the Neo-Hookean and 6<sup>th</sup> order reduced polynomial strain energy density functions for the media, adventitia, intima and plaques of the human vessels A and C.

	$C_{10}$	$C_{20}$	$C_{30}$	$C_{40}$	$C_{50}$	$C_{60}$	$D_1$	Yield Stress MPa ( $\sigma_y$ )
Media	0.072916	3.70859	-155.918	9183.27	-261159.0	$2.91 \times 10^6$	0.0	-
Adventitia	0.260211	47.5549	-4086.68	529231	$-2.69 \times 10^{-7}$	$5.65 \times 10^8$	0.0	-
Intima- Plaque	0.15	-	-	-	-	-	0.0	0.4
Lipidic Pool	$2.5 \times 10^{-4}$	-	-	-	-	-	0.0	-

Table 7.6. Elastic-plastic material properties used to represent the material response of animal vessels B and D.

Elastic Modulus (E) GPa	Poisson's Ratio ( $\nu$ )	Yield Stress MPa ( $\sigma_y$ )
0.0032	0.45	0.47

#### 7.2.3.4 Clinical Outputs

A critical clinical output for the long-term follow up of BRS is the evolution in minimal lumen area (MLA) (Auricchio *et al.*, 2011). Looking at the undeformed artery, the section with the maximum stenosis was found and two diametrically opposed nodes were identified, and their coordinates are extracted for the different time steps. The distance between these identified nodes was then calculated in order to find how the MLA evolves over time. A control was also performed about the position of the nodes over time since mesh modifications can change the relative position of nodes. A schematic of MLA measurement is shown below in Figure 7.5. The change in MLA across the stenosed region was also recorded by measuring the MLA at

various points along the vessel in the as deployed and degraded states. The contact stress in the vessels and stress state within the degraded scaffolds was also recorded.

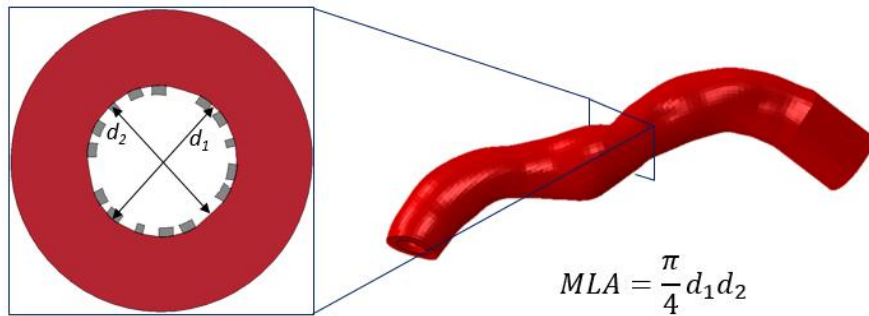


Figure 7.5. Schematic showing the method of computing the minimal lumen area from the most occluded section of the patient specific anatomy.

## 8.3. Results

### 8.3.1. Scenario 1 – Comparison of Patient Anatomies

The first scenario considered deployment of the same BRS, the Abbott Absorb into different human virtual vessels vessel A and vessel C. A slightly longer BRS was selected for vessel C to account for the occlusion sizing. Contour plots showing the maximum principal stress of both scaffolds deployed in the vessel are shown below in Figure 7.6. They show a decrease in the vessel stress over the 24-month degradation period. Figure 7.7 shows the stress within the vessel over the degradation period. It shows a decrease in the stress within the various layers of the vessel over the degradation period.

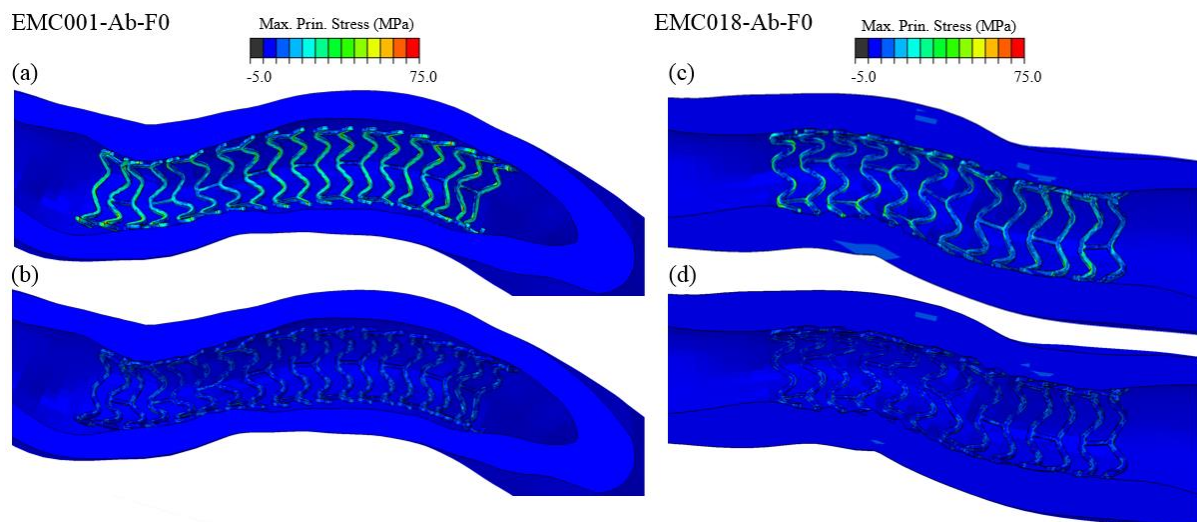


Figure 7.6. Contour plots showing the maximum principal stress as deployed (a, c) and after (b, d) 24 months degradation for the Abbott Absorb BRS deployed in virtual human vessel anatomies.

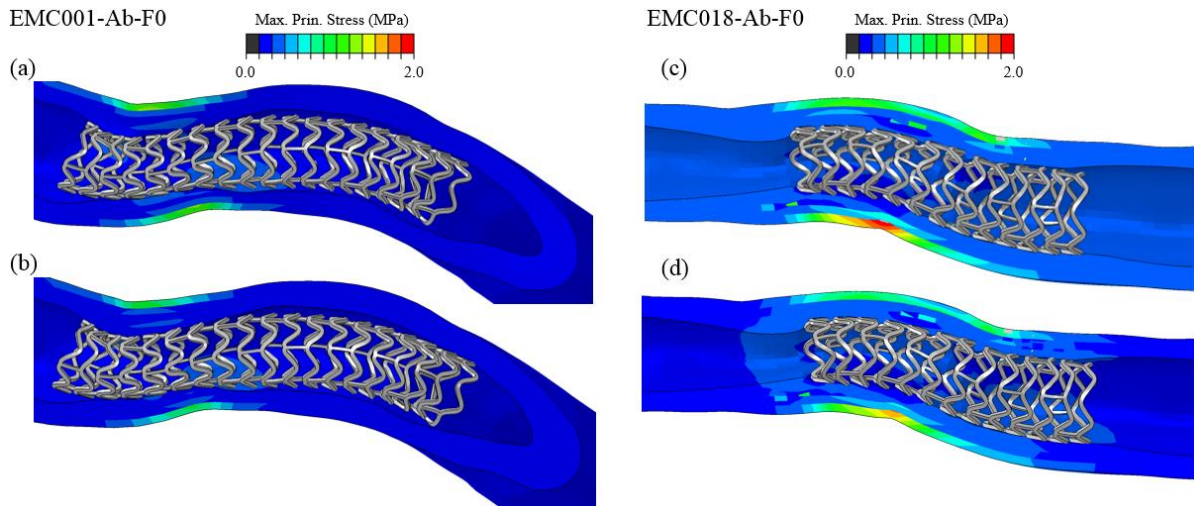


Figure 7.7. Contour plots showing the maximum principal stress of the vessel as deployed (a, c) and after (b, d) 24 months degradation for the Absorb BRS deployed in virtual human vessel anatomies.

The evolution in MLA and the change in MLA across the stenosed regions are captured in Figure 7.8 over the simulated 24-month period for the Absorb in the two different vessel geometries. Here, it is evident that the initial MLA for both vessels is different, with scenario EMC018-Ab-F0 showing a higher MLA immediately following deployment. Following this, Figure 7.8(a) shows a largely linear reduction in MLA area for the two different vessel geometries, with both predicting a similar reduction in MLA over the 24-month period. Figure 7.8(b) shows the reduction in MLA across the stented region of the vessel, the largest reduction in MLA was found to occur at the location of the highest stenosis. While Figure 7.8(c) again shows the reduction in MLA across the stented region, for this vessel case the reduction in MLA is more disturbed across the stent region, this is due to a different plaque and stenosed region morphology compared with the localised instance shown in Figure 7.8(b).

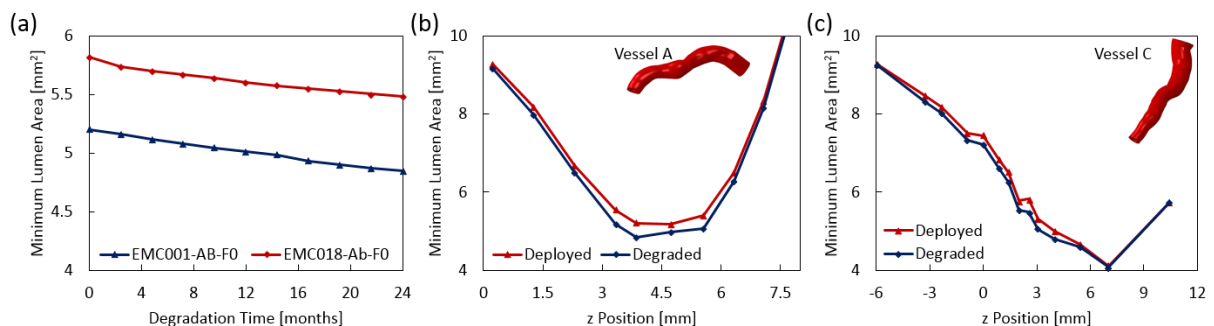


Figure 7.8. (a) Reduction in minimum lumen area over 24-month degradation period, (b) change in minimum lumen area across the stenosed region for scenario EMC001-Ab-F0 and (c) change in minimum lumen area across the stenosed region for scenario EMC018-Ab-F0.



### 8.3.2.Scenario 2 – Comparison of Stent Designs

This scenario considered two similar PLLA BRS, one of which possessed a design tweak to include no slots in the hinge regions, the difference between the two designs can be seen in the cut-out in Figure 7.9 below. The introduction of the slots slightly reduced the stress concentration at the bottom of the hinge points in the non-commercial BRS. Contour plots showing the maximum principal stress in the vessel of both scaffolds deployed in the same virtual animal vessel anatomy (Vessel D) are shown below in Figure 7.10. The inclusion of the slots is positive in reducing the concentration of high stresses in the hinge regions of the stent.

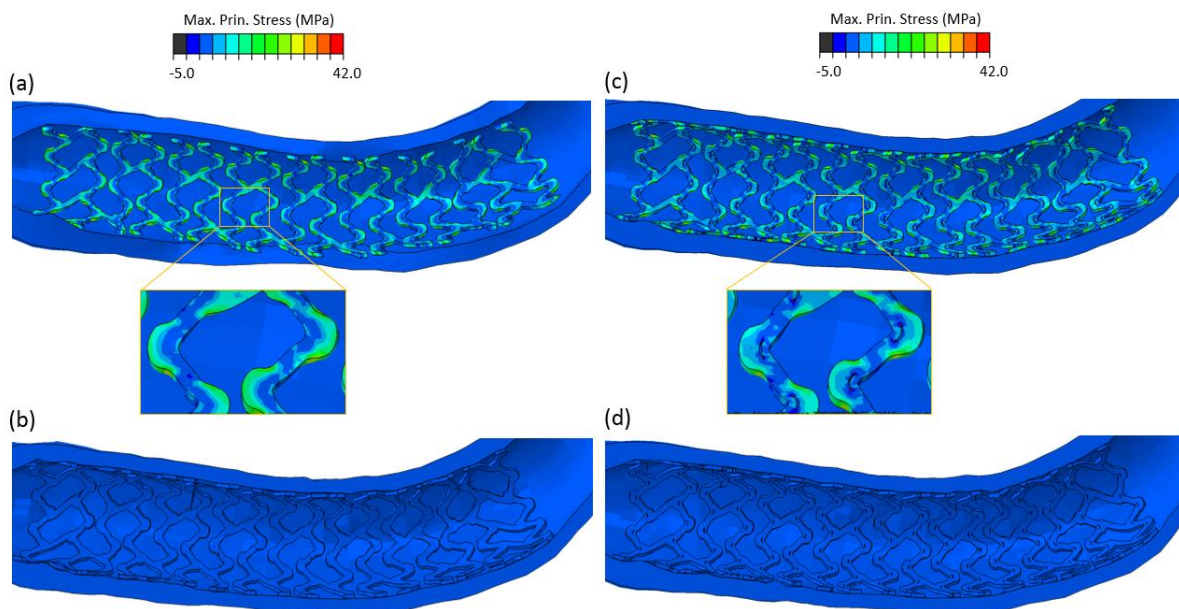


Figure 7.9. Contour plots showing the maximum principal stress as deployed (a, c) and after (b, d) 24 months degradation for the non-commercial BRS deployed in virtual animal vessel anatomies.

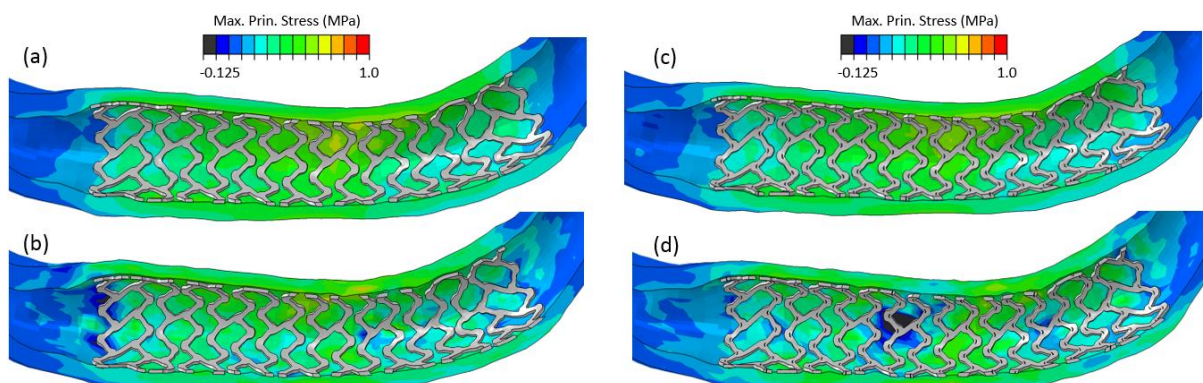


Figure 7.10. Contour plots showing the maximum principal stress of the vessel as deployed (a, c) and after (b, d) 24 months degradation for the non-commercial BRS with and without the design tweak respectively deployed in virtual animal vessel anatomies.



While the stress state in the BRS is greatly reduced due to degrading the  $d_2$  (yield stress) parameter in the vessel maintains the deployed diameter, Figure 7.10 above. Figure 7.11 below shows that there is very little change in the minimal lumen area over the simulated 24-month period, which can be attributed to the plastic deformation in the vessel and lower elastic forces applied to the BRS compared with the virtual human vessel anatomies.

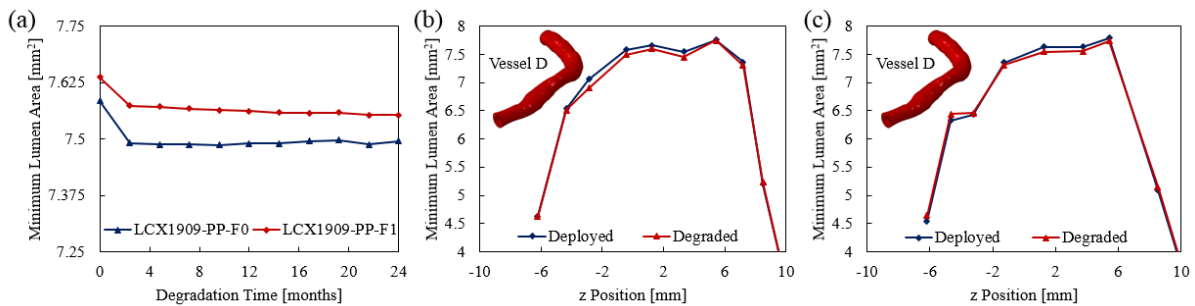


Figure 7.11. (a) Reduction in minimum lumen area over 24-month degradation period, (b) change in minimum lumen area across the stenosed region for scenario LCX1909-PP-F0 and (c) change in minimum lumen area across the stenosed region for scenario LCX1909-PP-F1.

### 8.3.3. Scenario 3 – Comparison of Different Stents

Scenario 3 considered two different BRS, the Absorb and a non-commercial BRS deployed in the same virtual animal vessel anatomy (Vessel B). Contour plots show the maximum principal stress of both BRS deployed in the vessel are shown below in Figure 7.12. Stress within the artery is shown in Figure 7.13, show a small decrease in stress over the degradation period.

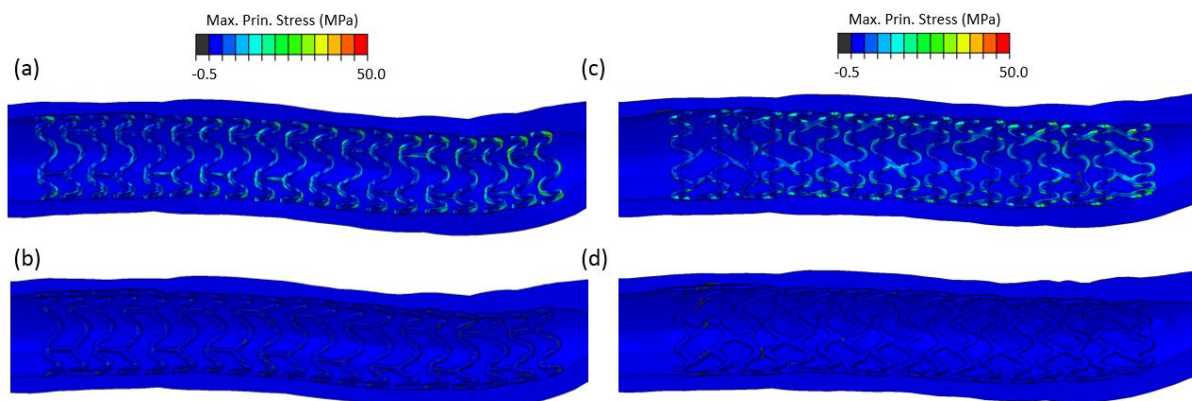


Figure 7.12. Contour plots showing the maximum principal stress as deployed (a, c) and after 24 months (b, d) degradation for the Absorb (a-b) and non-commercial BRS (c-d) deployed in virtual human vessel anatomies.

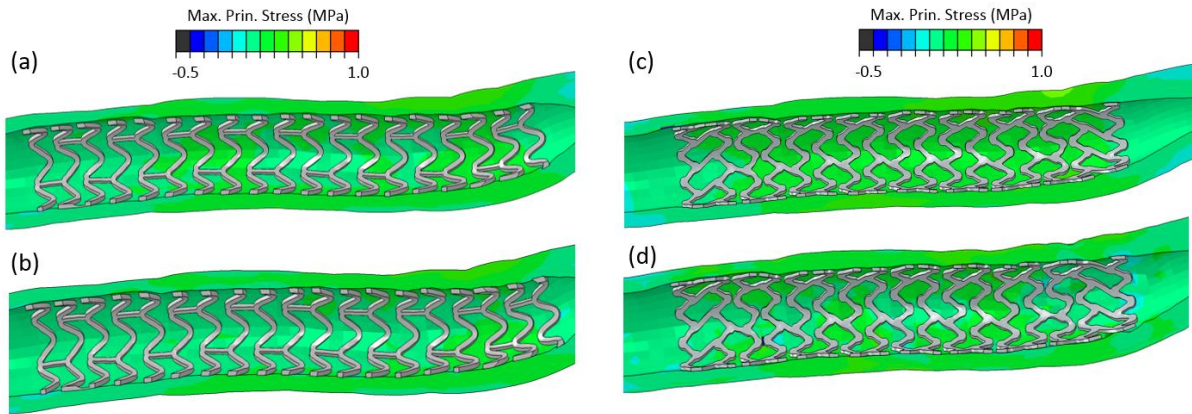


Figure 7.13. Contour plots showing the maximum principal stress of the vessel as deployed (a, c) and after 24 months degradation for the Absorb (a-b) non-commercial BRS (c-d) deployed in virtual animal vessel anatomies.

Figure 7.14 below shows the change in the minimal lumen area over the simulated 24-month period. Here, it is evident that the different BRS devices provided a substantial different in initial lumen area immediately following deployment. Following this, there is a relatively small loss in MLA over the 24-month period, which is attributed to the plastic deformation of the vessel.

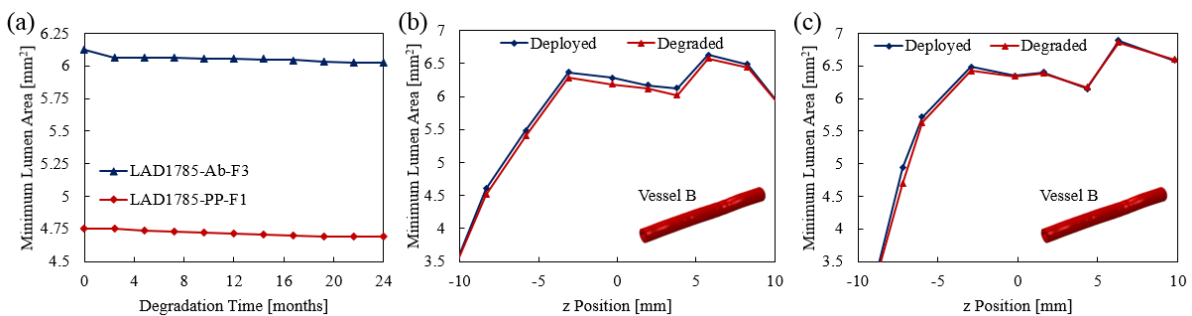


Figure 7.14. (a) Reduction in minimum lumen area over 24-month degradation period, (b) change in minimum lumen area across the stenosed region for scenario LAD1785-Ab-F3 and (c) change in minimum lumen area across the stenosed region for scenario LAD1785-PP-F1.

## 8.4. Discussion

This chapter described the development of the Degradation Module for the InSilc platform, which used the degradation framework developed in Chapter 5 and applied to a number of virtual scenarios as part of the InSilc ISCT platform to demonstrate its functionality. The scenarios consisted of (i) comparing the effects of a design tweak to the long-term performance of two BRS deployed in the same virtual animal vessel, (ii) comparing the long-term performance of two different polymer BRS in the same virtual animal vessel and (iii)

---

comparing the long-term performance of the same polymer BRS in different patient specific virtual vessels. The degradation process from each of the scenarios resulted in a decrease in the minimum lumen area and provided a clear demonstration of the capabilities of the degradation module in providing predictions of image-based reconstructed patient-specific anatomies.

Scenario 1 investigated the use of the same BRS (Abbott Absorb) in different virtual human vessel anatomies. Figure 7.8 shows the lumen loss across the stenosed region, it shows a small difference between the as deployed and degraded minimum lumen area. The small reduction in minimum lumen area can be attributed to the plastic deformation in the vessel and an absence of elastic layers used in Scenario 1, meaning limited elastic recoil of the vessel once the deployment of the devices was completed. While the small reduction in area could also be attributed to the poor sizing of the BRS for the virtual vessels and a lack of a local stenosed region, this scenario presents an interesting case in that the plastic behaviour of the vessel limited the amount of recoil during the degradation process. Considering the results of Chapter 5, the short-term creep response observed in the experimental tests would not be as detrimental if deployed in a vessel that had its elastic recoil limited by the plastic behaviour. It is very possible that clinical deployments of devices result in such plastic behaviour, which may be a reason that the short-term behaviour of BRS has not proven problematic. Scenario 3 compared the same BRS device deployed within the same virtual animal vessel. While there were some differences in the initial deployed diameter and stress state of the deployed configuration, there was little difference in the long-term performance with both devices showing a similar reduction in lumen area. Again, for Scenario 3, a comparison between different BRS devices in the same vessel geometry, it showed differences in the initial deployed diameter with similar long-term degradation performance. While these two scenarios provided useful information on the initial configuration of the devices, it highlights the importance of the representative material models for predicting the long-term degradation performance as well as proper sizing

of the stent for the vessel region to be treated. As seen in Chapter 6, vessels represented with multiple hyperelastic layers show a larger reduction in the lumen area when the in-situ BRS is degraded. These vessels are more representative of what is found *in vivo* (Holzapfel *et al.*, 2005) and more representative of the kind of anatomies that are treated clinically in percutaneous interventions.

These scenarios demonstrate some of the possibilities and the resulting information available using an ISCT platform over traditional animal and human trials where performance comparisons of different BRS or design tweak on the same BRS device can be assessed in the same vessel anatomy which is not possible *in vivo*. While the degradation model that was developed in this thesis had certain limitations in predicting the long-term performance of non-static behaviour, this platform may still provide insight into the performance of stents, allowing design changes and/or patient anatomies to be easily compared (particularly short-term performance). However, despite their usefulness in giving insight into the device performance ISCT are still not at a stage where they can predict the life-time behaviour of a polymer BRS. Some future challenges of *in silico* clinical trials stem from validation of *in silico* models and reluctance from governing bodies to adopt ISCT as part of the approval process reducing the reliance on the current animal and human clinical trial systems. While ISCT cannot fully replace real world and *in vivo* testing, adoption of ISCT platforms could improve device outcomes owing to the number of scenarios that can be considered without extensive costs in material, human patients and animals involved. Verification and validation is a critical component of *in silico* modelling and recently the ASME V&V Standard Committee for medical devices released a document providing a Risk-Informed Credibility Assessment Framework, known as V&V 40 (ASME, 2018). This document is intended to provide guidance on assessing computational models' credibility within a context of use. It consists of verifying the computational models to assess they are implemented and computed correctly and

validating the models to assess if the model is an accurate representation of the reality of interest. This document can be used in conjunction with the development of future *in silico* clinical trials to ensure they are accurately representing the clinical problem and increase trust with regulating bodies (Viceconti *et al.*, 2019). Indeed some studies have already implemented this framework for the validation of their computation studies (Berti *et al.*, 2021).

Some limitations of this study include the degradation behaviour used to inform the degradation framework to predict the long-term performance. In particular the Abbott Absorb BRS based on the two year real-time degradation study performed by Qiu *et al* (Qiu *et al.*, 2018). This study shows that the only material property affected by the degradation process to be the yield stress while experimental degradation studies have shown that a number of mechanical properties are affected during degradation for PLLA (Duek, Zavaglia and Belangero, 1999; Tsuji, Mizuno and Ikada, 2000). Extensive degradation testing should be performed at both device and material level to gain greater understanding of the degradation process such that representative material behaviour can be used to accurately predict the long-term performance. A further limitation to the current degradation framework is the effect of encapsulation of the BRS and neointimal modelling over time and how this effects or alters the degradation process. The scenarios presented here predict the long-term behaviour over a two year period, however it has been shown that in most cases neo-intimal tissue begins to encapsulate the scaffold after implantation (Boland, Grogan and McHugh, 2017). These scenarios do not currently account for this process however future modelling could account for this using further improving the predicted long-term degradation behaviour.

## **8.5. Conclusions**

In this chapter, a demonstration of the computational degradation framework developed in chapter 5 and applied through an ISCT. It has demonstrated the possibility to simulate the

performance of a potential new BRS in terms of pre-defined preclinical and clinical objective performance criteria and to predict *in silico* the effect (positive or negative), the variation of some parameters (such as overall design, materials, design tweaks, etc.) have on the long-term performance and indeed the performance in general. It is also possible to compare the behaviours of a potential new BRS with respect to an existing design or to compare the behaviour of two existing stents in target patient populations or specific lesion types, which could prove particularly useful in the future development of BRS.

## 8.6. References

- Antonini, Luca, Gianluca Poletti, Lorenzo Mandelli, Gabriele Dubini, Giancarlo Pennati, and Lorenza Petrini. 2021. “Comprehensive Computational Analysis of the Crimping Procedure of PLLA BVS : Effects of Material Viscous-Plastic and Temperature Dependent Behavior.” *Journal of the Mechanical Behavior of Biomedical Materials* 123 (April): 104713. <https://doi.org/10.1016/j.jmbbm.2021.104713>.
- ASME. 2018. “Assessing Credibility of Computational Modeling through Verification and Validation: Application to Medical Devices.” *The American Society of Mechanical Engineers: ASME*. <https://www.asme.org/codes-standards/find-codes-standards/v-v-40-assessing-credibility-computational-modeling-verification-validation-application-medical-devices>.
- Auricchio, F., M. Conti, M. De Beule, G. De Santis, and B. Verheghe. 2011. “Carotid Artery Stenting Simulation: From Patient-Specific Images to Finite Element Analysis.” *Medical Engineering and Physics* 33 (3): 281–89. <https://doi.org/10.1016/j.medengphy.2010.10.011>.
- Berti, Francesca, Luca Antonini, Gianluca Poletti, Constantino Fiuza, Ted J. Vaughan, Francesco Migliavacca, Lorenza Petrini, and Giancarlo Pennati. 2021. “How to Validate in Silico Deployment of Coronary Stents: Strategies and Limitations in the Choice of Comparator.” *Frontiers in Medical Technology* 3 (August). <https://doi.org/10.3389/fmedt.2021.702656>.
- Boland, Enda L., James A. Grogan, and Peter E. McHugh. 2017. “Computational Modeling of the Mechanical Performance of a Magnesium Stent Undergoing Uniform and Pitting Corrosion in a Remodeling Artery.” *Journal of Medical Devices* 11 (2): 021013. <https://doi.org/10.1115/1.4035895>.
- Byrne, Robert A., Patrick W. Serruys, Andreas Baumbach, Javier Escaned, Jean Fajadet, Stefan James, Michael Joner, et al. 2015. “Report of a European Society of Cardiology-European Association of Percutaneous Cardiovascular Interventions Task Force on the Evaluation of Coronary Stents in Europe: Executive Summary.” *European Heart Journal* 36 (38): 2608–20. <https://doi.org/10.1093/eurheartj/ehv203>.
- Desai, Mira. 2020. “Recruitment and Retention of Participants in Clinical Studies: Critical Issues and Challenges.” *Perspectives in Clinical Research* 11 (2): 51–53. [https://doi.org/10.4103/picr.PICR\\_6\\_20](https://doi.org/10.4103/picr.PICR_6_20).
- Duek, E. A.R., C. A.C. Zavaglia, and W. D. Belangero. 1999. “In Vitro Study of Poly(Lactic Acid) Pin Degradation.” *Polymer* 40 (23): 6465–73. [https://doi.org/10.1016/S0032-3861\(98\)00846-5](https://doi.org/10.1016/S0032-3861(98)00846-5).
- FDA. 2010. “Guidance Document for Industry and FDA Staff Non-Clinical Engineering Tests and Recommended Labeling for Intravascular Stents and Associated Delivery Systems and Human Services Food and Drug Administration Center for Devices and Radiological Health Interv.” *US Department of Health and Human Services; Food and Drug Administration, Centre for Devices and Radiological, Health*, 18–20. <http://www.fda.gov/MedicalDevices/DeviceRegulationandGuidance/GuidanceDocuments/ucm0>.
- “FDA PMA Review Process.” 2021. *Fda.Gov*. <https://www.fda.gov/medical-devices/premarket-approval-pma/pma-review-process>.
- Holzappel, Gerhard A., Gerhard Sommer, Christian T. Gasser, and Peter Regitnig. 2005. “Determination of Layer-Specific Mechanical Properties of Human Coronary Arteries with Nonatherosclerotic Intimal Thickening and Related Constitutive Modeling.” *American Journal of Physiology-Heart and Circulatory Physiology* 289 (5): H2048–58. <https://doi.org/10.1152/ajpheart.00934.2004>.
- “INSILC Cloud.” 2018. *Insilc.Eu*. <https://insilc.eu/insilc-cloud/>.
- Poletti, Gianluca, Luca Antonini, Lorenzo Mandelli, Panagiota Tsompou, Georgia S. Karanasiou, Michail I. Papafaklis, Lampros K. Michalis, Dimitrios I. Fotiadis, Lorenza Petrini, and Giancarlo Pennati. 2022. “Towards a Digital Twin of Coronary Stenting: A Suitable and Validated Image-Based Approach for Mimicking Patient-Specific Coronary Arteries.” *Electronics (Switzerland)* 11 (3).

<https://doi.org/10.3390/electronics11030502>.

Qiu, T., R. He, C. Abunassar, S. Hossainy, and L. G. Zhao. 2018. "Effect of Two-Year Degradation on Mechanical Interaction between a Bioresorbable Scaffold and Blood Vessel." *Journal of the Mechanical Behavior of Biomedical Materials* 78 (November 2017): 254–65. <https://doi.org/10.1016/j.jmbbm.2017.11.031>.

Sastry, Ashwani. 2014. "Overview of the US FDA Medical Device Approval Process." *Current Cardiology Reports* 16 (6): 3–7. <https://doi.org/10.1007/s11886-014-0494-3>.

Singh, Achintya D., Aayush K. Singal, Agrima Mian, Samir R. Kapadia, David P. Hedrick, Anmar Kanaa’N, Jaikirshan J. Khatri, Rishi Puri, and Ankur Kalra. 2020. "Recurrent Drug-Eluting Stent In-Stent Restenosis: A State-of-the-Art Review of Pathophysiology, Diagnosis, and Management." *Cardiovascular Revascularization Medicine* 21 (9): 1157–63. <https://doi.org/10.1016/j.carrev.2020.01.005>.

Tsuji, Hideto, Akira Mizuno, and Yoshito Ikada. 2000. "Properties and Morphology of Poly(L-Lactide). III. Effects of Initial Crystallinity on Long-Term In Vitro Hydrolysis of High Molecular Weight Poly(L-Lactide) Film in Phosphate-Buffered Solution." *Journal of Applied Polymer Science* 77 (7): 1452–64. [https://doi.org/10.1002/1097-4628\(20000815\)77:7<1452::AID-APP7>3.0.CO;2-S](https://doi.org/10.1002/1097-4628(20000815)77:7<1452::AID-APP7>3.0.CO;2-S).

Viceconti, Marco, Miguel A. Juárez, Cristina Curreli, Marzio Pennisi, Giulia Russo, and Francesco Pappalardo. 2019. "Credibility of in Silico Trial Technologies - A Theoretical Framing." *IEEE Journal of Biomedical and Health Informatics* 24 (1): 4–13.

Vukicevic, Arso M., Serkan Çimen, Nikola Jagic, Gordana Jovicic, Alejandro F. Frangi, and Nenad Filipovic. 2018. "Three-Dimensional Reconstruction and NURBS-Based Structured Meshing of Coronary Arteries from the Conventional X-Ray Angiography Projection Images." *Scientific Reports* 8 (1): 1–20. <https://doi.org/10.1038/s41598-018-19440-9>.



